Transport and optical spectroscopy of a quantum point contact

Dissertation
an der Fakultät für Physik
der Ludwig–Maximilians–Universität München

vorgelegt von
Enrico Schubert
aus Dresden

München, Dezember 2016

Erstgutachter: Prof. Dr. Alexander Högele
Zweitgutachter: PD Dr. Stefan Ludwig
Tag der Abgabe: 15.11.2016
Tag der mündlichen Prüfung: 20.12.2016

Zusammenfassung

Ein kurzer, eindimensionaler Kanal in einem zweidimensionalen Elektronensystem (two-dimensional electron system, 2DES) wird als Quantenpunktkontakt (quantum point contact, QPC) bezeichnet. Der elektrische Leitwert eines QPC ist bei tiefenen Temperaturen von einigen Kelvin in Vielfachen des Leitwertsquantums $G_\mathrm{Q} = 2e^2/h$ quantisiert. Zusätzliche kann eine Stufe bei $\simeq 0.7 G_\mathrm{Q}$ auftreten, bekannt als die 0.7-Anomalie.

In dieser Dissertation wurden QPCs mithilfe von Elektronentransport und optischen Methoden untersucht. Die QPCs wurden dabei durch Verarmung eines 2DES realisiert. Unter Ausnutzung einer neuartigen Gattergeometrie wurde in Transportexperimenten der Tieftemperatur-Leitwert von QPCs mit einer kontrollierten Abstimmung des QPC-Einschlusspotentials untersucht. Zudem wurde ein theoretisches Model eingeführt, welches erstmals eine konsistente Erklärung für den mikroskopischen Ursprung der 0.7-Anomalie liefert. Es wurde gezeigt, dass die gemessenen und die berechneten Änderungen des Leitwerts eines QPC im Regime der 0.7-Anomalie mit niederenergetischen Anregungen des externen Magnetfeldes, der Temperatur und der an das 2DES angelegten elektrischen Spannung qualitativ übereinstimmen. Die Übereinstimmung bestätigt das theoretische Model, welches die 0.7-Anomalie als Folge von im Bereich des QPC lokal auftretenden Elektron-Spinfluktuationen erklärt. Desweiteren sagt die Theorie voraus, dass die Elektron-Spinfluktuationen mit einer im Bereich des QPC stark erhöhten Elektron-Spinsuszeptibilität bei verschwindendem Magnetfeld einhergehen, welche inhärent mit der Leitwertsantwort des QPC auf das externe Magnetfeld in Verbindung steht.

Vorbereitend für eine mögliche Überprüfung des theoretisch vorhergesagten Zusammenhangs zwischen der 0.7-Anomalie und der lokalen Spinsuszeptibilität mit optischen Methoden wurden Charakteristiken eines QPC unter optischer Anregung untersucht. Mittels eines speziell für optische Anregung angepassten 2DES wurde die Transportantwort eines QPC auf lokale, resonante optische Anregung des 2DES nahe am QPC analysiert. Dabei wurde gezeigt, dass der dominante Anteil der Transportantwort eines QPC auf intensitätsmodulierte optische Anregung mittels eines elementaren Relaxator-Modells beschrieben werden kann. Aus dem Modell folgt, dass die dominante dynamische Transportantwort eines QPC durch optisch induzierte Modulation des statischen Stromes im 2DES hervorgerufen wird. Als Ursache der Modulation des QPC-Leitwertes werden optisch induzierte Ladungsträger im Valenzband des 2DES vermutet. Durch detaillierte Analyse wurde zusätzlich ein statischer Beitrag zum Transport des QPC bestimmt, welcher zwei Größenordnungen kleiner als die dominante Transportantwort war und als

Photostrom im 2DES identifiziert wurde. Es konnte demnach gezeigt werden, dass die Anwendung des elementaren Relaxator-Modells die Unterscheidung von dynamischen und statischen Beiträgen der Transportantwort eines QPC auf lokale optische Anregung ermöglicht.

Abstract

A quantum point contact (QPC) is a short, one-dimensional channel in a two-dimensional electron system (2DES). At low temperatures of a few kelvin the electrical conductance of a QPC is quantized in multiples of the conductance quantum $G_{\mathrm{Q}} = 2e^2/h$. Additionally a shoulder can arise at $\simeq 0.7G_{\mathrm{Q}}$, known as the 0.7-anomaly.

In this dissertation, QPCs defined by 2DES-depleting metal gates were investigated by means of electron transport spectroscopy. In transport experiments the low-temperature conductance of a novel gate design using additional metal gates for a controlled tuning of the QPC confinement potential was investigated. Moreover, a theoretical model was presented which provides a consistent explanation for the microscopic origin of the 0.7-anomaly for the first time. It was shown that the measured and the calculated responses of the conductance of a QPC in the 0.7-anomaly regime to low-energy excitations of the external magnetic field, the temperature, and the voltage applied to the 2DES are in good qualitative agreement. The agreement strongly substantiates the theoretical model that explains the 0.7-anomaly as a consequence of electron-spin fluctuations emerging locally at the QPC. Furthermore, the theory predicts that the electron-spin fluctuations are accompanied by a strongly enhanced local electron-spin susceptibility at zero magnetic field which is inherently linked to the magnetoconductance response of the QPC.

In preparation for an experimental test of the theoretically predicted interplay between the 0.7-anomaly and the local spin susceptibility by optical means, the characteristics of a QPC under optical excitation were investigated. Using a 2DES specifically adapted for optical studies, transport of a QPC under local resonant optical excitation of the 2DES in the QPC proximity was analyzed. It was shown that the dominant part of the transport response of a QPC to intensity-modulated optical excitation can be described by a relaxation model. The model suggests that the dominant transport response stems from an optically induced modulation of the static QPC current. The related QPC conductance modulation was attributed to optically induced charge carriers in the valence band of the 2DES. Moreover, the contribution of a small photocurrent, two orders of magnitude weaker than the dominant transport photoresponse, was identified in a detailed analysis. Overall, the relaxation model was shown to be instructive to quantify both the dynamic and the static transport responses of a QPC to proximal optical excitation.

Contents

Introduction

The first realization of an electrically controlled amplifying current switch - the transistor - in 1947 launched an evolution of unprecedented extent. Subsequent fundamental understanding of semiconductor bulk and surface effects paired with progress in material quality and fabrication have resulted in tailor-built information storing and logic-gate structures of increasing size and complexity. The constantly decreasing dimensions of the processing elements anticipated by the Moore's law project that the number of components per integrated circuit doubles every two years. The implications of this developments for the society are evident in todays extensive computational technologies and global communication networks. Present fabrication technologies enable the realization of semiconductor-based integrated circuitry with spatial dimensions down to 14 nm, or some 50 atoms, and a lateral pitch of 70 nm. The related structures are thus on the verge of becoming susceptible to critical variations in device dimensions and losses caused by leakage currents or passive power dissipation due to electron tunneling through short channels or thin insulator layers.

In parallel to this development, molecular beam epitaxy (MBE) has enabled controlled stacking of layers of different semiconductor materials with atomic-layer precision. Together with the capability of controlled doping, advanced semiconductor heterostructures enable the realization of low-dimensional electron systems with densities and mobilities comparable to the characteristics of metals. Electron beam lithography with a resolution down to ~ 10 nm in combination with etching techniques or the deposition of electrostatic gates enables to further configure mesoscopic and nanoscopic systems virtually at will. This paved the way toward the investigation of basic quantum mechanical phenomena in highly stable and controlled solid state environments, such as real-time detection of single-electron tunneling events [1], experimental confirmation of the spin-Hall effect [2], imaging of spin accumulation, precession and decay dynamics with both temporal and spatial resolution [3], or the observation of a tunable Kondo effect in an artificial quantum dot [4].

The most elementary building block contained in a variety of semiconductor-based nanostructures is the quantum point contact (QPC), a single constriction within a two-dimensional electron system (2DES) which constitutes a narrow channel separating two 2D reservoirs. A QPC is conceptionally similar to a wave guide where electrons near the Fermi edge can propagate in a number of transverse modes. QPCs have been used for all-electrical spin current generation and detection [5–7], the demonstration of coherent

electron-wave quantum interference by the realization of the electronic analogue to an optical Mach-Zehnder interferometer [8], or the control and detection of quantum interference between different nuclear spin levels in a nanostructure [9] for quantum information processing. A straightforward QPC implementation is achieved by a pair of metal split gates on top of a heterostructure hosting a 2DES. An electrostatic potential at surface metal gates depletes the 2DES underneath and thereby introduces a one-dimensional constriction in the 2D system. Based on the resulting capacitive coupling to the local environment [10], depletion-gate defined QPCs are widely used as remote electric charge detectors with sensitivity to single electron charging events in the local QPC vicinity [11–14]. At low temperatures of a few kelvin, the high mobilities in e. g. GaAs/$Al_xGa_{1-x}As$ 2DESs enable the QPC to operate in the ballistic regime where the mean free path exceeds the effective QPC channel length. A one-dimensional confinement comparable to or smaller than the electron Fermi wavelength then induces the formation of discrete transverse modes in the QPC constriction such that the current I_{QPC} through the QPC becomes quantized. Equivalently, the conductance I_{QPC}/V in the voltage-biased QPC is quantized in multiples of the spin-degenerate conductance quantum $G_{\mathrm{Q}} = 2e^2/h$ [15–17] with the electron charge e and the Planck constant h. The unique conductance quantization is also observed in various one-dimensional systems such as nanowires [18], atomic-scale break junctions [19], carbon nanotubes [20] or graphene constrictions [21]. It can be observed up to room temperature in metal contacts [22] facilitated by the required atom-sized contact dimensions due to the high Fermi energy that yield very large transverse mode energy spacings. Interestingly, neutral atoms that pass a QPC-like constriction generated by laser light potentials also exhibit quantized conductance, in units of $1/h$ [23].

In addition to the regular QPC conductance pattern, a shoulder at $\simeq 0.7G_{\mathrm{Q}}$ is often observed, known as the 0.7-anomaly [24–33]. Though its actual value can vary between $0.5G_{\mathrm{Q}}$ and $0.9G_{\mathrm{Q}}$ [30, 34], the 0.7-anomaly shows uniform features such as becoming more pronounced at intermediate temperatures of a few kelvin [24, 25], an accompanying conductance peak as a function of the 2DES bias voltage, termed the zero-bias peak (ZBP) [27, 32, 35], or a gradual evolution into the spin-resolved quantum $0.5G_{\mathrm{Q}}$ with increasing external magnetic field [24, 25]. Various theoretical explanations have been proposed including Wigner crystallization [36, 37], ferromagnetic spin coupling [38], or the formation of a quasi-bound state in the QPC channel leading to the Kondo effect [39–42]. A close relationship between the occurrence of the 0.7-anomaly and the spontaneous lifting of the spin degeneracy was hypothesized [24, 25], and experimental signatures both in favor of [43, 44] and against [6] this assumption are known. However, a microscopic model for the various experimental observations in the regime of the 0.7-anomaly remained elusive.

In this dissertation, QPCs defined by 2DES-depleting metal gates were investigated. A combined experimental and theoretical analysis of a QPC in the 0.7-anomaly regime was performed. The electron transport experiments at low temperatures down to 30 mK used a novel gate design including additional metal gates that enabled the tuning of the confinement potential in situ. For the QPC calculations a theoretical model was introduced which, for the first time, provided a consistent explanation for the microscopic origin of the 0.7-anomaly. The analysis was carried out in collaboration with the theoretical group

of Prof. Jan von Delft at the LMU. It was shown that the measured and the calculated QPC conductance in the 0.7-anomaly regime agreed in that for low-energy excitations the conductance responses to external magnetic field, temperature, and the voltage applied to the 2DES were similarly determined by a single low-energy scale. This agreement strongly substantiates the theoretical model which ascribes the microscopic origin of the 0.7-anomaly to electron-spin fluctuations emerging locally at the QPC. The spin fluctuations are increased by local interactions which, according to the theory, are strongest in the 0.7-anomaly regime. The calculations predict that the interaction-enhanced spin fluctuations imply a correspondingly increased local spin susceptibility at zero magnetic field which inherently determines the correspondingly enhanced conductance response of the QPC to external magnetic field. Together with the governing low-energy scales, this close connection between local spin fluctuations, the local spin susceptibility, and the magnetoconductance of a QPC in the 0.7-anomaly regime constitute fundamental features of a quantum dot in the Kondo effect regime [4, 45–47]. Although it closely relates both phenomena, a theoretical analysis in the limit of high magnetic fields indicated that the 0.7-anomaly and the Kondo effect are fundamentally different owing to the absence of a quasi-bound state in the QPC. This conclusion was supported by a combined experimental and theoretical analysis of the transition of the confinement potential between a QPC and a quantum dot that did not indicate any connection between the neighboring 0.7-anomaly and the Kondo effect regime.

In preparation for a possible experimental test of the predicted local enhancement of the spin susceptibility in the 0.7-anomaly regime by optical means, additional experiments were carried out at liquid-helium temperatures of 4.2 K. An optical microscope setup sensitive to local magnetization by means of Faraday rotation was presented. The sensitivity of the microscope was tested on a single spin-polarized electron state confined in a self-assembled QD. Furthermore, the behavior of a QPC under optical excitation in the QPC proximity was investigated. To this end, a 2DES was specifically adapted for optical excitation based on simulations and subsequent experimental characterizations of 2DES transport and optical properties. In the accordingly adapted heterostructure, the transport response of a QPC to local, resonant optical excitation of the 2DES in QPC proximity was investigated. It was shown that the governing part of the QPC transport response to intensity-modulated optical excitation is captured by a basic relaxation model. The model suggests that the governing transport response stems from an optically induced modulation of the static QPC current by photoexcited charge carriers in the valence band. Additionally a static contribution to the optically induced transport response of the QPC two orders of magnitude smaller than the dominant dynamic response was identified and attributed to the photocurrent in the 2DES.

The combined experimental and theoretical analysis of the 0.7-anomaly is presented in Chapter 2 and Chapter 3. Chapter 2 describes the QPC characteristics in the 0.7-anomaly regime, while Chapter 3 emphasizes the comparison between the 0.7-anomaly in a QPC and the Kondo effect in a quantum dot. In Chapter 4 the optical microscope setup is presented and the determination of the microscope sensitivity and spatial resolution based on the test experiment with the single polarized spin state are discussed. In Chapter 5 the

design of the heterostructure that hosts a 2DES adapted for optical studies is explained. The results of the simulations of basic transport and optical 2DES properties are discussed and compared with the corresponding experimental results. The characteristics of a QPC under optical excitation is presented in Chapter 6. First the setup used for combined readout of the QPC response to transport and optical excitation is explained. Then initial QPC transport measurements before optical illumination of the sample are evaluated. And finally the relaxation model is introduced and used to infer the dynamic and static components of the QPC response from the measurements. Finally, a summary is provided and an outlook for potential follow-up experiments is given in the concluding section.

Chapter 1

Fundamentals

1.1 Quantum point contact in a two-dimensional electron system

A two-dimensional electron system (2DES), also termed two-dimensional electron gas (2DEG) if electron-electron interactions are neglected a priori, is a degenerate electron system. It is strongly confined in one spatial direction such that the allowed wavenumbers for the electrons in the confinement direction become discrete resulting in an effectively two-dimensional system. A semiconductor-based 2DES is typically created by the use of a tailor-made heterostructure, a stack of layers of various semiconductor materials with similar lattice constants but different band gap energies, that results in a single quantum well (QW) layer for conduction band electrons due to the inherent band alignment of the contributing layers. The QW can be supplied with a steady-state electron density by e. g. modulation-doping for which a remote semiconductor layer within the heterostructure is intentionally doped with impurities. For common III-V gallium-arsenide (GaAs) - based heterostructures which typically additionally incorporate GaAs alloys that contain aluminium (Al) or indium (In), silicon impurities can be used which provide the required excess electron charges up to a certain impurity density. Placing the impurities distantly to the eventual 2DES location greatly reduces Coulomb scattering of the 2DES electrons which ultimately forms the basis for high 2DES mobilities accompanied by large, elastic and inelastic, electron mean free paths l_{mfp} paving the way to the ballistic transport regime. The resulting 2DES electron states in a single QW subband in the effective-mass approximation behave like free particles with the dispersion relation $E(\vec{k}) = \hbar^2 k^2 / 2m_*$ with the wavevector k and the effective mass m_* in the QW plane and the reduced Planck constant $\hbar$.

A quantum point contact (QPC) is a short, narrow constriction usually realized in the 2D-potential landscape of a 2DES. If the imposed narrowing becomes comparable to or exceeds the 2DES Fermi wavelength the constriction becomes effectively one-dimensional (1D). A common technique to generate a QPC is based on a pair of local metal split gates, referred to as QPC gates, which are fabricated on top of the heterostructure in

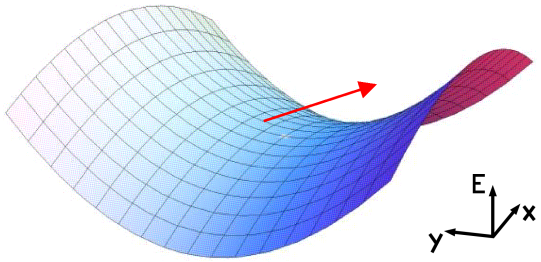

Figure 1.1: Characteristic saddle point potential energy E of a QPC channel (red arrow) imposed on the conduction band bottom in a 2DES which is confined in the z direction.

close proximity to the 2DES (typically located of the order of 100 nm underneath). An appropriate negative electric voltage V_{QPC} applied to the QPC gates electrostatically depletes the 2DES areas beneath to form the QPC, a 1D transport channel, which separates the resulting two adjacent 2DES leads. The shapes and dimensions of the depleted 2DES areas directly depend on the geometry of the QPC gates. This provides high flexibility in and control over the resulting 1D channel design by virtue of standard electron-beam lithography techniques for the QPC gate fabrication with attainable resolutions of the order of 10 nm.

The 2DES potential in the QPC constriction forms a characteristic saddle point as sketched in Fig. 1.1 with the resulting 1D channel indicated by the red arrow. The allowed transverse (y direction in Fig. 1.1) electron modes in the 1D QPC channel are quantized as is the corresponding energy spectrum. The separation of the spatial wave function components yields the electron dispersion relation in the QPC constriction

$$E_n(k) = E_n^0 + \frac{\hbar^2 k_x^2}{2m_*} \,, \tag{1.1}$$

with the wave number k_x of the longitudinal plane wave component, the effective electron mass m_*, and the energy E_n^0 of the bound transverse mode with the quantum number n. Thus within the constriction the longitudinal component maintains the free particle characteristics. The energy spectrum E_n^0 related to the transverse modes generally depends on the particular QPC potential shape and can also depend on the mass of the traversing particles (the latter does not hold for e.g. the harmonic oscillator potential). In Eq. 1.1, $E_n(k = 0) - E_n^0$ equals the bottom of the the QW conduction band plus the zero-point energy stemming from the 2DES confinement in the QW perpendicular to the 2DES x-y plane.

It turns out that in the case of a 1D QPC channel the discrete energy spectrum, naturally occurring in absence of the external magnetic field B_{ext}, evolves gradually into the (QPC-constriction-independent) quantized 2DES electron energy spectrum at $B_{\mathrm{ext}} \gg 0$ which is referred to as the Quantum Hall Effect (QHE) regime. The fundamental physical reason for this similarity is that both regimes are caused by the reduction of the 2DES dimensionality by one due to either the spatial constriction or the cyclotron orbital mo-

tion. In the case of a harmonic 1D confinement (or for any confining potential which is approximated harmonically at small k), in Fig. 1.1 the total energy spectrum of the n'th transverse mode simplifies to [48]

$$\begin{aligned} E_n(k) &= \hbar\omega(n+\frac{1}{2}) + E_{\text{Zeeman}}(B_z) + \frac{\hbar^2 k_x^2}{2\widetilde{m}_*} \,, \\ \text{with } \omega &= \sqrt{{\omega_y}^2 + {\omega_{\text{cyc}}}^2} \,, \\ \text{and } \widetilde{m}_* &= m_* \frac{\omega^2}{\omega_y^2} \,. \end{aligned} \tag{1.2}$$

Increasing $B_{\text{ext}} = B_z$ gradually influences the energy spectrum via the electron cyclotron frequency $\omega_{\text{cyc}} = eB_z/m_*$, in addition to the Zeeman energy E_{Zeeman} and the consistently acting harmonic confinement potential $V = m_*\omega_y^2 y^2/2$ (m_* is the effective electron mass at $B_z = 0$ and e is the elementary charge). Raising B_z selectively depopulates the 1D QPC subbands due to the increasing subband spacing $\hbar\omega$ while the gradual transition to the emerging QHE edge channels preserves the quantization. The onset of B_z affects the dispersion relation, however, the free particle character of the remaining longitudinal component is retained. It should be noted, though, that Eq. 1.2 at high B_{ext} differs from the real QHE regime, because the number of contributing edge channels in the QHE regime is determined by the 2DES Fermi energy E_{F}, whereas it is set by the QPC constriction potential for Eq. 1.2. At $B_{\text{ext}} \gg 0$, the conductance of the 2DES is determined by the number of Landau levels in the QPC, independently of the total occupied number of Landau levels in the 2DES, due to selective coupling of the QPC to certain edge channels, a phenomenon also referred to as anomalous integer-QHE [48]. Also in Eq. 1.2 the subband spacing maintains a dependency on the actual QPC constriction potential via ω_y.

Now the case of $B_{\text{ext}} = 0$ is considered again. At low temperatures T with thermal energies smaller than the subband spacings all QPC modes n with $E_n^0 \leq E_{\text{F}}$ are occupied and the remaining modes are empty. A decrease of V_{QPC} raises the conduction band bottom (with respect to E_{F}) and it increases the energy spacing between the levels E_n^0 due to increased transverse confinement [48]. Both effects diminish the number of occupied QPC levels. Thus, by tuning V_{QPC}, the QPC channel width can be tuned continuously between an open and fully closed, or pinched-off, channel. This is shown in Fig. 1.2 which illustrates the electron energy dispersion in the QPC channel for two different QPC gate voltages V_{Q}. Shown is the case of a harmonic 1D confinement in the y direction which is given by the frequency ω_y that determines the transverse potential. The relevant states for the QPC transmission exhibit $k_x > 0$ on the QPC source side where the chemical potential is μ_{S}, and $k < 0$ on the QPC drain side where the chemical potential is μ_{D}. In Fig. 1.2(a) overall three modes contribute to the electron transport through the QPC. By decreasing V_{Q}, two modes become fully depopulated in Fig. 1.2(b). The linear transport regime is characterized by small differences $\mu_{\text{S}} - \mu_{\text{D}}$ with respect to the QPC subband spacing, as illustrated in Fig. 1.2. The linear transport properties are determined by electrons around the Fermi energy $\mu_{\text{S}} \simeq \mu_{\text{D}} \simeq E_{\text{F}}$ with the group velocity $v_n \simeq v_{\text{F}} = \hbar k_{\text{F}}/m_*$. Thus v_n is

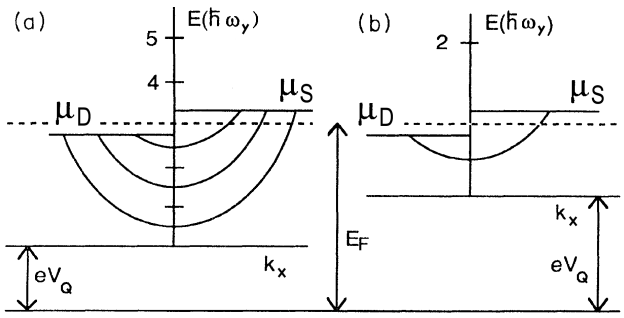

Figure 1.2: Dispersion relation of the QPC modes in case of harmonic transverse confinement determined by the frequency ω_y. The electron occupation in the channel is illustrated for a DC source-drain voltage $V_{\rm sd}^{\rm dc} = (\mu_{\rm S} - \mu_{\rm D})/e$ applied across the QPC with respect to the equilibrium Fermi energy $E_{\rm F}$. In (b) the applied QPC gate voltage $V_{\rm Q}$ is more negative than in (a) (data from [48]).

determined by the Fermi wave vector $k_{\rm F} = \sqrt{2\pi n_{\rm 2DES}}$ which is given by the 2DES density $n_{\rm 2DES}$ owing to the fermionic nature of the electrons.

If reflections of the traversing electron states at the constriction entry and exit can be neglected the QPC conductance $G_{\rm QPC}$ resulting from N occupied modes is determined by the electron group velocities v_n and the 1D densities of states ρ_n of the modes $n \leq N$ [48]

$$G_{\rm QPC} \propto \Sigma_{n=1}^{N} \int_{\mu_{\rm D}}^{\mu_{\rm S}} \rho_n(E) v_n(E) {\rm d}E \ . \tag{1.3}$$

Due to $v_n = \hbar^{-1} \partial E_n / \partial k$ and $\rho_n = 2(\pi \partial E_n / \partial k)^{-1}$, one directly obtains the significant result: $G_n = {\rm const}$, the conductance contributed by each QPC mode n is an invariant and energy independent because the dependence on the actual dispersion relation cancels out. The latter implies that $G_n = {\rm const}$ is valid also in the case of externally applied magnetic field, $B_{\rm ext} > 0$.

Now incorporating electron wave reflections, the total conductance G of a QPC of N fully occupied modes can be calculated at $T = 0$ in terms of the ratio of transmission t_n and reflection probabilities r_n, yielding

$$G_{\rm QPC} = \frac{2e^2}{h} \Sigma_{n=1}^{N} t_n \ . \tag{1.4}$$

Thus each contributing channel accounts for one spin-degenerate conductance quantum $G_{\rm Q} = 2e^2/h \simeq 1/12.9{\rm k}\Omega$, weighted by its transmission probability t_n. The factor of 2 in $G_{\rm Q}$ stems from the residual spin degeneracy at zero magnetic field. Eq. 1.4 corresponds to the well-known Landauer formula, however, after having taken into account the finite contact resistance of each 1D channel mode to the adjacent 2DES source and drain reservoirs [49] that *adds* electron energy dissipation. The latter imposes a crucial constraint because if omitted Landauer's original result $G_n/G_{\rm Q} = (r_n/(1-r_n))^{-1} = t_n/(1-t_n)$ is obtained [49, 50] where the conductance diverges in case of vanishing scattering $r_n \to 0$ ($t_n \to 1$), a

regime actually feasible experimentally, as explained below. In principle, Eq. 1.4 is valid for arbitrary N. However, the larger N the more insignificant is the difference between the quantum and classical G_{QPC}.

At low temperatures of a few kelvin the phonon occupation number is negligible leading to negligible phonon-induced 2DES electron scattering. Then electron scattering at charged impurities is the dominant electron energy dissipation process. If the latter is additionally reduced sufficiently by the fabrication of clean 2DES samples and by the use of modulation-doping in the heterostructure, the elastic and inelastic electron mean free paths can exceed feasible QPC channel lengths which is referred to as the ballistic regime. In the ideal case or asymptotic limit, the transmission coefficient t_n of each occupied (empty) mode is one (zero). Therefore in this case Eq. 1.4 yields the remarkable result that G_{QPC} changes in integer steps of the universal conductance quantum $G_{\mathrm{Q}} = 2e^2/h$ which is determined by fundamental constants only. G_{QPC} becomes independent of any specific experimental parameter such as the particular sample material, the shape or dimensions of the 1D confining potential (in the ballistic limit), the length of the resulting 1D channel, and so forth. This further implies that the electron current I_n contributed by each QPC mode n is similarly invariant, since, for an unchanged bias $\mu_{\mathrm{S}} - \mu_{\mathrm{D}}$ across the QPC, tuning V_{QPC} then yields $I_n = G_{\mathrm{Q}}(\mu_{\mathrm{S}} - \mu_{\mathrm{D}})/e$.

The experimentally obtained conductance of a ballistic QPC as a function of the QPC gate voltage is shown in Fig. 1.3 for different bath temperatures between $T = 0.3$ K and 4.2 K (offset for clarity). At the lowest $T = 0.3$ K, the regular plateau pattern of integer multiples of G_{Q} is distinctly pronounced as marked by the dotted lines. The excellent agreement with the ballistic form of Eq. 1.4 confirms the non-locality of the electron interactions as a prerequisite for the ballistic transport regime. The dispersion of the out-of-equilibrium electrons in the 1D QPC channel is determined by *remote* scattering processes in the 2DES which is in local equilibrium. This explicitly renders the classical *local* electric field-driven description non-applicable. The phenomenon is rather understood by the difference between the chemical potentials μ_{S} and μ_{D} across the QPC which induces a current I through the 1D constriction that becomes equally distributed among N occupied channel modes.

Experimentally the ballistic regime is commonly obtained in a 2DES based on a $\mathrm{GaAs/Al}_x\mathrm{Ga}_{1-x}\mathrm{As}$ heterostructure where extremely high mobilities exceeding $\mu_{\mathrm{2DES}} = 10^6\ \mathrm{cm^2V^{-1}s^{-1}}$ have been achieved [51–53] leading to electron mean free paths of hundreds of μm. This length scale can by far exceed feasible QPC constriction dimensions. The deviations from exact quantization in QPCs are typically about 1 %.

Being able to reach the ballistic regime in the experiment additionally requires that each QPC channel mode couples adiabatically to the leads. This implies that (partial) reflection of electron waves off the 1D channel onset and ending for each occupied mode is insignificant. A basic QPC feature is that in the case of adiabatic mode coupling potential residual electron scattering processes conserve the quantum number. The transmission probabilities are non-zero only on reflections into equal incident and leaving QPC modes with no channel mixing being present. In terms of the constriction geometry, adiabatic

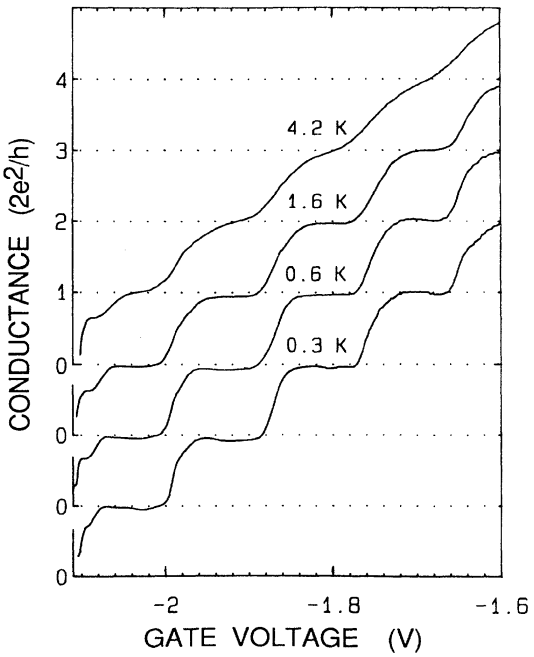

Figure 1.3: QPC conductance in units of the spin-degenerate conductance quantum $G_{\mathrm{Q}} = 2e^2/h$ as a function of the QPC gate voltage, measured at different bath temperatures between 0.3 K and 4.2 K. Each conductance curve is offset by G_{Q} for clarity (data from [48]).

coupling is usually achieved using a gradually varying QPC constriction width along the 1D channel entry and exit, for instance by deploying rounded QPC gates.

In short QPC channels with comparatively sharp constriction edges, evanescent electron waves can give rise to non-zero transmission probability contributions to the QPC conductance (this was assumed to be negligible and hence was omitted in the derivation of Eq. 1.4). On the other hand, longer channels of the order of several electron Fermi wavelengths tend to exhibit transmission resonances which map on the resulting G_{QPC} as the quantum mechanical wave character of the particles then comes into play [48]. Such deviations from the ideal step-like shape of G_{QPC} become apparent typically on the plateaus in terms of curved oscillating features as can already be seen rudimentary in Fig. 1.3 for $T = 0.3$ K.

The shape of the transitions between the conductance plateaus can depend on the particular geometry of the QPC constriction [54], which also follows from the results presented in Chapter 2. Additionally, energy broadening due to finite thermal energies or finite $V_{\mathrm{sd}}^{\mathrm{dc}}$ can contribute to an increased width of the transition between the G_{QPC} plateaus. If the temperature T, or $V_{\mathrm{sd}}^{\mathrm{dc}}$, is raised, the contributing electrons around $\mu_{\mathrm{S,D}}$ begin to occupy more than one QPC mode. The conductance steps blur and finally the conductance plateaus disappear when the thermal energy or the chemical potential difference $\mu_{\mathrm{S}} - \mu_{\mathrm{D}}$ become comparable to, or exceed, the QPC mode energy separation $E_j(0) - E_{j-1}(0)$. This is clearly visible in Fig. 1.3 where for $T = 4.2$ K the classically expected behavior $G_{\mathrm{QPC}} \propto V_{\mathrm{QPC}}$ [48] is nearly reached. It can be used to smooth out or

even completely purge residual resonances at the G_{QPC} plateaus by a controlled increase of the bath temperature, as in Fig. 1.3 for the first three plateaus on the increase to 0.6 K.

As evident from Fig. 1.3, the regular conductance pattern can consistently feature an additional distinct kink around $0.7G_{\mathrm{Q}}$. This deviation can also appear at transitions to higher QPC conductance plateaus, as can be seen at around $1.7G_{\mathrm{Q}}$ in Fig. 1.3. This feature is called the 0.7-anomaly and is introduced in the following section.

1.2 The 0.7-anomaly

The regular steplike pattern nG_{Q} of the QPC conductance at low temperatures frequently shows an additional shoulder around $0.7G_{\mathrm{Q}}$ even without externally applied magnetic field. It is termed the 0.7-anomaly, although experiments also showed that the precise occurrence can vary between $0.5G_{\mathrm{Q}}$ and $0.9G_{\mathrm{Q}}$ [30, 34]. Interestingly, the very first experimental observations of the quantized QPC channel conductance already contained a distinct shoulder around $0.7G_{\mathrm{Q}}$ [15, 48]. However, the nature of the 0.7-anomaly remained elusive in spite of the well-understood underlying physics of the QPC as well as the intrinsic simplicity of the essential sample design and the required experimental configuration. This section provides a brief overview over the main characteristic experimental features of the 0.7-anomaly.

An example of the 0.7-anomaly is shown in Fig. 1.4. The QPC conductance is measured as a function of the QPC potential-tuning gate voltage V_{g} for several constant low temperatures between $T = 70$ mK and 1.5 K. The distinct kink below the first conductance plateau with the onset at $\sim 0.65G_{\mathrm{Q}}$ is visible in all conductance curves. While the actual conductance plateaus blur on increasing T (compare Sec. 1.1) the shoulder around $0.7G_{\mathrm{Q}}$ becomes even more pronounced and dominates the QPC conductance pattern at intermediate temperatures around a few kelvins. This peculiar feature of the 0.7-anomaly is universal. It can be used to distinguish a 0.7-anomaly from other influences that can induce deviations from the regular QPC conductance pattern (compare Sec. 3.1). At intermediate temperatures of a few kelvins, a pronounced 0.7-anomaly can even remain the only feature in an otherwise about linear QPC conductance at varying QPC channel width (compare Sec. 6.1.3).

Another symptomatic feature of the 0.7-anomaly is apparent in the non-linear conductance response which is the regime of a finite DC source-drain bias voltage ($|V_{\mathrm{sd}}| > 0$) applied across the QPC constriction. Three examples of the QPC non-linear conductance at different T and magnetic fields $B_{\parallel}$ in the 2DES plane are shown Fig. 1.5. The QPC differential conductance $g = \mathrm{d}I_{\mathrm{QPC}}/\mathrm{d}V_{\mathrm{sd}}$ is repeatedly measured as a function of V_{sd}, each time with a different applied constant QPC gate voltage V_{g} that is altered in equidistant steps. The QPC plateaus in g emerge as clusters of multiple curves. The (average) conductance g/G_{Q} at each plateau is labeled in Fig. 1.5. The regular QPC conductance pattern $g/G_{\mathrm{Q}} = 1, 2$ at $T = 80$ mK and $B_{\parallel} = 0$ in Fig. 1.5(a) is visible in the linear regime $V_{\mathrm{sd}} \sim 0$. It emerges again in the form of half-integer plateaus 1/2, 3/2,

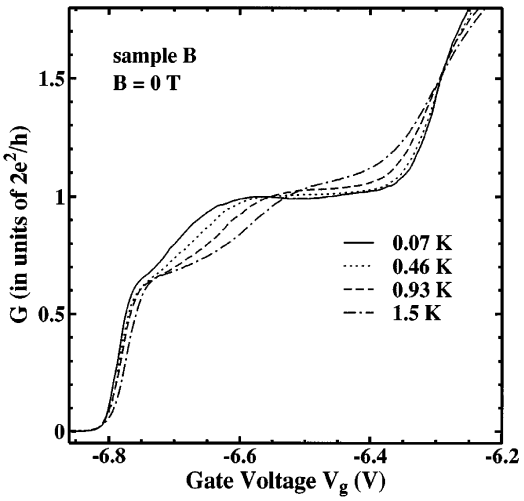

Figure 1.4: Differential conductance G of a QPC in units of the spin-degenerate conductance quantum $G_Q = 2e^2/h$, measured for different temperatures between 70 mK and 1.5 K around the first conductance plateau $G = G_Q$ with no external magnetic field B applied. The transition to the plateau shows a distinct shoulder around $0.7G_Q$ at each temperature (data from [24])

etc. around $V_{sd} = |(\mu_S - \mu_D)/e| \sim 1$ mV where the differences between the source and the drain chemical potentials $|\mu_S - \mu_D|$ match the spacing between adjacent QPC modes and hence are in resonance. Additionally, a 0.7-anomaly occurs which continues to be visible in the non-linear regime symmetrically toward about $0.8G_Q$. The 0.7-anomaly is accompanied by a narrow local maximum in g around $V_{sd} = 0$, termed the zero-bias peak (ZBP) [27, 32, 35]. The appearance of the ZBP in Fig. 1.5(a) is most obvious when compared to the transitions toward $2G_Q$ where the ZBP is only visible above $1.5G_Q$ and toward $3G_Q$ where no ZBP is visible anymore. The ZBP responds to the raise of the temperature T as shown in Fig. 1.5(b). Is is not visible anymore above the pronounced shoulder ($0.7 < g/G_Q < 1$), though, it still appears below $0.7G_Q$. This can also be viewed the other way around: the ZBP forms simultaneously to the 0.7-anomaly as a result of lowering T leading to a weakening of the 0.7-shoulder at lower T.

For large magnetic fields $B_\parallel$ both the ZBP and the 0.7-shoulder vanish and the spin-split conductance plateau at $0.5G_Q$ determines the QPC conductance, as shown in Fig. 1.5(c). Unlike Figs. 1.5(a) and 1.5(b), at high $B_\parallel$ the non-linear conductance pattern becomes homogeneous as a function of V_g around $V_{sd} = 0$ ($|V_{sd}| \lesssim 0.5$ mV in Fig. 1.5(c)) with a periodicity $\Delta g = 1G_Q$. The transition toward $1G_Q$ is no longer distinguished. A wing-shaped pattern is visible between each plateaus nG_Q and $(n - 1/2)G_Q$ around $|V_{sd}| = 0.5$ mV in Fig. 1.5(c) representing the Zeeman-split conductance plateaus which are in resonance with the chemical potentials $\mu_{S,D}$ (compare the similar pattern between nG_Q and $(n - 1)G_Q$ in Fig. 1.5(a)).

A smooth transition of the 0.7-anomaly is observed in the linear QPC response on increasing $B_\parallel$, moving toward and merging with the spin-split conductance plateau at

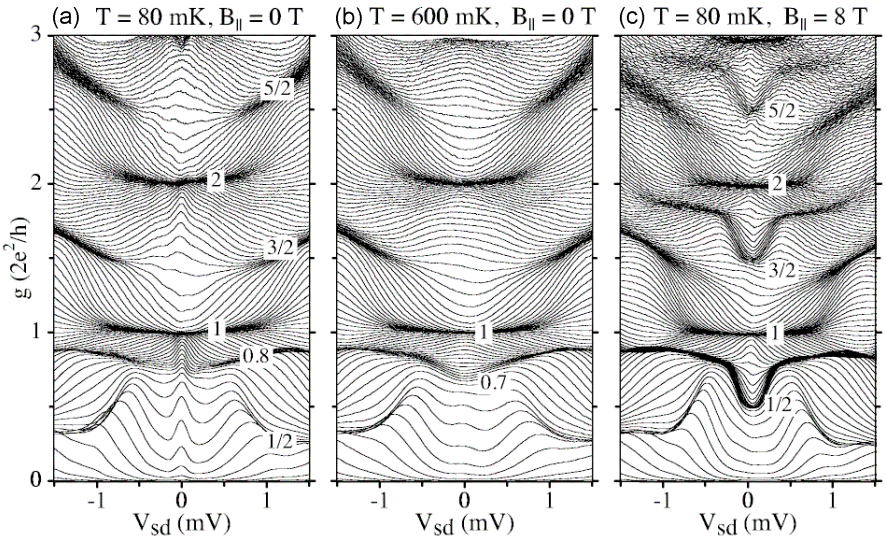

Figure 1.5: Non-linear differential conductance $g = \mathrm{d}I_{\mathrm{QPC}}/\mathrm{d}V_{\mathrm{sd}}$ of a QPC for various equidistant constant QPC gate voltages V_{g}, each time measured as a function of the DC source-drain bias voltage V_{sd} across the QPC. Emerging conductance plateaus become visible due to clustering of multiple curves and are labeled with their respective (mean) conductance g/G_{Q}. (a) g measured at the temperature $T = 80$ mK and in absence of a magnetic field $B_{\parallel} = 0$ in parallel to the plane of the 2DES. The regular QPC conductance plateaus $g/G_{\mathrm{Q}} = 1, 2$ are visible in the linear regime $V_{\mathrm{sd}} \sim 0$. The occurring shoulder at $0.7G_{\mathrm{Q}}$ is accompanied by a local conductance maximum around $V_{\mathrm{sd}} \sim 0$, the zero-bias peak (ZBP), and continues to be visible in the non-linear regime symmetrically toward about $0.8G_{\mathrm{Q}}$. (b) g measured at $T = 600$ mK and $B_{\parallel} = 0$. The ZBP has decreased, above the still pronounced $0.7G_{\mathrm{Q}}$-shoulder it has disappeared. (c) g measured at $T = 80$ mK and $B_{\parallel} = 8$ T. ZBP and 0.7-shoulder are not visible anymore (data from [27]).

$0.5G_{\mathrm{Q}}$. This is already rudimentary apparent in Fig. 1.5 but is shown again in terms of the linear QPC conductance in Fig. 1.6(a). The distinct 0.7-anomaly at $B_{\parallel} = 0$ (red curve) develops gradually (yellow to blue) into spin-resolved first conductance plateau $0.5G_{\mathrm{Q}}$ (violet curve). In combination with the occurrence of the anomaly between the first spin-degenerate and the first spin-split QPC channel it was early hypothesized that the 0.7-anomaly is closely related to emerging finite spin polarization at $B = 0$ [24]. It is further indicated in the non-linear regime of the 0.7-anomaly where sub-plateaus around $0.8G_{\mathrm{Q}}$ appear which are also observed for each spin-split conductance plateau at high $B_{\parallel}$ (compare Figs. 1.5(a) and 1.5(c)). The assumed connection with finite spin polarization did also not contradict subsequent experimental findings regarding deviations of the shot noise power spectrum from the expectations for full spin-degeneracy. Shot noise arises from random fluctuations which the DC transport current is subject to as a result of the discrete nature of the participating electrons. It is characterized by e. g. the shot noise power spectrum, also referred to as spectral noise density, which quantifies the contributing noise power at a given frequency. The fact that shot noise is white allows

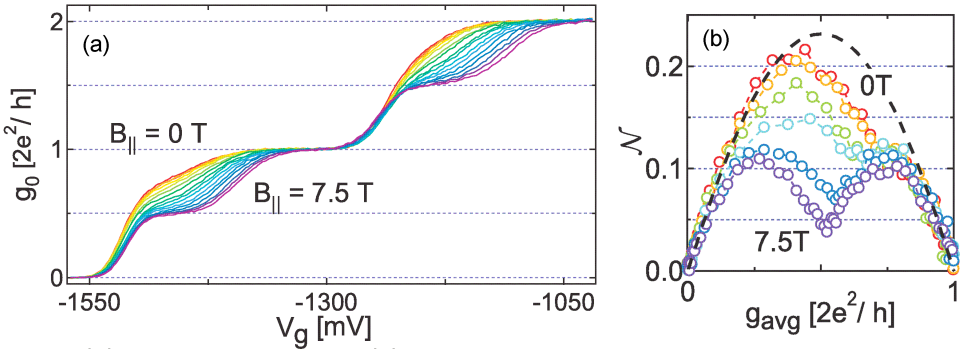

Figure 1.6: (a) Low-temperature differential QPC conductance measured versus the QPC gate voltage V_g multiple times, each at a different applied in-plane magnetic field $B_{\|}$ between 0 T (red) and 7.5 T (violet curve). The distinct 0.7-anomaly (red curve) develops smoothly into the spin-split plateau. (b) $B_{\|}$ evolution (same color-coding like in (a)) of the shot noise factor $\mathcal{N}$ which is extracted from the source-drain voltage dependence of the shot noise power spectrum at each constant QPC transmission g_{avg}. The expected result for $B_{\|} = 0$ if electron-electron interactions are omitted is also plotted (dashed curve) (data from [28]).

to investigate it at any frequency (range) of choice. Due to the basic connection to the quantum mechanical particle nature, shot noise can contain information about particle scattering processes or many-body effects [55].

In case of the current through the QPC constriction, the shot noise spectral density can be extracted from the QPC transmission in the non-linear response regime and is characterized by the the shot noise factor $\mathcal{N}$ [28]

$$\mathcal{N} = \frac{1}{2} \sum_{n,\sigma} \tau_{n,\sigma}(1 - \tau_{n,\sigma}) \,, \tag{1.5}$$

with $\tau_{n,\sigma}$ being the transmission of the n'th QPC channel with spin σ. $\mathcal{N}$ links the shot noise power spectral density to V_{sd}, being a gauge how strongly it responds to a given bias voltage [28] which causes the actual DC electron current.

Fig. 1.6(b) shows the shot noise factor $\mathcal{N}$ extracted from the measured QPC conductance at the different $B_{\|}$ in Fig. 1.6(a) (same color-coding) in the range $0 \leq g \leq 1.0 G_{\text{Q}}$. $\mathcal{N}$ is plotted as a function of the (about) constant g_{avg}, being g averaged over the finite V_{sd} range out of which the shot noise power spectrum was extracted at each constant V_g. The noise power spectrum was recorded at high frequencies $\sim$ MHz in order to suppress $1/f$ electronic noise contributions. Additionally the white thermal noise contribution was subtracted before the power spectrum analysis [28]. A suppression of the shot noise factor relative to the prediction by the theory for spin-degenerate transport [56, 57] (dashed curve) is observed in Fig. 1.6(b) around the actual occurrence of the 0.7-anomaly at $B_{\|} = 0$ (red dots). Moreover, this signature around $0.7 G_{\text{Q}}$ also evolves smoothly into the symmetric pattern of $\mathcal{N}$ for spin-resolved electron transmission at $B_{\|} = 7.5$ T. This added signature in $\mathcal{N}$ is another feature of the 0.7-anomaly which is compatible with the hypothesis that partial spin polarization is present and it also indicates a many-body effect.

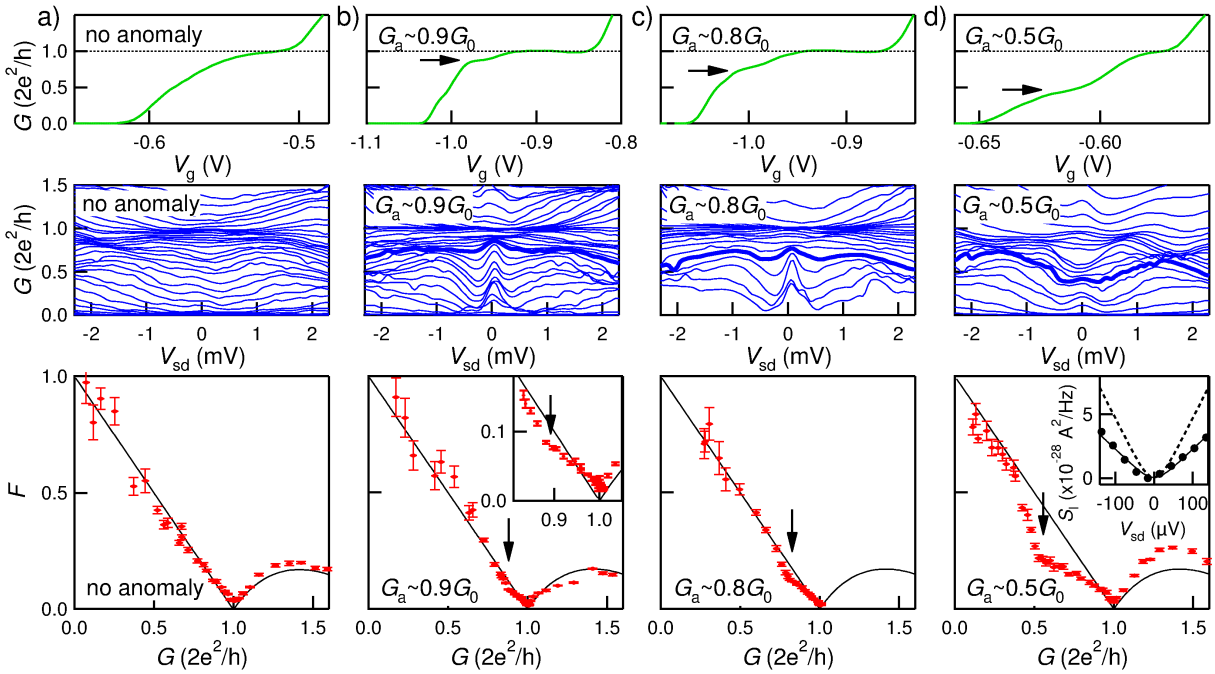

Figure 1.7: Differential conductance G of a QPC at low temperatures in (upper panels) the linear response and (middle panels) the non-linear response regime. Also shown are (lower panels) the corresponding Fano factors (red dots + errorbars) plotted on top of the theoretical prediction for full spin-degeneracy (black lines). The black arrows indicate each point where the Fano factor deviates most from the prediction. The shown cases are that (a) no 0.7-anomaly occurs, and that it does occur at (b) $0.9G_Q$, (c) $0.8G_Q$, and (d) $0.5G_Q$, as labeled by the arrows in the upper panels. The insets show (b) the local result zoomed in on the present Fano factor reduction and (d) the shot noise power spectrum S_I (black dots) in the non-linear QPC response regime. It is extracted from the QPC response in case (d) right at the strongest Fano factor reduction $G \sim 0.5G_Q$ and compared to the calculated variation at full spin-degeneracy (dashed lines) (data from [30]).

Remarkably, the experimental result of $\mathcal{N}$ in Fig. 1.6(b) already exhibits the asymmetry at $B_\parallel = 0$ which could be interpreted as a signature of *spontaneous* spin polarization. However, during the experiments of Fig. 1.6 a small ($\sim$ 0.1 T) perpendicular magnetic field was applied in order to reduce bias-voltage-induced heating effects [28]. Considering a potentially significant enhancement of the spin susceptibility (compare Sec. 3.3.2), this deprives the measured results in Fig. 1.6(b) from being related to strictly *spontaneous* spin splitting.

A similar measure of the electron-related shot noise is the Fano factor $\mathcal{F}$ which, as compared to $\mathcal{N}$, relates the shot noise power spectral density directly to the source-drain current I_{sd} [55] that represents the source of the noise. If only transport through the first QPC channel $0 \leq g \leq 1.0G_Q$ is considered in the linear transport regime, $\mathcal{F}$ is determined

by [55]

$$\mathcal{F} = \sum_{\sigma} \tau_\sigma(1-\tau_\sigma) / \sum_{\sigma} \tau_\sigma \ , \tag{1.6}$$

with τ_σ being the transmission of the first QPC channel with spin σ. This leads to an expected linear dependence $\mathcal{F} = 1 - g/G_\mathrm{Q}$ for fully spin-degenerate QPC transport. In Fig. 1.7 the bottom panels show the Fano factors (red dots including errorbars) as a function of the QPC conductances G at which they were extracted. G is accordingly shown in each respective top (linear QPC response) and middle panel (non-linear QPC response) of Fig. 1.7. The Fano factors were again extracted at $\sim$ MHz frequencies in order to reduce the $1/f$ noise significance [30]. The sample used for Fig. 1.7 allowed to vary the QPC constriction potential by means of V_g [30] such that the specific position of the 0.7-anomaly could be tuned from $0.9G_\mathrm{Q}$ (Fig. 1.7(b)) over $0.8G_\mathrm{Q}$ (Fig. 1.7(c)) toward $0.5G_\mathrm{Q}$ (Fig. 1.7(d)), as shown in the respective upper panels. The 0.7-anomaly occurrence could even be eliminated (Fig. 1.7(a), upper panel). The accompanying ZBP in the non-linear regime (respective middle panels) further affirms the actual appearances of the 0.7-anomalies. In each bottom panel of Fig. 1.7, the expected evolution Eq. 1.6 for full spin-degeneracy is added (black curves).

In absence of a 0.7-anomaly (Fig. 1.7(a)) the measured Fano factors coincide with the linear trend at $g < 1.0G_\mathrm{Q}$ within the errorbars in the majority of cases. For present 0.7-anomalies the measured Fano factors, within the errorbars, show a singular reduction with respect to the linear expectation, as shown in the bottom panels of Figs. 1.7(b-d). The Fano factor reduction shifts in accordance with the actual 0.7-anomaly position, as indicated by the arrows in the bottom panels (the inset in (b) is zoomed in to the kink). The reduction further becomes the more pronounced the farther the 0.7-anomaly is located from $1G_\mathrm{Q}$. In addition, the inset of bottom panel (d) shows the shot noise power spectrum S_I (black dots) in the non-linear regime right at the emerging Fano factor dip at $g \sim 0.5G_\mathrm{Q}$. The measured power spectra are reduced compared to the theoretically calculated values for full spin-degeneracy (dashed curve).

The result that the 0.7-anomaly is accompanied by a lowered Fano factor therefore indicates asymmetric transmission of both contributing spin channels [30]. It is thus consistent with the result Fig. 1.6(b) above. Moreover, due to the tuning ability in Fig. 1.7, it expands the scope of the experimental indication. However, similarly to the measurements of $\mathcal{N}$ explained above, in Fig. 1.7 also a small magnetic field was applied during all performed experiments in order to reduce V_sd-induced noise contributions [30]. This again leaves the question unrelated whether or not strictly *spontaneous* spin polarization is present in the regime of the 0.7-anomaly.

1.3 Kondo effect in quantum dots

The fundamental properties of the 0.7-anomaly in QPCs which will be discussed in more detail in Sec. 2.3 and Sec. 3.3 show striking similaries to the Kondo effect which arises

in quantum dot (QD) systems. Therefore in this section a brief overview of the basic features of the latter is given.

If the temperature T is decreased the electrical resistivity of a metal drops due to phonon freeze out. It further saturates at low temperatures T because of a present finite number of impurities in the solid. Yet it was observed experimentally in various metals that for decreasing T the resistivity started to rise again, producing a local minimum at non-zero temperatures. The source of this puzzling finding could be addressed for the first time by Jun Kondo [58] who used third-order perturbation theory to describe the many-body process of an impurity's residual magnetic moment caused by an unpaired electron coupled to the large reservoir of noninteracting conduction band electron spins via exchange coupling J. Kondo showed that the resulting DC resistivity ρ has a contribution [58]

$$\rho \sim J\log(T) \tag{1.7}$$

which at low temperatures $T \to 0$ diverges $\rho \to \infty$ if the exchange interaction J is negative, favoring antiferromagnetic coupling. The impurity spin can flip due to the exchange interaction, causing a synchronous flip in the spin-excited locally surrounding Fermi sea. The added resistivity contribution for electrons at the Fermi level E_F is thus caused by an additional scattering probability induced by the spin degree of freedom. Kondo already suggested that, under certain conditions, a constant non-diverging contribution $J\log(T_0)$ should be reached at $T \ll T_0$ [58].

The basic theoretical model which then proved to be successful in describing the physics of the formation of the local moment in metals is the single-impurity Anderson model [59]. It uses a form of scaling where the system is described by a coarse-grained model, and the degree of coarseness is raised while the temperature in the calculations is lowered. This simultaneously diminishes the degrees of freedom in the model and allows predictions of the system properties down to extremely low temperatures. In particular, the unphysical divergence of the metal resistivity Eq. 1.7 was revised later by using a numerical renormalization approach [60] showing that a finite resistance is reached in the limit $T \to 0$ because the magnetic moment of the impurity becomes fully screened by the spins of the surrounding electrons.

As there is no favored spin orientation, its mean is an uncorrelated spin singlet state. The resulting correlation effect causing the hybridization of impurity and surrounding electron states is known as the Kondo effect. A specific property is that it is non-negligible only for thermal energies below a characteristic energy scale which is defined by the Kondo temperature T_K. Another remarkable characteristic feature of the Kondo effect is the *universal scaling* behavior: For $T < T_\mathrm{K}$ the resistivity, as a macroscopic quantity, is fully determined by a universal function of the normalized temperature, $\rho/\rho_{T\to 0} = \mathrm{fct}(T/T_\mathrm{K})$, which is identical for all spin-1/2 impurities [61].

In a QD an analogue phenomenon can emerge [4, 45, 47]. A QD can be fabricated using the same depletion gates technique alike in the case of the QPC fabrication [1, 11, 12, 45]. The 2DES is confined in two dimensions which generates a zero-dimensional QD potential.

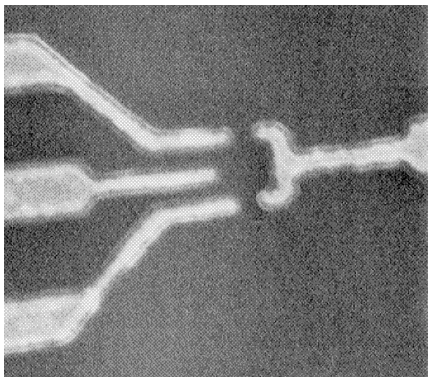

Figure 1.8: Scanning electron micrograph of a quantum dot (QD) gate design on top of a 2DES containing heterostructure (gate-defined QD width ~ 100 nm) (micrograph from [45]).

Local tuning of the 2DES potential by separate gates then enables a continuous tuning of the QD energy spectrum with respect to the 2DES Fermi energy E_F. The tuning of the QD energy also determines the potential number of electrons trapped within the QD. Depending on the particular QD design, it can furthermore be possible to adjust the tunnel coupling Γ of the QD to its adjacent 2DES reservoirs independently of the QD spectrum. Figure 1.8 shows an example of a QD gate design comprising four gates of which the left center gate tunes the QD potential. Its two adjacent gates are used to selectively adjust the tunnel barriers to the 2DES leads (upper and lower area) of the QD.

In the most basic approach the charging energy needed in order to occupy the QD with a further electron is $\Delta E_\mathrm{QD} = U = e^2/C_\mathrm{QD}$ (e is the elementary charge). The energy U required to overcome the electron-electron Coulomb repulsion is thus reflected in the self-capacitance C_QD of the QD. A QD at low temperatures in the linear transport response regime is sketched in Fig. 1.9(a). The QD's highest occupied energy level (ϵ_0) hosts an electron (blue arrow) which is (partly) decoupled from the leads (red) via tunnel barriers (intermediate rectangles). Neither the energy $\tilde{\epsilon}$ needed for the electron to leave the QD nor U for a further electron to occupy the QD is available. Thus the QD transmission is negligible and the QD is in the so-called Coulomb blockade. Since the QD exhibits one unpaired electron, exchange interactions can couple the localized spin to the locally surrounding 2DES reservoirs. This exchange interactions can mediate mutual spin flip processes as shown in Figs. 1.9(a-c). Within a time window restricted by the uncertainty principle, a virtual intermediate state is allowed at which the spin-up electron has left the QD toward the drain-side reservoir (Fig. 1.9(b)), followed by the tunneling of an exchange-coupled spin-down electron from the source reservoir in the QD (Fig. 1.9(c)). Hence the exchange interactions enable the otherwise Coulomb-blockaded QD to become more transparent for 2DES electrons around E_F. This gives rise to a net charge transport through the QD accompanied by mutual spin flip processes. The charge transport is expressed in an emerging additional state in the density of states (DOS) of the QD, known as the Kondo resonance, as depicted in Fig. 1.9(d). A QD with an unpaired electron is

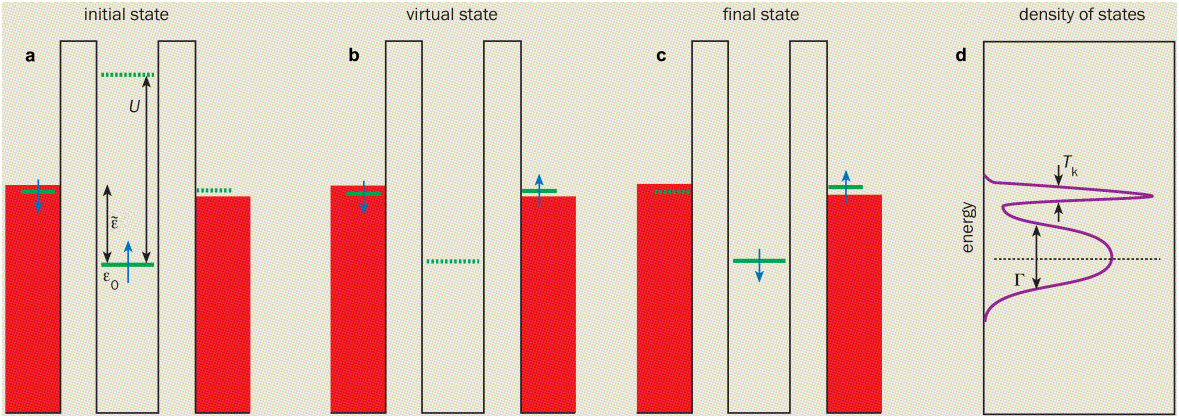

Figure 1.9: Each panel (a-c): Linear transport through a QD (center) in the Kondo regime from the left (red, source) to the right (red, drain) 2DES reservoir. The QD energy levels (green) are at least separated by the QD charging energy U. (a) Initial state, Coulomb blockade: an unpaired spin-up electron (blue arrow) with QD energy ϵ_0 lies $\tilde{\epsilon} < U$ below E_F of the source reservoir. (b) Virtual intermediate state: exchange interactions with the leads allow the QD spin-up electron to tunnel to the drain reservoir. (c) Final state: within the time scale $h/\tilde{\epsilon}$ a source reservoir spin-down electron has tunneled into the QD resulting in a net charge transport through the QD accompanied by a mutual spin flip. (d) In the resulting density of states (DOS) of the QD, additionally to the ϵ_0-related peak of width determined by the tunnel coupling Γ, the Kondo peak arises due to the exchange-mediated QD transport. It is pinned at the Fermi level and its (minimum) width is set by the Kondo temperature T_K (illustration from [61]).

hence called a Kondo QD (KQD). The Kondo resonance is pinned at E_F which renders the QD in the Kondo regime to be in resonance with the lead reservoirs in the linear transport regime. Though similar to the magnetic-exchange coupling in bulk metals, in contrast, the Kondo effect in QDs induces a decrease of the QD resistivity, or alternatively an increase of the QD conductivity.

The spacing $\Delta\epsilon = \epsilon_j - \epsilon_{j-1}$ of the QD levels must exceed the width Γ of a confined QD state so that the discrete QD energy spectrum, and therefore Coulomb blockade, governs the QD transmission. On the other hand, the tunneling rate Γ/h must be large enough in order to allow a finite current through the QD by sufficient coupling to the leads. The fabrication of small QD islands with tunable coupling strengths allows both criteria to be feasible at the same time. The intermediate regime of strong tunnel coupling but maintained discrete QD charge states is a prerequisite for higher order tunneling processes through virtual intermediate states. The need of a strong coupling is also evident from the Kondo temperature T_K in the QD case [62],

$$T_\mathrm{K}^\mathrm{QD} \sim \sqrt{U\Gamma_\mathrm{tot}}\exp[-\pi(E_\mathrm{F} - \epsilon_\mathrm{n})/(2\Gamma_\mathrm{tot})] \,, \tag{1.8}$$

with $\Gamma_\mathrm{tot} = \Gamma_\mathrm{QD-S} + \Gamma_\mathrm{QD-D}$ of the n'th QD level. Hence T_K^QD can become experimentally accessible if Γ_tot is large. Furthermore, according to Eq. 1.8, T_K^QD can also be increased by shifting the single occupied QD level ϵ_n closer to E_F [4].

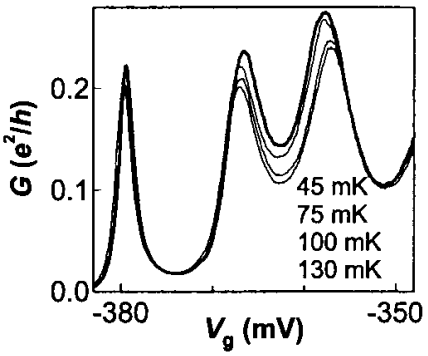

Figure 1.10: Linear conductance $G/(0.5G_{\mathrm{Q}})$ as a function of the tuning gate voltage V_{g} of a QD in the Kondo regime for temperatures $T = 45$ mK (bold, upper curve) to 130 mK (bottom curve). The left minimum between the three visible conductance peaks corresponds to an evenly filled QD, there G is low and virtually independent of ΔT. The right minimum corresponds to an oddly filled QD showing a higher conductance G already at $T = 130$ mK and G is clearly raised further at the continued cooling down (data from [4]).

Figure 1.10 shows the linear QD conductance G measured as a function of the tuning voltage V_{g} of a QD in the Kondo regime for various temperatures between $T = 45$ mK (bold) to 130 mK (bottom curve). Three peaks are visible which border two Coulomb blockade valleys in G. The right valley at the higher temperatures lies clearly above the left one. Decreasing T raises it further whereas the left valley is basically unaffected. The responding local minimum in G corresponds to an odd number of electrons in the QD. Its increase with decreasing T represents the tail of the Kondo-related QD conductance. The condition $T \sim T_{\mathrm{K}}^{\mathrm{QD}}$ would be finally reached if $G(T)$ eventually would start to saturate [61]. In addition, Fig. 1.10 illustrates an important advantage of the QD-related Kondo regime: the QD tunability allows to switch back and forth between non-Kondo (Coulomb blockade) and Kondo transport across the QD.

The QD differential conductance $g = \mathrm{d}I/\mathrm{d}V_{\mathrm{sd}}$, if measured as a function of V_{sd}, shows three characteristic features right in an odd KQD valley which are to be outlined now. In Fig. 1.11(a), $g(V_{\mathrm{sd}})$ of the odd KQD valley in Fig. 1.10 is shown. It is measured at multiple temperatures between $T = 45$ mK (bold) and 270 mK (dashed curve). Considering $T = 45$ mK first, the Kondo resonance is mapped on the QD conductance around $V_{\mathrm{sd}} \sim 0$. For increasing V_{sd} the peak conductance in Fig. 1.11(a) drops. The reason is that the confined QD electron couples to both the source and the drain reservoir which induces two Kondo resonances accordingly [63, 64]. Their mutual overlap decreases for increasing V_{sd}, which surpresses and eventually prevents the tunneling processes through the QD. This suppression creates a ZBP in the conductance, a fundamental characteristic of the Kondo effect in QDs. If T is increased the observed decrease of G in Fig. 1.10 diminishes the height of the ZBP which eventually vanishes for $T \gg T_{\mathrm{K}}$ [45]. And finally, if a magnetic field $B_{\parallel}$ is applied parallel to the 2DES plane, the ZBP splits [4, 45, 47], as shown in Fig. 1.11(b). The splitting of the ZBP results from the Zeeman splitting of

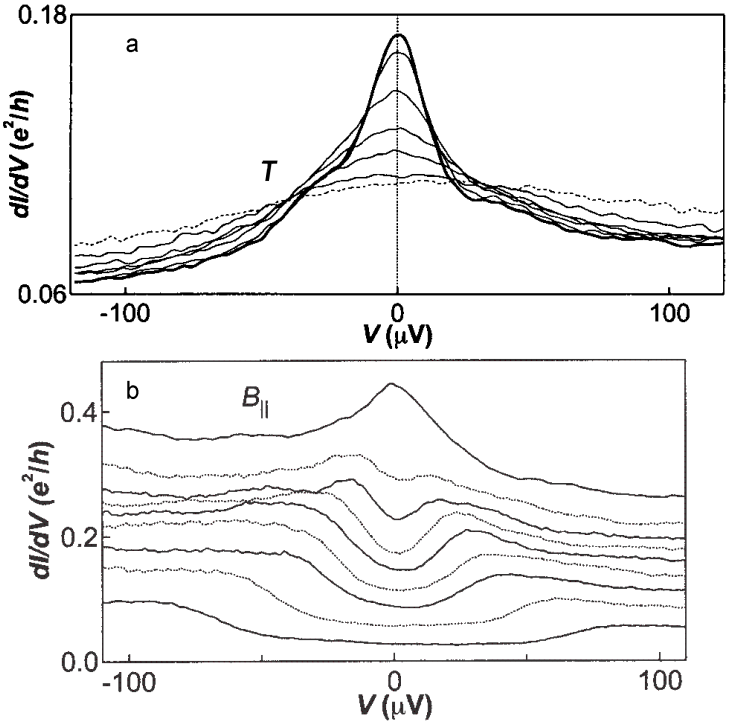

Figure 1.11: (a) Differential QD conductance at a constant tuning gate voltage which is chosen right in the center of the KQD valley of Fig. 1.10. The conductance is measured as a function of the source-drain voltage $V = V_{\mathrm{sd}}$ across the QD, once for each temperature $T = 45, 50, 75, 100, 130, 200, 270$ mK (bold to dashed curves). (b) The same valley conductance peak as in (a), measured as a function of the source-drain voltage at different constant magnetic fields $B_{\|} = 0.10, 0.43, 0.56, 0.80, 0.98, 1.28, 1.48, 2.49, 3.49$ T parallel to the 2DES (upper to lower curve). The curves are offset by 0.02 e^2/h for clarity (data from [4]).

both the confined electron state and the DOS-Kondo resonance [64]. It leads to the third characteristic of the Kondo conductance, namely that the ZBP, at $V_{\mathrm{sd}} = 0$, effectively drops and eventually disappears with increasing $B_{\|}$.

Chapter 2

Origin of the 0.7-anomaly

In this chapter, the 0.7-anomaly is investigated in detail experimentally and theoretically in terms of the sensitive response of the QPC conductance to varying temperature, magnetic field and source-drain voltage. Based on the analysis, a detailed theoretical model is presented which achieves a consistent, microscopic explanation for both the 0.7-anomaly and the accompanying ZBP including their interlinked appearance. It is shown that the 0.7-anomaly shows numerous analogies to the QD-related Kondo effect. Therefore both the experimental setting and the model are designed to incorporate both the QPC and QD regime and additionally to facilitate stepless transitions between both conditions. In particular, this tuning capability will be made use of in Chapter 3 for a detailed evaluation of the transition between a QPC and a QD in general, and between the 0.7-anomaly and the Kondo effect in particular.

The theoretical work of the modeling and the calculations presented in this Chapter 2 as well as in Chapter 3 were performed by Jan Heyder and Florian Bauer from the theoretical group of Prof. Jan von Delft at the LMU.

2.1 Experimental setup

The experimental results that are presented in this Chapter 2 and in Chapter 3 were performed on one setup using the same sample which incorporates an interface 2DES defined within a GaAs/AlGaAs heterostructure 85 nm beneath the surface. The investigated nanostructure was laterally defined in the 2DES by the use of a multi-gate layout on the surface of the heterostructure which is shown in Fig. 2.1. Six thin elongated Au gates were deposited on top of the etched and electrically contacted mesa by means of common electron-beam lithography. All six gates were independently tunable by individual applied electric voltages. For the measurements the gates were used pairwise symmetrically to form one center QPC (c) with a pair of adjacent QPCs, one on each side (s), as labeled in Fig. 2.1. Furthermore, a global Au top gate (t) was deposited on the sample, spatially separated and electrically insulated from the six bottom gates by an intermediate layer

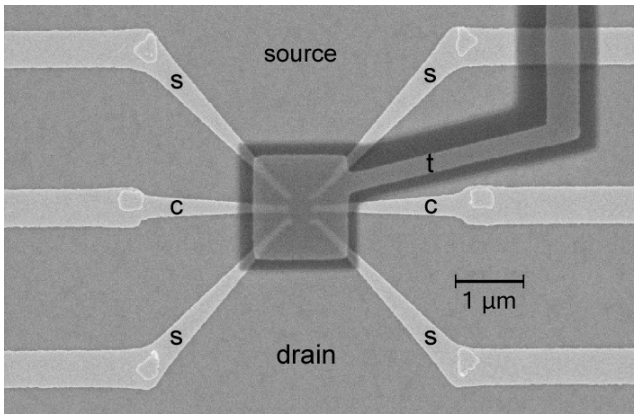

Figure 2.1: Scanning electron micrograph of the QPC layout which features a top gate (t), two central gates (c), and four side gates (s) to which the voltages V_t, V_c, and V_s are applied, respectively. Negative voltages V_c and V_s locally deplete the 2DES located 85 nm beneath the sample surface. Together with V_t it generates a highly tunable electrostatic potential landscape in the 2DES (gate defined constriction width ~ 250 nm). In contrast to the sample used for the measurements, on the sample shown in the micrograph the top gate is a few nanometer thin semitransparent layer of titanium in order to display the constriction region below.

of cross-linked PMMA (poly methyl-methacrylate) which appears as a dark gray border around the top gate in Fig. 2.1.

The sample was mounted in a dilution refrigerator at a stable bath temperature of $T_{\mathrm{bath}} \simeq 20$ mK. The corresponding 2DES electron temperature of $T_{\mathrm{2DES}} \simeq 30$ mK was slightly above T_{bath} according to temperature dependent conductance measurements. The experimentally determined 2DES carrier density and mobility at T_{bath} were $1.9\times10^{11}\,\mathrm{cm}^{-2}$ and $1.2\times10^{6}\,\mathrm{cm}^2/\mathrm{Vs}$. Using standard lock-in techniques, the two-terminal differential conductance $g = \mathrm{d}I_{\mathrm{sd}}/\mathrm{d}V_{\mathrm{sd}}^{\mathrm{ac}}$ was measured between the source and drain ohmic connections (compare Fig. 2.1) via the linear current response I_{sd} to a source-drain voltage modulation $V_{\mathrm{sd}}^{\mathrm{ac}}$ of small amplitude. Parallel to the 2DES plane as well as to the 1D channel of the QPCs an external magnetic field could be applied. Optimized parallel alignment of the magnetic field was assured by the use of a two-axis magnet and controlled by separate magnetotransport measurements. Further details regarding the setup and the magnetic field alignment procedure can be found elsewhere [65].

By using applied negative voltages the 2DES underneath the tip gates was locally depleted. The remaining 2DES area between the tip ends of the center and side gates formed the central constriction region (CCR), located at the center of Fig. 2.1. The seven gates provide a particularly high tunability of the CCR of the device. A negative voltage V_c at both center gates tuned the energy spectrum of the CCR. Another negative voltage V_s is applied to all four side gates in order to symmetrically arrange the local potential landscape of the CCR separately. The voltage V_t at the top gate was adjusted in order to control the carrier density in the local 2DES leads of the CCR which determines the effective interaction strength of the electrons (see Sec. 2.3.1). By suitably tuning both

voltages V_c and V_s at a fixed top gate voltage V_t, the CCR of the device was tuned to either define a short 1D channel containing a smooth symmetric barrier in the 2DES, the characteristic QPC potential, or to define a QD potential (compare Figs. 3.2(b) and 3.2(c) of Sec. 3.2). This Chapter 2 focuses on the QPC regime properties. Alternatively, adequate tuning of V_c and V_s allowed for a gradual tuning from the QPC to the QD potential or vice versa which was used for the experimental results presented in Chapter 3.

2.2 Theoretical model

In order to calculate the properties of the CCR for both the QPC and the QD regime two theoretical approaches were used, based on the perturbative treatment of the interaction U: second-order perturbation theory (SOPT) [66] and the functional renormalization group (fRG) procedure [67–69]. The fRG flow equations are used for the calculations at zero temperature $\widetilde{T} = 0$ and are based on a crucial assumption: The local magnetization at $\widetilde{B} = 0$ is assumed to be $m_j = 0$. This implies that spontaneous symmetry breaking is ruled out *a priori*. This supposition is justified *a posteriori* by the agreement of the fRG results with the experimental findings in this Chapter 2 as well as in Chapter 3. Moreover, for the fRG flow of the interaction vertex two further approximations were made which are both exact to the second order in U: three-particle vertices contributions are neglected, and two-particle vertex contributions which are not already generated to second order in the bare on-site interaction are neglected. The latter is called the coupled ladder approximation. As a computational simplification, a "static" version of it was used for most of the calculations of the zero-temperature properties of the 0.7-anomaly (referred to as "static fRG") which neglects all frequency dependencies in self-energies and vertices. Additionally, SOPT is used to access the effects of inelastic scattering for finite temperatures $\widetilde{T} > 0$ or source-drain voltages $\widetilde{V}_{sd} > 0$ at a fixed U.

The lowest 1D subband of the nanostructure is modeled by

$$\hat{H} = \sum_{j\sigma} \left[E_{j\sigma} \hat{n}_{j\sigma} - \tau_j (d^\dagger_{j+1\,\sigma} d_{j\sigma} + \text{h.c.}) \right] + \sum_j U_j \hat{n}_{j\uparrow} \hat{n}_{j\downarrow} \tag{2.1}$$

where $\hat{n}_{j\sigma} = d^\dagger_{j\sigma} d_{j\sigma}$ counts the number of electrons with spin σ ($= \pm$ for $\uparrow$,$\downarrow$) at site j. Equation 2.1 represents an infinite tight-binding chain as illustrated in Fig. 2.2, with hopping amplitude τ_j, local interaction U_j, and on-site potential energy $E_{j\sigma} = E_j - \sigma \widetilde{B}/2$. The Zeeman energy $\widetilde{B} = |g_{el}| \mu_B B_{ext}$ accounts for a uniform external parallel magnetic field B_{ext} where μ_B is the Bohr magneton and the electron g-factor is $g_{el} < 0$ for GaAs. Spin-orbit interactions and other orbital effects are neglected.

The bulk dispersion relation of the tight-binding chain (for $E_j = U = \widetilde{B} = 0$) is shown in Fig. 2.3(a), with the respective bulk local density of states (LDOS) $\mathcal{A}^0_{bulk}(\omega)$ plotted graphically and color-coded in Fig. 2.3(b) and related parameters being indicated. E_j, U_j and τ_j vary smoothly with j and differ from their bulk values, $E_{bulk} = U_{bulk} = 0$ and

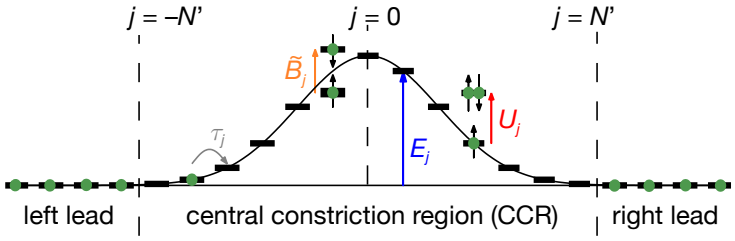

Figure 2.2: Schematic depiction of the used one-dimensional model for the case of a QPC barrier shape. It represents an infinite tight-binding chain with hopping matrix element τ_j (gray). The local potential E_j (blue) and the on-site interaction U_j (red) are nonzero only within a central constriction region (CCR) of $N = 2N' + 1$ sites. The CCR is connected to two semi-infinite non-interacting leads on the left and right. A homogeneous Zeeman magnetic field $\widetilde{B}$ (orange) can be added.

$\tau_{\mathrm{bulk}} = \tau$ (in units of energy), only within a CCR of $2N + 1$ sites symmetrically around $j = 0$ which comprises the modeled nanostructure (compare Fig. 2.2).

There are two models used, "model I" for the numerical calculations of the QPC and QD regimes and the transitions between both, presented in Chapter 3, and "model II" which is used for the numerical results of the detailed QPC properties, mainly discussed in this Chapter 2. Both models differ in the approaches for the on-site potential E_j and the hopping amplitude τ_j in Eq. 2.1. "Model I" uses a j-independent $\tau_j = \tau$ and the on-site potential E_j is defined with respect to the Fermi energy E_{F} of the left and right lead as

$$E_j^{\mathrm{I}} = \begin{cases} 0\,, & \forall\ |j| \geq N', \\ (\widetilde{V}_{\mathrm{s}} + E_{\mathrm{F}}) \left[2 \left(\frac{|j|-N'}{j_{\mathrm{s}}-N'} \right)^2 - \left(\frac{|j|-N'}{j_{\mathrm{s}}-N'} \right)^4 \right], & \forall\ j_0 \leq |j| \leq N', \\ \widetilde{V}_{\mathrm{c}} + E_{\mathrm{F}} + \frac{\overline{\Omega}_x^2 j^2}{4\tau} \operatorname{sgn}(\widetilde{V}_{\mathrm{s}} - \widetilde{V}_{\mathrm{c}}), & \forall\ 0 \leq |j| < j_0\,. \end{cases} \tag{2.2}$$

It represents a smooth, symmetric potential barrier within the CCR that can be adopted to describe both the QPC and the QD regime of the nanostructure. Eq. 2.2 is illustrated in Figs. 2.3(c) and 2.3(d) (black dashed lines) which show two choices for E_j, one for the QD and one for the QPC regime, respectively (Fig. 2.2 shows the QPC regime only). It consists of a quadratic (blue) and quartic (red) component (in Figs. 2.3(c) and 2.3(d) only shown for $j > 0$) which are continuously joint at j_0 dynamically. The inner region is given by $|j| < j_0$ where the barrier curvature is governed by the parameter $\overline{\Omega}_x$ (≥ 0) (in units of energy). The parameters $\widetilde{V}_{\mathrm{s}}$ and $\widetilde{V}_{\mathrm{c}}$ set the height of the potential with respect to E_{F} at the sites $j = \pm j_{\mathrm{s}}$ and 0, respectively. They in principle concur with the experimental locations of the side gates ($j = j_s$) and center gates ($j = 0$), compare Figs. 2.3(c) and 2.3(d). ("in principle" is conceded because in the model j_s can be changed

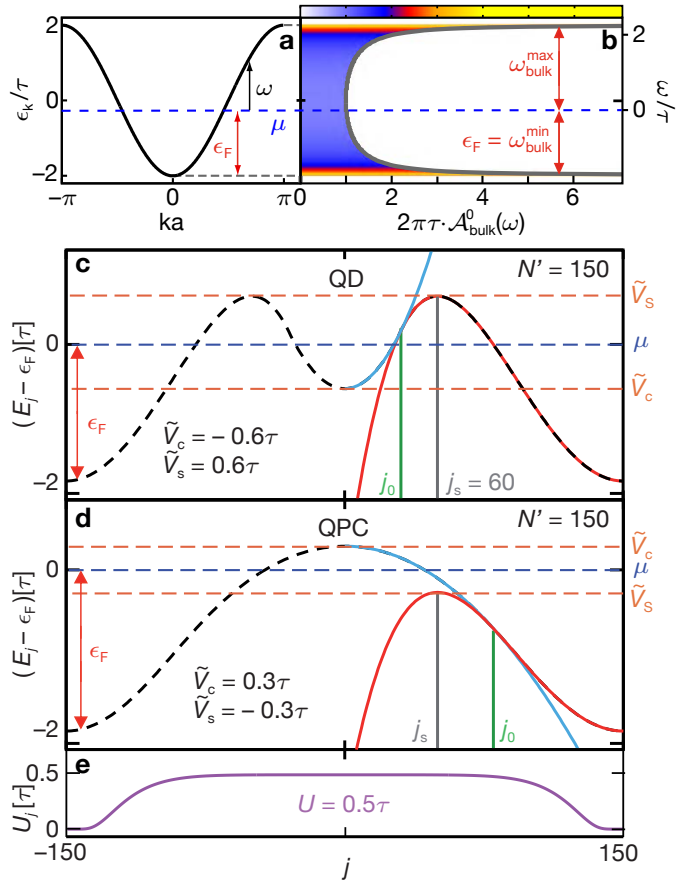

Figure 2.3: (a) Dispersion relation ϵ_k vs. k for a bulk non-interacting tight-binding chain without magnetic field (infinite, homogeneous, $E_{j\sigma} = U_j = 0$). The filling of the leads is controlled by the global chemical potential μ (blue dashed line). It is depicted at $\mu \neq 0$ for generality, for the calculations $\mu = 0$ was actually used. (b) The corresponding j-independent bulk LDOS, shown both as $\mathcal{A}^0_{\rm bulk}(\omega)$ (on the x-axis) versus energy ω (on the y-axis) and using a color scale. The chemical potential lies $E_{\rm F} = \epsilon_{\rm F} = 2\tau + \mu$ above the band bottom of the bulk. (c,d): The one-dimensional potential E_j (thick dashed black line) of "model I" for (c) a QD potential ($\widetilde{V}_{\rm s} > \widetilde{V}_{\rm c}$) and (d) a QPC potential ($\widetilde{V}_{\rm c} > \widetilde{V}_{\rm s}$). In the outer region of the central constriction region (CCR) ($j_0 \leq |j| \leq N'$), E_j is described by a quartic polynomial, and in the inner region ($|j| < j_0$) by a quadratic one with a curvature governed by $\overline{\Omega}_x$ (thin red and blue lines, respectively, shown only for $j > 0$). For a given N', $j_{\rm s}$, $\widetilde{V}_{\rm s}$, and $\widetilde{V}_{\rm c}$, the parameters j_0 and $\overline{\Omega}_x$ are adjusted such that the resulting potential E_j depends smoothly on j throughout the CCR. (e) The spatial variation of the on-site interaction U_j used in the model.

freely, say during the modeling of the QPC-QD crossover, whereas in the experiment the locations of the side gates are fixed due to the rigid sample gates layout.)

On the other hand, "model II" uses an on-site potential E_j being defined within the

CCR $j \leq j_{\max}$ as

$$E_j^{\mathrm{II}} \propto (\widetilde{V}_{\mathrm{c}} + E_{\mathrm{F}})\exp[-(\frac{j}{j_{\max}})^2/(1-(\frac{j}{j_{\max}})^2)] \; . \tag{2.3}$$

τ_j is chosen to be site-dependent within the CCR including a smooth (adiabatic) reduction proportional to the local barrier height. The reason for the introduction of "model II" is, briefly explained, that it allows to use a shorter CCR while retaining a small curvature $\overline{\Omega}_x$ at the barrier top. And it furthermore avoids the occurrence of *artificial* bound states in the bare density of states of the QPC which are observed close to the upper band edge when using "model I". However, both models have in common that the resulting QPC barriers are all parabolic near the top (unless stated otherwise).

Outside of the CCR, the sites $j < -N/2$ and $j > N/2$ represent two noninteracting leads, each with a bandwidth 4τ, the effective mass $m = \hbar^2/(2\tau a^2)$ as defined by the curvature of the bulk dispersion at the band bottom, the chemical potential μ and the bulk Fermi energy $E_{\mathrm{F}} = 2\tau + \mu$. $\mu = 0$ is consistently chosen in the calculations which implies half-filled leads (compare Fig. 2.4(b) in Sec. 2.2.1). The interaction U_j is fixed at $U_j = U$ for all but the outermost sites of the CCR where it drops smoothly to zero, as plotted in Fig. 2.3(e) for $U = 0.5\tau$.

For the comparison with the experimental results, the conductance g of the CCR is calculated as well as the local quantities

$$n_j = \langle \hat{n}_{j\uparrow} + \hat{n}_{j\downarrow} \rangle \; , \tag{2.4a}$$
$$m_j = \langle \hat{n}_{j\uparrow} - \hat{n}_{j\downarrow} \rangle /2 \; , \tag{2.4b}$$
$$\chi_j = \partial_{\widetilde{B}} m_j|_{\widetilde{B}=0} \; , \tag{2.4c}$$

being the occupation n_j, the magnetization m_j, and the spin susceptibility χ_j of the 2DES electrons evaluated at site j, respectively.

In order to delimit experimental and theoretical parameters from each other, symbols with and without tildes are used, e. g. $\widetilde{B}$ or B. This proceeding is useful because associated parameters are not equivalent in either case, e. g. a gate voltage V as opposed to $\widetilde{V} = -|e|V$ that represents the resulting potential energy of a particle with the elementary charge e.

2.2.1 Local quantum point contact properties

First the QPC properties are calculated using "model II" (compare Sec. 2.2) for the considered theoretical case of zero temperature $\widetilde{T} = k_{\mathrm{B}}T = 0$, source-drain voltage $\widetilde{V}_{\mathrm{sd}} = -|e|V_{\mathrm{sd}} = 0$ and magnetic field $\widetilde{B} = |g_{\mathrm{el}}|\mu_{\mathrm{B}}B = 0$. The spatial shape of the bare LDOS defining the barrier in the CCR is shown in Fig. 2.4(b) (color scaled; similarly depicted in Figs. 2.4(f-h) too for three different values of $\widetilde{V}_{\mathrm{c}}$). The corresponding "band bottom" is given by $\omega_j^{\min} = E_j - (\tau_{j-1} + \tau_j) - \mu$ (black solid line in Fig. 2.4(b)). $\omega_j^{\min}$ defines the smooth, symmetric barrier within the CCR that is parabolic near the top [17] where it is approximated by $\omega_j^{\min} \simeq \widetilde{V}_{\mathrm{c}} - \Omega_x^2 j^2/(4\tau_{j=0})$. The center potential $\widetilde{V}_{\mathrm{c}}$ sets the barrier

height with respect to μ (black dashed line in Fig. 2.4(b)), and Ω_x ($\ll \tau$) characterizes its curvature. As $\widetilde{V}_\mathrm{c}$ is lowered below zero, the conductance $g = G/G_\mathrm{Q}$ rises from 0 to 1 showing a step of width $\simeq \Omega_x$ (about 1.5 meV in the experiment) whose shape depends on U, as shown in Fig. 2.4(k). In the upper part of the step, around $0.5 \lesssim g/G_\mathrm{Q} \lesssim 0.9$, the QPC will be called "sub-open". The sub-open regime is of special interest as for the measured $g(V_\mathrm{c})$ curves it contains the 0.7-anomaly.

The bare LDOS $\mathcal{A}_j^0(\omega)$ has a strong maximum just above the band bottom around $j = 0$ [70], visible as a yellow to red elongated formation in Fig. 2.4(b). Semiclassically there is $\mathcal{A}_j^0(\omega) \propto 1/v_j(\omega)$ where $v_j(\omega)$ is the velocity at site j of an electron with energy ω. Thus the ridge-like maximum of $\mathcal{A}_j^0(\omega)$ above the barrier reflects the fact that electrons move slowest there. In the outer flanks of the CCR this ridge evolves smoothly into a van Hove singularity $\mathcal{A}_\mathrm{bulk}^0 \propto [(\omega - \omega_\mathrm{bulk}^\mathrm{min})\tau]^{-1/2}$ (see Fig. 2.4(b)) being exhibited by the bulk LDOS at the bulk band bottom in the leads, $\omega_\mathrm{bulk}^\mathrm{min} = -2\tau$. Therefore the LDOS structure around $j = 0$ is referred to as "Hove ridge". It directly determines the effective strength of interaction effects which scale as U/U_c where $U_\mathrm{c} = \sqrt{\hbar^2\Omega_x/(2ma^2)}$ is inversely proportional to $\max[\mathcal{A}_j^0(\omega)]$, the height of the Hove ridge at the barrier center (a is the lattice spacing of the tight binding chain).

Near the barrier center, the barrier curvature causes the singularity to be smeared out on a scale set by Ω_x. This shifts the Hove ridge $\max[\mathcal{A}_j^0(\omega)]$ upwards relative to the band bottom by an energy of the order of Ω_x, $\omega_j^\mathrm{min} + \mathcal{O}(\Omega_x)$ (compare Figs. 2.4(f-h)), and sets an upper limit for the maximum amplitude of the Hove ridge as its height scales as $1/\sqrt{\tau\Omega_x}$. This implies that all local quantities which exhibit a dependence on the LDOS, such as the local magnetic susceptibility χ_j, depend as well on Ω_x and therefore on the particular shape of the QPC barrier.

The van Hove ridge has a strong impact on numerous QPC properties that also depend on $\widetilde{V}_\mathrm{c}$ due to the ridge geometry around $j = 0$. Near those spatial locations where it intersects the chemical potential μ the LDOS is enhanced, thus amplifying the effects of interactions by $\mathcal{O}(\Omega_x\tau_0)^{-1/2}$ (which grows with the QPC length). The semiclassical reasoning for it is that slower electrons feel interactions particularly stronger. When the QPC is opened by lowering the barrier top $\widetilde{V}_\mathrm{c}$, the Hove ridge is swept downwards too (see Figs. 2.4(f-h)). Its interaction-amplifying effects are strongest in that $\widetilde{V}_\mathrm{c}$-regime where its apex having the most weight crosses μ. This happens for $0 \gtrsim \widetilde{V}_\mathrm{c} \gtrsim -\mathcal{O}(\Omega_x)$ (Fig. 2.4(g)), which, very importantly, encompasses the sub-open regime hosting the 0.7-anomaly. It is shown below that the 0.7-anomaly and the ZBP can be explained from the amplification of interaction effects at the locations where the Hove ridge intersects μ. The relevant implications are increase of the effective Hartree barrier governing elastic transmission, the spin susceptibility as well as the inelastic scattering rate, all of which lead to an anomalous reduction of g in the sub-open regime, especially for $\widetilde{B}, \widetilde{T}, \widetilde{V}_\mathrm{sd} > 0$.

Figures 2.4(c-e) illustrate several local properties, calculated at $\widetilde{T} = 0$, for the sub-open QPC barrier shown in Fig. 2.4(b). Shown are the local density n_j for two different magnetic fields $\widetilde{B}$ (Fig. 2.4(c)), the local magnetization m_j for various $\widetilde{B}$ (Fig. 2.4(d)), and

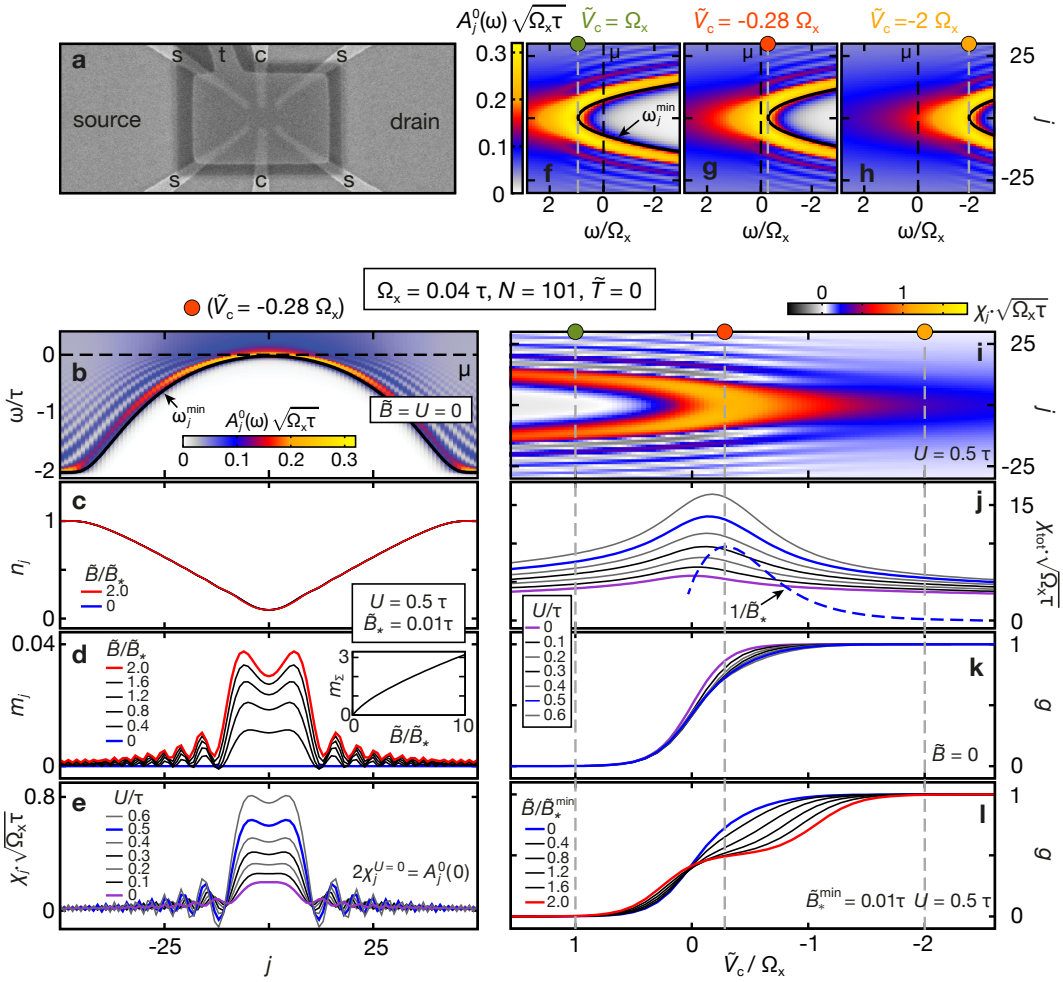

Figure 2.4: (a) Fig. 2.1 shown again for comparison. (b) The bare ($U_j = 0, \widetilde{B} = 0$) 1D local density of states (LDOS) $\mathcal{A}_j^0(\omega)$ (color scale) vs. energy ω and site j. The LDOS shows a Hove ridge (yellow/red) just above the "band bottom" $\omega_j^{\min}$ (solid black line), and Friedel oscillations (white fringes) at $\omega \lesssim \widetilde{V}_c$. (c-e) fRG results for the sub-open barrier shown in (b): (c) Local density n_j and (d) magnetization m_j for several $\widetilde{B}$. Inset of (d): $m_\Sigma = \sum_{|j|\leq 10} m_j$ vs. $\widetilde{B}$. (e) Local spin susceptibility χ_j for several U. (f-l) Changing barrier height: (f-h) Bare LDOS $\mathcal{A}_j^0(\omega)$ for three barrier heights $\widetilde{V}_c/\Omega_x = 1, -0.28$ and -2. The LDOS is fixed relative to $\widetilde{V}_c$ (dashed gray) but shifts relative to μ (dashed black lines). (i-l) fRG results: $\widetilde{V}_c$-dependence of (i) χ_j (color scale) at fixed $U = 0.5\tau$, (j) total spin susceptibility $\chi_{\rm tot} = \sum_j^{\rm CCR} \chi_j$ for several U (solid lines) and the inverse low-energy scale $1/\widetilde{B}_*$ for $U = 0.5\tau$ (dashed line, same y-axis), (k) $g = G/G_Q$ (linear response) for several U ($\widetilde{B}, \widetilde{T}, \widetilde{V}_{\rm sd} = 0$), (l) g for several $\widetilde{B}$ ($U = 0.5\tau$). Identical $\widetilde{V}_c$ (vertical lines in (f-l)) are marked by dots of matching colors for comparison.

the local spin susceptibility χ_j of the 2DES electrons for several interaction strengths U (Fig. 2.4(e)), all plotted as a function of the site j. Four outstanding features are noted which are all intuitively expected:

(i) n_j is minimal at the barrier center.
(ii) m_j vanishes at $\widetilde{B} = 0$, as depicted in Fig. 2.4(d) (blue line). This reflects a physical assumption implicated by the calculations (compare Sec. 2.2), namely that no spontaneous spin polarization occurs.
(iii) $m_j(\widetilde{B})$ increases without saturation which indicates a smooth redistribution of spins, as expected for the open QPC structure. This is evident from the inset of Fig. 2.4(d) which shows the local mean magnetization $m_\Sigma = \sum_{|j|\leq 10} m_j$ plotted as a function of the magnetic field $\widetilde{B}$.
(iv) χ_j is strongly increased with increasing interaction U since the latter amplifies any field-induced spin imbalance. The j-dependence of χ_j is governed by that of $\mathcal{A}_j^0(0)$ (in fact, $\chi_j^{U=0} = \mathcal{A}_j^0(0)/2$) so that χ_j has maxima near those locations where the $\mathcal{A}_j^0(0)$ intersects μ (compare Figs. 2.4(b) and 2.4(e)).

The characteristics of the CCR for changing $\widetilde{V}_\mathrm{c}$ and thus a changing barrier height are summarized in Figs. 2.4(i-l). Plotted as a function of $\widetilde{V}_\mathrm{c}$ and j, Fig. 2.4(i) shows the local spin susceptibility χ_j color-coded at a fixed $U = 0.5\tau$. Figures 2.4(j) and 2.4(k) depict the total spin susceptibility $\chi_\mathrm{tot} = \sum_j^\mathrm{CCR} \chi_j$ (solid lines) and the QPC conductance $g = G/G_\mathrm{Q}$ ($\widetilde{B}, \widetilde{T}, \widetilde{V}_\mathrm{sd} = 0$), respectively, for various U as indicated. The inverse low-energy scale $1/\widetilde{B}_*$ (compare Sec. 2.3.3) for $U = 0.5\tau$ is also overlaid in Fig. 2.4(j) (dashed line). Eventually Fig. 2.4(l) shows the calculated $g(\widetilde{V}_\mathrm{c})$ for multiple magnetic fields $\widetilde{B}$ as indicated. The vertical dashed gray lines in Figs. 2.4(i-l), in connection with the color-coded dots, mark identical $\widetilde{V}_\mathrm{c}$ for comparison within Fig. 2.4.

When $\widetilde{V}_\mathrm{c}$ is lowered from above to below zero (see Figs. 2.4(f-h)), the intersection points of the Hove ridge and μ sweep out a parabolic arch in the $\widetilde{V}_\mathrm{c}$-j plane along which $\chi_j(\widetilde{V}_\mathrm{c})$ is peaked (see Fig. 2.4(i)), with most weight near the arch's apex. This induces a corresponding peak in the total spin susceptibility, χ_tot as function of $\widetilde{V}_\mathrm{c}$, as evident from Fig. 2.4(j). The peak of χ_tot is strongly increased by increasing U which is in accordance with the statement (iv) above. The peak location further corresponds to the $\widetilde{V}_\mathrm{c}$-value where $g \simeq 0.7$ (compare Fig. 2.4(k)). As will be shown below, the shape of χ_tot strongly affects the $\widetilde{B}$-dependence of the conductance, plotted in Fig. 2.4(l).

Next the effect of the LDOS ridge on the conductance g is discussed, first by considering the calculated $g(\widetilde{V}_\mathrm{c})$ as a function of U at $\widetilde{B}, \widetilde{T}, \widetilde{V}_\mathrm{sd} = 0$ shown in Fig. 2.4(k). Increasing U skews the shape of the step in $g(\widetilde{V}_\mathrm{c})$, eventually causing it to develop a shoulder near $g \simeq 0.7$. This shoulder develops because the ($\widetilde{V}_\mathrm{c}$-dependent) increase in the local density is slightly nonlinear when the apex of the van Hove ridge drops past μ causing a corresponding upward shift in the effective (Hartree) barrier which induces a decrease of the elastic transmission that is nonlinear too. According to the calculations, this happens to occur around $g \simeq 0.7$ for a parabolic barrier top. If the shape of the barrier top is changed to be flatter (sharper) than parabolic, the Hove ridge at a given $\widetilde{V}_\mathrm{c}$ shifts down closer toward ω_j^min (shifts up further away from ω_j^min). Thus, when $\widetilde{V}_\mathrm{c}$ is lowered, the Hove ridge apex crosses μ earlier (later), causing the shoulder in g to shift down toward $0.5G_\mathrm{Q}$ (up toward $1G_\mathrm{Q}$). This explains the experimentally observed spread

of shoulders within $0.5 \lesssim g/G_\mathrm{Q} \lesssim 0.9$ [30, 34] for the various constriction geometries and 2DES burying depths within the heterostructure used which are uniformly associated with the anomaly around $0.7G_\mathrm{Q}$ due to their identical characteristic behavior.

Finally, an essential feature which constitutes one main result of this work can be concluded directly from Fig. 2.4(k): at a large enough interaction strength, the calculated conductance $g(\widetilde{V}_\mathrm{c})$ already exhibits a distinct kink at $g \simeq 0.7G_\mathrm{Q}$, the 0.7-anomaly, even for $\widetilde{T} = 0$, and most importantly, even for $\widetilde{B} = 0$ despite the imposed constraint of absent spontaneous spin polarization. This kink furthermore gradually evolves into the spin-split plateau $g = 0.5G_\mathrm{Q}$ on increasing $\widetilde{B}$ as shown in Fig. 2.4(l) (the blue curve is identical to the one being blue in Fig. 2.4(k)), which is in conformity with the magnetic field behavior of the 0.7-anomaly [24, 27–29].

2.3 Comparison between theory and experiment

In this section the experimentally measured conductance of a QPC as a function of the QPC channel width, the 2DES density in the leads, the magnetic field B externally applied in parallel to the 2DES plane, the 2DES temperature T, and the source-drain bias voltage V_sd across the QPC constriction are presented. The introduced model (Sec. 2.2) is used to calculate the respective variations of the QPC conductance which are qualitatively compared with the experiments. Furthermore, within both measurements and calculations the conductance as a function of B, T, and V_sd are quantitatively compared with respect to each other, with the main focus being on the response at low excitation energies.

2.3.1 Variation of the local interaction strength

In this section the relation between the 2DES density and the interaction strength U in the CCR is investigated in the light of the introduced model (Sec. 2.2). Increasing the top gate voltage V_t increases the carrier density in the 2DES leads of the CCR and hence both the source and drain chemical potential. It deepens the trenches between the regions of higher potential energy caused by the central and side gates [71]. This changes not only the shape of the QPC potential along the 1D channel. It also causes the transverse wave functions in the QPC constriction to be more localized which increases the effective 1D on-site interaction strength U within the CCR. This can be summarized as: Increasing the top gate voltage V_t increases the effective interaction strength U in the CCR. Furthermore, increasing V_t has an additional effect on the QPC potential. Due to the deepened trenches in the CCR, the energy spacing of the QPC transverse modes increases which increases the subband spacing [17]. This trend is revealed in Fig. 2.5(b), which is extracted from the measured pinch-off curves at different applied top gate voltages $-0.7\ \mathrm{V} \leq V_\mathrm{t} \leq 0.8\ \mathrm{V}$ shown in Fig. 2.5(a), measured in the QPC regime of the nanostructure. As V_t is decreased in Fig. 2.5(a) the carrier density in the 2DES leads drops which results in increased pinch-

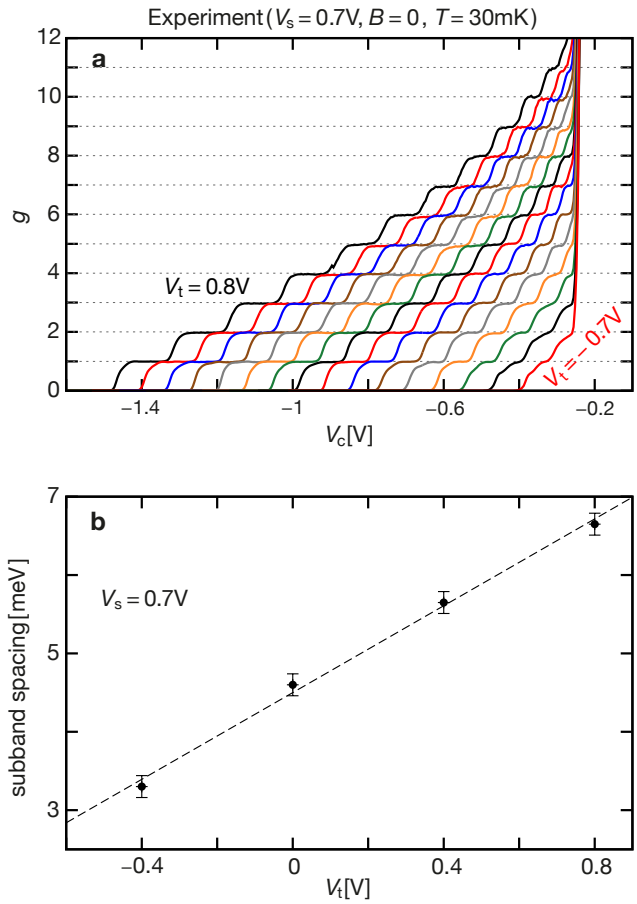

Figure 2.5: Top gate voltage V_t dependence of the subband spacing: (a) Measured QPC pinch-off curves $g(V_c)$ for various $-0.7\ \mathrm{V} \leq V_t \leq 0.8\ \mathrm{V}$. (b) Energy spacing between the lowest two 1D subbands as a function of V_t. The spacings and error margins were evaluated from finite-V_{sd} measurements [65]. The dashed straight line is a guide to the eye.

off voltages V_c accompanied by narrowing conductance plateaus. The V_t-independent steep gain in $g(V_c)$ at $V_c \simeq -0.25\ \mathrm{V}$ marks the transition from the 1D QPC to the 2D transport regime as the QPC channel disappears due to insufficient 2DES depletion. Combining both Fig. 2.5(b) and the relation between V_t and U allows to identify the (V_t-induced) increase (or decrease) in U with the aid of the (V_t-induced) increase (or decrease) in the QPC subband spacing [72].

Now the the magnetic field-induced QPC subband splitting caused by the lift of spin degeneracy is evaluated. The splitting is deduced from the derivative $\mathrm{d}g/\mathrm{d}V_c$ extracted numerically from the measured conductance g [24, 25, 29]. The respective experimental result, with $g(V_c)$ measured at $V_t = 0.8\ \mathrm{V}$ for various B, is plotted in Fig. 2.6(a) as a function of V_c in the range $0 < g < 1$ (red dots). Two local peaks are visible (blue dots) which were extracted using fits of two Gaussians (black curves). Their splitting $\Delta E \simeq g_{ss} B + \Delta_{hfo}$ (arrow in (a)), which is converted into energy for multiple V_t in

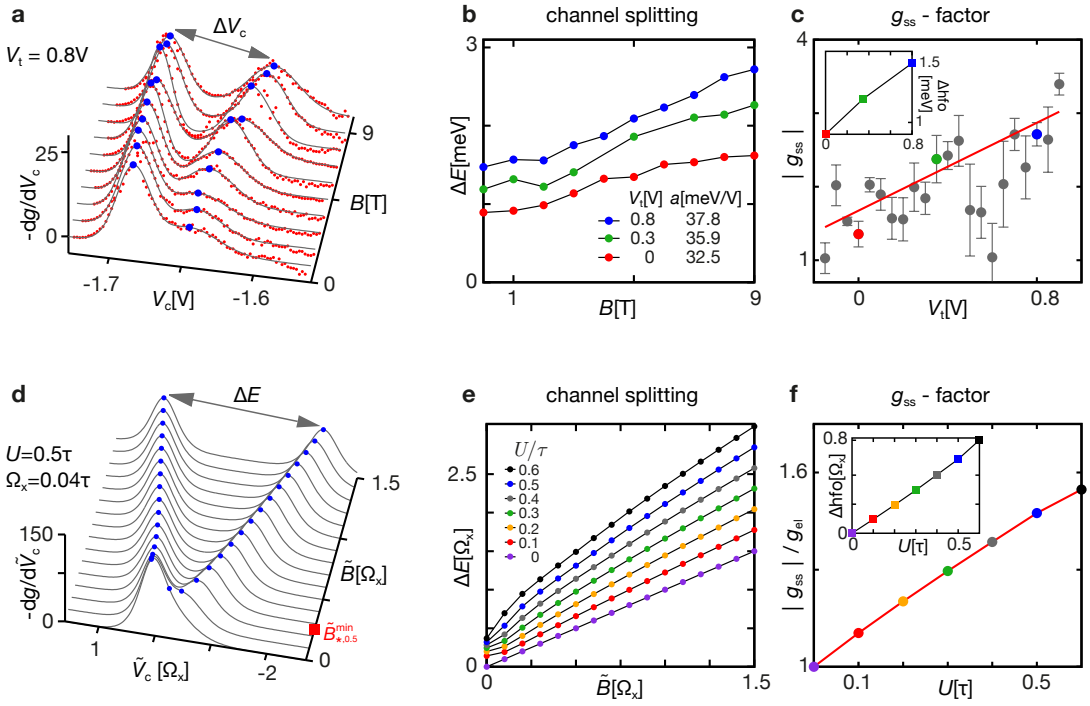

Figure 2.6: Determination of the g-factor $g_{\rm ss}$ from the QPC subband-splitting: (a-c) Results from experimental measurements on a sample of similar design as that discussed in Sec. 2.1 and (d-f) respective fRG calculation results. (a,d) Derivative of the measured (calculated) conductance with respect to the gate voltage $V_{\rm c}$ ($\widetilde{V}_{\rm c}$), shown by red dots (black lines) and plotted versus $V_{\rm c}$ ($\widetilde{V}_{\rm c}$) for several magnetic fields B ($\widetilde{B}$) at a constant interaction strength characterized by $V_{\rm t}$ (U) as indicated. The occurring local maxima are marked in both panels (blue dots). In (d) $\widetilde{B}^{\rm min}_{*,0.5}$ is drawn in (red square) being $\widetilde{B}^{\rm min}_{*}$ for the interaction strength $U/\tau = 0.5$. (b,e) Local maxima separation as indicated by the arrows in (a,d) in units of energy ΔE, plotted as a function of magnetic field for several interaction strengths $V_{\rm t}$ and U, respectively, as indicated. The ΔE were determined in the experiment by fitting a pair of Gaussians (gray lines in (a)) to the data, and were read out directly from the calculated results. (To convert $\Delta V_{\rm c}$ in (a) to ΔE in (b), $V_{\rm t}$-dependent conversion factors $a = \Delta E/\Delta V_{\rm c}$ are used, as listed in the legend of (b), obtained approximately from nonlinear transport measurements [24, 29].) (c,f) $|g_{\rm ss}|$ (main panels) and $\Delta_{\rm hfo}$ (insets), plotted versus $V_{\rm t}$ and U, which were extracted by linear fits to the data in the large B ($\widetilde{B}$) range such as in (b,e) using $\Delta E \simeq g_{\rm ss} B + \Delta_{\rm hfo}$. The red line in (c) ((f)) is a error-weighted linear fit (guide to the eye).

Fig. 2.6(b), increases about linearly for large fields ($B \gg B_*$). The inferred g-factors $g_{\rm ss}$ and the offsets at high magnetic fields $\Delta_{\rm hfo}$ (linear extrapolations of the high-field trend to $B = 0$) are summarized in the main panel and the inset of Fig. 2.6(c), respectively. Both are observed to increase with raised $V_{\rm t}$ and therefore with stronger interactions U. This increase of $g_{\rm ss}$ and $\Delta_{\rm hfo}$ with U is verified by the calculated results Figs. 2.6(d-f) (equivalent representation such as in Figs. 2.6(a-c)) which confirms that both serve as measures of the effective interaction strength. Moreover, the qualitative accordance of

the measured and calculated g_{ss} in Figs. 2.6(c) and 2.6(f) confirms the relation between V_{t} and U (being tested at $B > 0$).

Eventually it is concluded that: (1) Local interactions are the reason for the anomalous enhancement of the effective electron g-factor $|g_{\mathrm{ss}}|$ in the CCR of the QPC [24, 25, 29, 34]. This enhancement could further be reproduced in Fig. 2.6(f) by assuming no spontaneous spin polarization (at $B = 0$) (compare Sec. 2.2). Hence it is consistent with the results of this Chapter 2 and of Chapter 3. And (2) the experimental observation of $\Delta_{\mathrm{hfo}} \neq 0$ [24, 29, 73] can be understood as well by assuming spontaneous spin polarization to be absent. This further confirmation of the experiment by the model Sec. 2.2 additionally reinforces the inferred results (Chapter 2 and Chapter 3).

2.3.2 Linear quantum point contact conductance

Next the calculated QPC conductance is compared with the experimental results around the first spin-degenerate plateau for varying temperature as well as magnetic field. This is shown in Fig. 2.7 for the measured (Figs. 2.7(e-h)) and calculated (Figs. 2.7(a-d)) conductance $g(V_{\mathrm{c}})$ and $g(\widetilde{V}_{\mathrm{c}})$, respectively. The invariant relative interaction strengths are indicated via V_{t} and U. The measured pinch-off curves $g(V_{\mathrm{c}})$ are plotted versus $\Delta V_{\mathrm{c}} = V_{\mathrm{c}} - V_{0.5}$ with $V_{0.5}$ being determined by $g(V_{0.5}) = 0.5$ (at $B = 0$, $T = T_0$). The magnetic field dependence is shown (left y-axis) in Fig. 2.7(e) as well as in Fig. 2.7(a) (fRG results) and Fig. 2.7(c) (SOPT results for comparison) for several magnetic fields and constant temperatures T, $\widetilde{T}$ as indicated. In addition, the fRG result of Fig. 2.7(a) is shown spin-resolved, $g_{\uparrow}$ and $g_{\downarrow}$, in Fig. 2.7(b) with the noise factor $\mathcal{N}$ plotted versus g in the inset. Similarly to the magnetic field dependence, the temperature dependence is compared in Fig. 2.7(f) and Fig. 2.7(d) for zero magnetic field. The matching colors both for the magnetic field and the temperature dependence are chosen to provide comparability. The measured conductance $g(V_{\mathrm{c}} = \mathrm{const})$ for varying magnetic field (at $T = T_0$) and varying temperature ($B = 0$) is depicted in Fig. 2.7(g) and Fig. 2.7(h), respectively, in log-linear scaling (main panels) and log-log scaling (insets). The black lines in (g) and (h) are the fitted dependencies $1 - (B/B_*)^2$ and $1 - (T/T_*)^2$. They are dictated by the corresponding low-energy scales $E_* = \mu_{\mathrm{B}} B_*(V_{\mathrm{c}})$ and $E_* = k_{\mathrm{B}} T_*(V_{\mathrm{c}})$ which are plotted in log-linear scaling (right y-axis) in (e) (for B_*) and (f) (for B_* and T_*). The symbol colors in Figs. 2.7(e) and 2.7(g) (Figs. 2.7(f) and 2.7(h)) match in order to highlight the constant V_{c} values of the different datasets in Fig. 2.7(g) (Fig. 2.7(h)). Both low-energy scales were extracted from the calculated g curves too and are similarly plotted in the associated panels, $\widetilde{B}_*$ in Figs. 2.7(a) and 2.7(c) (of which the latter is again shown in Fig. 2.7(d)) (solid gray lines) as well as $\widetilde{T}_*$ in Fig. 2.7(d) (black line). Additionally the corresponding energy scale $\widetilde{V}_{\mathrm{sd}*}$ calculated from the non-linear QPC conductance is superimposed in Fig. 2.7(d) (brown line) for comparison.

The well-known feature Fig. 2.7(e) of the the 0.7-anomaly shoulder of becoming more pronounced on increasing B eventually passing into the spin-split plateau [24, 27–29] is

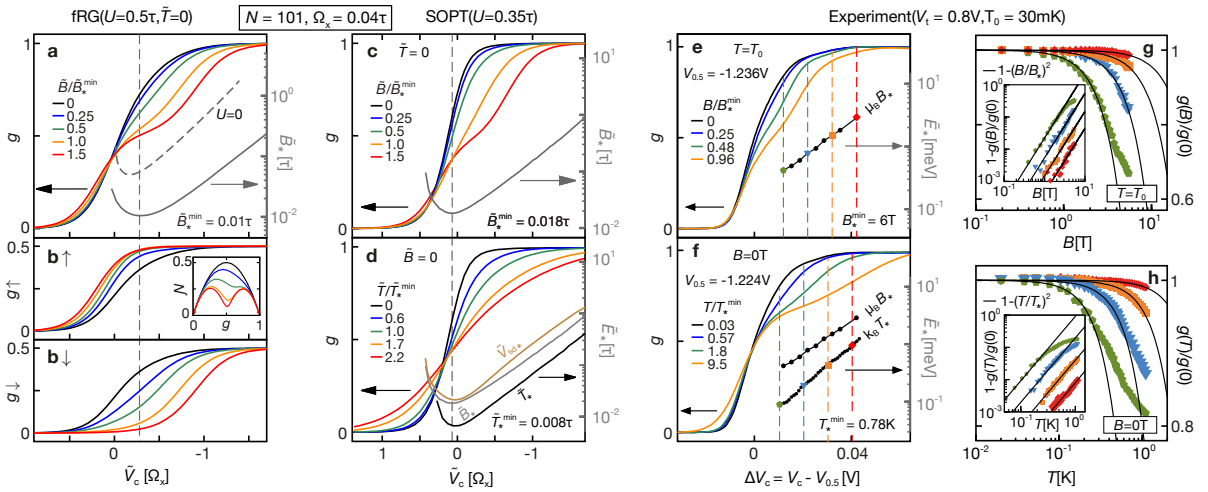

Figure 2.7: (a-d) Calculated QPC conductance $g(\widetilde{V}_c/\Omega_x)$ using (a,b) fRG and (c,d) SOPT: (a) Linear response $g(\widetilde{V}_c, \widetilde{B})$ and (b) spin-resolved components $g_\uparrow$ and $g_\downarrow$ for several $\widetilde{B}$ as indicated ($\widetilde{T} = 0$, $U = 0.5\tau$). Additionally (a) shows the low-energy scale $\widetilde{B}_*(\widetilde{V}_c)$ at $U = 0$ (dashed) and $U = 0.5$ (solid gray line) on a log-linear scale on the right y-axis, having a minimum $\widetilde{B}_*^{\min}$ marked by the vertical dashed line. Inset of (b): Noise factor $\mathcal{N} = 0.5\sum_\sigma g_\sigma(1 - g_\sigma)$ plotted versus g. (c) g for several $\widetilde{B}$ ($\widetilde{T} = 0$) and (d) g for various $\widetilde{T}$ ($\widetilde{B} = 0$). $\widetilde{B}_*(\widetilde{V}_c)$ (gray line) is shown in (c) and repeated in (d), $\widetilde{T}_*(\widetilde{V}_c)$ (black) and $\widetilde{V}_{\mathrm{sd}*}(\widetilde{V}_c)$ (brown line) are added to (d) and $\widetilde{B}_*^{\min}$ is again indicated (vertical dashed line). (e,f) Measured pinch-off curves $g(V_c)$, plotted as functions of $\Delta V_c = V_c - V_{0.5}$. The gate voltage $V_{0.5}$ is determined by $g(V_{0.5}) = 0.5$ at $B = 0$ and $T = T_0$. (e) g for various magnetic fields B parallel to the 2DES ($T = T_0$) and (f) g for various temperatures T ($B = 0$), as indicated. Colors in (e) and (f) are chosen to provide comparability with the theory curves in (a,c,d) with the correspondence $|e|\Delta V_c \propto -\widetilde{V}_c$. (g,h) Experiments: (g) $g(B)/g(B = 0)$ as function of B ($T = T_0$) and (h) $g(T)/g(T = T_0)$ as function of T ($B = 0$), shown on log-linear scales (insets show their differences to unity on log-log scales) to emphasize small values of B and T. Colored symbols distinguish data taken at different fixed V_c-values, indicated by equal symbols and dashed lines of corresponding colors in (e,f). Black lines in (g) and (h) show $1 - (B/B_*)^2$ and $1 - (T/T_*)^2$ which determine the corresponding scales $B_*(V_c)$ and $T_*(V_c)$, respectively. The resulting energies $E_* = \mu_B B_*(V_c)$ and $E_* = k_B T_*(V_c)$ are plotted versus V_c on a log-linear scale in (e) (for B_*) and (f) (for B_* and T_*).

well reproduced in Fig. 2.7(a) where the agreement was optimized by using U as a fit parameter. The confirming calculated results further allow to investigate the magnetic field evolutions of the corresponding spin-resolved conductances $g_\uparrow$ and $g_\downarrow$ in Fig. 2.7(b) which show a strong asymmetry. Although the bare barrier heights for spin $\uparrow$ and $\downarrow$ are shifted symmetrically by $\mp\widetilde{B}/2$, $g_\downarrow$ is decreased to a greater extent than $g_\uparrow$ is increased. This is caused by exchange interactions. Increasing the spin-up density near the CCR center strongly raises the (Hartree) barrier, and more so for spin-down than for spin-up electrons, due to the Pauli principle. It is most pronounced in the sub-open regime where the Hove-ridge-induced peak in χ_{tot} emerges (compare Fig. 2.4(j)). Thus this spin

asymmetry directly induces the calculated resulting magnetoresponse in Fig. 2.7(a). The imbalance of $g_\uparrow$ and $g_\downarrow$ further accounts for the asymmetric evolution of the noise factor $\mathcal{N}$, shown in the inset of Fig. 2.7(b), which agrees qualitatively with the experiment [28]. However, at $\widetilde{B} = 0$ there is $g_\uparrow = g_\downarrow$ indeed, reflecting the assumption imposed on the theory that no spontaneous spin splitting occurs (see Sec. 2.2).

Since the fRG approach is limited to the case of zero temperature and zero source-drain voltage, for which no inelastic scattering occurs, SOPT is used instead in order to qualitatively access the inelastic regime (at fixed U). Figs. 2.7(c) and 2.7(d) show the SOPT results for the linear conductance $g(\widetilde{V}_\mathrm{c})$ calculated for several magnetic fields and temperatures $\widetilde{T} = k_\mathrm{B}T$, respectively. As reproduced by the fRG calculations, at raised $\widetilde{B}$ the calculated shoulder in Fig. 2.7(c) gets more pronounced and eventually turns into the spin-split conductance plateau. Moreover, the further distinct feature of the 0.7-anomaly of becoming increasingly more pronounced with raised temperatures, shown in Fig. 2.7(f), is reflected in the SOPT result in Fig. 2.7(d) albeit to a lesser extent. For the SOPT, though, the conformity is fulfilled except for one constraint: For the low magnetic field dependence and the low temperature dependence, the experimental pinch-off curves in Figs. 2.7(e) and 2.7(f) show observable 0.7-shoulders whereas in the respective SOPT curves in Figs. 2.7(c) and 2.7(d) the shoulders are hardly visible. In contrast to this failure of SOPT, the more powerful fRG approach does reproduce the weak shoulder even for $\widetilde{B} = \widetilde{T} = 0$, as discussed above and apparent from the black $g(\widetilde{V}_\mathrm{c})$ curves of the fRG and SOPT results in Figs. 2.7(a) and 2.7(c).

As it is already plotted in Fig. 2.7 for comparison with the familiar QPC conductance, in the following section the low-energy scales B_*, T_*, and $V_{\mathrm{sd}*}$ of the response of the QPC conductance are inferred and examined in more detail.

2.3.3 Limit of low-energy excitations

In this section the characteristics of B, T, and V_sd in the limit of low energies are discussed. In this limit the model calculations yield three predictions which are all shown to be consistent with the results of the performed measurements:
(I) For a given $\widetilde{V}_\mathrm{c}$, the leading dependence of the nonlinear conductance g_nl on $\widetilde{B}$, $\widetilde{T}$ and $\widetilde{V}_\mathrm{sd}$ is predicted to be quadratic. This implies a valid expansion of the form

$$\frac{g_\mathrm{nl}(\widetilde{B},\widetilde{T},\widetilde{V}_\mathrm{sd})}{g_\mathrm{nl}(0,0,0)} \simeq 1 - \frac{\widetilde{B}^2}{\widetilde{B}_*^2} - \frac{\widetilde{T}^2}{\widetilde{T}_*^2} - \frac{\widetilde{V}_\mathrm{sd}^2}{\widetilde{V}_{\mathrm{sd}*}^2} \tag{2.5}$$

for $\widetilde{B}/\widetilde{B}_*, \widetilde{T}/\widetilde{T}_*, \widetilde{V}_\mathrm{sd}/\widetilde{V}_{\mathrm{sd}*} \ll 1$. $\widetilde{B}_*$, $\widetilde{T}_*$ and $\widetilde{V}_{\mathrm{sd}*}$ are $\widetilde{V}_\mathrm{c}$-dependent energy scales which determine the strength of the anomalous deviation of g around $0.7G_\mathrm{Q}$ for finite interactions $U \neq 0$. Though inferred for a QPC, Eq. 2.5 constitutes a key characteristic of the Fermi-liquid theory description of the Kondo effect in QDs and thus establishes a fundamental link between both regimes. The smaller these scales, the stronger the $\widetilde{B}$-, $\widetilde{T}$-, or $\widetilde{V}_\mathrm{sd}$-dependencies of g at a given $\widetilde{V}_\mathrm{c}$. The relevant measurement results are shown in the

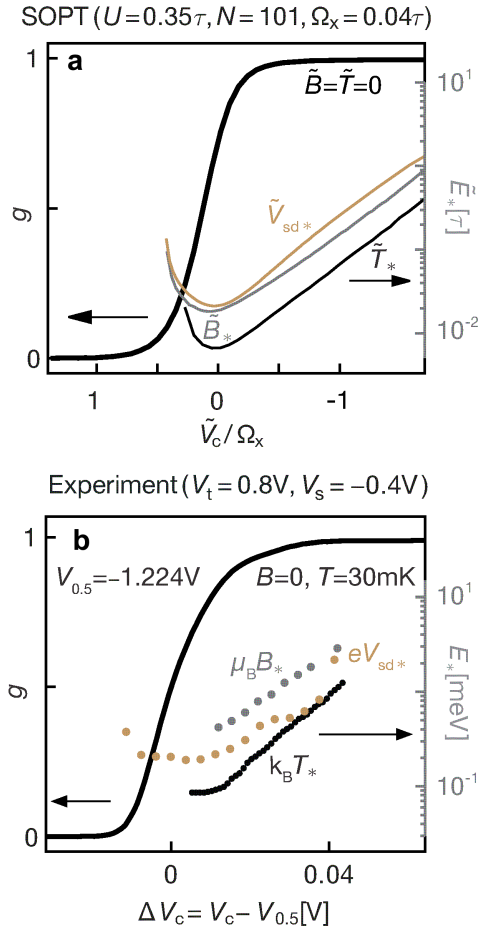

Figure 2.8: Comparison of low-energy scales from theory and experiment. (a) SOPT results ("model II"): $\widetilde{V}_c$ dependence of the conductance g (thick black line) and the low-energy scales $\widetilde{B}_*$ (gray), $\widetilde{T}_*$ (black), and $\widetilde{V}_{sd*}$ (brown line) (identical to the corresponding data in Fig. 2.7(d)). (b) Equivalent experimental results for g, $\mu_B B_*$, and $k_B T_*$ (compare Figs. 2.7(e) and 2.7(f)) and eV_{sd*} as a function of $\Delta V_c = V_c - V_{0.5}$. $V_{0.5}$ is defined by $g(V_{0.5}) = 0.5$ (at $B = 0$, $T = T_0$).

above Figs. 2.7(g) and 2.7(h) (Sec. 2.3.2) for the quadratic B- and T-dependencies, respectively, and were extracted from Fig. 2.10(a) for the V_{sd}-dependence (see Sec. 2.3.5). They all confirm the behavior Eq. 2.5. For smaller conductances where the presuppositions $B \ll B_*$, $T \ll T_*$, or $V_{sd} \ll V_{sd*}$ are invalid the measured B-, T-, and V_{sd}-dependencies of g deviate from the quadratic behavior by bending upward and tending toward saturation (compare Figs. 2.7(g) and 2.7(h)).

Furthermore, in the sub-open regime $0.5 \lesssim g_{nl}(0,0,0)/G_Q \lesssim 0.9$
(II) all crossover scales depend exponentially on $\widetilde{V}_c$,

$$\widetilde{B}_*, \widetilde{T}_*, \widetilde{V}_{sd*} \propto \exp[-\pi \widetilde{V}_c/\Omega_x] \; . \tag{2.6}$$

This prediction extracted from the SOPT calculations is summarized in Fig. 2.8(a) (same

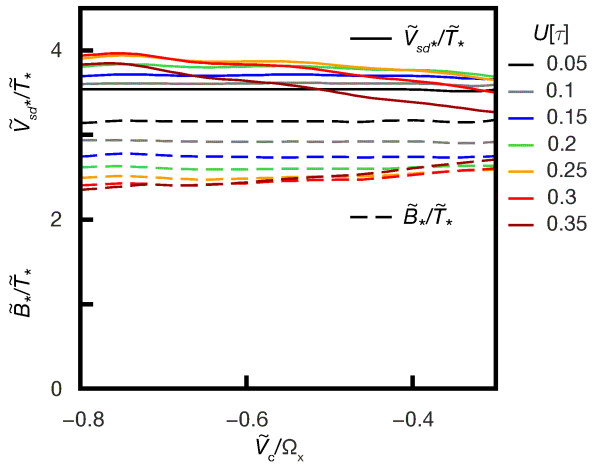

Figure 2.9: Calculated ratios of the low-energy scales $\widetilde{V}_{\mathrm{sd}*}/\widetilde{T}_*$ (solid lines) and $\widetilde{B}_*/\widetilde{T}_*$ (dashed lines) as a function of $\widetilde{V}_{\mathrm{c}}$ in units of the longitudinal QPC constriction curvature Ω_x for various interaction strengths U (using SOPT, "model II", $\Omega_x = 0.04\tau$).

graphs as in Fig. 2.7(d)) which shows $\widetilde{B}_*$ (gray line), $\widetilde{T}_*$ (black line), and $\widetilde{V}_{\mathrm{sd}*}$ (brown line) log-linearly scaled exhibiting adequately linear behavior in the sub-open regime. And finally,
(III) the ratios of the low-energy scales, such as $\widetilde{B}_*/\widetilde{T}_*$ and $\widetilde{V}_{\mathrm{sd}*}/\widetilde{T}_*$, are essentially independent of $\widetilde{V}_{\mathrm{c}}$. The latter is already foreshadowed by Fig. 2.8(a), however, it is revealed quantitatively in Fig. 2.9 where $\widetilde{B}_*/\widetilde{T}_*$ (dashed) and $\widetilde{V}_{\mathrm{sd}*}/\widetilde{T}_*$ (solid lines) are plotted versus $\widetilde{V}_{\mathrm{c}}$ in the sub-open regime for several interaction strengths U, as indicated by the color coding. Accordingly, for lower values of U the ratios are expected to be independent of the exact operation point in the sub-open range, whereas for increased U theory predicts not only a shifting value of the ratios but also an accreting slight dependence on $\widetilde{V}_{\mathrm{c}}$, though the influence remains insignificant for $U \leq 0.35\tau$. The fundamental reason for the latter is that despite both, B and T, shift the effective barrier height for electrons (spin-asymmetrically in case of B, spin-symmetrically for T), T additionally introduces inelastic scattering in contrast to B. Changes in barrier height are described by the Hartree contribution whereas inelastic scattering is ruled by the Fock contribution, with both depending differently on U and on $\widetilde{V}_{\mathrm{c}}$. This leads to the observed induced offsets of the ratios as well as the finite $\widetilde{V}_{\mathrm{c}}$-dependence which sets in.

Both conclusions (II) and (III) are remarkably well confirmed. This is evident from the comparison with Fig. 2.8(b) which summarizes the experimentally determined energy scales $E_* = \mu_{\mathrm{B}} B_*(V_{\mathrm{c}})$ (gray) and $E_* = k_{\mathrm{B}} T_*(V_{\mathrm{c}})$ (black dots) as well as $E_* = eV_{\mathrm{sd}*}$ (brown dots). The experimental $V_{\mathrm{sd}*}$ were extracted from the leading quadratic dependence of the curvature of the measured ZBP (see Sec. 2.3.5) in $g(V_{\mathrm{sd}})$ around $V_{\mathrm{sd}} = 0$. Compared to B_* and T_*, $V_{\mathrm{sd}*}$ exhibits larger error margins owing to a comparatively larger signal-to-noise ratio. Log-linearly scaled, all three experimental scales in the sub-open regime are nearly

straight and have roughly the same slope confirming nearly exponential V_c-dependences at nearly invariant ratios.

In addition, the experimental results Fig. 2.8(b) are also consistent with the predicted behavior in Fig. 2.8(a) that all three scales feature a local minimum, located around $0.7G_Q$ within the sub-open region. The minimum in V_{sd*}, yet appearing broader (at the similar y range) in comparison to the prediction, is directly revealed in Fig. 2.8(b). The decrease of T_* clearly shows a saturating behavior. And, though not covered sufficiently far toward the correspondingly expected minimum, the measured B_* range turns out to be consistent with each low-energy scale exhibiting a minimum, equivalent with the strongest response in g, close to $g = 0.7G_Q$. At these low-energy excitations, the QPC conductance thus behaves similar to that of the Kondo effect in QDs. The deduced behavior Eq. 2.6 for $\widetilde{T}_*$ is also in accord with previous experiments [27] as well as with calculated results derived from a perturbative treatment of interactions using WKB wavefunctions [72].

As it was shown in Fig. 2.4(j) (Sec. 2.2.1), $1/\widetilde{B}_*(\widetilde{V}_c)$ is predicted to have a local maximum in the sub-open regime just before the onset of the exponential dependence of Eqs. 2.6. The shape and the position in $\widetilde{V}_c$ of this peak are roughly equal to that of χ_{tot} (dashed and solid blue lines in Fig. 2.4(j)), except for the fact that the latter has a finite offset due to the nonzero QPC spin susceptibility in the open regime. Thus, in addition to the conclusions (I-III) which were experimentally supported, the model predicts that (IV) $1/\widetilde{B}_*$, which sets the strength of the low-B magnetoconductance response, is about proportional to the spin susceptibility χ_{tot} in the CCR. These above four characteristics (I-IV) of the very similar behavior of the 0.7-anomaly and the QD in the Kondo regime are referred to as "0.7-Kondo similarity" in the text and are explored further in Chapter 3. Moreover, based on the finding Fig. 2.4(j) the particular correlation between $\widetilde{B}_*$ and the spin susceptibility will be elaborated on in more detail in Sec. 3.3.2 below.

2.3.4 The similarities between the 0.7-anomaly and the Kondo effect

This section further explores the 0.7-Kondo similarity, the outstanding finding that many low-energy properties of the 0.7-anomaly (including (I-III) of Sec. 2.3.3) show similarities to those seen in transport through a KQD [27], a quantum dot which hosts an odd number of electrons hence leaving a single electron spin magnetic moment unscreened. Early indications led to the proposal that a QPC harbors a quasi-bound state whose local moment induces the Kondo effect [39–42]. In contrast, the Hove-ridge scenario fully explains the 0.7-anomaly including its various experimentally demonstrated attributes and it neither includes any correlation to nor imposes any necessity for an *actually* emerging Kondo effect. In particular, no indication is found that the 0.7-anomaly is related to a single localized spin (e. g. compare statement (iii) in Sec. 2.2.1). No similarities between the Kondo effect and the 0.7-anomaly are expected at high excitation energies ($\gtrsim \widetilde{B}_*$) where the Kondo effect is governed by the very unscreened local magnetic moment. This is also elaborated on comprehensively in Chapter 3.

However, the low-energy behavior of the 0.7-anomaly in QPCs and the Kondo effect in QDs indeed does show remarkable similarities. According to the model calculations, the fundamental cause is that both exhibit a spin singlet ground state which goes hand in hand with spatially confined spin fluctuations. The difference between both regimes, that for a KQD these fluctuations arise from the screening of the localized spin whereas for a QPC they are generated by the extended structure of the Hove ridge, is decisive only at high-energy scales. On the other hand, the similarity of both regimes, that the spin fluctuations are spatially well localized due to the KQD's localized spin and the QPC's van Hove ridge influence which is restricted to the CCR, governs at low-energy scales only. The spin fluctuations are characterized by the exponentially small energy scales in both regimes which accounts for the similar low-energy transport properties of a QPC and a KQD.

2.3.5 Nonlinear excitations: the zero-bias peak

Finite excitation energies are now investigated in more detail for the case $\widetilde{T}, \widetilde{V}_{\mathrm{sd}} > 0$ where inelastic scattering sets in. First the non-linear differential conductance g_{nl} is analyzed as function of source-drain voltage V_{sd} which is shown in Fig. 2.10(a). $g_{\mathrm{nl}}(V_{\mathrm{sd}})$ is measured at $B = 0$ around $V_{\mathrm{sd}} = 0$ for several constant V_{c} values between pinch-off ($g_{\mathrm{nl}} \to 0$) and the first conductance plateau ($g_{\mathrm{nl}} \to 1$). The corresponding calculated non-linear conductance is equally plotted in Fig. 2.10(b) (for $T = 0$) and the corresponding dependence on $\widetilde{B}$ is exemplarily shown in Figs. 2.10(d-f) for several magnetic fields as indicated. The respective locations of Figs. 2.10(d-f) on the pinch-off curve are indicated by the color-coded dots, matching those in Figs. 2.10(b) and 2.10(c).

Experimentally, g_{nl} shows a ZBP at $V_{\mathrm{sd}} = 0$ [27, 32, 35], as observed in Fig. 2.10(a), where the ZBP appears strongest in the sub-open regime ($0.5 \lesssim g/G_{\mathrm{Q}} \lesssim 0.9$) but continues to be visible even very close to the pinch-off [32]. This characteristic ZBP occurrence is reproduced by the calculated result Fig. 2.10(b), in particular including its appearance at $g < 0.5G_{\mathrm{Q}}$. Furthermore, the ZBP splits with increasing magnetic field on a V_{c}-dependent B-scale which is smallest if g is close to $0.7G_{\mathrm{Q}}$ [27]. It is further qualitatively reproduced by the calculated conductance in Figs. 2.10(d-f) showing the ZBP that splits into two subpeaks if $\widetilde{B} \gtrsim \widetilde{B}_*(\widetilde{V}_{\mathrm{c}})$ depending on the center potential $\widetilde{V}_{\mathrm{c}}$. According to the calculations, in the sub-open regime a ZBP arises even without interactions. However, interactions modify it twofold: a finite $\widetilde{V}_{\mathrm{sd}}$ (i) causes a net charge increase at the barrier resulting in a reduced transmission due to Coulomb repulsion, and (ii) opens up a finite phase space for inelastic backscattering. Both effects strongly depend on the interacting LDOS $\mathcal{A}_j(\omega)$ near μ, which is shown in Figs. 2.10(g) and 2.10(h) versus site j and energy ω, color-coded for two constant gate voltage values $\widetilde{V}_{\mathrm{c}}/\Omega_x = 0$ and -0.75 (red dashed lines which correspond to those in Figs. 2.10(i-n)). Hence (i) and (ii) are strongest when the Hove ridge apex lies around μ (as depicted in Fig. 2.10(g), or in Fig. 2.4(g) of Sec. 2.2.1). However, the Hove ridge intersects μ for $g < 0.5$ too (compare Fig. 2.4(f) in Sec. 2.2.1). This explains the experimental observation that the ZBP is present even close to the

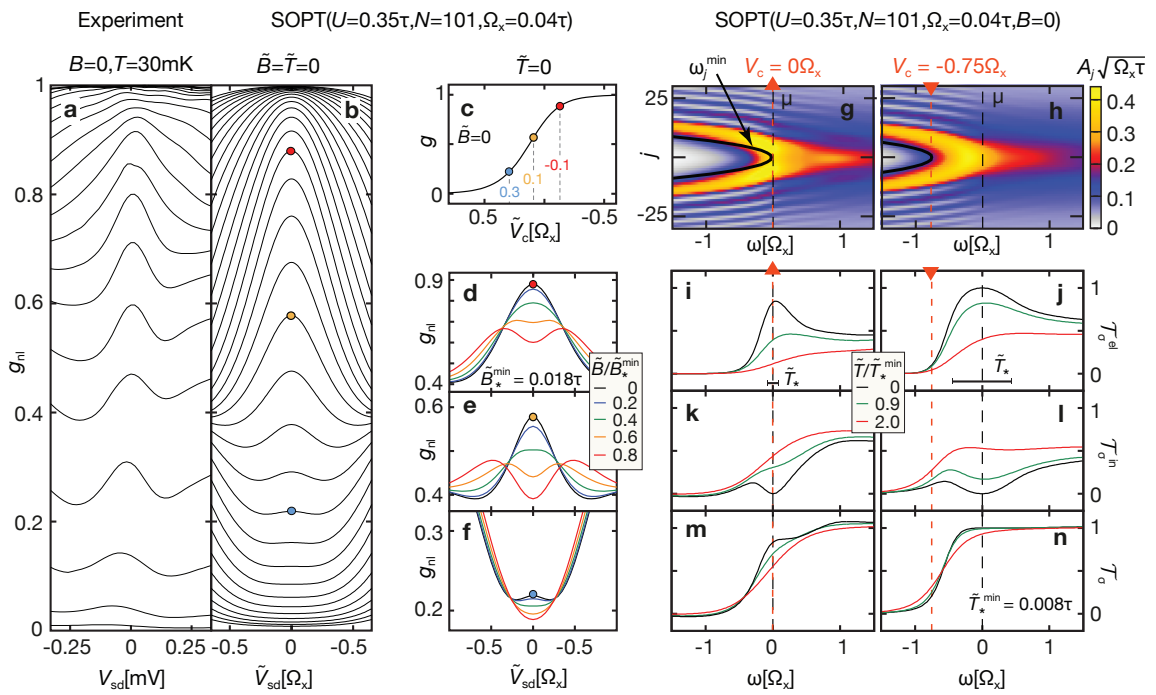

Figure 2.10: (a-f) Zero-bias peak (ZBP): (a) Non-linear conductance $g_{\rm nl} = g(V_{\rm sd})$ as function of source-drain voltage $V_{\rm sd}$, measured at several $V_{\rm c}$ ($T = T_0$, $B = 0$). (b) Calculated $g_{\rm nl}(\widetilde{V}_{\rm sd})$ results for several $\widetilde{V}_{\rm c}$ ($\widetilde{T} = \widetilde{B} = 0$) and (c) linear conductance $g(\widetilde{V}_{\rm c})$ ($\widetilde{B} = \widetilde{T} = 0$). (d-f) $g_{\rm nl}$ for three different $\widetilde{V}_{\rm c}$-values (identical dot colors in (b-f)) and different $\widetilde{B}$ as indicated. The increase of $\widetilde{B}$ causes the ZBP to split into two subpeaks if $\widetilde{B} \gtrsim \widetilde{B}_*$. (g,h) Interacting LDOS $\mathcal{A}_j(\omega)$ (color-coded) shown for two constant gate voltage values, $\widetilde{V}_{\rm c}/\Omega_x = 0$ and -0.75 (red dashed lines). (i-n) Equilibrium transmission probabilities: (i,j) Elastic $\mathcal{T}_\sigma^{\rm el}$, (k,l) inelastic $\mathcal{T}_\sigma^{\rm in}$, and (m,n) total transmission probability $\mathcal{T}_\sigma$ corresponding to (g,h), plotted versus energy ω for different temperatures $\widetilde{T}$ as indicated. The shown calculations were performed using SOPT with the remaining parameter values as indicated.

pinch-off of the QPC [32]. The above-mentioned mechanisms (i) and (ii) apply to the case of raised temperatures too.

The equilibrium total transmission probability $\mathcal{T}_\sigma(\omega) = \mathcal{T}_\sigma^{\rm el}(\omega) + \mathcal{T}_\sigma^{\rm in}(\omega)$ (for $\widetilde{B} = \widetilde{V}_{\rm sd} = 0$) consisting of the elastic and the inelastic contribution can be used to demonstrate the influence of inelastic scattering due to finite $\widetilde{V}_{\rm sd}$ or $\widetilde{T}$. In Figs. 2.10(i-n) the three constituents are shown at two different gate voltages $\widetilde{V}_{\rm c}$ (correspondent to Figs. 2.10(g) and 2.10(h)) and for three different temperatures $\widetilde{T}$. At $\widetilde{T} = 0$ (black curves) $\mathcal{T}_\sigma^{\rm in}(\omega)$ in Figs. 2.10(k) and 2.10(l) vanishes at $\omega = \mu$ due to absent phase space for inelastic scattering. But it is increasing on changing ω away from μ (corresponding to $\widetilde{V}_{\rm sd} \neq 0$) which causes a corresponding decline of the elastic transmission $\mathcal{T}_\sigma^{\rm el}$ in Figs. 2.10(i) and 2.10(j) and thus induces a narrow "low-energy peak" in $\mathcal{T}_\sigma^{\rm el}$ around $\omega = \mu$. Raising the temperature $\widetilde{T}$ increases the probability for inelastic scattering. The corre-

spondingly increased minimum in $\mathcal{T}_\sigma^{\mathrm{in}}(\omega)$ (Figs. 2.10(k) and 2.10(l)) smears out, accompanied by a respective decrease and broadening of the $\mathcal{T}_\sigma^{\mathrm{el}}(\omega)$ peak (Figs. 2.10(i) and 2.10(j)). The result is a temperature-induced reduction in the total transmission $\mathcal{T}_\sigma(\omega)$, shown in Figs. 2.10(m) and 2.10(n), which entails a corresponding decline in the QPC conductance g, as observed in Figs. 2.7(d) and 2.7(f) in Sec. 2.3.2. This reduction of $\mathcal{T}_\sigma(\omega)$ is stronger for $\widetilde{V}_\mathrm{c}/\Omega_x = 0$ (Figs. 2.10(g) and 2.10(m)) than for -0.75 (Figs. 2.10(h) and 2.10(n)) because the probability for electron-hole pair creation during inelastic scattering is largest when the Hove ridge apex lies closest to μ. The fact that the total transmission probability adopts a significant dependence on temperature due to interactions in the sub-open regime is consistent with the experimental fact that the Mott relation, which is based on the assumption of noninteracting electrons, is violated in case of the thermopower near $g \simeq 0.7$ [26].

Hence, the characteristic decline in the QPC conductance around $0.7G_\mathrm{Q}$ at raised T, causing the dominating 0.7-anomaly at intermediate temperatures, is qualitatively explained by the model. Furthermore, both the emergence of the ZBP in the nonlinear transport response regime $V_\mathrm{sd} \neq 0$ and its decrease, observed in the linear response regime, on raised magnetic fields due to the occurring splitting of the ZBP are covered by the model calculations. These constitute further crucial features of the QD-related Kondo effect that are very similarly observed in the QPC around $0.7G_\mathrm{Q}$. They cause the low-energy conductance response to T, V_sd, and B, of which the extracted low-energy scales T_*, $V_{\mathrm{sd}*}$, and B_* were already presented and discussed in Sec. 2.3.3.

2.4 Conclusions

The theoretical evaluation showed that the QPC transmission in the sub-open regime is explained by a governing Hove ridge, a strong local maximum in the LDOS around the QPC constriction center. The combined analysis of the qualitatively well agreeing experimental and calculated results revealed that the 0.7-anomaly and the ZBP can be consistently explained by the amplification of interaction effects of "slow" electrons due to the enhanced LDOS at the locations where the Hove ridge crosses E_F. Interactions cause a reduction of the conductance at finite source-drain voltage $\widetilde{V}_\mathrm{sd}$ due to the raise of the effective local charge in the CCR that induces stronger Coulomb repulsion and due to inelastic backscattering, leading to the actual emergence of a ZBP. Furthermore, the onset of interactions induced by finite temperatures causes the ZBP to become reduced due to additional inelastic backscattering. This not only explains the experimentally verified interlinked appearance of the 0.7-anomaly and the ZBP. It also clarifies how the actual 0.7-shoulder is amplified due to a diminished ZBP at increased temperatures. This illuminates the peculiar dominance of the 0.7-shoulder over the regular QPC conductance pattern at intermediate temperatures of a few kelvins due to remaining considerable inelastic backscattering of "slow" electrons around E_F at the Hove ridge.

The theory showed that the QPC saddle point potential curvature Ω_x determines the peak value, the width as well as the energy of the Hove ridge with respect to the band

bottom of the potential at the QPC constriction center. The latter explains the various experimentally observed locations $0.5 < g/G_\mathrm{Q} < 0.9$ of the 0.7-anomaly, depending on the various constriction-defining gate and heterostructure geometries used which can generate different curvatures at the barrier top. The occurrence of the anomaly at $0.7G_\mathrm{Q}$ was attributed to a parabolic barrier top. The fact that the Hove ridge is governed by Ω_x further implied that all local LDOS-dependent quantities such as the spin susceptibility, the elastic transmission and the inelastic scattering rate gain a dependence on the specific shape of the QPC channel barrier.

The theoretical model predicts that (1) the local spin susceptibility strength peaks in the sub-open regime around $0.7G_\mathrm{Q}$ where the interactions around E_F are strongest. (2) This local maximum in the spin susceptibility is accompanied by the strongest magnetoconductance response of the QPC, which (3) correspondingly induces an asymmetrically decreasing QPC transmission of the spin-resolved QPC channels at increasing magnetic field $\widetilde{B}$. The importance of the local interactions was reflected in the obtained remarkable result that at a large enough interaction strength the calculated conductance $g(\widetilde{V}_\mathrm{c})$ already exhibits a distinct 0.7-anomaly even in the case of vanishing magnetic field and temperature, $\widetilde{B} = \widetilde{T} = 0$. Hence, in combination with the calculated induced asymmetry in the spin-resolved conductances $g_\uparrow$ and $g_\downarrow$ on raising $\widetilde{B}$, the model fully explains the magnetoresponse of the 0.7-anomaly.

Eventually it could be demonstrated experimentally and theoretically that the low-energy excitations on $\Delta B > 0$, $\Delta T > 0$, and $\Delta V_\mathrm{sd} > 0$ of the QPC conductance around the 0.7-anomaly exhibit exceptional similarity to the respective low-energy conductance responses of a QD in the Kondo-effect regime. This termed 0.7-Kondo similarity was expressed in the identical quadratic dependence of the conductance on B/B_*, T/T_*, and $V_\mathrm{sd}/V_{\mathrm{sd}*}$ as well as the similar dependence of the low-energy scales B_*, T_*, and $V_{\mathrm{sd}*}$ on the CCR center potential V_c and their nearly constant mutual ratios. The inferred theoretical prediction that *all three* energy scales exhibit a local minimum at $g \sim 0.7G_\mathrm{Q}$, equivalent with the maximum conductance response strengths, could be partly confirmed experimentally.

The located fundamental cause of this common behavior is that the 0.7-anomaly and the Kondo QD have a spin singlet ground state that shows spatially confined spin fluctuations. However, the fundamental origin in both cases proved to be different. It arises from the screened localized spin in the Kondo QD whereas it is induced by the interaction of "slow" electrons at the spatially confined Hove-ridge-dominated area. Indications were presented showing that this very difference becomes important at higher energy excitations, a point which is elaborated on in the following Chapter 3. As a crucial consequence, it was shown that the 0.7-anomaly and thus the 0.7-Kondo similarity can be explained consistently by the established Hove-ridge scenario which included the explicit constraint of zero spontaneous spin polarization at $B = 0$ and therefore excluded an actually present quasi-bound state that induces the actual Kondo effect.

In the model calculations of the temperature dependent QPC conductance, though, it turned out to be more difficult to reproduce a distinct 0.7-anomaly. A cause could be the restriction of on-site interactions U imposed here.

Chapter 3

Comparison between a quantum point contact and a quantum dot

In Chapter 2 systematic experimental and theoretical investigations of the sensitivity of the QPC conductance on the temperature T, the magnetic field B, as well as the source-drain DC bias voltage V_{sd} were presented. The conductance in the regime of the 0.7-anomaly in the limit of low-energy scales was shown to be similar to that of a QD showing the Kondo effect. The similarity was referred to as "0.7-Kondo similarity".

In this chapter the concept of the 0.7-Kondo similarity is further pursued by studying both experimentally and theoretically the continuous crossover between a QPC and a QD in general, and between the 0.7-anomaly and the Kondo effect in particular, in terms of the geometry of the constituting 2DES potential. The measurements presented in this Chapter 3 were performed with the experimental setup used to obtain the results in Chapter 2 as explained in Sec. 2.1. First characteristics of the sample conductance and properties of the model in the transition regime are discussed in Sec. 3.1 and Sec. 3.2. The crossover is investigated by means of the magnetic field dependence of the conductance in Sec. 3.3.1. Section 3.3.2 and Sec. 3.4 present a theoretical analysis of the low-energy scale $\widetilde{B}_*$ and the the spin susceptibility in the CCR which in particular reflects local spin fluctuations. Beyond that, a more comprehensive analysis of the similarities and differences between the Kondo effect and the 0.7-anomaly is provided in Sec. 3.5.

3.1 Sample layout and characteristics

The smooth reshaping of the potential landscape in the 2DES is achieved experimentally by suitably tuning V_{c} and V_{s} at a fixed $V_{\mathrm{t}} = 0.8$ V such that it crosses over from a saddle point potential defining a QPC (compare Fig. 3.2(b)) to a symmetric local minimum defining a QD (compare Fig. 3.2(c)). The corresponding calculated effective 1D potential barrier shape that mimics this crossover changes from a single barrier (compare Figs. 3.2(d-f)) to a symmetric double barrier (compare Fig. 3.2(g)). The top of the single barrier is parabolic only in a relatively narrow range of gate voltages.

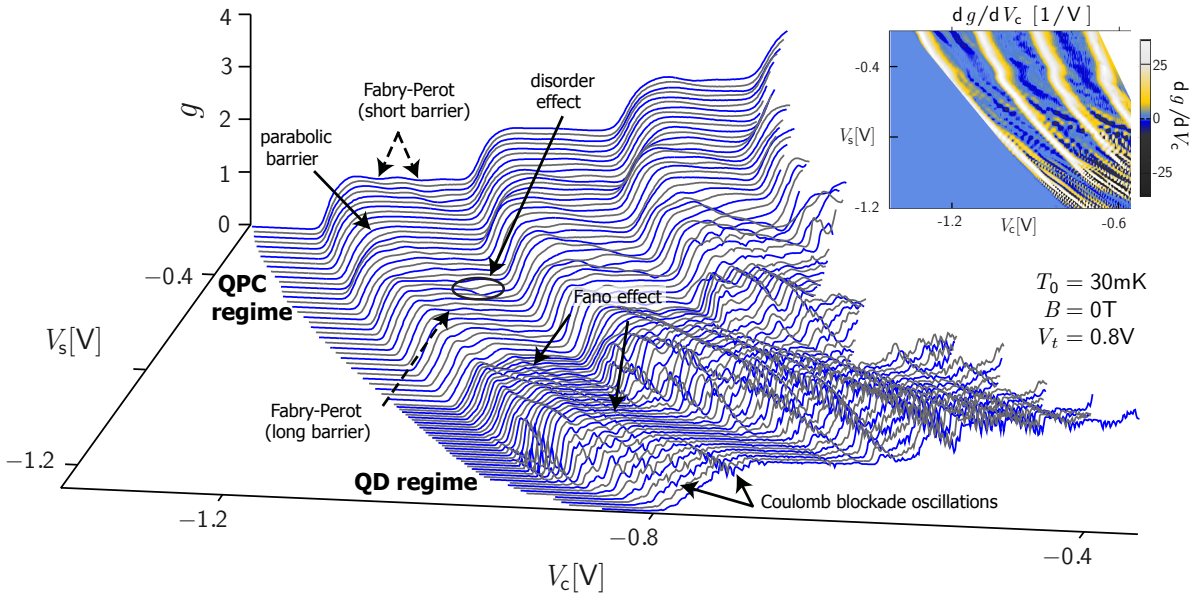

Figure 3.1: Measured geometric crossover between a QD and a QPC: Raw data of the linear-response two-terminal differential conductance g (main panel) which has already been corrected for the finite leads resistance and the corresponding transconductance dg/dV_c (inset, color-coded) as a function of center gate voltage V_c and side gate voltage V_s. The measurements for the detailed analysis of the 0.7-anomaly (see Chapter 2) were performed at the constant side gate voltage $V_s = -0.4$ V because the first plateau of g is observed to be flat there implying a parabolic shape of the barrier top according to the calculations. The features which are marked by the arrows are explained in the text.

Apart from being essential for studying this crossover experimentally, the high tunability of the used layout also turned out to be very useful in dealing with disorder effects. As known from experiments dealing with the statistical evaluation of the conductance of a multitude of QPCs [74], both the local disorder potential and small irregularities in the lithographically defined nanostructure can considerably affect the transport properties of a QPC. The multi-gate device allows to compensate for such effects to some extent because the individually tunable gate voltages dynamically reshape the constriction in real space and real time with high flexibility. It can be monitored in situ experimentally since disorder effects appear as additional features in transport such as small additional resonances on top of the conductance plateaus which respond to the variation of external parameters differently compared to the 0.7-anomaly. Therefore the layout allows tuning the gate voltages such that disorder effects are negligible or absent within the conductance range of interest.

Figure 3.1 shows the raw data, merely corrected for the lead resistance, of the differential conductance g measured as a function of V_c for several V_s at $B = 0$. $g(V_c)$ exhibits pronounced Coulomb blockade oscillations as function of V_c (labeled exemplar-

ily) for lower V_s and near pinch-off. The observed Coulomb blockade confirms that the CCR constitutes a single, well-defined QD with a significant Coulomb charging energy (referred to as QD regime in Fig. 3.1). By increasing V_s the Coulomb blockade oscillations entirely disappear within a broader range around $V_s = -0.9$ V (also depending on the conductance plateau number) due to the declining local electrostatic potentials around the side gates which eventually become smaller than the electrostatic potential around the center gates. In this transition process the localized QD states disappear and a QPC (QPC regime in Fig. 3.1) remains.

The adjacent center and side gates in the experimental configuration exhibit finite electrostatic coupling due to the close proximity. A negative voltage V_s applied to the side gates induces depletion of 2DES electrons also in their surroundings, e. g. below the center gates. The gates coupling is thus reflected in an emerging tilt in the V_c-V_s plane which is observed to be roughly linear. It is traceable in Fig. 3.1 using e. g. the pinch-off voltage V_c where the conductance vanishes, $V_c(g \to 0)$. The stronger residual 2DES depletion below the center gates on reducing V_s produces a similar effect as if V_c would have been lowered simultaneously. In order to retain a given working point on the conductance curve, e. g. the pinch-off, the coupling has to be compensated by a correspondingly more positive V_c.

The broad QD regime displays a combination of both 1D conductance steps and Coulomb blockade oscillations. The latter are most pronounced at the transitions between conductance plateaus ($0 < g < 1$, $1 < g < 2$, ...) and occur in clusters with a rather similar structure. This is best visible in the inset of Fig. 3.1 which shows $\mathrm{d}g/\mathrm{d}V_c$ of the data in the main panel using a color scale. The repeating pattern of Coulomb blockade oscillations suggests the coexistence of a QD and a not yet (fully) occupied 1D subband of the CCR. This feature occurs simultaneously to already fully occupied lower 1D subbands that add QPC behavior at $g > 1$. It causes the charge configurations of the QD to be very similarly repeated at adjacent QPC conductance plateaus when the number of fully occupied 1D subbands changes by one.

As also evident from the inset of Fig. 3.1, when V_s becomes more negative, the width of the Coulomb blockade gaps within each cluster tends to increase which causes each cluster to fan out. The broader Coulomb blockade gaps agree with the expected response to the correspondingly increased barriers of the QD confinement potential which effectively deepens the potential well of the QD further that increases its charging energy. Whenever a Coulomb-oscillation peak enters a conductance plateau at $g = 1, 2, \ldots$ the respective peak maxima of the QD pass into narrow conductance dips, some of which are marked by solid arrows in Fig. 3.1. This emergence is compatible with Fano resonances between the 1D channel of the QPC and localized states of the QD.

In addition, in the QPC regime several shallow oscillations with larger oscillation periods emerge on the conductance plateaus which vary as a function of V_s. They are visible in the inset of Fig. 3.1 and, as an example, some are marked by dashed arrows in the main panel of Fig. 3.1. The oscillations vanish only in a narrow region around $V_s \simeq -0.4$ V (regarding the first QPC plateau) and its oscillation periods tend to be shorter at lower V_s. They can be interpreted as Fabry-Perot-like resonances. According to the performed

calculations, they are expected to emerge if the barrier shape deviates from parabolic. The origin and the behavior of these Fabry-Perot-like resonances is discussed in Sec. 3.2.1 and Sec. 3.2.2 below. Also stronger dips on the conductance plateaus are observed more locally, one of which is indicated by an ellipse in Fig. 3.1. They can be interpreted as either caused by electron reflection arising from spatially confined disorder close to the CCR, maybe in the form of individual defects, or remnants of the Fabry-Perot-like resonances (compare inset of Fig. 3.1).

The tunability of the multi-gate sample has the important advantage that it allows to avoid impacts such as Fabry-Perot-like resonances or disorder-related deviations in g. Indeed, at side gate voltages near $V_\mathrm{s} \simeq -0.4$ V almost no deviations are visible, in particular yielding a completely flat first conductance plateau. As a consequence, $V_\mathrm{s} = -0.4$ V was used for the detailed measurements of the 0.7-anomaly discussed in Chapter 2 and in Sec. 3.3.2 below. An additional option would have been to apply multiple individual voltages to each of the four side gates or the two central gates to overcome possible disorder effects. However, based on the result Fig. 3.1 such corrections were not needed. This furthermore allowed to maintain a high degree of symmetry of the electrostatic potential comprising the CCR. As a consequence, the multi-gate layout facilitated the detailed experimental analysis of the geometry dependence of the conductance of the CCR covering both the QPC and the QD regime.

Fig. 3.1, in particular the inset, reveals another trend worth noticing. By increasing V_s the plateaus in $g(V_\mathrm{c})$ become broader. This broadening indicates that the lateral confinement in the QPC constriction becomes stronger with more positive V_s leading to a larger characteristic energy spacing between the 1D subbands, as expected in the clean QPC case. The stronger lateral confinement also induces a stronger on-site exchange energy U between the electrons. The spacing is also a function of the top gate voltage V_t (see Sec. 2.3.1).

3.2 Modeling the crossover regime

As has been explained in detail in Sec. 2.2, "model I" was used to describe the QPC-QD crossover and to evaluate the degree to which the conductance behavior characteristic of the Kondo effect reaches into the QPC regime. The shape of E_j (compare Eq. 2.1 and Eq. 2.2, Sec. 2.2) in the modeled crossover is foremost governed by two parameters, $\widetilde{V}_\mathrm{c}$ and $\widetilde{V}_\mathrm{s}$, which mimic the effects of the central and side gate voltages in the experiment, respectively. An illustration of the resulting 2DES potential landscape is shown in Figs. 3.2(b) and 3.2(c) (color-coded and vertical axis) for a QPC and a QD, respectively. The gates (gray) in both panels are only shown once in Fig. 3.2(b). Fig. 3.2(a) depicts the sample layout again for comparison. The condition $\widetilde{V}_\mathrm{c} < \widetilde{V}_\mathrm{s}$ defines a QD potential with side barrier height $\widetilde{V}_\mathrm{s}$ (Fig. 3.2(g)) whereas $\widetilde{V}_\mathrm{c} \geq \widetilde{V}_\mathrm{s}$ yields a QPC potential with a single central barrier (Figs. 3.2(d-f)). The barrier top in the QPC regime is consistently chosen to be parabolic in order to eliminate potential resonances on the conductance plateaus

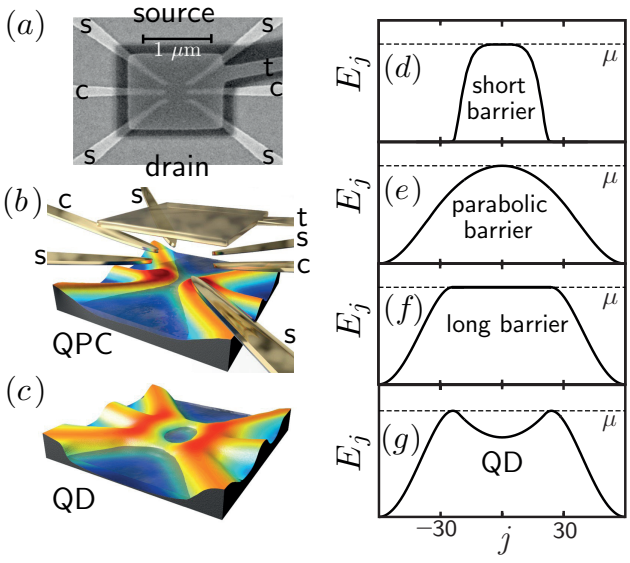

Figure 3.2: (a) Scanning electron micrograph of the gates layout with center gates (c), side gates (s) and top gate (t), shown again (compare Fig. 2.1) for the illustration of panel (b) and (c). (b,c) Artist's depiction of the 2DES potential landscape (vertical axis and color-coded) for a QPC (b) and QD (c) with the gates (gray structures) labeled again. High electrostatic potential is shown red/yellow, regions of lower potential are blue, and the Fermi sea is darkened. (d-g) The modeled effective potential E_j is shown with respect to the chemical potential μ of the reservoirs (dashed line) and plotted versus the site j along the source-drain direction in the CCR. Four different barrier shapes (black lines) are depicted which are generated in the calculations by means of $\widetilde{V}_\mathrm{c}$, $\widetilde{V}_\mathrm{s}$, $\widetilde{V}_\mathrm{t}$, and the spatial distance between the side barrier maxima j_s chosen about half as large in (d) compared to (e-g). The former three mimic the effect of the corresponding gate voltages in the experiment according to the labeling in (a). Shown are (d) a short QPC with a flat potential top ($\widetilde{V}_\mathrm{c} = \widetilde{V}_\mathrm{s}$), (e) a QPC with a parabolic potential top ($\widetilde{V}_\mathrm{c} > \widetilde{V}_\mathrm{s}$), (f) a long QPC with a flat potential top ($\widetilde{V}_\mathrm{c} = \widetilde{V}_\mathrm{s}$), and (g) a QD ($\widetilde{V}_\mathrm{c} < \widetilde{V}_\mathrm{s}$).

(see Sec. 3.2.2). These parabolic barrier tops are parametrized by

$$\widetilde{E}(x) \simeq \widetilde{V}_\mathrm{c} + E_\mathrm{F} - \frac{m\Omega_x^2 x^2}{2\hbar^2} \,, \tag{3.1}$$

defined with respect to the 2DES Fermi energy E_F (linear response regime). $\widetilde{V}_\mathrm{c}$ is the barrier height and the barrier curvature is characterized by the energy scale Ω_x. In this regard, "parabolic" means that the quadratic x-dependence of Eq. 3.1 holds over an energy range of at least Ω_x gauged from the barrier top. Or equivalently, it at least holds up to x-values for which $E(0) - E(x) \lesssim \Omega_x$. In each case where details regarding E_j are not explicitly specified Eq. 2.2 with $j_s = 60$ and $N' = 150$ is used in this chapter.

In the calculations of the transitions between the QPC and the QD, trajectories includ-

ing a wide flat barrier top which remains close to E_F during the crossover were purposely omitted. The reason is that this condition can promote a very low electron density accompanied by strongly increased interactions in the whole elongated region (e. g. if the barrier top lies close below E_F). Such strongly increased interactions are expected to lead to Wigner crystal states and they can induce a splitting of the ZBP into multiple subpeaks [42, 75], conditions very dissimilar from the aimed 0.7-anomaly regime.

3.2.1 Local density of states and transmission

In this section the geometrical properties of "model I" (see Sec. 2.2) are discussed without taking into account interactions. In Fig. 3.3 the noninteracting LDOS $\mathcal{A}_j^0(\omega)$ (color-coded) and the noninteracting transmission probability $\mathcal{T}^0(\omega)$ are evaluated. Both are plotted as a function of energy ω for five different choices of the barrier shape and $\mathcal{A}_j^0(\omega)$ is also spatially resolved. The individual characters of the barriers are labeled for clarity. The selection represents various stages of the geometric crossover between a QPC and a QD. For the parabolic QPC in Fig. 3.3(b) the LDOS has a broad single ridge (yellow, red) which follows the shape of the band bottom $\omega_j^{\min}$ (solid black line). The ridge represents the van Hove ridge which is smeared out within the CCR on an energy scale that is determined by the barrier curvature Ω_x. The corresponding increase of the energy ω from below to above the barrier top yields a change in the transmission $\mathcal{T}^0(\omega)$ from 0 to 1 in the form of a smooth single step of width $\sim \Omega_x$ and centered at $\omega \sim \widetilde{V}_c$. By raising the side gate potential using $\widetilde{V}_s$ at a fixed $\widetilde{V}_c$, the overall barrier top can eventually become flat, as shown in Fig. 3.3(c), accompanied by a narrowing ridge in the LDOS (the height of the LDOS maximum right above the barrier increases accordingly). This barrier which is now flatter than the parabolic shape causes added oscillations in the noninteracting transmission $\mathcal{T}^0(\omega)$ in Fig. 3.3(c) around the onset of the plateau at $\mathcal{T}^0(\omega) = 1$. These oscillations are interpreted as Fabry-Perot-like resonances and discussed systematically in Sec. 3.2.2.

The case of smaller $\widetilde{V}_s$ (larger V_s in the experiments) creates a short flat barrier as shown in Fig. 3.3(a). The short flat barrier is calculated using a short barrier with a quartic top (see Eq. 3.2 below, with $n = 4$). The transmission in Fig. 3.3(a) also shows oscillations around $\mathcal{T}^0(\omega) = 1$ though they exhibit a distinctly larger period as compared to Fig. 3.3(c). This finding fits in with the experimental results (see Sec. 3.1): the resonances in the measured conductance $g(V_c)$ were observed in the whole QPC regime covering a flat barrier close to the QD regime as well as a shorter barrier for larger V_s with an oscillation period that tended to be longer for the shorter barriers.

When the central gate parameter $\widetilde{V}_c$ is lowered below $\widetilde{V}_s$ the QD regime is entered in Figs. 3.3(d) and 3.3(e). The LDOS now exhibits a single-particle spectrum, bound states which are narrow in energy and spatially localized inside the QD potential. Each bound state generates an additional sharp resonance in the noninteracting transmission. However, the onset of the plateau at $\mathcal{T}^0(\omega) = 1$ and therefore full transmission is still determined by the broad LDOS ridges right above the left and right barrier top. Both ridges

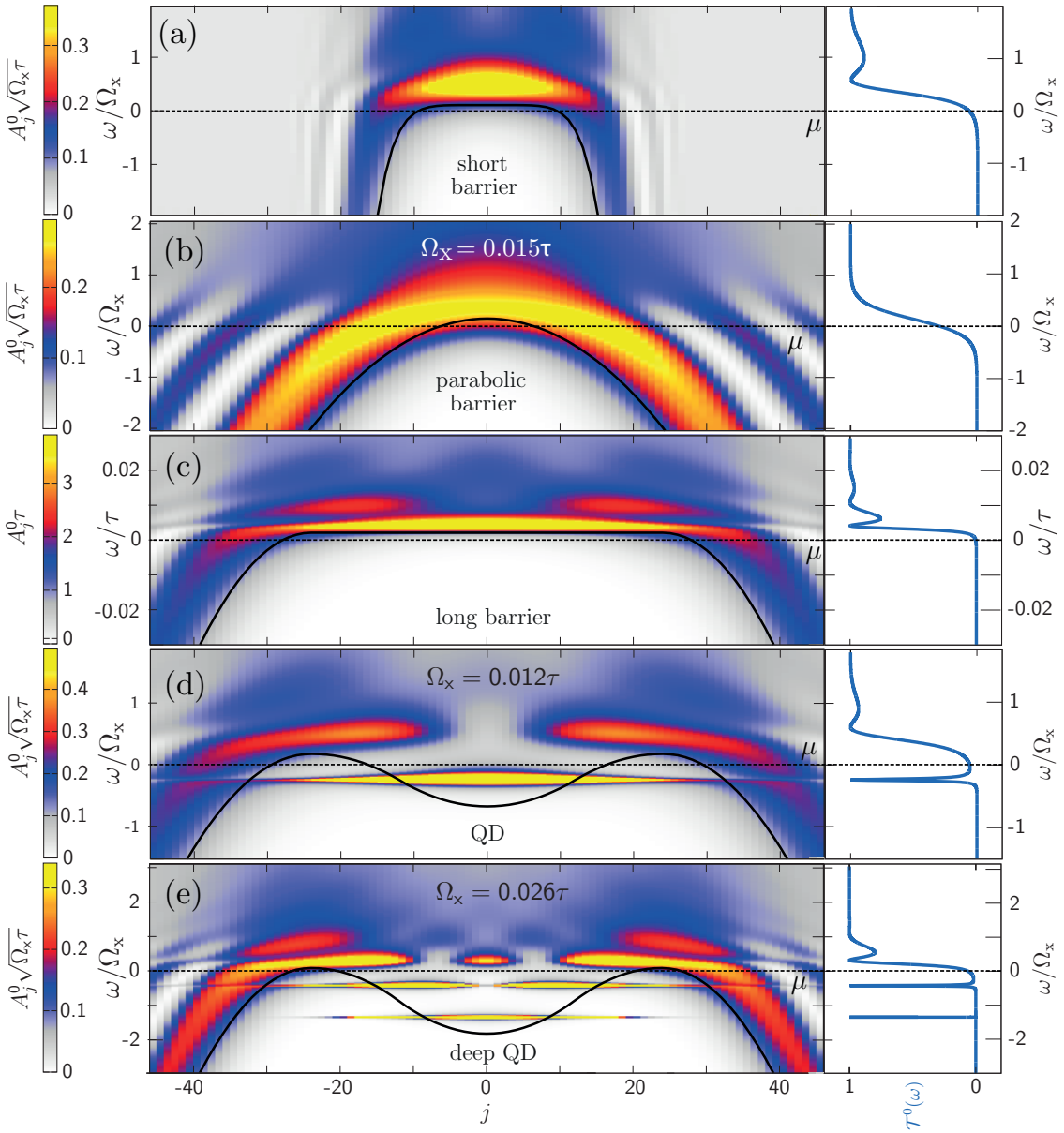

Figure 3.3: Left: Calculated noninteracting local density of states $\mathcal{A}_j^0(\omega)$ (color-coded) as a function of the site j and the energy ω. Right: Calculated noninteracting transmission $\mathcal{T}^0(\omega)$ versus energy ω ($\widetilde{B} = 0$). The five panels show five potential barrier shapes which can develop during the QPC-QD crossover: (a) a QPC with a short flat barrier, (b) a QPC with a parabolic barrier, (c) a QPC with a long flat barrier, (d) a shallow QD with just one discrete orbital state, and (e) a deeper QD containing two discrete states.

are remnants of the van Hove ridge of the QPC regime in Figs. 3.3(a-c), as evident from the transmission curves in panels (c) and (e), which exhibit very similar Fabry-Perot-like resonances near $\mathcal{T}^0(\omega) = 1$. The situation in Figs. 3.3(d) and 3.3(e) of sharp resonances

occurring simultaneously with a single conductance step definitely indicates the coexistence of a QD and a QPC. These coexisting features which occur toward and within the QD regime are in fact observed in the experiments (see Sec. 3.1 and Sec. 3.3.1).

The LDOS shows interference fringes in the outer flanks of the CCR which depend on the semiclassical velocity $v_j(\omega)$ of an electron with kinetic energy $\omega - \omega_j^{\min}$ at site j. At a constant energy ω, both the oscillation period of the fringes and the LDOS at a given interference fringe maximum as a function of j scale as $1/v_j$. The spatial dependence causes the different behavior of the LDOS at the flanks of the potential of the CCR in e. g. Figs. 3.3(a) and 3.3(b): For the short, flat barrier with steep flanks in Fig. 3.3(a), the velocity v_j of electrons with $\omega \simeq \mu$ increases rapidly for increasing distance $|j|$ from the barrier center. As a consequence, for increasing $|j|$ the local maxima and the oscillation period of the LDOS at $\omega \simeq \mu$ decrease rapidly too. In contrast, for the parabolic barrier in Fig. 3.3(b) the potential decreases much more slowly with increasing $|j|$. The corresponding slower increase of v_j at $\omega \simeq \mu$ for increasing $|j|$ generates a weaker decline of the local maxima and the oscillation period of the LDOS at $\omega \simeq \mu$.

As a result, various details of the calculated conductance in the mixed QPC-QD regime are in accordance with the experimental observations. It substantiates that the theory is able to model of the transition between the QPC and the QD regime.

3.2.2 Fabry-Perot resonances

In this section, the Fabry-Perot-type conductance resonances are discussed which occur in the form of wiggles, or decaying oscillations. Such oscillations were observed in the measured conducance (Sec. 3.1) as well as in the calculated results in terms of the noninteracting transmission $\mathcal{T}^0(\omega)$ in the QPC-QD-crossover regime (Sec. 3.2.1).

$\mathcal{T}^0(\omega)$ shows Fabry-Perot-like resonances if the very top of the QPC barrier has a flatter-than-parabolic shape. The behavior of the resonances is summarized in Fig. 3.4 showing $\mathcal{T}^0(\omega)$ (main panels) and the respective longitudinal barriers as a function of the site x around the barrier center (insets). $\mathcal{T}^0(\omega)$ is plotted for a sequence of barrier shapes with barrier tops given by

$$\widetilde{E}(x) = \widetilde{V}_{\mathrm{c}} + E_{\mathrm{F}} - \Omega_x \left(\frac{|x|}{l_x} \right)^n , \quad l_x = \sqrt{\frac{2\hbar^2}{m\Omega_x}} , \tag{3.2}$$

where l_x is a x-independent characteristic length scale depending on the electron mass m. For a truly parabolic barrier top ($n = 2$, black lines in Fig. 3.4), $\mathcal{T}^0(\omega)$ is a smooth function of energy given by [17]

$$\mathcal{T}^0(\omega) = [e^{2\pi(\widetilde{V}_{\mathrm{c}} - \omega)/\Omega_x} + 1]^{-1} . \tag{3.3}$$

The transmission for QPC-barrier tops with $n \geq 2$ are shown in Fig. 3.4(a). In the regime of the open QPC channel $\mathcal{T}^0(\omega) \simeq 1$ resonances emerge that become more pronounced for flatter barrier tops. Such resonances in the form of deviations from the completely

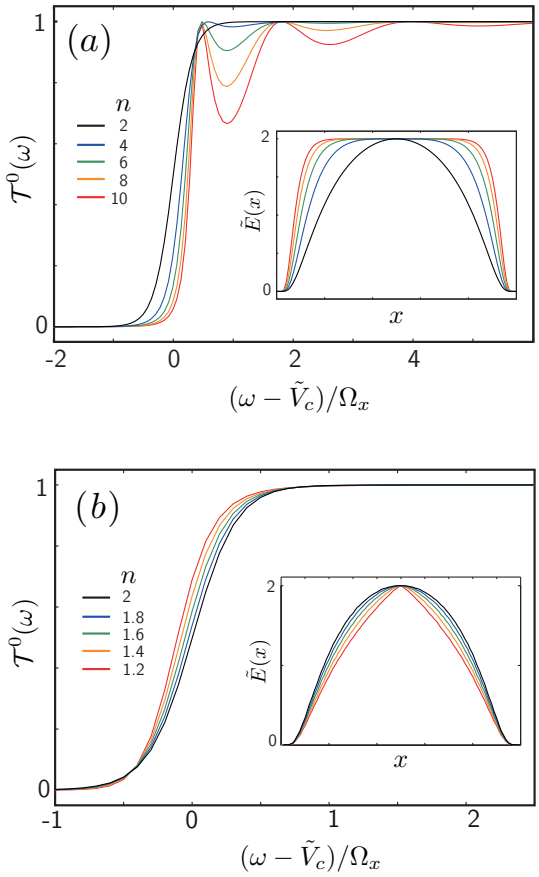

Figure 3.4: Calculated noninteracting transmission $T^0(\omega)$ for several barrier shapes in longitudinal direction, as indicated with matching colors in the insets. The different barriers are governed by $|x|^n$ at the barrier top according to Eq. 3.2, as shown by the color tables. (a) Flatter-than-parabolic barriers with $n \geq 2$ which arise during the QPC-KQD crossover. (b) Sharper-than-parabolic barriers with $n \leq 2$ which are shown for comparison.

flat conductance plateau regularly emerge in the measured conductance of longer QPCs [42, 75]. Fig. 3.4(a) thus indicates that their combined origin can be attributed to the particular flatness of the generated QPC barrier. Hence the measured QPC-QD transition (compare Sec. 3.1) most likely covers the regime of a long QPC with a barrier top flatter than parabolic. Furthermore, in combination with the results of Sec. 3.2.1, it suggest that a short QPC with steep flanks can also be viewed as a flatter-than-parabolic barrier which shows Fabry-Perot-like resonances.

Examples of barrier tops with $n \leq 2$ in Eq. 3.2 are shown for comparison in Fig. 3.4(b). In those cases the transmission increases monotonically without showing any resonant behavior. As depicted in the inset, decreasing n tends to flatten the potential flanks spatially which generates a narrower transition toward the first conductance plateau at $\mathcal{T}^0(\omega) \simeq 1$.

3.2.3 Adaption of the theoretical model

For the fRG method (Sec. 2.2) used for the evaluation of the effect of interactions on the properties of the CCR in the transition regime between a QPC and a QD adaptions were required. First the calculations were restricted to $\widetilde{T} = 0$. Despite the restriction, the calculated conductance reproduces the measurements at low temperatures of $T \sim 30$ mK in each case very well. Also, as already explained in Sec. 2.2, the fRG approach in the case of the QPC-QD crossover is based on *a priori* absent spontaneous symmetry breaking, $m_j(\widetilde{B} = 0) = 0$, as well as on the coupled ladder approximation used in the form of the static fRG in some cases. The results for the zero-temperature conductance obtained via this static simplification are qualitatively the same as those obtained by a "dynamic" calculation that retains the frequency dependence [76].

Because the effective expansion parameter for static fRG is $U_j \cdot \mathcal{A}_j^0(0)$, the fRG equations which describe vertex flow do not converge for geometries that cause $\mathcal{A}_j^0(\omega)$ to be sharply peaked near the chemical potential $\mu = 0$. This difficulty arises in the regime of a shallow few-electron QD with wide barriers near μ. As a consequence, the vertex flow was neglected for calculations that include this regime (referred to as "without vertex flow"). Vertex flow was included, however, for all remaining fRG results shown in this chapter. It is further essential for obtaining the 0.7-shoulder in the QPC conductance even at $\widetilde{B} = \widetilde{T} = 0$.

3.3 Comparison between theory and experiment: magnetoconductance

In this section, the low-temperature conductance for the geometric crossover between a QPC and a QD is compared with the corresponding calculated zero-temperature results at various magnetic fields. Further a discussion of the similar magnetoconductance features in the KQD and QPC regimes is given and the characteristic low-energy scale $\widetilde{B}_*$ is examined.

3.3.1 Transition between a quantum point contact and a quantum dot

In Fig. 3.5 the experimental data is compared with the fRG results for the crossover between a QPC and a QD at three different magnetic fields including the data at $B = 0$ which was already shown in Fig. 3.1. Figures 3.5(d-f) present the experimental data for the low-temperature ($T_0 \simeq 30$ mK) linear conductance $g(V_\mathrm{c}, V_\mathrm{s})$ for three different magnetic fields. Each dataset is shown around the first conductance plateau and plotted as a function of V_s and $\Delta V_\mathrm{c} = V_\mathrm{c} - V_\mathrm{c}^\mathrm{pinch}$ being V_c defined with respect to a V_s-dependent reference value $V_\mathrm{c}^\mathrm{pinch}(V_\mathrm{s})$ compensating for the coupling of the side- and center-gates actions. $V_\mathrm{c}^\mathrm{pinch}(V_\mathrm{s})$ is chosen so that it satisfies $g(V_\mathrm{c}^\mathrm{pinch}) = 0.5$ in the QPC regime ($V_\mathrm{s} \gtrsim -1$ V)

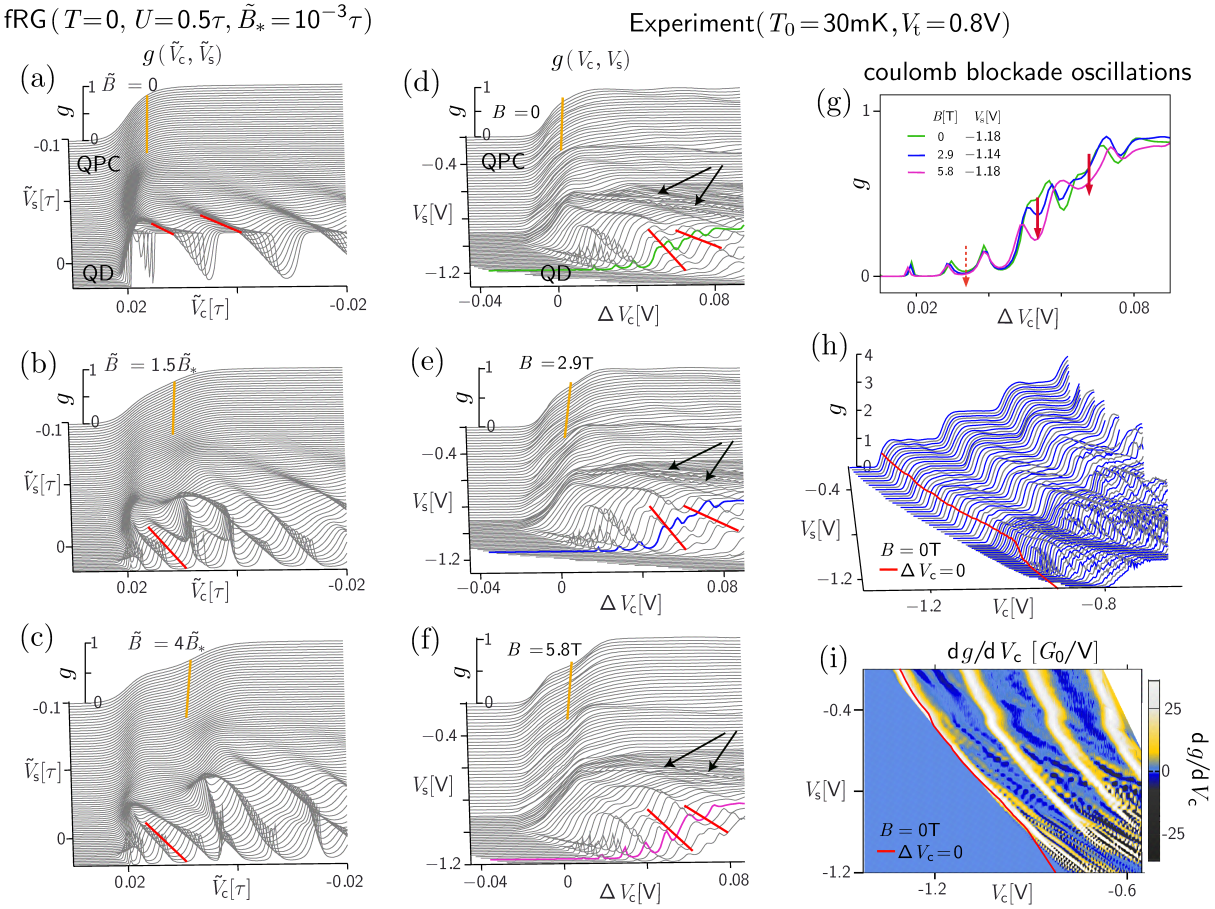

Figure 3.5: QPC-QD transition: (a-c) Conductance $g(\widetilde{V}_c, \widetilde{V}_s)$ (fRG "without vertex flow", $T = 0$) in the range $0 \leq g \leq 1$, calculated at three different magnetic fields $\widetilde{B}$ as indicated, and plotted as function of the center potential $\widetilde{V}_c$ for a large number of different $\widetilde{V}_s$. (d-f) Analogous to (a-c), but showing experimental data for the conductance $g(V_c, V_s)$ repeatedly measured as a function of V_c, each time for a different constant V_s, for three magnetic fields B as indicated ($T = 30$ mK). $g(V_c, V_s)$ is plotted as function of the relative center gate voltage $\Delta V_c = V_c - V_c^{\text{pinch}}$ with respect to a V_s-dependent reference value $V_c^{\text{pinch}}(V_s)$. The choice of V_c^{pinch} is indicated by the red line in panels (h) and (i), respectively. Orange lines in (a-f) mark the 0.7-anomaly, red lines mark the locations of Kondo valleys, black arrows in (d-f) mark Fano resonances. (g) Combined plot of the three colored pinch-off curves from (d-f), demonstrating the suppression of the Kondo-enhanced conductance in the Kondo valleys (solid arrows) on raised B. The dashed arrow indicates the anticipated adjacent Kondo valley. (h) Raw data set $g(V_c, V_s)$ at $B = 0$ (corresponding to (d)), and (i) its derivative dg/dV_c (color-coded). (h) and (i) are shown again (compare Fig. 3.1) for referencing $V_c^{\text{pinch}}(V_s)$.

and that it shifts linearly with V_s in the QD regime, with a slope such that the line does not cross any QD resonance. V_c^{pinch} is marked by the red line in Figs. 3.5(h) and 3.5(i), respectively (showing the raw data of Fig. 3.5(d)). Figs. 3.5(a-c) show the equivalent re-

sults from the model calculations at $T = 0$, plotted as a function of $\widetilde{V}_c$ and $\widetilde{V}_s$ which act independently of each other.

The covered V_s range in Figs. 3.5(d-f) clearly contains both the QPC regime showing a single conductance step toward $g = 1$ and a forming QD as evident from gradually emerging well separated Coulomb blockage oscillations toward more negative V_s. The regimes are labeled in Fig. 3.5(d) (as well as in Fig. 3.5(a)). Furthermore, the measured QPC-QD transitions are observed to be smooth for all B. Both the single contained regimes and the smooth transitions between them are well reproduced by the calculations Figs. 3.5(a-c) which also consistently exhibit the main features of the measured results. In the QPC regime which is determined by the single potential barrier, both measurements and calculations display the typical magnetic field dependence of the 0.7-anomaly which is marked by orange lines in Figs. 3.5(a-f): The transition from a weak shoulder around $g \simeq 0.7G_Q$ for $B = 0$ to an emerging plateau $g \to 0.5G_Q$ for increasing magnetic field.

In the QD regime both the measurements and the calculations also exhibit features indicative of the Kondo effect. In a limited V_c ($\widetilde{V}_c$) range every second Coulomb-blockaded conductance gap is increased. That displays the Kondo-typic raise for charge states with an odd number of electrons in the QD. In such Kondo valleys, highlighted in Figs. 3.5(a-f) by red lines, the Kondo-enhanced conductance shows the expected strong suppression with increasing magnetic field. Figure 3.5(g) illustrates this for the experimental data by summarizing the three colored pinch-off curves from Figs. 3.5(d-f) for three comparable values of V_s. These three values of V_s are specified in Fig. 3.5(g) and are not all the same. The cause is attributed to a change in the local electrostatic environment of the CCR between the respective measurement runs, most likely due to a random charge fluctuation, which temporarily shifted the potential landscape by a small but non-negligible amount (disregarding the slight shift, the full dataset Fig. 3.5(e) fits in consistently). Two Kondo valleys are marked by the solid red arrows in Fig. 3.5(g). The dashed red arrow in Fig. 3.5(g) marks an expected third Kondo valley toward more negative V_c where the Kondo effect is insignificant since the coupling to the leads has declined considerably, inducing $T_K \ll T$. The strongly decoupled QD center is also expressed by the decreased conductance peak values in that regime due to the CCR being almost pinched-off.

As a result, the measured and calculated conductances prove to cover both the 0.7-anomaly in the QPC and the Kondo effect in the QD regime. However, the QPC and the QD regime persist next to each other and adjoin around an unchanged $V_s \sim -0.9$ V ($\widetilde{V}_s \sim -0.03\tau$) at all B ($\widetilde{B}$). In particular, no indications are found for a common behavior or a mixing of the 0.7-anomaly of the QPC and the raised Kondo conductance in the KQD regime.

3.3.2 Connection to the spin susceptibility

First the measured and the calculated magnetoconductance are compared at two fixed side gate potentials of which one forms a KQD and the other forms a QPC in the CCR. For the QPC, the experimental data at $V_s = -0.4$ V is used in order to have a smooth plateau at $g = 1$ without any Fabry-Perot resonances (compare Sec. 3.1) while for the calculations

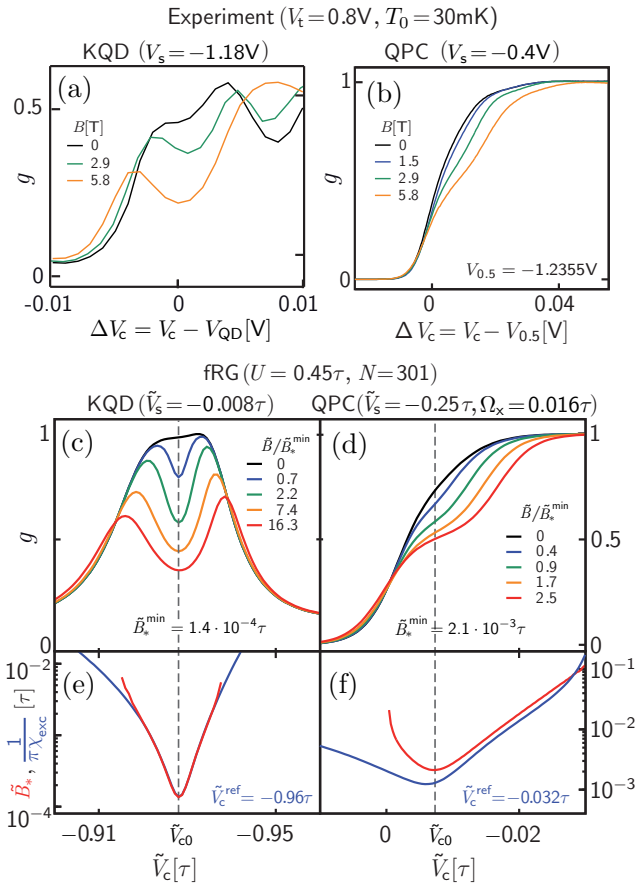

Figure 3.6: Comparison of the measured and calculated magnetoconductance g/G_Q of the KQD and the 0.7-anomaly. (a,b) Experimental conductance curves for a KQD and a QPC, given by two different V_s-values as indicated, at various magnetic fields B, plotted versus the offset center gate voltage V_c with respect to the Kondo valley center V_{QD} and the middle of the first conductance step $V_{0.5}$ ($T = T_0 = 30$ mK). (a) is taken from Fig. 3.5, (b) corresponds to Fig. 2.7(e). (c,d) fRG calculation results plotted analogously to (a,b) for the conductance $g(\widetilde{V}_c, \widetilde{B})$ at fixed $\widetilde{V}_s$ of a (deep) KQD containing $n^{KQD} = 49$ electrons and for the lowest QPC subband. (e,f) Respective calculated low-energy scales $\widetilde{B}_*(\widetilde{V}_c)$ (red lines, using Eq. 2.5) and inverse excess spin susceptibilities $1/(\pi\chi_{exc}(\widetilde{V}_c))$ (blue lines, using Eq. 3.6) for the KQD and the QPC, each plotted on a joint log-linear scale. In both cases, the gate voltage $\widetilde{V}_{c0}$ where $\widetilde{B}_*$ is minimal is drawn in (dashed line).

the case of the truly parabolic barrier top is considered. Figures 3.6(a) and 3.6(b) show the corresponding measured conductance of a KQD and a QPC, respectively, at several magnetic fields $0 \leq B \leq 5.8$ T. This characteristic tuning-gate voltage and magnetic field dependencies in both regimes are qualitatively reproduced by the associated fRG results Figs. 3.6(c) and 3.6(d). The conductance of the KQD shows a well-pronounced Kondo plateau for zero magnetic field that is suppressed to form a dip if B is raised, as expected

theoretically [68, 77] and experimentally [4]. The conductance step of the QPC exhibits a 0.7-shoulder at $B = 0$, which shows the well-known suppression into a double step on increasing B [24, 27, 29] whose width is proportional to B. Note that even for $B = 0$ the 0.7-shoulder in Fig. 3.6(d) is much more pronounced than in Fig. 3.5(a) above. The reason is that the fRG approach without vertex flow used for the latter underestimates the effects of interactions compared to fRG including vertex flow, used for Figs. 3.6(c) and 3.6(d).

Hence the established model (Sec. 2.2) very well reproduces the characteristic V_c-dependence of the magnetoconductance of a KQD too, in addition to the confirmed QPC characteristics including the 0.7-anomaly regime. Based on this compliance, the magnetic low-energy scale $\widetilde{B}_*$ and the spin susceptibility strength χ of the 0.7-anomaly and the KQD regime are inferred from the model calculations and compared with each other below.

As shown in Sec. 2.3.3 (see Eq. 2.5), the low-$\widetilde{B}$ expansion of the magnetoconductance of a QPC in the 0.7-regime is characterized by a $\widetilde{V}_c$-dependent energy scale, $\widetilde{B}_*$: The smaller $\widetilde{B}_*$ the stronger is the magnetoconductance response. The same holds for the KQD for which this scale corresponds to the Kondo temperature, $\widetilde{B}_*^{\mathrm{KQD}} = k_B T_K$ [78, 79]. The $\widetilde{B}^2$-dependence of Eq. 2.5 was observed experimentally for a QD [47, 80] whereas for a QPC it was confirmed by our experiments (Sec. 2.3.3). $\widetilde{B}_*(\widetilde{V}_c)$ was extracted from the calculated results Figs. 3.6(c) and 3.6(d) and is shown in Figs. 3.6(e) and 3.6(f) (red lines). It features a pronounced minimum, $\widetilde{B}_*^{\mathrm{min}}$, for both KQD and QPC at $\widetilde{V}_c = \widetilde{V}_{c0}$ (dashed lines in Figs. 3.6(e) and 3.6(f)) in the vicinity of which it is given as

$$\widetilde{B}_*^{\mathrm{KQD}} \propto \exp\left[c_1(\widetilde{V}_{c0} - \widetilde{V}_c)^2\right] , \tag{3.4a}$$

$$\widetilde{B}_*^{\mathrm{QPC}} \propto \exp\left[c_2(\widetilde{V}_{c0} - \widetilde{V}_c)/\Omega_x\right] , \quad (\widetilde{V}_c < \widetilde{V}_{c0}) , \tag{3.4b}$$

for the KQD and the QPC, respectively, where c_1 and c_2 are $\widetilde{V}_c$-independent constants. The $\widetilde{B}_*(\widetilde{V}_c)$ dependence in Eq. 3.4a conforms with the theoretical prediction [81] as well as with the experimental observations [46, 47] for the Kondo temperature of a KQD. Thus the model correctly replicates the full magnetoconductance of the KQD including this characteristic exponential dependence of B_*. On the other hand, Eq. 3.4b for a QPC is confirmed theoretically and experimentally in Sec. 2.3.3.

For the KQD, the scale $\widetilde{B}_*$ is inversely proportional to its excess contribution to the static spin susceptibility χ_{exc} at $T = 0$ [78],

$$1/\widetilde{B}_*^{\mathrm{KQD}} = \pi \chi_{\mathrm{exc}} , \tag{3.5}$$

which relates the strength of the magnetoconductance response to that of the local spin fluctuations. The excess spin susceptibility χ_{exc} is defined as the relative susceptibility averaged over the CCR

$$\chi_{\mathrm{exc}}(\widetilde{V}_c) = \sum_{j \in \mathrm{CCR}} \left[\chi_j(\widetilde{V}_c) - \chi_j(\widetilde{V}_c^{\mathrm{ref}})\right] , \tag{3.6}$$

where χ_j is the local spin susceptibility for $\widetilde{B} = 0$ at the site j. $\widetilde{V}_c^{\mathrm{ref}}$ is a reference potential where the magnetoconductance is very small. For a QPC it was chosen at the

first conductance plateau ($g > 0.999$) and for the KQD it was chosen in the adjacent Coulomb-blockade valley of the evenly charged QD (EQD). For the KQD, $\widetilde{B}_*^{\mathrm{KQD}}$ and $1/(\pi\chi_{\mathrm{exc}})$ were extracted from the calculated magnetoconductance Fig. 3.6(c) and are logarithmically plotted in Fig. 3.6(e) in red and blue, respectively (the actual $\widetilde{V}_{\mathrm{c}}^{\mathrm{ref}}$ is indicated). Both very well satisfy the relation Eq. 3.5 for small $|\widetilde{V}_{\mathrm{c}} - \widetilde{V}_{\mathrm{c0}}|$ and thus are consistent with the expectation. For the QPC around the 0.7-anomaly, χ_{exc} and $\widetilde{B}_*$ extracted from Fig. 3.6(d) reveal that the related result

$$1/\widetilde{B}_*^{\mathrm{QPC}} \propto \chi_{\mathrm{exc}} \,, \tag{3.7}$$

is remarkably closely fulfilled, as shown in Fig. 3.6(f) which is plotted analogously to (e). Although the inverse character of Eq. 3.7 was generally observed to be present in the calculations for the QPC around $\widetilde{V}_{\mathrm{c0}}$, for Fig. 3.6(f) $\widetilde{V}_{\mathrm{c}}^{\mathrm{ref}}$ was actually used as a fit parameter producing the shown validity of Eq. 3.7 over an even larger range of gate voltages $\widetilde{V}_{\mathrm{c}} < \widetilde{V}_{\mathrm{c0}}$. The fact that Eq. 3.7 expresses the behavior of a QPC so well is actually remarkable. It constitutes a so far experimentally unevaluated prediction in the framework of the 0.7-Kondo similarity: The fundamental, nontrivial connection between the magnetoconductance and the local spin fluctuations of the KQD is expected to be similarly fulfilled in the 0.7-anomaly regime of a QPC.

The 0.7-Kondo similarity only applies to physical quantities related to low-energy excitations relative to the ground state such as the magnetoconductance or the spin susceptibility. The 0.7-Kondo similarity is not a feature of pure ground state properties such as the actual conductance as evident from the comparison of Figs. 3.6(c) and 3.6(d) at $\widetilde{V}_{\mathrm{c}} \simeq \widetilde{V}_{\mathrm{c0}}$ (dashed lines in Figs. 3.6(c-f)) where $\widetilde{B}_* \simeq \widetilde{B}_*^{\mathrm{min}}$ implying the strongest magnetoconductance response to low-energy excitations. At zero magnetic field the KQD conductance at $\widetilde{B}_*^{\mathrm{min}}$ reaches the peak value of $g^{\mathrm{KQD}} \simeq 1G_{\mathrm{Q}}$ in contrast to the corresponding peak conductance $g^{\mathrm{QPC}} \simeq 0.7G_{\mathrm{Q}}$ of a QPC. The reason for this difference is the Kondo resonance of the KQD which can induce full QD transmission mediated by the Kondo effect. The Kondo resonance reaches the unitary limit $g^{\mathrm{KQD}}/G_{\mathrm{Q}} = 1$ in the center of the Kondo valley for sufficiently low temperatures and well balanced coupling (see Sec. 1.3). In contrast, the model calculations of the 0.7-anomaly reveal indications which explicitly exclude an actually emerging localized state (see Sec. 3.4 and Sec. 3.5) and the absolute QPC conductance is determined by the induced modified elastic transmission and inelastic backscattering due to the Hove-ridge-induced interactions. $g_{0,0}^{\mathrm{QPC}}$ is governed solely by the resulting effective height of the QPC barrier which shows a slight non-linearity when the van Hove ridge passes through the chemical potential, causing $g_{0,0}(\widetilde{V}_{\mathrm{c}})$ to show a slight shoulder around $g_{0,0}/G_{\mathrm{Q}} \simeq 0.7$ depending on the actual QPC barrier shape. The maximum value $g_{0,0}^{\mathrm{QPC}} = 1$ is reached merely if the QPC barrier height has become so low that the lowest 1D channel is actually opened.

In addition, the fact that our model well reproduces also the actual Kondo-regime further substantiates the findings derived from the comparison with the calculated results in Chapter 2.

3.4 Theory prediction for the local spin susceptibility

Based on the results of Sec. 3.3 in this section the 0.7-Kondo similarity is further investigated theoretically. The local density n_j, the local magnetization m_j, and the local spin susceptibility χ_j of the 2DES electrons are calculated as a function of site j at $T = 0$ and analyzed in detail focusing on the relation between the magnetoconductance and the *local* spin susceptibility in the QPC-QD-crossover regime.

The spatial dependencies of three different potential configurations, with respect to the uniform chemical potential of the leads $\mu = 0$, are shown in Figs. 3.7(a) and 3.7(b) for a KQD and a parabolic QPC, respectively. The marking colored symbols label both the regimes (symbol shapes) and the actual potential in each case (symbol colors). They indicate the corresponding occurring barrier shapes in all remaining panels Figs. 3.7(c-m). Figs. 3.7(c-f) compare the spatial dependence of n_j and m_j of the KQD and the QPC near pinch-off for equidistant $\widetilde{B} = 0$ (blue) to $\widetilde{B} = 10\widetilde{B}_*$ (red curve). The densities n_j in Figs. 3.7(c) and 3.7(d) rise toward the filling of the non-interacting leads at the edges of the CCR (at large $|j|$). The KQD is shown for $n^{\mathrm{KQD}} = 9$. n^{KQD} refers to n_j^{KQD} summed up between the two distinct minima in Fig. 3.7(c). The charge near the center of the KQD is discrete and localized. On the other hand, the QPC shows the local density n_j^{QPC} in Fig. 3.7(d) which is minimal at the CCR center and which shows no sign of discrete steps or localization. For $\widetilde{B} > 0$, m_j^{KQD} and m_j^{QPC} in Figs. 3.7(e) and 3.7(f) likewise show a standing-wave pattern of strongly enhanced oscillations in the CCR with a spatially varying oscillation period $\lambda \sim 1/n_j$ of each pattern. However, significant differences become evident if $\widetilde{B}$ increases far beyond $\widetilde{B}_*$. m_j^{KQD} of the KQD saturates and the positions of the corresponding maxima remain unchanged which reveals that the single spin magnetic moment becomes polarized. Also n_j^{KQD} is maintained independently of $\widetilde{B}$. In contrast, m_j^{QPC} increases without significant saturation for $\widetilde{B} \gg \widetilde{B}_*$ and its local maxima positions shift away from the CCR center. n_j^{QPC} furthermore increases near the barrier center on raising $\widetilde{B}$ as well as reacts in close vicinity. The QPC features indicate that a smooth redistribution of charge and spin takes place during the polarization of the CCR.

Moreover, the results Figs. 3.7(g) and 3.7(h) do yield further clues for the multi-spin distribution of the QPC as opposed to the single spin state of the KQD. Although $\chi_{j,\max}^{\mathrm{KQD}} > 10\chi_{j,\max}^{\mathrm{QPC}}$ at their respective peak values, the resulting magnetization at the lowest $\widetilde{B}$ in Figs. 3.7(e) and 3.7(f) already shows $m_{j,\max}^{\mathrm{KQD}} < m_{j,\max}^{\mathrm{QPC}}$. This contrast in absolute magnetization strength then becomes even more pronounced for further rising $\widetilde{B}$. Hence it can be concluded from the calculations that in contrast to the KQD which contains a discrete, localized spin-1/2 local moment, the QPC does not and its CCR contains various *contributing* spins which show clear signs of not being localized.

Aside from the above differences at large magnetic fields, both the KQD and the QPC show two remarkable similarities in the regime of small fields $\widetilde{B} \ll \widetilde{B}_*$ which are substantial for the 0.7-Kondo similarity. First of all, m_j vanishes at $\widetilde{B} = 0$ in both cases

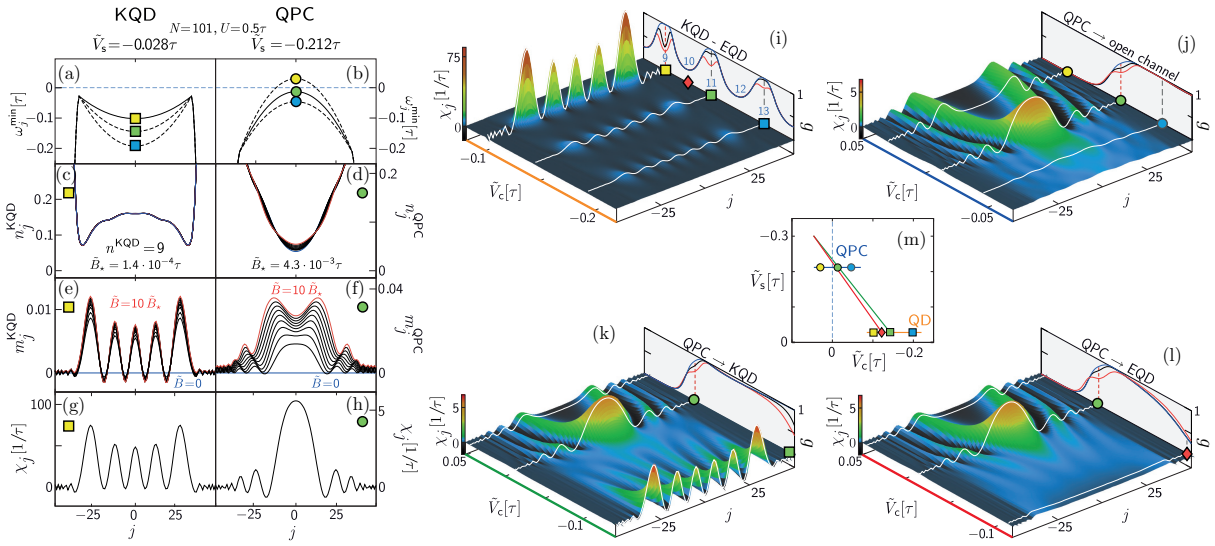

Figure 3.7: QD vs. QPC: comparison of calculated local properties (using fRG including vertex flow). (a-h) Site-dependent fixed KQD (left) and QPC (right column) geometry. (a,b) Barrier tops for a KQD and a QPC near pinch-off. The barriers $\omega_j^{\min} = E_j - E_F$ are labeled by colored symbols marking the barriers in (c-m). (c,d) Local density n_j and (e,f) local magnetization m_j for equidistant fields from $\widetilde{B} = 0$ (blue) to $\widetilde{B} = 10\widetilde{B}_*$ (red). (g,h) Local spin susceptibility χ_j. (i-l) Geometric crossovers: χ_j (z-axis and color-coded) plotted vs. site j and $\widetilde{V}_c = \widetilde{V}_{j=0}$ for four trajectories in the $(\widetilde{V}_c, \widetilde{V}_s)$ plane, indicated by the color-coding in (m) which matches the $\widetilde{V}_c$-axes colors. Each panel (i-l) also shows $g(\widetilde{V}_c)$ for three fields ($\widetilde{B}/\widetilde{B}_*^{\min} = 0$, ~ 1, and $\gg 1$) to illustrate each $\widetilde{V}_c$-dependence of the magnetoconductance. Red dashed lines mark the gate voltage $\widetilde{V}_{c0}$ where $\widetilde{B}_* = \widetilde{B}_*^{\min}$ for both KQD and QPC (red and black dashed lines in (i)). The trajectories match (i) a QD being charged with 9 to 13 electrons as indicated, (j) a QPC tuned from pinch-off to an open channel, (k) a transition from a QPC to a KQD with 11 electrons, and (l) a crossover from a QPC to an even QD (EQD) charged by 10 electrons.

as shown by Figs. 3.7(e) and 3.7(f) (blue lines) which reflects the initial assumption of absent spontaneous magnetization (see Sec. 2.2). Secondly, the spatial static spin susceptibility χ_j in Figs. 3.7(g) and 3.7(h) exhibits a strong enhancement in the CCR for both KQD and QPC that is modulated by standing-wave oscillations which are mapped on m_j (Figs. 3.7(e) and 3.7(f)) at low magnetic fields. The model explains that this enhancement results from an interplay between geometry and interactions. Without interactions, $U = 0$, the bare local spin susceptibility in a QPC is directly proportional to the LDOS at E_F, $\chi_j^0 = \mathcal{A}_j^0(0)/2$. It hence adopts the spatial dependence of it which reflects the geometry of the CCR potential. Interactions increase the spin susceptibility because they increase the spin imbalance if a small magnetic field is applied which favors spin up over spin down by further depleting the spin-down population. The same reasoning applies to the KQD in the low-energy regime which exhibits quasi-particles that experience a local interaction strength proportional to $1/T_K$ [78].

In contrast to the KQD, the EQD shows no increase in χ_j whatsoever. This is illustrated in Figs. 3.7(i-l) which display χ_j (vertical axis and color-coded) as a function of site j and center potential $\widetilde{V}_\mathrm{c}$. Also the corresponding conductance curves $g(\widetilde{V}_\mathrm{c})$ are added for three different magnetic fields projected on each rear vertical plane. Each of the four panels represents a different trajectory in the $(\widetilde{V}_\mathrm{c}, \widetilde{V}_\mathrm{s})$ plane corresponding to four types of geometric crossovers. They are marked by the lines in panel (m) using colors that match the associated $\widetilde{V}_\mathrm{c}$-axes in (i-l). Fig. 3.7(i) shows a QD at a fixed $\widetilde{V}_\mathrm{s}$ whose electron number (blue integers) is increased by lowering $\widetilde{V}_\mathrm{c}$. It exhibits adjacent odd-even effects for both $\chi_j(\widetilde{V}_\mathrm{c})$ and $g(\widetilde{V}_\mathrm{c})$. The Kondo-plateaus in $g(\widetilde{V}_\mathrm{c})$ for odd electron numbers (KQDs) are accompanied by distinct peaks in $\chi_j(j, \widetilde{V}_\mathrm{c})$ (white lines) whereas the Coulomb valleys for even electron numbers (EQDs) do not show any comparable feature. Fig. 3.7(j), on the other hand, shows a QPC at a fixed $\widetilde{V}_\mathrm{s}$ which is tuned in $\widetilde{V}_\mathrm{c}$ from pinch-off to an open channel with $g = 1$. The 0.7-anomaly in $g(\widetilde{V}_\mathrm{c})$ occurs at $\widetilde{V}_\mathrm{c} \sim \widetilde{V}_{\mathrm{c}0}$ (red dashed line) where $\widetilde{B}_*$ is minimal (compare Sec. 2.3.3 and Sec. 3.3.2). The two maxima of χ_j at $\widetilde{V}_\mathrm{c} > \widetilde{V}_{\mathrm{c}0}$ are merged into a single peak at $\widetilde{V}_\mathrm{c} \sim \widetilde{V}_{\mathrm{c}0}$ where the barrier top is located below E_F (green dot in Fig. 3.7(b)) corresponding to E_F crossing the apex of the Hove ridge. The whole characteristics of the shape of $\chi_j^{\mathrm{QPC}}(j, \widetilde{V}_\mathrm{c})$ in Fig. 3.7(j) (analogously in Figs. 3.7(k) and 3.7(l)) represent a direct "image" of the LDOS including the Hove ridge around E_F (compare Fig. 3.3(b), Sec. 3.2.1).

The remaining two examples represent mixed transitions between a QPC and a QD that correspond to tilted trajectories in Fig. 3.7(m). Fig. 3.7(k) shows a QPC-KQD crossover that terminates in an KQD containing 11 electrons (compare Fig. 3.7(i)). χ_j exhibits the pronounced pattern of local maxima of the QPC regime (Fig. 3.7(j)) which start to weaken toward the open-channel regime, transform at a small yet finite mean magnitude during the crossover (around $\widetilde{V}_\mathrm{c} = -0.03\tau$), and start to increase again close to the KQD forming its characteristic spatial pattern (Fig. 3.7(i)). During this transition, no clear indication of a connection between both regimes can be inferred. The positions of the strongly weakened local χ_j maxima of both the QPC and the KQD regime seem to be offset with respect to each other in the $\widetilde{V}_\mathrm{c}$-j plane, separated by a blurred region.

It should be noted, however, that the trajectories in Figs. 3.7(k) and 3.7(l) were deliberately chosen such that the point where the barrier top changes from a local maximum (QPC) to a local minimum (QD) (around $\widetilde{V}_\mathrm{s} = \widetilde{V}_\mathrm{c}$) occurs far in the open channel implying the barrier center including the Hove ridge lying well below E_F. These transitions imply $g \simeq 1$ at $\widetilde{V}_\mathrm{s} = \widetilde{V}_\mathrm{c}$ yielding very small spin susceptibilities χ_j demonstrating that a truly open channel implies very little spin fluctuations. However, the particular characteristics during the crossover depend on the precise shape of the crossover trajectory (which can follow any path in the $\widetilde{V}_\mathrm{c}$-$\widetilde{V}_\mathrm{s}$ plane). For instance, it would be possible to construct trajectories that entirely avoid the open-channel regime so that $g \ll 1$ throughout the crossover which therefore would sustain a large spin susceptibility. In the light of the chosen trajectories, the above conclusion regarding absent evidence of a link between χ_j^{QPC} and χ_j^{KQD} in Fig. 3.7(k) is still correct. The reason is that the interpreted intermediate

regime fully lies in the open channel with a constant $g \sim 1$. Though the local maxima of χ_j are decreased they remain visible and transform at the homogeneous conditions within the channel allowing the comparison.

Eventually Fig. 3.7(l) shows a QPC-EQD crossover ending in a EQD which comprises 10 electrons. The susceptibility χ_j in the regime of the EQD remains very small and spatially homogeneous, contrary to the case of the 11-electron KQD in Fig. 3.7(k).

The main conclusion which is drawn from Figs. 3.7(i-l) can be summarized by the observation that the strong negative magnetoconductance which emerges likewise for both KQDs and QPCs is consistently accompanied by a strongly enhanced spin susceptibility. In contrast, in the EQD regime no magneto-response is present and correspondingly for the EQD, as well as for the open 1D channel, the calculated spin susceptibility is spatially constant showing a comparatively insignificant magnitude. This yields direct evidence that the strong negative magnetoconductance, being one of the key features of the 0.7-Kondo similarity, originates from the fact that QPC contains strong local spin fluctuations similar to those emerging in the KQD. However, the restriction is crucial that the 0.7-Kondo similarity applies only for low excitation energies $\widetilde{B} \ll \widetilde{B}_*$ owing to the different predicted spin configurations. For the case of large magnetic fields $B \gg B_*$, a continuing analysis is provided in the subsequent Section 3.5.

This section is concluded by pointing out that Fig. 3.7(j) provides a clue to why the approximate relation Eq. 3.7 was found to be bound to $\widetilde{V}_\mathrm{c} \leq \widetilde{V}_{\mathrm{c}0}$ only. In the range $\widetilde{V}_\mathrm{c} \leq \widetilde{V}_{\mathrm{c}0}$ the apex of the Hove ridge lies below E_F so that for each $\widetilde{V}_\mathrm{c}$ the local spin susceptibility $\chi_i(\widetilde{V}_\mathrm{c})$ has just one maximum. Leaving this regime toward $\widetilde{V}_\mathrm{c} > \widetilde{V}_{\mathrm{c}0}$ in Fig. 3.7(j) induces a splitting into two separate maxima of $\chi_i(\widetilde{V}_\mathrm{c})$, and consequently, the zone of strongest spin fluctuations around E_F is divided accordingly. Eq. 3.7 was deduced from the Fermi-liquid theory which supposes the strong spin fluctuations to be restricted to a single, spatially confined region which is not the case for $\widetilde{V}_\mathrm{c} > \widetilde{V}_{\mathrm{c}0}$. Consequently, Eq. 3.7 actually becomes invalid.

3.5 Limit of high-energy excitations

In the previous section it was concluded that the local magnetization m_j^{KQD} of the KQD clearly saturates at $\widetilde{B} \gg \widetilde{B}_*$, in contrast to the continuously rising m_j^{QPC} which shows no signs of saturation. The difference was attributed to the magnetic moment of a localized single spin present in the KQD as compared to the continuous smooth rearrangement of the spin configuration of various contributing electrons in the QPC. In this section a theoretical analysis of the high-energy excitation limit $\widetilde{B} \gtrsim \widetilde{B}_*$ of the magnetoconductance G, magnetization m, and charge n is performed for each QPC and KQD regime individually. It is demonstrated that this yields further evidence for the above finding that the behavior of the strongly interacting electrons in the QPC differs substantially from the characteristics of the localized magnetic moment in a KQD beyond low-energy scales.

For the comparison, the total charge and magnetization in the “inner” region of the

CCR is defined by

$$n_{\text{inner}} = \sum_{|j|\leq j_{\text{inner}}} n_j \ , \quad m_{\text{inner}} = \sum_{|j|\leq j_{\text{inner}}} m_j \ . \tag{3.8}$$

For the KQD geometry, the inner region is set between the two confining maxima of the KQD potential at $\pm j_{\text{inner}}^{\text{KQD}}$. The remaining sites j in the CCR with $j_{\text{inner}}^{\text{KQD}} < |j| \leq N'$ lie outside the dot. Their total charge (or magnetization) contribution is proportional to the length of the outer flanks thus representing an extensive quantity. Therefore the remaining sites were excluded for the discussion of the intensive properties of the KQD. For the QPC geometry there is no natural separation between an inner region and the barrier's outer flanks. Therefore results are shown for inner regions of three different chosen sizes, $j_{\text{inner}}^{\text{QPC}} = 150$, 60, and 30, each at a fixed $N' = 150$ (they all yield qualitatively similar results, as shown below).

The KQD and QPC findings are additionally compared to fRG results for the single-impurity Anderson model (SIAM) describing a local energy level $\varepsilon_d = \widetilde{V}_{\text{c}}$ with Coulomb repulsion U for double occupancy (compare Sec. 1.3). The SIAM level has a width Γ due to hybridization with the electrons of a conduction band of width D (with $D \gg U \gg \Gamma$). In case of the SIAM, the CCR consists of just one single central site which comprise the local d-level, hence $n_{\text{inner}}^{\text{SIAM}} = n_{\text{d}}^{\text{SIAM}}$ and $m_{\text{inner}}^{\text{SIAM}} = m_{\text{d}}^{\text{SIAM}}$.

Figure 3.8 compares G, n and m of a KQD (middle column) with that of a QPC (right column) toward large $\widetilde{B}$. The left column summarizes the respective SIAM results G, $n_{\text{d}}^{\text{SIAM}}$, and $m_{\text{d}}^{\text{SIAM}}$ for comparison. Panels (a-c) of Fig. 3.8 show G/G_{Q} as function of the tuning potential $\widetilde{V}_{\text{c}}$ for SIAM, KQD and QPC at five magnetic fields $\widetilde{B}$ in units of the $\widetilde{V}_{\text{c}}$-independent reference field strength $\widetilde{B}_*^{\text{min}} = \min[\widetilde{B}_*(\widetilde{V}_{\text{c}})]$ corresponding to the strongest magnetoresponse. The color-coded arrows indicate five chosen $\widetilde{V}_{\text{c}}$-values each where the corresponding results of the remaining panels were calculated. The conductance G/G_{Q} (panels d-f), the charge n (g-i), and the magnetization m (j-l) are shown as functions of the magnetic field normalized to $\widetilde{B}_*^{\text{min}}$. Additionally, the conductance $G(\widetilde{B})$ scaled to $G(\widetilde{B} = 0)$ (m-o) and the magnetization m (p-r) are plotted as a function of the magnetic field scaled to the individual $\widetilde{V}_{\text{c}}$-dependent energy scale of the magnetoconductance, $\widetilde{B}/\widetilde{B}_*$. In case of the SIAM and the KQD, the blue, green, and orange curves correspond to the local-moment regime defined by $G/G_{\text{Q}}(\widetilde{B} = 0) \simeq 1$ in (a,b). In the local-moment regime the local charge in (g,h) lies close to an integer whereas the respective red and purple curves correspond to the mixed-valence regime.

The comparison of the three regimes in Fig. 3.8 yields the following main features:
(I) The extracted local charge variations $n_{\text{d}}^{\text{SIAM}}$, $n_{\text{inner}}^{\text{KQD}}$, and $n_{\text{inner}}^{\text{QPC}}$ at all five center potentials $\widetilde{V}_{\text{c}}$ depend rather weakly on the magnetic field $\widetilde{B}$ (g-i).
(II) For small magnetic fields $\widetilde{B}/\widetilde{B}_*^{\text{min}}$, the characteristic regime of the 0.7-Kondo similarity, the magnetization increases linearly with the field (j-l). In the regime of large magnetic field
(III) the plateau in $m_{\text{d}}^{\text{SIAM}}$ of the SIAM asymptotically approaches 0.5 (j), characteristic

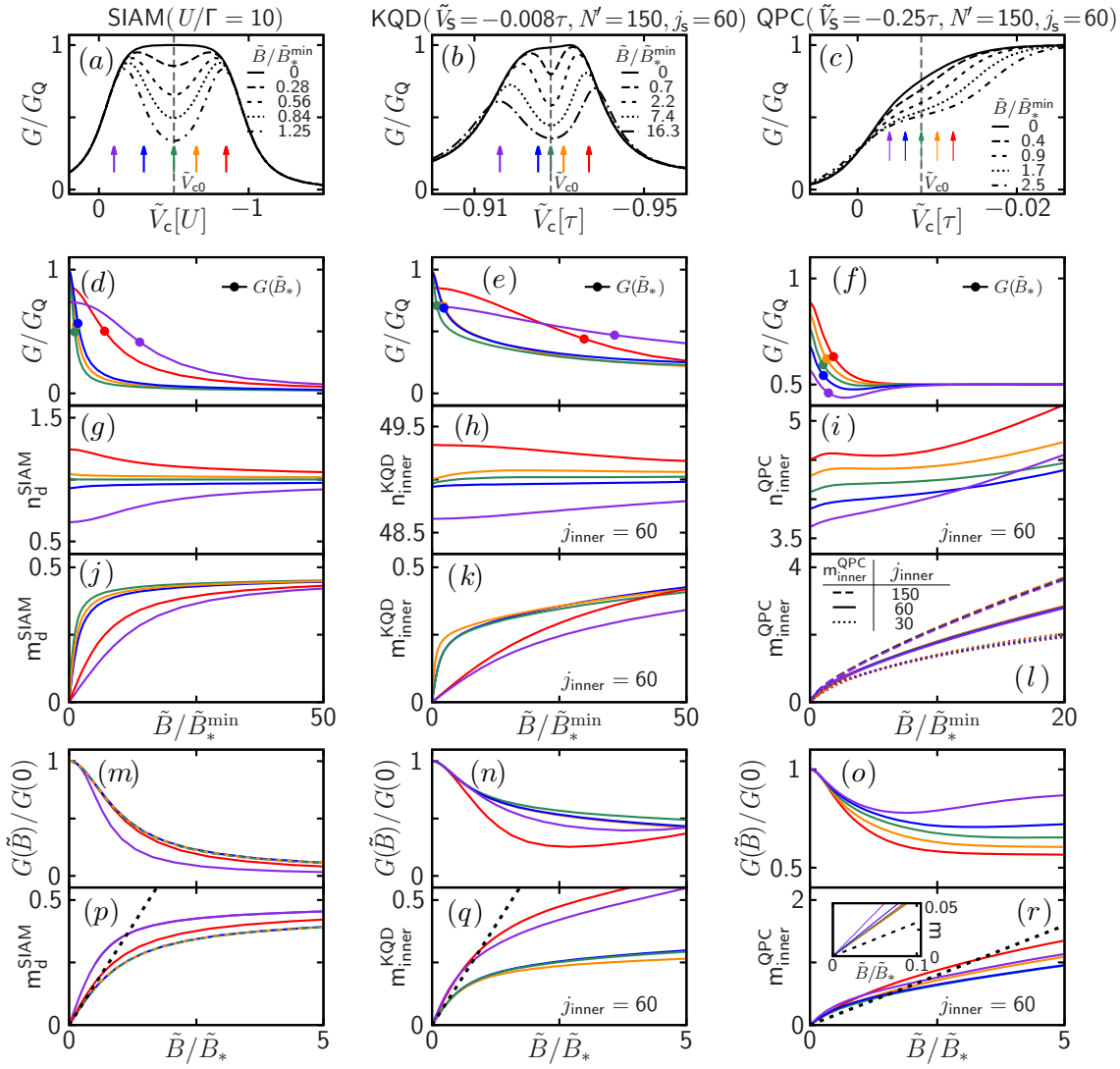

Figure 3.8: Calculations (fRG including vertex flow) of the large-$\widetilde{B}$ behavior for the single-impurity Anderson model (SIAM, left), a KQD (middle, same parameters as in Fig. 3.6(c)), and a QPC (right column, same parameters as in Fig. 3.6(d)). (a-c) Conductance for five values of $\widetilde{B}$ each. Vertical dashed lines indicate the $\widetilde{V}_{c0}$ where $\widetilde{B}_*(\widetilde{V}_{c0}) = \widetilde{B}_*^{\min}$. (d-r) Dependence on (d-l) $\widetilde{B}/\widetilde{B}_*^{\min}$ and (m-r) $\widetilde{B}/\widetilde{B}_*$ at constant $\widetilde{V}_c$-values as indicated by the correspondingly colored arrows in (a-c). (d-f) Normalized conductance, (g-i) the total charge n_{inner}, and (j-l) the total magnetization m_{inner} in the inner CCR, comprising sites $|j| \leq j_{\text{inner}}$ as indicated (Eqs. 3.8). (m-o) and (p-r): Same data as in (d-f) and (j-l), respectively, though plotted vs. $\widetilde{B}/\widetilde{B}_*$. Each graph in (m-o) is normalized to $G(\widetilde{B} = 0)$. The black dotted lines in (p-r) have the slope $1/\pi$ and indicate the small-$\widetilde{B}$ limiting behavior $m_{\text{inner}} = \widetilde{B}/(\pi\widetilde{B}_*)$ which is expected in the Kondo limit (Eq. 3.5). Inset of (r): Zoomed in to $\widetilde{B}/\widetilde{B}_* \to 0$.

of a gradually polarizing spin-1/2 local moment, and
(IV) the plateau in $m_{\text{inner}}^{\text{KQD}}$ is fairly flat too (k), however, it does not exactly saturate.

Instead it slowly increases past 0.5 for sufficiently large fields $\widetilde{B}/\widetilde{B}_*^{\min}$. The reason is that the KQD in Fig. 3.8 not only contains one single spin-1/2 local moment. Yet many (48) additional levels are occupied of which several start to contribute to $m_{\text{inner}}^{\text{KQD}}$ if $\widetilde{B}$ becomes comparable to the level spacing of the QD.
(V) The QPC magnetization continues to increase beyond 0.5 toward $\widetilde{B}/\widetilde{B}_*^{\min} \gg 1$ without emerging saturation (l). This reflects the fact that the QPC barrier lacks the isolated "inner region" of a KQD. Instead, it is entirely composed of outer flanks along which electrons of both spin species can move freely. As the magnetic field is increased, the magnetization of the QPC can therefore increase without imposed limitation. Thus the slope of $m_{\text{inner}}^{\text{QPC}}(\widetilde{B}/\widetilde{B}_*^{\min})$ in (l) depends on the width of the inner region: the larger j_{inner} the stronger the initial linear increase in magnetization (dotted, solid, dashed curves). A larger spatial QPC region on average contains more electrons whose higher number of possibly contributing spin-magnetic moments can induce the larger overall magnetization at a given $\widetilde{B}$.

The conductance G and the magnetization m of the SIAM and the KQD on the one hand and the QPC on the other hand show different characteristics when plotted as a function of the magnetic field scaled to the center-potential-dependent low-energy scale $\widetilde{B}_*(\widetilde{V}_{\text{c}})$:
(VI) For the SIAM within the local-moment regime (blue, green, and orange curves) the scaled conductances $G(\widetilde{B})/G(0)$ (m) and the magnetizations (p) each collapse onto a single curve.
(VII) The same approximately happens for the conductance (n) and magnetization (q) of the KQD. The deviations again arise from the additional occupied QD levels that can contribute to the total magnetization. Thus for both the SIAM and KQD, the $\widetilde{V}_{\text{c}}$-*dependent* low-energy scale $\widetilde{B}_*$ governs both the small- *and* large-field behavior of the magnetization and the conductance.
(VIII) The QPC conductance (o) and magnetization (r) also about collapse for $\widetilde{B} \ll \widetilde{B}_*$ in the sub-open regime $\widetilde{V}_{\text{c}} < \widetilde{V}_{\text{c0}}$ (green, orange, and red curves, compare the inset in (r)). Though both do not show a tendency to collapse onto a single behavior at large $\widetilde{B}/\widetilde{B}_*$.
(IX) The large-field behavior of the QPC magnetization is instead approximately determined by the $\widetilde{V}_{\text{c}}$-*independent* scale $\widetilde{B}_*^{\min}$ (l): the magnetizations as a function of $\widetilde{B}/\widetilde{B}_*^{\min}$ very closely overlap in the limit of not too large $\widetilde{B}/\widetilde{B}_*^{\min}$ (the range where the $m_{\text{inner}}^{\text{QPC}}$ curves clearly deviate from each other is not resolved in (l)).
(X) The tail of $m(\widetilde{B}/\widetilde{B}_*)$ is linear in the small-field limit ($\widetilde{B} \ll \widetilde{B}_*$) where the magnetization m is governed by $\widetilde{B}_*$ for the SIAM (p) and the KQD (q) in the local moment regime and for the QPC in the sub-open regime $\widetilde{V}_{\text{c}} < \widetilde{V}_{\text{c0}}$ (resolved in the inset of panel (r)). Thus at low $\widetilde{B}$ the spin susceptibility $\partial m/\partial \widetilde{B}$ is proportional to $1/\widetilde{B}_*$. Due to (VI,VII) it implies that for the SIAM and the KQD in the local-moment regime the magnetization curves $m(\widetilde{B}/\widetilde{B}_*)$ have the same slope for $\widetilde{B}/\widetilde{B}_* \to 0$. It is illustrated by the blue, green, orange lines in (p,q) which all have slope $1/\pi$ (dashed black lines), in accordance with Eq. 3.5 (Sec. 3.3.2). The magnetizations of the QPC in the sub-open regime (green, orange, and red curves in the inset of (r)) have mutually similar slopes, though not equal

to $1/\pi$ (dashed black lines in (r)), confirming Eq. 3.7 (Sec. 3.3.2).

In summary, the conductances and magnetizations of the SIAM and the KQD are governed by the single energy scale $\widetilde{B}_*(\widetilde{V}_c)$ in the *entire* $\widetilde{B}$ range which represents a characteristic trait of the Kondo effect (VI,VII). In contrast, for the conductance and the magnetization of a QPC this universal scaling is only approximately fulfilled for $\widetilde{B} \ll \widetilde{B}_*$ at $\widetilde{V}_c < \widetilde{V}_{c0}$ and the smaller $\widetilde{B}$ gets the more the approximate scaling resembles a true scaling (VIII). Hence this further confirms that although the characteristics of the 0.7-anomaly and a QD which acts in the Kondo-effect regime are very similar, making both similarly appearing physical effects, in the range of high magnetic fields both clearly differ the more from each other the larger $\widetilde{B}$ gets. There actually exist experimental evidence already that the total magnetic moment of a QPC around $0.7G_Q$ clearly exceeds 0.5 [44]. This can furthermore be attributed to the quantitative amount of spin-polarization which is achievable at most, owing to the non-localization of contributing (partly) polarized spins in the QPC as opposed to the local single spin-moment which dominates the overall KQD magnetization. The fact that the small-field limit of the QPC magnetization is governed by $\widetilde{B}_*$ (X) underlies the low-energy Kondo-typical behavior of the QPC conductance discussed in Sec. 3.3.2.

3.6 Conclusions

The tuning ability of the experimental as well as the theoretical setup proved to be highly productive. Both measurements and calculations covered the QPC and the KQD regime as evident from the observed 0.7-anomaly and the raised magnetoconductance in the Kondo valleys, being Coulomb-blockaded gaps of the unevenly charged QD. The QPC-QD crossover was investigated in terms of the magnetoconductance at various magnetic fields $B \geq 0$ where the measurements and the calculations uniformly showed a smooth transition. The good qualitative agreement of the calculated results with the measurements, including all of the main features of the measured conductance, further strengthens the capability of the model and the results of Chapter 2. It provides evidence that the restrictions which were conceded from the theoretical point of view are insignificant for the correct description of the determinative physics of the CCR in the QPC as well as in the QD regime.

Moreover, the link between the conductance response to the magnetic field and the spin susceptibility was investigated theoretically. The main conclusion is summarized by the deduced central prediction: As it holds for the KQD, the observed strong negative magnetoconductance inseparably implies an strong gain of the local spin susceptibility in the CCR also in the 0.7-anomaly regime of the QPC, $1/\widetilde{B}_* \sim \chi_{exc}$. This relation can be considered the fundamental connection that constitutes the microscopic origin of the 0.7-Kondo similarity and therefore of the 0.7-anomaly since it establishes a link between the spin fluctuations (cause) and the generated QPC conductance anomaly (effect). Furthermore, the well-established model was shown to predict, for both KQD and QPC, that the spin susceptibility exhibits a characteristic spatially oscillating pattern around the CCR.

Its source could be addressed to the interplay between geometry and interactions: the spin susceptibility inherits the spatial dependence of the LDOS which becomes amplified by interactions that increase the spin imbalance at finite $\widetilde{B}$. The calculations furthermore revealed that this spatial pattern transforms smoothly during the QPC-QD crossover.

Eventually the regime of excitations at higher energies $\widetilde{B}/\widetilde{B}_* \gg 1$ was investigated theoretically. In this regime the 0.7-Kondo similarity was shown to become invalid due to the fundamental difference between the underlying physical systems in the 0.7-anomaly and the KQD case. This became evident by the magnitude of the magnetization at increasing $\widetilde{B}$ which does not saturate in the 0.7-anomaly regime as opposed to the KQD, caused by a finite number of contributing electron spins in the QPC case which can built up much stronger magnetizations as opposed to the KQD's single magnetic moment which eventually becomes fully polarized. It was bolstered by the calculated conductances $G(\widetilde{B}/\widetilde{B}_*)$ as well as magnetizations $m(\widetilde{B}/\widetilde{B}_*)$ each collapsing into a single curve around the KQD plateau center whereas for the 0.7-anomaly regime they distinctly spread at $\widetilde{B}/\widetilde{B}_* \gg 1$. This showed that $\widetilde{B}_*$ governs the full $\widetilde{B}$ range of the KQD in contrast to the validity only at low $\widetilde{B}/\widetilde{B}_*$ in case of the 0.7-anomaly. Additionally, by increasing $\widetilde{B}$ toward the high-energy limit the calculations showed that the spatial distribution of the local maxima in the magnetization were completely unaffected in the KQD whereas for the QPC 0.7-regime the maxima clearly shifted spatially away from the CCR center. This furthermore indicated the ongoing dynamic redistribution of electron spins in the 0.7-regime, as opposed to the fixed governing single electron magnetic moment of the KQD.

Chapter 4

Optical readout of a single spin state

The theory that was presented and shown to conform to the experiments in Chapter 2 and Chapter 3 explains the 0.7-anomaly as a result of electron-spin fluctuations emerging locally at the QPC accompanied by a locally increased electron-spin susceptibility. In preparation for a possible examination of the predicted increase in the local spin-susceptibility that is reflected in the local electron-spin polarization in response to a small external magnetic field additional experiments based on optical techniques were performed.

In this chapter, an experimental setup based on Faraday rotation is presented that enables the readout of local spin polarization. The Faraday effect as well as the related Kerr effect are efficient all-optical spin-detection techniques as demonstrated in various experiments studying spin polarization of electrons or holes in nanoscopic and mesoscopic semiconductor systems [2, 82–84]. The experimental setup is based on a home-built optical microscope of confocal resolution enabling spatially resolved detection. The efficiency and the sensitivity of the microscope setup were assessed by using an initialized spin state of a single electron state confined in a self-assembled QD as a test bed. The results are presented and discussed in this chapter.

4.1 Spin detection via Faraday rotation

The detection of spin-magnetic moments of electrons is accomplished by exploiting the Faraday effect as a form of spin-tagged light-matter interaction. In general, it can occur if electromagnetic radiation propagates through a medium which is exposed to a static magnetic field. For linearly polarized light the Faraday effect induces circular dichroism: the constituting left- and right-handed circularly polarized components experience different scattering probabilities which causes different propagation speeds. It imposes unequal dispersion and thus different refractive indices for both circularly polarized propagating modes. The difference in the propagation speeds of the circular components generates a rotation of the polarization plane of the overall linearly polarized light. Hence the Faraday effect is also generally referred to as Faraday rotation (FR). The rotation angle is proportional to the magnetic field component parallel to the propagation direction of the

interacting light.

The case of light interacting with the magnetic moment of a single spin is slightly different since the zero-dimensional quantum system is local. However, the underlying mechanism for the occurring FR is of identical character: it induces a phase shift arising from the dispersive part of the light-matter interaction which can be exploited in order to determine single spin-polarization. The complex response function of matter to the radiation field contains both the absorptive and dispersive terms which are interlinked by the Kramers-Kronig relation. Even in the limit of single atoms, molecules, or semiconductor QDs both terms of the response are experimentally accessible in resonant laser experiments with remarkable signal-to-noise contrasts [85, 86]. Spin information is obtained whenever the used optical transition obeys spin-selective dipolar selection rules. The dispersive optical response can be analyzed in a basis which decomposes the photon polarization (see Sec. 4.2). The extent of spin polarization is given by the scattering cross section, which in turn is linked to the wavelength λ of the respective optical transition. As a rule of thumb one can consider the scattering volume of real or artificial atoms to be of the order of λ^3. This limitation for spatial spin sensing with optical techniques may be overcome in experiments bypassing the diffraction limit [87].

4.2 Experimental setup

The performance of the home-built diffraction-limited microscope setup in terms of the analysis of local magnetization was evaluated in a liquid-helium bath cryostat at the bath temperature of 4.2 K. A single electron spin state was initialized by optical means in a self-assembled QD with typical dimensions of about 10 nm in a controlled environment [88] and read out with the microscope. Figure 4.1 schematically shows the experimental setup. The simultaneous spin initialization and detection is performed by two individual tunable narrow-band CW lasers serving as a pump and a probe laser. A single-mode fiber serves as an optical path to a micro-objective located in a helium bath cryostat with the base temperature of 4.2 K. The fiber contains a device ("paddles" in Fig. 4.1) which enables the compensation for the change in laser-light polarization that is induced by the fiber. The objective focuses on the sample which is mounted on a compact polarization analysis unit consisting of a linearly polarizing beam splitter (LPS) and two photo detectors (PD1 and PD2). Thus the PDs provide the normalized transmitted power resolved in a linear polarization basis. The heterostructure on top of the sample contains a layer of self-assembled QDs (magenta) as well as a built-in highly doped back gate layer (light blue) that is contacted electrically via ohmic connections (yellow, grounded). Additionally a semitransparent global metal gate (light blue) is deposited on top of the heterostructure.

A DC voltage applied to the top gate adjusts the QD interband transition energies by using the quantum confined Stark effect (QCSE) in the Schottky device [89, 90]. The added AC voltage modulation, supplied by a waveform generator, modulates the QD transitions via QCSE modulation which serves the highly sensitive readout of the PDs using differential transmission [91]. Each PD response is analyzed by a separate

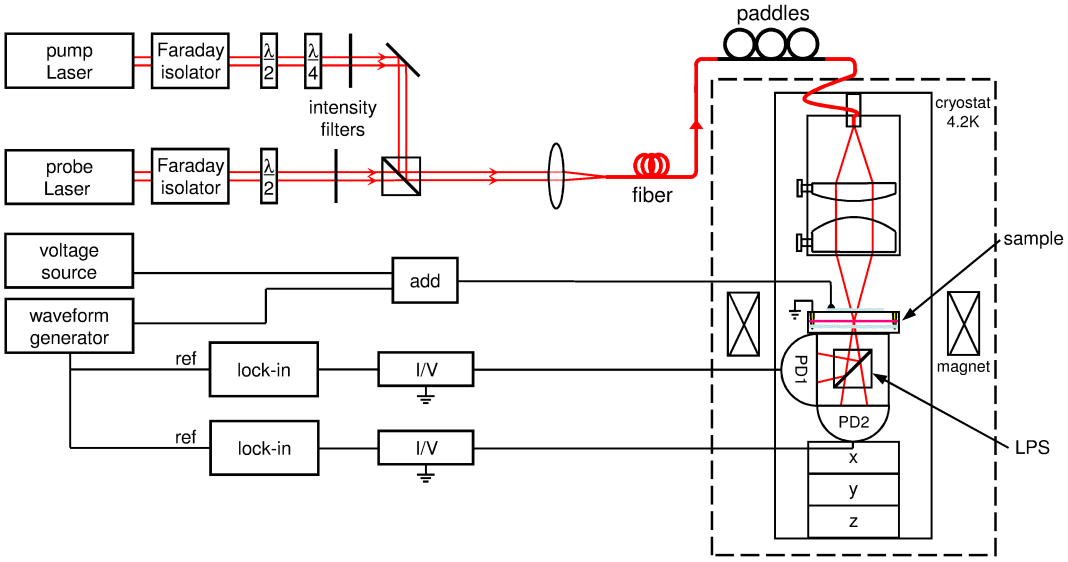

Figure 4.1: Experimental setup for spin polarization analysis: The QD spin initialization and detection is done separately by a pump and a probe laser, respectively. A single-mode fiber including paddles for polarization adjustment serves as an optical path to the micro-objective in a helium bath cryostat at 4.2 K. A linearly polarizing beam splitter (LPS) and two photo detectors (PD) analyze the light transmitted through the sample in a linear basis. The PD lock-in readout is performed via modulation of the electric field between the sample gates (light blue) which sandwich the QD layer (magenta).

transimpedance amplifier (I/V) as well as lock-in amplifier. The sample positioning with respect to the micro-objective is provided by a xyz-nanopositioner stack to which the analysis unit is attached.

The microscope further complies with the analysis of the photoluminescence (PL) of the QD (not shown in Fig. 4.1). PL readout was exploited in the microscope-test experiment for the selection of a proper QD. The required optical interband transition rules of the chosen QD were then mapped out experimentally under an externally applied magnetic field by aid of the differential transmission technique using one of the PDs.

For the subsequent actual single-spin detection experiment, the paddles are adjusted so that the optical path of the fiber becomes neutral in terms of polarization deformation, e. g. incident light of vertically linear polarization is fully mapped on one of the PDs only. The Faraday-isolator-mediated linear polarization of the pump and the probe laser can then be adjusted by the respective quarter and half wave plate to (left or right) circular and 45°-linear polarization in the basis of the readout unit, respectively. The choice of the initial 45° orientation of the probe beam polarization ensured a maximum signal-to-noise contrast of either PD signal in the spin detection experiment. The section of the single-mode fiber which crossed the lab freely toward the cryostat was pinned in order to maintain the pre-adjusted correction of the polarization deformation.

The experiment can in principle be operated at various temperatures and magnetic

fields. The implementation of the microscope into a He3-system with a target base temperature of 300 mK is straightforward. Further details of the microscope design are can be found elsewhere [92].

4.3 Readout sensitivity and spatial resolution

A proof-of-principle experiment for the home-built microscope (Sec. 4.2) was carried out at a liquid-helium bath temperature of $T = 4.2$ K where the spectroscopy of an individual self-assembled QD was used as a test bed of the diffraction-limited performance. A QD-confined single electron spin was initialized in a known spin state which was detected by means of Faraday rotation in order to quantify the sensitivity and the spatial resolution. To this end, the Schottky device was tuned to a gate voltage interval where the chosen QD is charged with one single electron [88]. The Zeeman splitting at a finite magnetic field $B = 300$ mT induces correspondingly blue-sifted and red-shifted interband optical transitions of negatively charged trion states. In the Coulomb-blockaded QD, selective optical pumping of the blue (red) trion transition yields spin-state preparation if the trion decays into the ground state of the red (blue) transition owing to strongly suppressed spin-flip rates at finite magnetic fields [93, 94].

The optical selection rules of the trion transitions were experimentally identified in resonant laser absorption experiments via polarization-resolved differential transmission (Sec. 4.2). The result is shown in Fig. 4.2 which displays a false-color plot of the measured absorption contrast as a function of the tuning gate voltage and the excitation laser wavelength for the case of pumping the blue-sifted (a) and red-shifted (b) trion transition via a σ^+- and σ^-- polarized laser, respectively. The stable trion states appear within the gate voltage interval of about -750 mV to -600 mV, as marked by the tilted solid blue and red lines in Fig. 4.2. In either case the transmission contrast is strongly suppressed in the center of the plateau due to optical spin pumping with a fidelity of virtually 100 % [95]. The spin pumping principle is visualized by the reversing arrows in the insets of (a) and (b). Thus both the upper and the lower branch of the Zeeman split trion transitions allow for controlled spin initialization.

Optical spin pumping was achieved by resonantly pumping the spin-down state via the red trion transition at a working point which is marked by the open dot and the dashed red arrows in Fig. 4.2(b). The spin detection was then carried out by means of the dispersive QD response [86] to a second linearly polarized (Sec. 4.1) laser which simultaneously scanned over the blue trion resonance, indicated by the blue upward arrow in (b). The measured absorption (dispersion) is evaluated in terms of the sum (difference) of the polarization-resolved transmitted relative intensities $\Delta T_{\mathrm{PD1}}/T_{\mathrm{PD1}}$ and $\Delta T_{\mathrm{PD2}}/T_{\mathrm{PD2}}$. For the detection of the polarization of the transmitted photons in the linear basis the measured dispersive signal is proportional to the Faraday rotation angle [92].

Figure 4.3(a) presents the measured (dots) absorptive response in differential transmission (black) and dispersive response giving rise to Faraday rotation (red), plotted versus

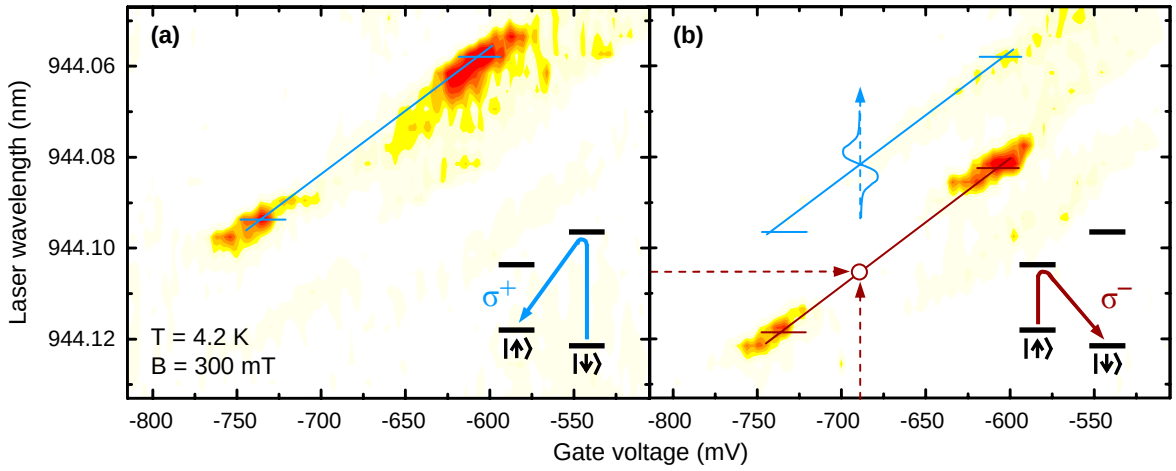

Figure 4.2: All-optical initialization and readout principle of a single electron spin confined in a self-assembled QD: Main panels: Color-coded differential absorptions (high absorption contrast is red) as a function of tuning gate voltage and Laser excitation wavelength. In the external magnetic field of $B = 300$ mT both the ground states and excited trion states are Zeeman-split, as indicated in the level diagrams (insets). A σ^+- (σ^--) polarized laser resonantly pumps the spin selective upper (lower) trion transition, marked blue (red) in the inset of (a) (of (b)). After the Trion recombination, the electron remains shelved in the non-resonant state (reversing arrows in the insets), leading to an absorption quench on the trion stability plateaus. Each plateau in (a) and (b) is marked for clarity by a tilted straight line, with colors matching the respective transitions in the insets. (b) Spin readout: One laser resonantly pumps the red transition for spin shelving (red circle) while a second laser scans the blue transition (blue dashed arrow).

relative laser energy detuning (solid lines are guides to the eye). A maximum Faraday rotation angle of about ± 0.01 deg was detected near the resonance. The deviations of the spectra from ideal responses which are indicated by the gray dashed lines are attributed to the non-linear Fano effect due to quantum interference [96].

Figure 4.3(a) provides the first main result as it allows to experimentally quantify the sensitivity of the Faraday rotation measurement on a single electron spin confined in a QD. The optical resonance linewidth of $\Gamma = 10$ μeV and a maximum absorption contrast of 7×10^{-4} yields the sensitivity of ~ 500 $\mu\text{rad}/\sqrt{\text{Hz}}$ for the microscope setup at a signal-to-noise ratio (SNR) of 10. This sensitivity is sufficient to allow for a reduction of roughly a factor of 10 in the scattering contrast or, alternatively, an increase of the same order of magnitude in the transition linewidth in order to resolve the polarization of a single local electron spin with SNR = 1 at an integration time of $t_{\text{int}} = 1$ s.

The SNR can be increased further by extending t_{int}. This is shown for different values of t_{int} in Fig. 4.3(b) (dots). It exhibits a square-root dependence $\text{FR}_{\text{SNR}} = A\sqrt{t_{\text{int}}}$ as expected from $\text{SNR} = N/\sqrt{N}$ due to the shot noise of N detected probe laser photons as well as from the corresponding PD-generated electrons and holes (compare Sec. 1.2), with

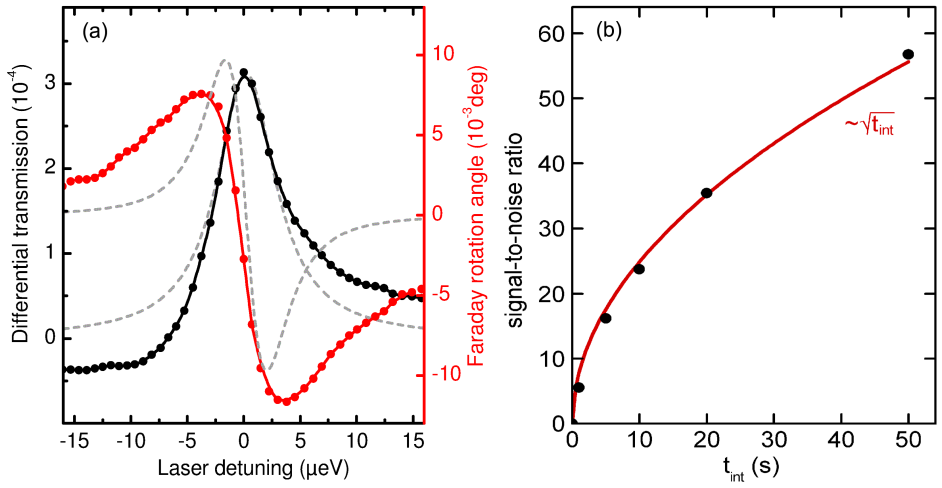

Figure 4.3: (a) Results of the spin measurement: Absorptive (black) and dispersive (red) responses (dots) to the laser scan over the blue Zeeman transition resonance in the presence of a resonant laser on the red Zeeman transition. It is plotted as a function of the scanning laser energy detuning relative to the blue Zeeman transition (integration time $t_{\mathrm{int}} = 50$ s). Solid lines are guide to the eye. The maximum Faraday rotation corresponds to phase shifts of about ± 0.01 deg near the resonance. The deviation of the spectra from an ideal scenario (dashed lines) can be attributed to quantum interference effects. (b) Experimentally obtained signal-to-noise ratios of the measured rotation angle (dots) for Faraday rotation off a single electron spin-down state at various integration times t_{int}. It fits a square-root dependence (red) anticipated from shot noise.

$N \propto t_{\mathrm{int}}$. The proportionality factor A is determined by the fit (red curve in Fig. 4.3(b)) to the experimental SNR which results in SNR $= 10$ at $t_{\mathrm{int}} \sim$ s.

Eventually local spin detection was demonstrated by laterally displacing the QD relative to the focal spot of the micro-objective. For each given displacement, the maximum Faraday rotation angle caused by a single spin-polarized electron was measured by scanning over the minimum of the dispersive resonance in Fig. 4.3(a). The data are presented in Fig. 4.4 in a false-color contour plot (main panel) and a 3D color map representation (inset).

The focal spot dimensions of the microscope setup were determined in an independent experiment. It revealed a slightly asymmetric spot shape with a full width at half maximum in X and Y direction of 1.1 μm and 0.9 μm, respectively. The slight asymmetry is caused by an uni-axial misalignment of the optical fiber within the micro-objective. For one chosen spot position, the corresponding spot shape is indicated in Fig. 4.4 (dashed ellipse). It very well coincides with the observed resolution of the Faraday response. Hence the local spin related Faraday rotation signal has a characteristic spatial distribution that is determined by the dimensions of the optical microscope spot. Aside from the preceding experimental inspection of the spot dimensions, it would be straightforward to readjust the setup in order to correct for a potential focal spot asymmetry and obtain an

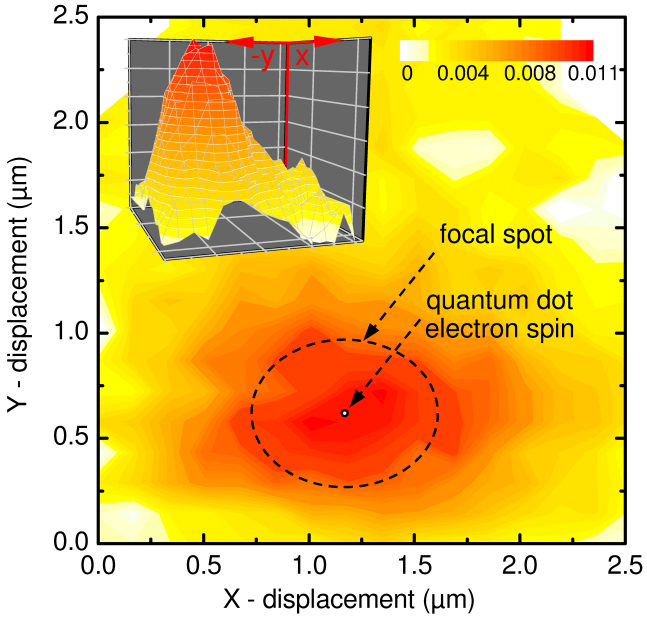

Figure 4.4: Spatially resolved single electron spin polarization. Main panel: False-color contour plot of the Faraday rotation response (in deg) as a function of the spatial displacement of the focal spot relative to the QD position (white dot) (the point of origin in the QD plane is arbitrary). Dashed ellipse: Shape of the focal spot for one single spot position. It is slightly asymmetric, having diameters of 1.1 μm (X) and 0.9 μm (Y direction) full width at half maximum. Maximum Faraday rotation is achieved when the QD spin is centered in the focal spot. Inset: Three-dimensional color map representation of the data in the main panel.

undistorted map of the local spin polarization.

Hence the introduced compact yet highly efficient microscope enables the experimental access to the degree of local spin polarization down to the level of a single electron spin via the detection of the Faraday rotation of the polarization of the probing photons.

4.4 Conclusions

The sensitivity and the spatial resolution of a home-built confocal microscope setup for the detection of local polarization of spin-magnetic moments was quantified. The induced Faraday rotation of the linear polarization of the probe laser photons was detected in a linear polarization basis. The test experiment on a polarized single electron spin state confined in a self-assembled QD was performed by means of a Zeeman-split trion transition during simultaneous resonant optical spin pumping. A maximum Faraday rotation angle of about ± 0.01 deg was measured that corresponds to a microscope setup sensitivity of $\sim 500\ \mu\mathrm{rad}/\sqrt{\mathrm{Hz}}$ at a signal-to-noise ratio of 10. The quantified shot-noise-limited signal-to-noise-ratio of the measured Faraday rotation signal was 10 for an integration time of the order of 1 s. The spatial resolution of the spin polarization detection was determined

by the optical spot dimensions of the confocal microscope setup in accordance with the expectation. Hence the microscope setup proved to be capable of the detection of local spin polarization with single-spin resolution.

Chapter 5

Sample layout for combined optical and transport spectroscopy

A semiconductor heterostructure containing a 2DES was specifically adapted for facilitating optical access to the 2DES. The specific requirements for the heterostructure were an adequate density and mobility of a 2DES that additionally provides well-defined selection rules for optical interband excitation and readout. In this chapter, the optimization process of the heterostructure design based on semiconductor heterostructure simulations and subsequent experimental characterizations of 2DES transport and optical properties is presented and discussed.

5.1 Band structure simulations with *Nextnano3*

For the design of the semiconductor heterostructure, simulations were performed using *nextnano3* [97] which are presented and discussed in this section. The design of the heterostructure for the combined transport and optical experiments was guided by two main objectives. On the one hand, the realization of a high quality 2DES was intented to support the observation of the 0.7-anomaly in a QPC. On the other hand, the 2DES should allow for optical interband excitation of charge carriers in the 2DES. The heterostructure design should furthermore avoid charge carrier excitations in any other heterostructure layer aside from the 2DES in order to eliminate undesired remote charge accumulation or parallel conductivity effects in the sample.

In order to meet the demands, a 2DES was aimed in an $In_xGa_{(1-x)}As$ (GaAs that contains x % In) QW embedded in higher bandgap materials such as GaAs or AlGaAs. The higher-bandgap surroundings make all sample regions but the 2DES transparent to light at optical frequencies which meet the resonance condition for interband excitation of electrons into the reservoir of the 2DES. Provided that the In concentration x is low, optical interband excitations within the $In_xGa_{(1-x)}As$ QW exhibit the lowest energy for interband transitions. At the same time, the quantum confinement in the QW removes the degeneracy of heavy- and light-hole subbands at the Γ-point of bulk zinc blende

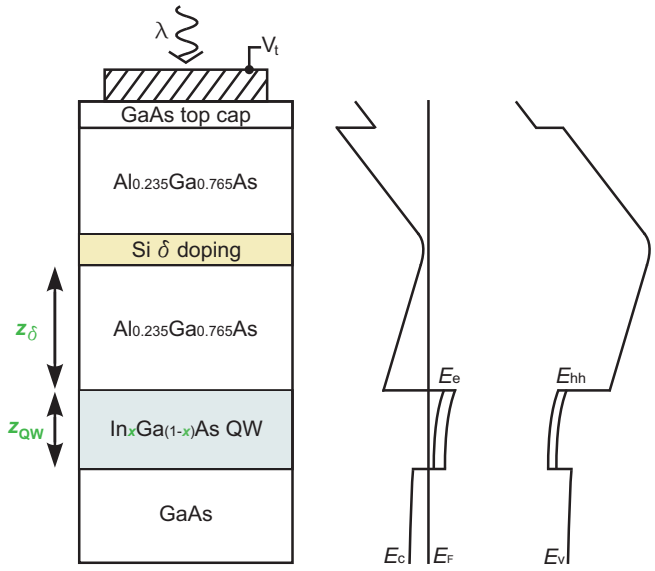

Figure 5.1: Left: Schematic design of the heterostructure on top of a GaAs layer which is MBE-grown on a GaAs substrate. It consists of an $In_xGa_{(1-x)}As$ QW (blue), a AlGaAs spacer layer including a Si δ-doping region (yellow), and a GaAs capping layer. The 2DES forms in the InGaAs quantum well for which the Si impurities provide the excees electrons. A metal gate (hatched, semitransparent in the experiment) induces a built-in Schottky potential and further band structure deformation is provided by an applied voltage V_t. Green: the QW thickness z_{QW}, the QW indium portion x, and the distance z_δ of Si layer from the QW serve as optimization parameters in the *nextnano3* simulations. Right: Band structure profile along the heterostructure growth direction z obtained from the simulation for $V_t = 0$. Shown are the conduction and valance band edges E_c and E_v, the lowest QW-confined electron and heavy-hole levels E_e and E_{hh}, and the 2DES Fermi energy E_F.

semiconductors such as $In_xGa_{(1-x)}As$. This in turn ensures pure dipolar selection rules for optical excitations from the heavy hole subband at the energy E_{hh} into the states at the Fermi energy E_F of the 2DES.

Figure 5.1 illustrates the corresponding basic layout for the simulations of the heterostructure design. The semiconductor layer sequence along the sample growth direction z is shown in the left panel. An $Al_{0.235}Ga_{0.765}As$ layer was sandwiched between GaAs and an $In_xGa_{(1-x)}As$ QW of variable thickness z_{QW} with indium fraction x in the range of $0 < x < 0.1$. The $Al_{0.235}Ga_{0.765}As$ layer contains a few monolayers thin region doped with Si (silicon "δ-doping"). It is located at a distance z_δ above the QW to provide a modulation-doped excess electron population for the 2DES inside the QW. The AlGaAs acts as a tunneling barrier between the 2DES and the Schottky gate (hatched in Fig. 5.1) on top of the heterostructure. By means of an iterative procedure, the overall thickness of the AlGaAs barrier was chosen to be half the wavelength of the simulated QW interband transition to minimize optical interference effects. The topmost GaAs capping layer

prevents oxidization of the AlGaAs barrier. In terms of the heterostructure simulations, the Schottky metal gate is a Schottky potential with tunable potential V_t. This feature integrates the ability of a tunable band bending.

In the right panel of Fig. 5.1, the resulting band structure profile calculated with *nextnano3* is plotted for $V_t = 0$, $x = 0.07$, $z_{QW} = 10$ nm and $z_\delta = 50$ nm. The bended band profile is generated by the built-in Schottky potential at the heterostructure surface as well as the distributions of the excess charges induced by the doping. The bending accounts for the lowest QW electron level E_e to lie below the Fermi energy E_F, in accord with the intented finite 2DES density within the InGaAs QW. In the 1D simulations the Schottky gate is equivalent to an experimental top gate which uniformly covers the heterostructure. This further allows to simulate the pinch-off of the 2DES at sufficiently low V_t.

After having introduced the design, the identified key properties of the intended heterostructure are examined. (1) The 2DES should exhibit well-defined dipolar selection rules for spin-selective excitations or readout which is accomplished by the QW confinement. (2) The semiconductor heterostructure above and below the QW layer should be transparent at the intended optical frequencies. This criterion can intrinsically be satisfied by the heterostructure layout, as evident from the illustrative band structure simulation result in Fig. 5.1. (3) The density of the 2DES should be at least of the order of 3×10^{11} cm^{-2} in order to ensure adequate transport characteristics. To this end, *nextnano3* was used to monitor the 2DES density inside the QW as a function of the optimization parameters x, z_{QW} and z_δ. The density was extracted directly from the simulation results for comparison with the aimed threshold value. (4) At the same time the interband transition wavelength of the QW region, which follows from the energy difference between the lowest QW hole level E_{hh} and E_F, was intended to lie above 830 nm. At this wavelength, optical transitions of carbon impurities [98] are found which inevitably contaminate the heterostructure during the heterostructure-generating MBE growth process. The aimed range $\lambda > 830$ nm is furthermore energetically below the interband transition of the surrounding GaAs (~ 815 nm at 4.2 K) and AlGaAs.

The adjustable parameters in the simulations are highlighted in green in Fig. 5.1. Raising the QW thickness z_{QW} or the QW indium content x predominantly increases the QW interband transition wavelength (equivalent to a redshift in energy). Furthermore, by reducing the distance z_δ between the QW and the δ-doping layer the 2DES density tends to increase. However, conditions such as a smaller z_δ, a smaller QW thickness z_{QW}, or an increased indium concentration x generally reduce the mobility of the QW electrons and are thus to be avoided. This is particularly crucial since the scope of the performed simulations does not include the possibility of mobility calculations.

Figure 5.2 shows the calculated results for three different heterostructures with an indium concentration of $x = 0.07$ and $z_{QW} = 50$ nm. They exhibit the QW thicknesses of 8 nm (dots), 10 nm (rectangles), and 15 nm (squares). This yields a variation in the QW electron density (blue) and the interband transition wavelength (black) as a function of the voltage applied to the Schottky gate. Decreasing the gate voltage increases the

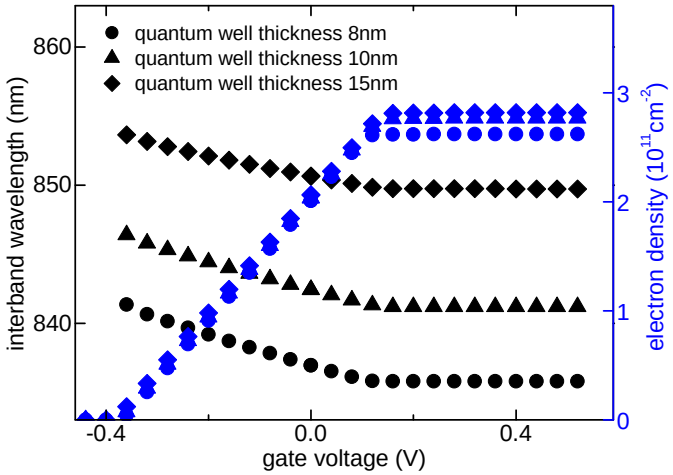

Figure 5.2: Simulated QW electron density (blue) and lowest QW interband transition wavelength (black) as a function of the Schottky gate voltage V_t. Simulations were performed for three different QW thicknesses of $z_{QW} = 8$ nm (circles), 10 nm (triangles) and 15 nm (squares) at a fixed QW indium content of $x = 0.07$ as well as a constant distance $z_\delta = 50$ nm between the δ-doping layer and the QW.

energy of the QW electron levels with respect to E_F which gradually depletes the 2DES inside the QW. This depletion dominates in all three heterostructures at gate voltages below ~ 0.15 V until the 2DES is fully pinched-off around -0.4 V. On the other hand, the interband transition wavelength remains constant for $V_t > 0.25$ V (the onset of the wavelength variation at ~ 0.25 V is not resolved in Fig. 5.2). For lower V_t, the result Fig. 5.2 predicts an universal onset of a pronounced redshift of the optical resonance condition that is associated with a decrease of E_F.

As a result, the predicted maximum 2DES density $n_{2DES} > 2.5 \times 10^{11}$ cm^{-2} as well as the calculated optical transition wavelengths $\lambda > 830$ nm about match the required properties of the 2DES in a 8 nm to 15 nm wide QW within the heterostructure. The obtained result Fig. 5.2 was used as the starting point for the experimental evaluation of the 2DES properties in the following section.

5.2 Basic transport and photoluminescence characterization

The experimental setup used for the sample characterization is very similar to the setup used for the results presented in Sec. 6 and explained in detail in Sec. 6.1.2. Therefore the differences of the characterization setup are discussed here only.

For the purpose of experimental determination of the density and mobility of the 2DES a Hall-bar structure was chosen. Additionally, the sample was intended to enable optical access to the 2DES in order to allow to evaluate accessible optical 2DES transitions.

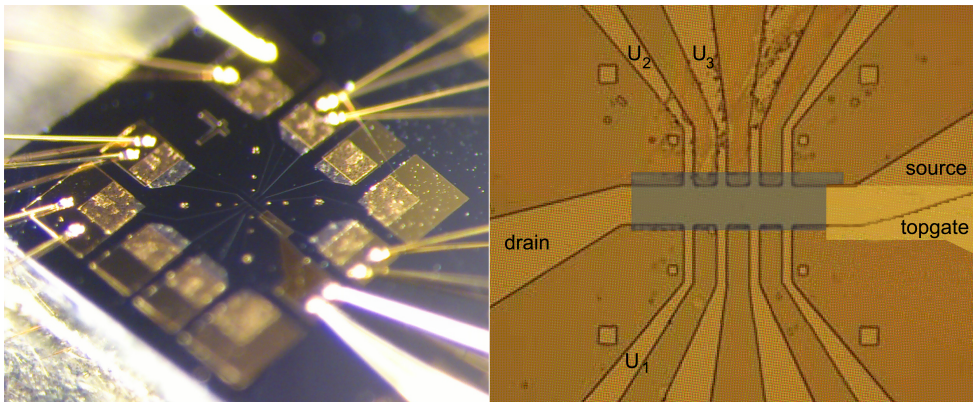

Figure 5.3: Left: Optical microscope image of the bonded Hall bar in the corner of the sample (each connection is bonded twice as a precautionary measure). Right: Scanning electron micrograph showing the mesa edges (dark lines) of the centered Hall-bar section with the used connections being labeled. The top gate consists of a thicker gold part to bridge the mesa edge (bright yellow, labeled) that is also visible in the optical image. The adjoining semitransparent top gate extension (transparent gray rectangle) is made of 5 nm thin titanium and covers the actual Hall bar (covered area of the Hall bar $\sim 200 \times 40\ \mu\text{m}^2$), though it is not apparent in the optical image. Both top gate sections were drawn on top of the actual micrograph for illustration.

The suitably fabricated Hall bar is depicted in Fig. 5.3. The left image shows an optical micrograph of the Hall-bar sample. The mesa was fabricated by conventional wet etching techniques. The resulting mesa edges which form the Hall bar are partly visible in the optical image (bright straight lines). The resulting 2DES areas are connected on the outside via AuGe/Ni/AuGe (gold, germanium, nickel) ohmic contacts (reflective areas) which were interdiffused into the heterostructure. They are covered by larger Au pads, fabricated by optical lithography, which were bonded for the electrical contact to the sample (each is bonded twofold).

On the right in Fig. 5.3 a scanning electron micrograph of the corresponding central Hall-bar section is depicted. The 2DES-bordering mesa edges appear as dark lines. On top of the Hall bar an additional metal gate was fabricated by optical lithography, it is drawn in by hand in the micrograph (bright yellow and gray, labeled) for visualization. This top gate enables the tuning of the 2DES density below the gate via the tuning of an applied voltage (compare Sec. 2.1). The top gate consists of two parts. The actually active section is a thin semitransparent Ti (titanium) layer (transparent gray in the micrograph) that covers the Hall bar. It is contacted across the mesa edge via a second thicker Au layer (bright yellow). The Ti top gate extension provides the required functionality of optical access to the 2DES region of interest. Since the top gate covers the full width of the Hall bar it also enables to pinch off the 2DES source-drain transport channel. As opposed to the Au section, the Ti layer is not visible in the optical image in Fig. 5.3. The electrical connections used for the Hall-bar measurements are apparent from the bond wires in the

optical image and are labeled in the of Fig. 5.3.

In the experiments, the electron density and mobility were extracted from four-terminal DC Hall-voltage measurements which were performed several times before the sample was subjected to laser light for the first time as well as after broad-band and global sample illumination. For this purpose, an external magnetic field $B = B_z$ was applied perpendicular to the 2DES plane. The sample was mounted horizontally planar in a confocal microscope and electric filtering was not performed (as opposed to the geometry and the wiring used in Chapter 6). The initial broad-area sample illumination was performed with the sample deliberately positioned out of the focal plane of the microscope. Subsequently, the confocal microscope with an optical spot size of about 1 μm was solely used to record the local PL response. The PL was spectrally dispersed using a monochromator and detected with a low-noise CCD cooled by liquid nitrogen. All measurements were carried out at a cryogenic bath temperature of 4.2 K.

Based on the heterostructure Fig. 5.1 obtained from the simulation results of the previous section, three heterostructures were grown by MBE with an indium concentration of $x = 0.07$ and a separation between the QW and the δ-doping layer of $z_{\mathrm{QW}} = 50$ nm. The heterostructures only differed in the exhibited QW thicknesses of 8 nm, 10 nm, and 15 nm. First an initial experimental check on the resulting PL energy range at $T = 4.2$ K was done using bare unprocessed samples. Based on this results, the heterostructure with the n-modulation-doped 2DES inside the QW of thickness 10 nm was elected for a detailed experimental analysis of the basic transport and optical properties.

The electron density n_{2DES} and mobility μ_{2DES} of the 2DES were extracted from the measurements of the four-terminal DC Hall voltage $U_{1,2}$ and the longitudinal voltage $U_{2,3}$ (compare Fig. 5.3) at varying magnetic field $0 \leq B_z \leq 5.7$ T. Figure 5.4 presents an illustrative result for both $U_{1,2}(B)$ (blue) and $U_{2,3}(B)$ (black) measured at $V_{\mathrm{t}} = 0$ V as well as $V_{\mathrm{t}} = -1.7$ V. A linear fit of the Hall voltage $U_{1,2}(B)$ at low B determines the carrier density of the 2DES n_{2DES} using

$$n_{\mathrm{2DES}} = \frac{I}{e \cdot \mathrm{d}U_{1,2}/\mathrm{d}B}. \tag{5.1}$$

Here e is the elementary charge and I is the measured source-drain current through the Hall bar. The mobility μ_{2DES} of the 2DES was obtained from the longitudinal voltage at zero magnetic field $U_{2,3}(B = 0)$ using both the relation

$$\mu_{\mathrm{2DES}} = \frac{0.75}{e \cdot n_{\mathrm{2DES}} \cdot U_{2,3}(B = 0)} \tag{5.2}$$

and the electron density n_{2DES} obtained from Eq. 5.1. The scaling factor 0.75 in the numerator adjusts to the particular geometry of the used Hall bar (Fig. 5.3). Furthermore, the basic optical properties of the sample at 4.2 K were studied in terms of the spectral position of the peak of the PL collected from the central gate-covered Hall-bar section.

The transport and optical measurement results are compared with the simulations in Fig. 5.5. Shown are the interband transition wavelength (black) and the 2DES density

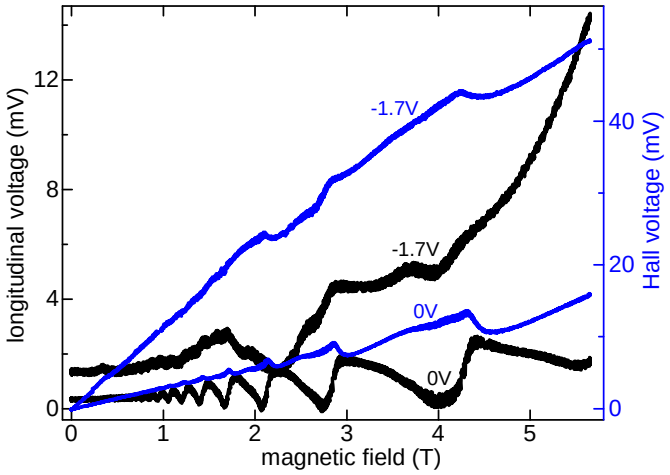

Figure 5.4: Measured longitudinal voltages $U_{2,3}$ (black) and Hall voltages $U_{1,2}$ (blue) as a function of the perpendicularly applied magnetic field at two top gate voltages $V_t = 0$ V and -1.7 V. The distortions of the Hall voltage between plateaus are caused by an asymmetry of the geometry of the used Hall bar (compare Fig. 5.3) which effects a finite Ohmic resistance contribution to $U_{1,2}$. The data was measured at the temperature 4.2 K.

(blue) as a function of the top gate voltage. The circles (triangles) indicate the measurement results obtained before (after) the first global Hall-bar illumination with continuous wave (CW) lasers at 815 nm and 830 nm. The dashed lines are the corresponding simulation results taken from Fig. 5.2 for comparison. In the simulations, all silicon atoms of the δ-doping region were assumed to be ionized which is realized experimentally by sample illumination.

The initial 2DES densities are in good agreement with the predictions of the calculations. Before sample illumination, both differ by $\sim 1 \times 10^{11}$ cm^{-2} and exhibit a very similar slope if V_t is decreased leading to a similar 2DES pinch-off at $V_t \sim -0.5$ V. An increase in n_{2DES} on sample illumination is anticipated due to induced donor level depletion which releases charges trapped during the sample cool down. This is consistent with the observed illumination-induced change by $\sim +30$ % to $n_{2DES} \sim 4.2 \times 10^{11}$ cm^{-2} (blue triangles in Fig. 5.5). The increase of the 2DES charge density, compared to the simulated result, could partly stem from illumination-induced excess charge release of other impurities (e. g. carbon) present in the heterostructure. The corresponding increase in E_F requires stronger depletion in order to fully pinch off the 2DES. This is expressed in the considerably decreased pinch-off voltage of $V_t = -2$ V after sample illumination (blue triangles). Moreover, both the calculated (at $V_t \gtrsim 0.2$ V) and the measured n_{2DES} (at $V_t \gtrsim -0.9$ V) are almost unaffected by the change of the top gate voltage in the higher 2DES density range. That indicates strong pinning of the residual positively charged donor levels of the δ-doping layer at E_F. Repeated illumination of the sample did not yield significant changes in the 2DES density (half-filled triangles in Fig. 5.5) indicating the long-term low-temperature stability of the electrostatic environment after the initial Si

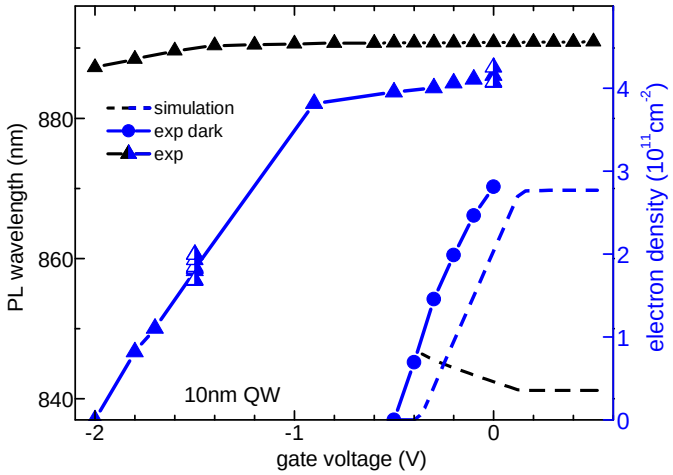

Figure 5.5: Basic transport and optical characterization of the heterostructure containing the QW of thickness $z_{\mathrm{QW}} = 10$ nm, 7 % QW indium concentration, and a doping layer separation of $z_\delta = 50$ nm. Shown are the 2DES electron density n_{2DES} (blue) and the lowest QW transition wavelength λ_{QW} (black) versus top gate voltage, for both the measured data (symbols, lines are guides to the eye) and the calculated results (dashed lines, equal to Fig. 5.2). For the experimental data, n_{2DES} was determined using Eq. 5.1 and λ_{QW} was extracted from the PL maximum (compare Fig. 5.6 below). Circles and triangles furthermore distinguish the measurements performed before and after the first illumination of the central Hall-bar area. Half-filled triangles correspond to 2DES densities after repeated sample illuminations. The PL was obtained from the confocal microscope spot being positioned in the center of the top-gate-covered Hall-bar region (compare Fig. 5.3). Excitation power: 7 μW for -1 V $\leq V_{\mathrm{t}} \leq 0.6$ V and 0.3 μW for $V_{\mathrm{t}} < -1$ V, uniform excitation wavelength: 830 nm, bath temperature: $T = 4.2$ K.

donor ionization has been initiated. The mobility of the 2DES $\mu_{\mathrm{2DES}} \sim 70000$ cm^{2}V^{-1}s^{-1} was experimentally determined within the entire gate voltage range above -1.5 V after sample illumination (data not shown).

Despite the good agreement of the 2DES densities obtained from the simulations and the experiments, considerable discrepancy is found between the calculated and the observed optical interband transition wavelengths in Fig. 5.5. The PL peak as a function of V_{t} (black triangles) was read out around the center of the gate-covered Hall-bar section using the excitation wavelength of 830 nm set close to the transitions associated with the intrinsic carbon impurity states in GaAs at 4.2 K [98] for an efficient optical generation of charge carriers. In comparison to the calculated lowest QW optical transition wavelength (dashed black line), the measured PL is shifted by about 50 nm (83 meV) toward lower energies. Furthermore a reversed energy dispersion as a function of top gate voltage is present in the form of an experimental blueshift as opposed to the calculated redshift for decreasing 2DES densities. The disagreement could partly originate from excitonic effects and the QCSE present in the heterostructure which were both omitted in the simulations. However, the main requirement for the heterostructure design has been successfully ac-

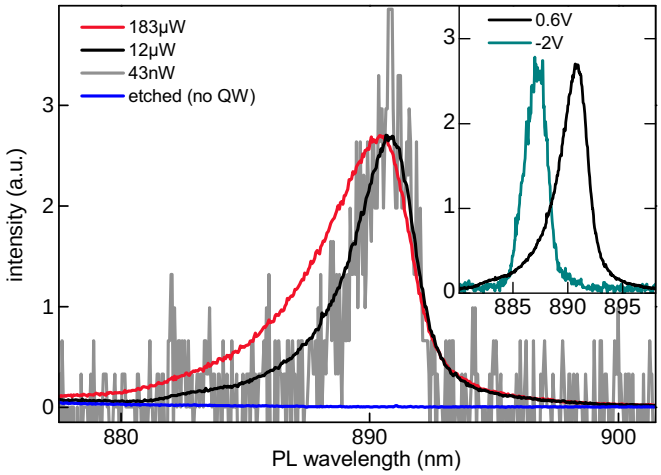

Figure 5.6: Hall-bar sample ($z_{\mathrm{QW}} = 10$ nm): Spectrally resolved PL collected from the confocal microscope spot and equally scaled to the PL peak. Main panel: PL from the center of the gate-covered Hall-bar section using sample-incident excitation powers of $P_{\mathrm{exc}} = 183$ μW (red), 12 μW (black curve, main panel and inset), and 43 nW (gray). Added is a PL spectrum recorded with the spot located next to the Hall bar where the QW was etched away (blue) (top gate voltage $V_{\mathrm{t}} = 0.6$ V (flatband in GaAs)). Inset: PL spectra at two different top gate voltages of $V_{\mathrm{t}} = 0.6$ V (black) and -2.0 V (green, $P_{\mathrm{exc}} = 300$ nW). (CW excitation wavelength: 830 nm, bath temperature: $T = 4.2$ K)

complished: Intrinsic optical transitions in the QW-based 2DES with adequate density and mobility were found in the transparent sample.

Figure 5.6 presents the spectral shape of the measured PL of the sample. Three spectra are shown (gray, black, red) that were obtained from the central gate-covered Hall-bar region at a CW laser excitation wavelength of 830 nm and $V_{\mathrm{t}} = 0.6$ V (flatband in GaAs, 4.2 K). The PL main peak at $\sim$ 891 nm exhibits an asymmetric line shape even at the lowest excitation powers down to $\sim$ 40 nW (gray spectrum). The PL line shape very much resembles the characteristic shape of a Fermi edge singularity [99–101] which is expected to be present in the environment of high 2DES densities. There is also evidence of (at least) one higher-energy shoulder, spotted around $\sim$ 883 nm, with indications remaining at $\sim$ 40 nW. Increasing P_{exc} considerably (red PL curve) further induces a minor blueshift of the PL maximum that is accompanied by a pronounced increasingly asymmetric broadening. These PL features were uniformly found at all investigated excitation spot locations along the Hall bar. The measured PL line shape is consistent with an expected double peak due to the recombination of excitons X (residual higher-energy peak) and negatively charged excitons X^- (trions, dominating PL peak) consisting of one photo-excited hole Coulomb-bound to two electrons in a QW-based 2DES [102, 103]. Similarly increased differences between the binding energies of X and X^- of $\sim$ 10 meV have been observed in high-density 2DESs [104]. Moreover, the relative heights of the correspondingly two peaks with the strongly favored trion recombination is compatible with recombination in the presence of the experimentally verified high 2DES "background" den-

sity 4.2×10^{11} cm^{-2} [105]. This argument is also in accord with the observed unchanged PL line shape in the main panel of Fig. 5.6 at the constant 2DEG background density (V_t is kept fix) and illumination powers that differ by nearly four orders of magnitude: the high dopant-induced 2DES density ensures the favored trion transitions independently of the optically generated electron or hole population.

One spectrum is added in Fig. 5.6 taken from a sample region where the QW was etched away (blue). No PL response is visible in the relevant spectral range. Thus all features inferred above justify the conclusion that the observed PL stems from optical recombination within the QW of electrons with energies $\sim E_F$ which is trion-dominated.

A dependence of the PL on the 2DES density is visible in the inset of Fig. 5.6 showing the 12 μW spectrum (black, $V_t = 0.6$ V) of the main panel and the PL measured at $V_t = -2.0$ V (green spectrum). Additionally to a gradual evolution of the PL main peak toward a symmetric Gaussian peak (fit not shown) the peak exhibits a distinct blueshift if the 2DES density decreases (compare Fig. 5.5). Similar PL shifts toward higher energies for reduced 2DES densities have been observed in the case of QW-confined 2DESs [104]. Moreover, the vanishing Fermi-edge singularity at decreased 2DES densities further substantiates the origin of the PL sample response.

5.3 Conclusions

Guided by the results of the performed *nextnano3* simulations a semiconductor heterostructure was obtained which complies with the required specifications. Due to the QW-based design, the 2DES intrinsically provided the interband optical selection rules which form the basis for controlled 2DES excitation and readout. The experimentally verified 2DES densities and mobility at the same time facilitate ballistic electron transport through a QPC constriction in the 2DES. The QW interband transition energies were located below the known carbon impurity optical transitions in the heterostructure yielding a promising starting point for well-defined opto-transport experiments in the 2DES. The measured PL characteristics furthermore provided the experimental verification of the actual specific QW recombination energies around the Fermi energy. Additionally, the dominating recombination of negatively charged excitons (trions) in the QW at the high permanent 2DES "background" density was indicated.

Chapter 6

Photoresponse of a quantum point contact

The basic transport and optical properties of the heterostructure characterized in Chapter 5 proved to be very promising for combined opto-transport studies of a QPC. To this end, a sample with QPCs in different geometries was fabricated. This chapter presents the investigation of the response of a QPC to local, resonant optical excitation of charge carriers in QPC proximity. First the transport properties of a specific QPC were evaluated, both before and after optical illumination of the sample. The QPC performance *during* illumination was subsequently studied using an experimental setup which allowed the simultaneous detection of both the transport current response and the current response of the QPC due to the local optical excitation without mutual interference. For all results presented in this chapter the current response caused by the optical excitation of the 2DES in QPC vicinity is referred to as the photoresponse (PR) of the QPC.

6.1 Combined optical and transport spectroscopy

6.1.1 Sample layout

A specific layout was designed to access the vicinity of a QPC by means of a confocal laser spot for excitation. Based on the characterization results presented in Chapter 5, the QPC was processed on a sample that contains a n-modulation-doped 2DES located in an $In_{0.07}Ga_{0.93}As$ QW with a thickness of 10 nm. Figure 6.1 shows optical microscope images of the QPC layout. In panel (a) the selected and bonded writing field is shown as a whole whereas (b) is a zoom to the central section of (a). Various QPC geometries were fabricated to comprise constriction geometries which facilitate the regime of the 0.7-anomaly. The chosen QPC arrangement is shown in the close-up of Fig. 6.1(b). The centered square mesa with the starlike surrounding mesa connections contains two neighboring sections each composed of 4 different QPC geometries and one large covering semitransparent top gate. The Au gates (darker yellow) on top of the mesa were fabricated

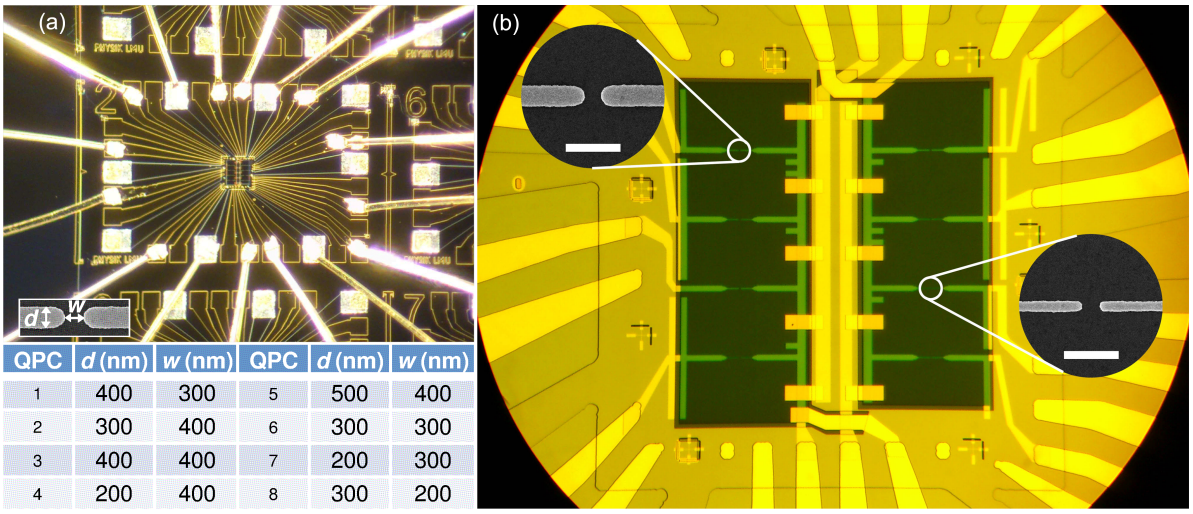

QPC	d (nm)	w (nm)	QPC	d (nm)	w (nm)
1	400	300	5	500	400
2	300	400	6	300	300
3	400	400	7	200	300
4	200	400	8	300	200

Figure 6.1: (a) Optical microscope image of the fabricated sample that shows the writing field composed of gold gates (yellow) and mesa (tapered white lines). (b) Zoom to the central field of (a): The mesa square (dark lines, edge length: 160 μm) contains two adjacent arrangements of 4 different QPC geometries of which two are magnified in SEM pictures (scale bars: 1 μm). Every QPC group is covered with a large top gate (dark gray rectangles) of 5 nm semitransparent nickel-chromium (NiCr) that is electrically disconnected from the gates below by a layer of cross-linked PMMA, visible as brighter gray rims framing the top gates. The outer gates bridge the mesa edges (brighter yellow, thickness: 200 nm) and the inner gates (darker yellow, thickness: 30 nm) include the QPCs. The QPC dimensions are summarized in the table in (a). They are listed according to their actual positions in (b).

via standard electron beam lithography. They define the QPCs of which two are shown in the SEM images of Fig. 6.1(b) (scale bars: 1 μm). Thicker Au contacts (brighter yellow, processed with optical lithography) connect the inner Au gates across the mesa edges to the outer bond pads visible in Fig. 6.1(a). Each top gate (dark gray rectangle) is spatially and electrically disconnected from the underneath gates by a layer of cross-linked PMMA (poly-methyl-methacrylate) visible as a slightly brighter narrow frame around each top gate in Fig. 6.1(b). As a precautionary measure, each top gate was designed to allow to be contacted by one out of two separate outer bond pads (compare Fig. 6.1(b)). The Au below the top gates appears green in the optical microscope close-up.

Eight different QPC geometries with rounded tip gates were chosen based on an earlier work on the visibility of the 0.7-anomaly in GaAs-based QPCs [106]. Their dimensions are summarized in the table in Fig. 6.1 according to the actual arrangement on the sample using the notation of the inset in (a). Each of the two QPC sets comprises one shared gate in the middle of the mesa and four individual gates facing laterally. This enables to control each QPC individually with a minimum number of separate gate connections. The QPCs were purposely placed with as large as possible mutual lateral distances which intends to facilitate optical characterization of each QPC surroundings without the interference of nearby structures. Moreover, the top gates were designed to cover an as large as possible

area of the optically accessible QPC vicinity in order to enable simultaneous 2DES density control in the optically investigated regions. Each QPC set in Fig. 6.1(b) has a separate source (below) and drain (above) connection, also evident from the bonding scheme in panel (a).

6.1.2 Experimental setup

The measurements discussed in this Chapter 6 were performed at the QPC no. 8 (QPC8, compare Fig. 6.1) using a home-built combined optical and transport setup. The wiring of the setup is shown schematically in Fig. 6.2. The source (bottom) and drain (top) 2DES connections are indicated by black squares on top of the sample picture. Using QPC8 in Fig. 6.2, its source contact is supplied by a DC voltage via a passive DC-AC adding unit ("add"). A transimpedance amplifier (I/V) on the drain side grounds the 2DES current I enabling electrical readout. The transport DC current $I_{\mathrm{sd}}^{\mathrm{dc}}$ with a voltmeter (at the I/V output in Fig. 6.2), the AC transport current (lock-in 1), and the AC photoresponse current (lock-in 2) with 2-channel lock-ins were measured simultaneously. The lock-in 1 is triggered by an internal frequency generator ("f" in Fig. 6.2) which delivers an AC current at the frequency f_{tr} to the source contact via the adding unit, with the applied amplitude after the adder of $\delta V = 52\ \mu$V. The lock-in 2 is triggered by the controller of the laser chopper with modulates the sample excitation intensity at an independent modulation frequency $f = f_{\mathrm{chop}}$ (see the explanation of the optical part of the setup below). In the experiments $f_{\mathrm{tr}} = 77.1$ Hz was maintained while the variable f_{chop} was chosen so that $|f_{\mathrm{tr}} - f_{\mathrm{chop}}| > 10$ Hz was retained. This constraint for the difference in modulation frequencies well exceeds each lock-in band width. Thus it is sufficient for separate transport and PR readout. While measuring the QPC8 responses all remaining QPCs of the right QPC section were kept open via a separate voltage source (top right in Fig. 6.2) allowing to collectively ground the respective remaining right QPC gates. The voltage applied to the corresponding top gate is supplied by a fourth voltage source (depicted just left of the source-supplying voltage source in Fig. 6.2). The remaining two unused 2DES connections of the left sample gates section were kept floating. Additionally all other unused sample gates (which may include the top gate of QPC8 itself) were grounded in the experiments. This procedure ensured a well-defined electrostatic environment under optical excitation. All electrical sample connections were filtered (LPF in Fig. 6.2) for AC noise reduction. Furthermore, for each used gate as well as each idle gate connection the current flowing onto (or off) the gate was recorded simultaneously during each measurement via the voltage drop at a serial ohmic resistor, as indicated in Fig. 6.2.

One section of the optical part of the setup is shown schematically in Fig. 6.3. Two single-mode emission lasers were used. Laser 1 (laser 2) is tunable in the wavelength range of 860 - 930 nm (780 - 840 nm). As opposed to laser 2, laser 1 is equipped with an external Faraday isolator to avoid back reflections for laser stability. While laser 2 was mainly used for initial optical characterizations of the 2DES, laser 1 was used for the resonant 2DES

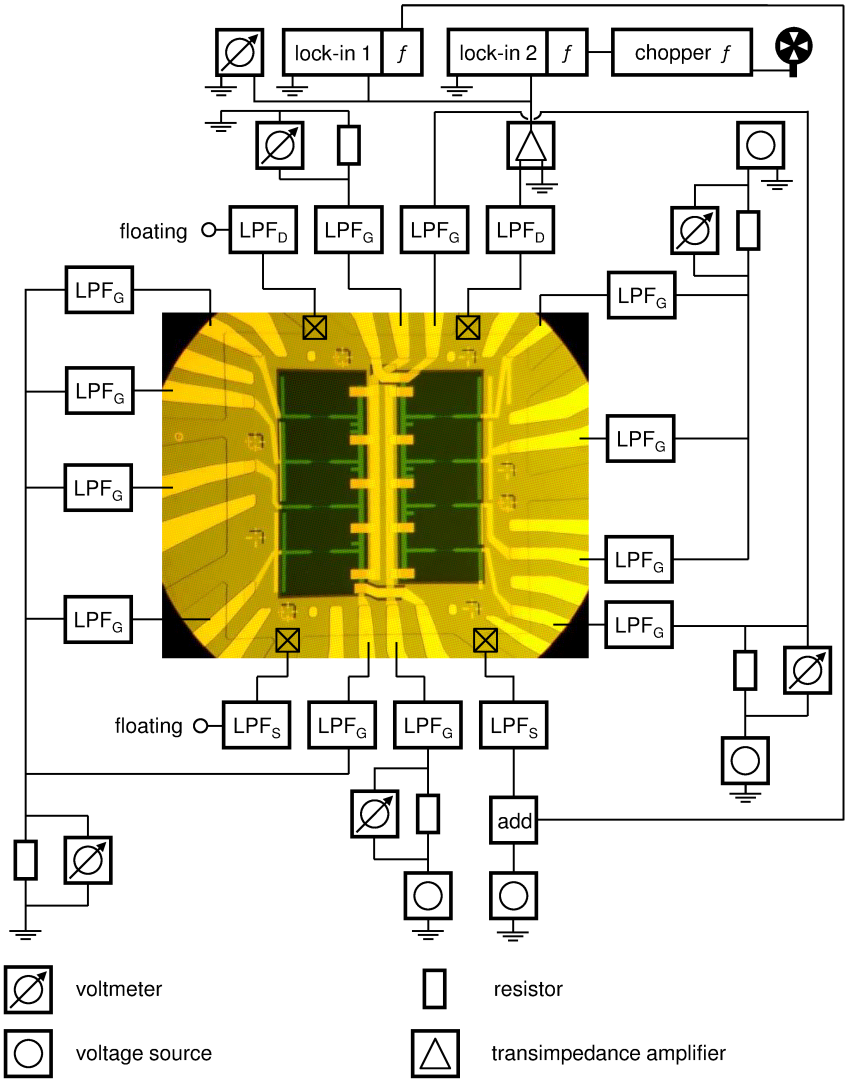

Figure 6.2: Schematic of the wiring of the sample. See text for details.

excitation measurements (Sec. 6.2). A constant excitation power of laser 1 is crucial to conduct sensitive QPC PR measurements. Thus laser 1 was equipped with an active power stabilization unit [107] of which the main optical components are marked by the dashed rectangle in Fig. 6.3. The power stabilization is controlled by an active PID controller which stabilizes the emission power of laser 1 in its full emission wavelength range. In order to maintain single-mode emission of laser 1 a scanning Fabry-Perot was used for monitoring. The emission power of both lasers could be chopped with a chopper wheel (shown in Fig. 6.3, and in Fig. 6.2 for clarity) for differential lock-in measurements. The laser intensity was adjusted (intensity filters in Fig. 6.3) before coupling into a single-mode optical fiber. Fiber paddles (polarization controller in Fig. 6.3) were used to compensate for the change in laser-light polarization induced by the fiber.

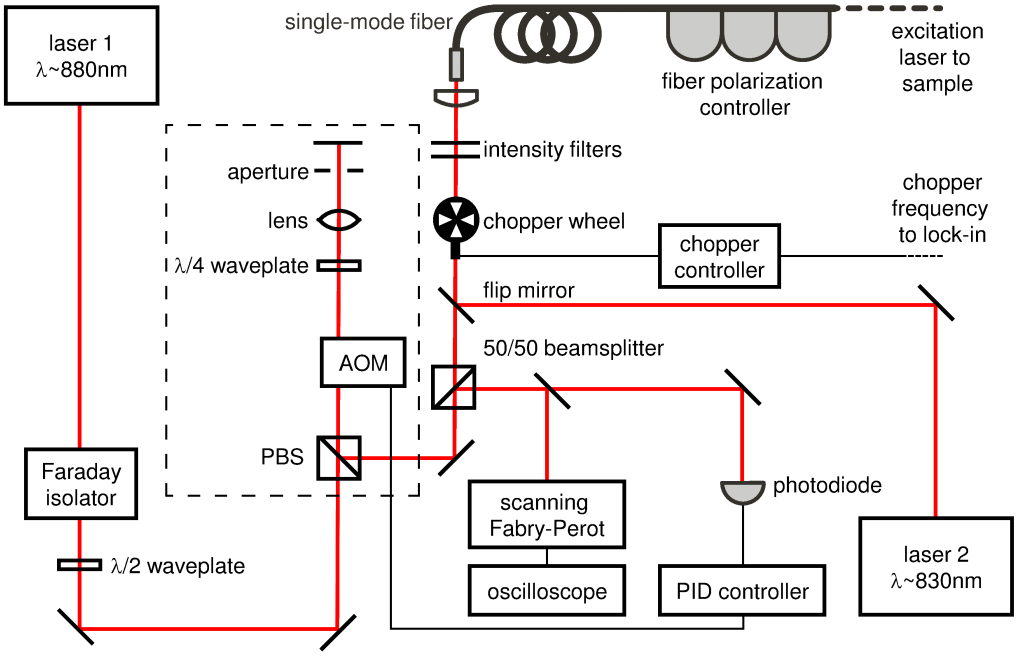

Figure 6.3: Overview of one section of the optical part of the setup. It mainly contains two excitation lasers of which one is equipped with a power stabilization (dashed rectangle). Both lasers can be chopped before being coupled into the single-mode optical fiber. See the text for further details.

The single-mode fiber output was connected to the horizontal side arm ("excitation" arm) of the optical microscope shown schematically in Fig. 6.4. Band pass filters (BP) block secondary light generated within the optical fiber. Subsequent polarization optics permit the adjustment of the polarization of the excitation (green optical path in Fig. 6.4). In the experiments, the photodiode used for the power stabilization of laser 1 was positioned on the opposite side of the beam splitter that directs the excitation light toward the sample. This additionally compensates for potential temporal changes of the excitation power after the polarization optics in the microscope's side arm. The sample was mounted on a "L"-shaped adapter, referred to as Voigt adapter, which positioned the sample vertically in the laboratory frame of reference. The Voigt geometry allows the application of the magnetic field parallel to the sample surface and thus the 2DES plane in the employed configuration using a magnet with a rigid coil position, as illustrated in Fig. 6.4. The Voigt adapter was mounted on a xyz-nanopositioner unit for individual sample positioning. The excitation spot of the microscope is diffraction-limited to about 1.5 μm full width at half maximum (FWHM) on the sample surface. The FWHM was determined by a separate measurement [92] by means of one of the gold gates on top of the mesa (see Sec. 6.1.1). The laser light reflected off the sample surface was monitored by a CCD image sensor ("imaging CCD" in Fig. 6.4). It was used as a reference while aligning

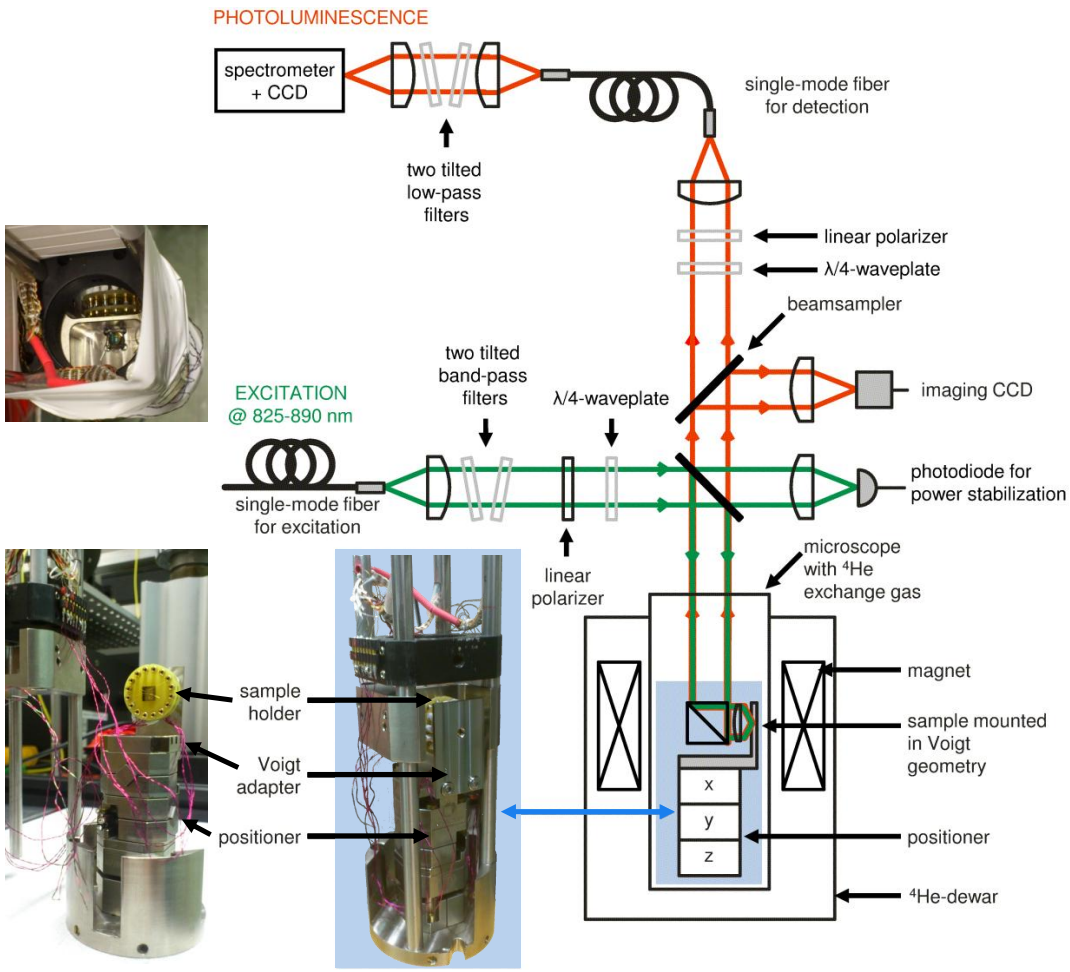

Figure 6.4: Schematic of the second section of the optical part of the setup. The blue highlighted component is also shown in the photographs in the assembled (right and upper left photograph) and disassembled state (lower left photograph). For comparison, the sample located in the center of the sample holder has an edge length of around 5mm. See text for details.

the sample with respect to the position or the focal plane of the confocal excitation spot. The setup additionally allows to read out the sample photoluminescence (contained in the red optical path in Fig. 6.4), optionally in a polarization-resolved basis, via a second vertical microscope arm. The photoluminescence is coupled into a second single-mode fiber on top of the microscope and analyzed with a spectrometer and a liquid-nitrogen-cooled CCD. Additional BP filters are used in front of the spectrometer in order to block the laser.

The lower part of the microscope is located in a closed housing (see Fig. 6.4) which was evacuated and subsequently filled with He^4 exchange gas of low pressure. The housed microscope part was placed in a liquid He^4 bath cryostat. All measurements presented in this Chapter 6 were performed at the bath temperature of 4.2 K. For the illustration, Fig. 6.4 also presents photographic pictures taken from the blue framed section of the

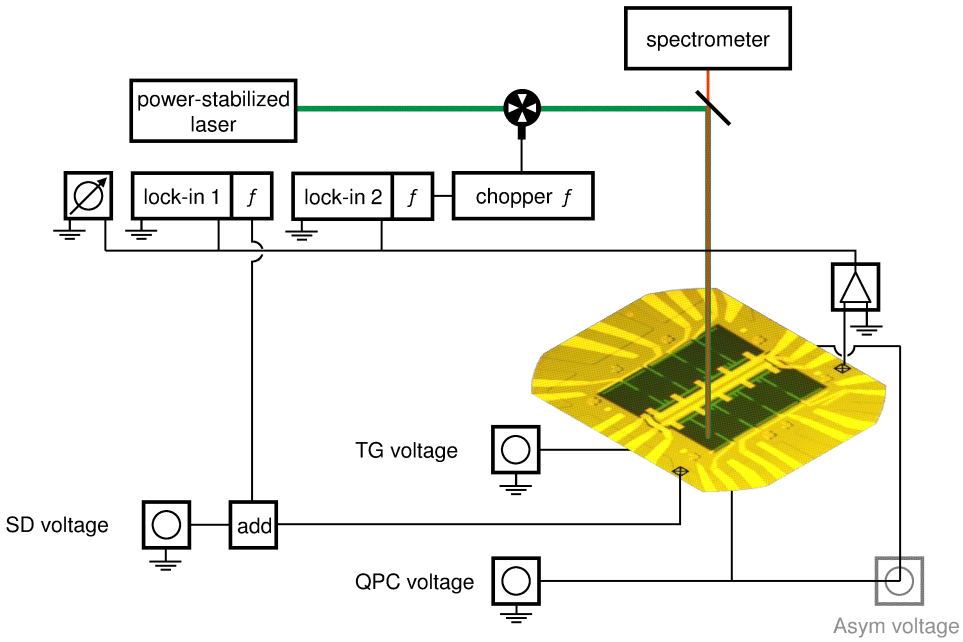

Figure 6.5: Simplified overview of the combined arrangement of the electrical and optical setup parts.

microscope. Finally Fig. 6.5 provides a simplified overview over the overall setup arrangement for clarity.

6.1.3 Initial characterization with transport spectroscopy

This section presents and discusses the measured conductance of the QPC8 of the sample Fig. 6.1 (Sec. 6.1.1) before sample illumination has been induced for the first time after the sample cool down. A series of conductance curves as a function of the QPC gate voltage V_{QPC} is presented in Fig. 6.6. Each of the pinch-off curves was measured at a different top gate voltage V_{t} equidistantly chosen between -0.8 V (rightmost) and 0.6 V (leftmost pinch-off curve). Raising the top gate voltage increases the 2DES carrier density and thus E_{F} in the vicinity of the QPC. This has to be compensated for by a lowered QPC gate voltage in order to keep the QPC potential in the 1D channel center above E_{F} and therefore the QPC pinched-off. Although thermally smeared out, four QPC conductance plateaus are visible toward the highest 2DES densities at $V_{\mathrm{t}} = 0.6$ V marked by the horizontal gray lines in Fig. 6.6. Each emerging plateau broadens and becomes increasingly pronounced at higher 2DES densities because the induced steeper lateral confining potential at a given subband state raises the QPC sub-level spacing within the constriction region. Additionally a distinct kink occurs at about $0.6G_{\mathrm{Q}}$ throughout the whole top gate voltage range of $\Delta V_{\mathrm{t}} = 1.4$ V (dashed line in Fig. 6.6). The position of the kink as well as its shape and prominent appearance with respect to the increasingly

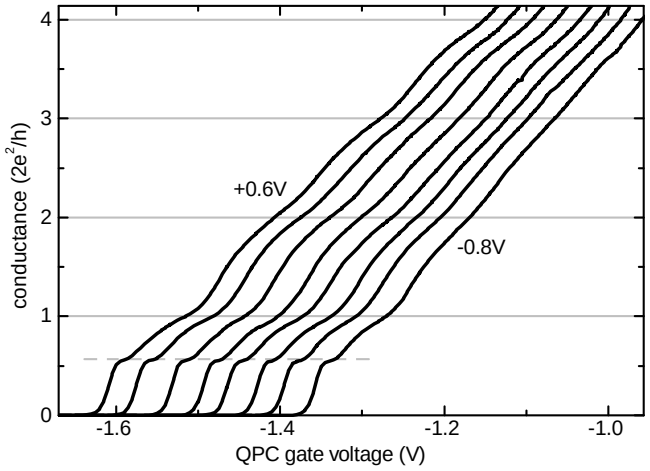

Figure 6.6: Conductance of QPC8 measured before the first sample illumination ($T = 4.2$ K). Eight pinch-off curves were recorded as function of the QPC gate voltage, each at a different top gate voltage between $V_t = -0.8$ V and 0.6 V in steps of $\Delta V_t = 0.2$ V (the constant setup resistance has been subtracted). Integer values of the spin-degenerate conductance quantum $2e^2/h$ are highlighted by the gray solid lines. The additional pronounced shoulder at around $0.6G_Q$ (dashed line) is attributed to the 0.7-anomaly.

smeared out QPC conductance plateaus [24, 25] are clear indications of a 0.7-anomaly.

6.2 Dynamic and static photoresponses

For all the following results the responses caused by the source-drain current modulation, termed the transport response, and the PR of the QPC were measured simultaneously at $V_t = 0$.

6.2.1 Simultaneous transport response and photoresponse

For the PR, the excitation spot position in the 2DES plane $(x, y)_{exc}$ is defined as shown by the QPC SEM image in the inset of Fig. 6.7(b). In particular, the laser exciting the 2DES on the source side of the QPC is referred to as $x_{exc} > 0$. For all measurements $y_{exc} = 0$ was chosen.

Figure 6.7 presents in (a) the measured transport differential conductance g_{tot} (light blue dots, left y-axis) as well as in (b) the simultaneous PR magnitude $|I_{ph}|$ as a function of the QPC gate voltage V_{QPC} (dots). The excitation spot was positioned at $x_{exc} = 0.5$ μm and a constant DC voltage of $V_{sd}^{dc} = -100$ μV was applied at the source contact of the QPC. Figure 6.7 was measured after the central region of the used writing field (compare Sec. 6.1.1) had been globally illuminated within the whole accessible wavelength range beyond the GaAs bandgap, 815 nm $\leq \lambda_{exc} \leq$ 930 nm. As a result, without any sample

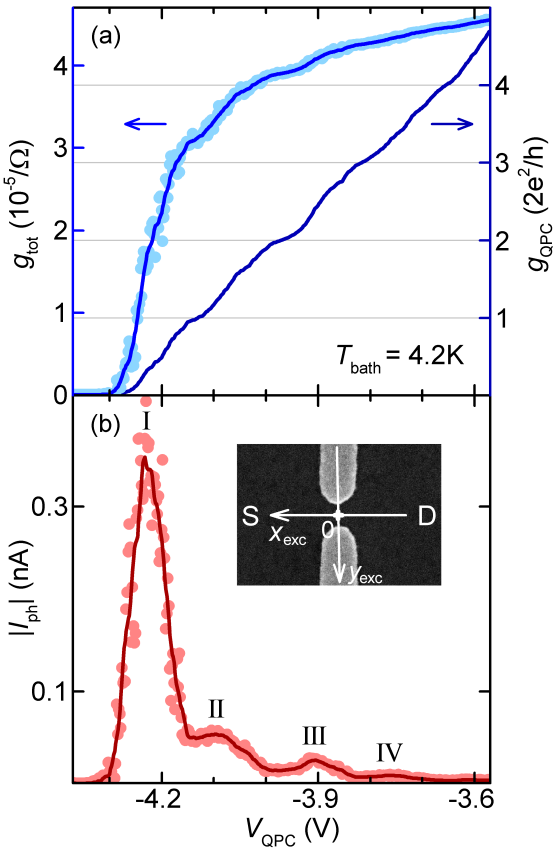

Figure 6.7: Simultaneously measured transport response (a) and PR (b) of a QPC after global sample illumination. Circles are raw data and solid lines are a moving-average of the raw data (bin: $\Delta V_{\mathrm{QPC}} = 25$ mV). (a) Differential conductance g_{tot} (light blue) and the corresponding QPC conductance g_{QPC} (dark blue). (b) The PR exhibits consecutive maxima numbered for reference ($T_{\mathrm{bath}} = 4.2$ K, $P_{\mathrm{exc}} = 42$ nW, $f_{\mathrm{chop}} = 112$ Hz, $V_{\mathrm{sd}}^{\mathrm{dc}} = -100$ μV, excitation spot position $(x, y)_{\mathrm{exc}} = (0.5, 0)$ μm). Inset: SEM image of the QPC, the coordinate system specifies $(x, y)_{\mathrm{exc}}$.

illumination the QPC consistently pinched-off at about $V_{\mathrm{QPC}}^{\mathrm{pinch-off}} = -3.5$ V (data not shown) which corresponds to an illumination-induced shift of $\Delta V_{\mathrm{QPC}}^{\mathrm{pinch-off}} \simeq -2$ V (compare Fig. 6.6). According to the 2DES characterization results in Sec. 5.2 (see Fig. 5.5) $\Delta V_{\mathrm{QPC}}^{\mathrm{pinch-off}} \simeq -1.5$ V is expected to arise from the illumination-induced increase in E_{F}. A further contribution can be anticipated from the fact that this $\Delta V_{\mathrm{QPC}}^{\mathrm{pinch-off}}$ can induce a change in the QPC constriction potential toward steeper barriers which raise the level spacing of the 1D energy spectrum. This most likely accounts for the whole residual $\Delta V_{\mathrm{QPC}}^{\mathrm{pinch-off}} \simeq -0.5$ V. On top of that, another considerable shift $V_{\mathrm{QPC}}^{\mathrm{pinch-off}} \simeq -0.8$ V is evident from Fig. 6.7(a) which adds *during* local illumination of the QPC surroundings. It can be attributed to both an effective voltage drop across the heterostructure and a local screening effect, both caused by the illumination-induced finite conductivity in the heterostructure.

Before the evaluation of the recorded data a moving-average was applied which is shown in Fig. 6.7 by the lines on top of the data. By correcting for the constant overall lead resistance, g_{tot} yields the QPC contribution to the conductance g_{QPC} in Fig. 6.7(a) (dark blue). Weak conductance plateaus at integer multiples of G_0 (horizontal lines) are visible. In contrast to Fig. 6.6, however, no indication of the 0.7-anomaly was observed after the first sample illumination (both without and during local QPC illumination).

The measured PR $|I_{\mathrm{ph}}|$ in Fig. 6.7(b) features distinct local maxima of decreasing height which appear about between QPC conductance plateaus. They are labeled I - IV for reference and are discussed in detail below.

6.2.2 Dynamic photoresponse

Fig. 6.8(a) shows the phase-resolved PR measured as a function of V_{QPC} at various modulation frequencies f_{chop} between 113 Hz (light red) and 1713 Hz (black). The real (upper panel) and imaginary part (lower panel) of I_{ph} were recorded at constant $x_{\mathrm{exc}} = 0.6\ \mu$m. With increasing f_{chop}, $\mathrm{Re}\,[I_{\mathrm{ph}}]$ monotonically decreases whereas $\mathrm{Im}\,[I_{\mathrm{ph}}]$ passes through a maximum as indicated by the arrows. This dependence is semi-logarithmically plotted versus f_{chop} in Fig. 6.8(b) (dots for $x_{\mathrm{exc}} = 0.6\ \mu$m) for the PR maximum I (compare the dots in Fig. 6.8(a)) for the real (upper panel) and imaginary PR part (lower panel). Fig. 6.8(b) additionally shows the corresponding PR maximum I in the covered frequency range $f_{\mathrm{chop}} \leq 2$ kHz for four similar measurements at various excitation spot positions $x_{\mathrm{exc}} = 0\ \mu$m (black dots) to 1.5 μm (lightest gray dots) (lock-in phase for all x_{exc}: $9 \pm 10\,^{\circ}$). The data were offset for clarity as indicated by the short horizontal lines on the right y-axis in Fig. 6.8(b).

This representation is reminiscent of the relaxation dynamics conceptual similar to the Drude model [108]:

$$\begin{aligned} \mathrm{Re}\,[I_{\mathrm{D}}] &= \frac{I_0}{1+\omega^2\tau^2} \\ \mathrm{Im}\,[I_{\mathrm{D}}] &= \frac{\omega\tau I_0}{1+\omega^2\tau^2}\ . \end{aligned} \tag{6.1}$$

For each x_{exc} in Fig. 6.8(b), Eqs. 6.1 were used to simultaneously fit $\mathrm{Re}[I^{\mathrm{I}}_{\mathrm{ph}}]$ and $\mathrm{Im}[I^{\mathrm{I}}_{\mathrm{ph}}]$ with $\omega = 2\pi f_{\mathrm{chop}}$. The corresponding relaxation time τ and the static PR limit I_0 (I_{D} for $\omega \to 0$) were used as free fitting parameters. The fit results shown in Fig. 6.8(b) (solid lines) reproduce the data very well. Two main features are revealed upon moving the confocal excitation spot away from the QPC which are best visible in the lower panel of Fig. 6.8(b): the peak values of both $\mathrm{Re}[I^{\mathrm{I}}_{\mathrm{ph}}]$ and $\mathrm{Im}[I^{\mathrm{I}}_{\mathrm{ph}}]$ drop and the resonance shifts to lower f_{chop} values. Both properties are reflected in the behavior of the deduced fit parameters in the context of the relaxation model Eqs. 6.1: if x_{exc} is increased the static PR limit I_0 is decreased and the characteristic relaxation time τ is increased.

Eqs. 6.1 were correspondingly fitted to the maxima II, III and IV of the PR for all $0 \leq x_{\mathrm{exc}} \leq 1.5\ \mu$m. In all fit results the above properties of I_0 and τ were present, corre-

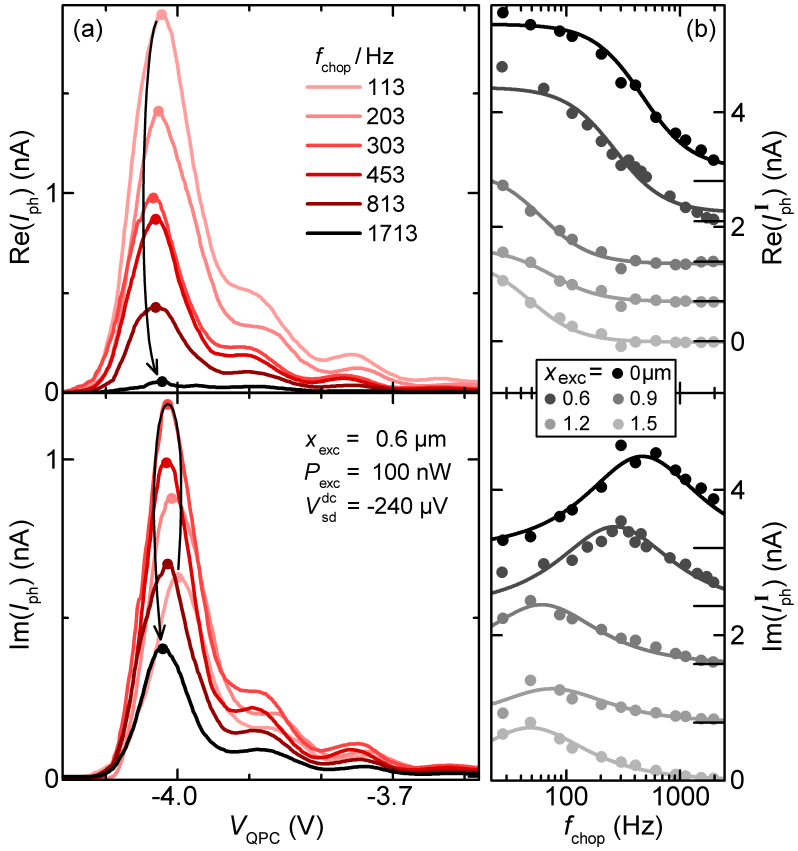

Figure 6.8: (a) Real (upper panel) and imaginary part (lower panel) of the phase-sensitive photoresponse I_{ph} for different intensity-modulating frequencies 113 Hz $\leq f_{\mathrm{chop}} \leq$ 1713 Hz (red to black) and $V_{\mathrm{sd}}^{\mathrm{dc}}$, x_{exc}, and the excitation power P_{exc} as specified ($y_{\mathrm{exc}} = 0$). (b) Measured real (upper panel) and imaginary part (lower panel) of I_{ph} at maximum I (dots, also indicated by the dots in (a)) plotted as a function of f_{chop} for various x_{exc} as indicated (semi-logarithmic representation). The solid lines are fits according to Eqs. 6.1 (see text for details). The real (imaginary) PR in (b) is successively offset by 0.7 nA (0.8 nA) for clarity, as indicated by the short horizontal lines on the right.

sponding to the investigated QPC transmission range in Fig. 6.8(a). The inferred relaxation times lie in the range of 0.3 ms $\leq \tau \leq$ 6 ms depending on the actual location x_{exc} of the local laser excitation. A detailed discussion of the two model parameters I_0 and τ is provided in Sec. 6.2.4 below.

Though Eqs. 6.1 generally reproduce the frequency-dependence of the measured PR very well, a more detailed analysis of the PR reveals deviations which are going to be discussed in the following section. This will also shed more light on the physics behind Eqs. 6.1 which is discussed in a summarized form in Sec. 6.2.6 at the end of this chapter.

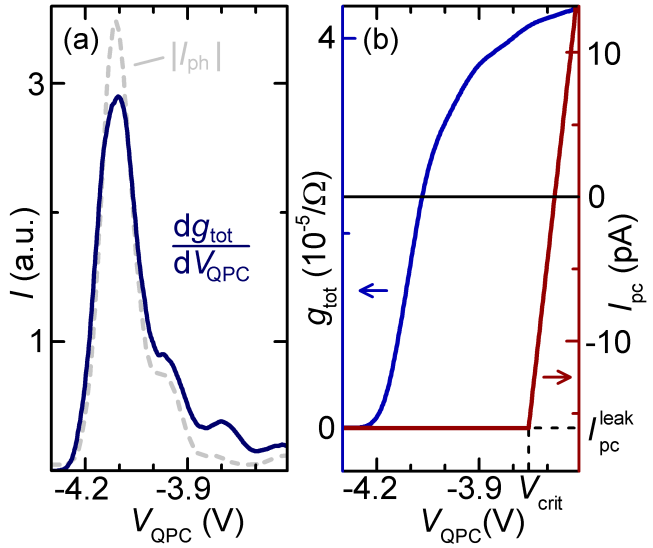

Figure 6.9: (a) Scaled transconductance of the transport total conductance $\mathrm{d}g_{\mathrm{tot}}/\mathrm{d}V_{\mathrm{QPC}}$ (blue) and respective in situ measured PR $|I_{\mathrm{ph}}|$ (dashed gray) plotted as a function of the QPC gate voltage V_{QPC}. (b) Total conductance g_{tot} (blue) and the static current contribution I_{pc} (red) which is determined by the critical QPC voltage V_{crit} and the leakage current $I_{\mathrm{pc}}^{\mathrm{leak}}$ as indicated. The shown results were used to calculate Fig. 6.10(b) (see text for details).

6.2.3 Static photoresponse contributions

The previous section showed that the general dependence of the QPC PR on the modulation frequency of the excitation power is well captured by Eqs. 6.1. However, they do not adequately account for the full observed PR behavior. This is apparent from the PR measured at $f_{\mathrm{chop}} = \mathrm{const}$ at finite source-drain DC voltage $V_{\mathrm{sd}}^{\mathrm{dc}}$ shown in Fig. 6.10(a). $|I_{\mathrm{ph}}|$ as a function of V_{QPC} is plotted (color-coded, logarithmic scale) at various $-12\ \mu\mathrm{V} \leq V_{\mathrm{sd}}^{\mathrm{dc}} \leq 56\ \mu\mathrm{V}$ (step size 1 μV) for constant $f_{\mathrm{chop}} = 112$ Hz and $x_{\mathrm{exc}} = 2\ \mu$m. For comparison, two line cuts (black) are also shown.

The characteristic PR maxima I, II, and III are visible in Fig. 6.10(a) at $V_{\mathrm{QPC}} \simeq -4.1$ V (white), $\simeq -3.95$ V (yellow), and $\simeq -3.8$ V (orange), respectively, as also marked for clarity by the arrowheads at the upper line cut. However, according to Eqs. 6.1 $|I_{\mathrm{ph}}|$ is expected to uniformly vanish at $V_{\mathrm{sd}}^{\mathrm{dc}} = 0$ (see Fig. 6.11 and the corresponding discussion in the subsequent section). But the corresponding region (violet and black "ribbon" in Fig. 6.10(a)), referred to as minimum-PR line (MPL), clearly disagrees. In the range $V_{\mathrm{QPC}} > -4.0$ V it first bends upward to larger $V_{\mathrm{sd}}^{\mathrm{dc}}$ and subsequently drops steeply. In order to explain this unexpected feature three more findings have to be taken into account: (1) As shown in Fig. 6.9(a), the transconductance of the measured transport *total* conductance $\mathrm{d}g_{\mathrm{tot}}/\mathrm{d}V_{\mathrm{QPC}}$ (blue, obtained by numerical differentiation) reproduces all essential features of the *in situ* measured PR $|I_{\mathrm{ph}}|$ (dashed gray). In particular, the PR maxima including their varying shapes and relative heights are reflected. $|I_{\mathrm{ph}}|$ of Fig. 6.9(a)

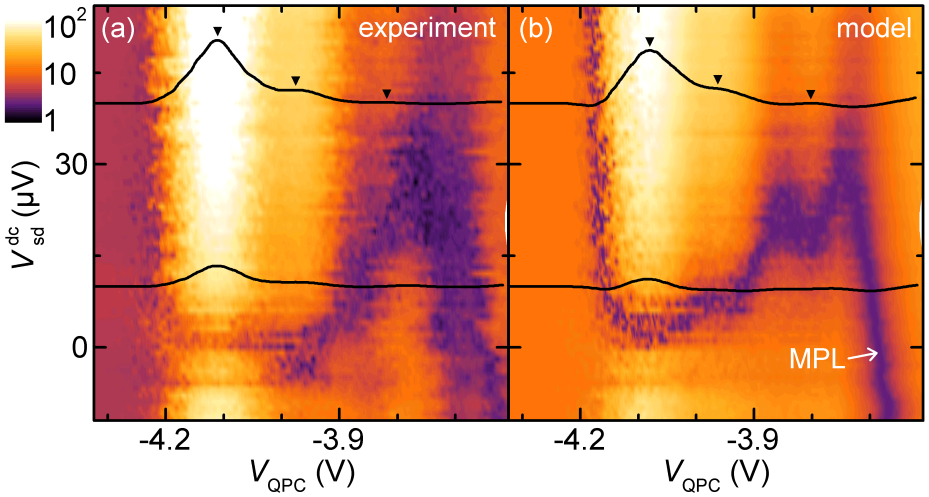

Figure 6.10: (a) PR $|I_{ph}|$ measured as a function of V_{QPC} for different constant source-drain voltages V_{sd}^{dc} (step size $\Delta V_{sd}^{dc} = 1\ \mu V$) ($f_{chop} = 112$ Hz, $P_{exc} = 160$ nW, $x_{exc} = 2\ \mu$m, $y_{exc} = 0$). (b) Calculated $|I_D|$ (see text for details). (a) and (b) have the same color scale (logarithmic, scale bar in pA) and line cuts at $V_{sd}^{dc} = 10$, 40 μV are superimposed (black, linear scale). Both the measured and the calculated PR maxima are marked by the black arrowheads on each upper line cut for clarity. The minimum-PR line (MPL) is indicated.

is taken from the topmost V_{sd}^{dc} region (farthest from the distorted MPL) of Fig. 6.10(a) and averaged over $\Delta V_{sd}^{dc} = 5\ \mu V$, and dg_{tot}/dV_{QPC} of Fig. 6.9(a) has been scaled as explained below. Note that the deviations around the PR maximum III ($V_{QPC} \sim -3.8$ V) in Fig. 6.9(a) are caused by the MPL whose tails still extend up to the V_{sd}^{dc} range where $|I_{ph}|$ was extracted (compare Fig. 6.10(a) at $V_{QPC} \simeq -3.85$ V and $\simeq -3.7$ V).
(2) The static PR limit I_0 of Eqs. 6.1 is proportional to I_{sd}^{dc} (this is evident from the subsequent section as well as from Sec. 6.2.5 below).
(3) The calculated $|I_D|$ exhibits a distorted MPL only if an *additional* static current component I_{pc} is assumed to be present. In summary, (1)-(3) yield

$$I_0(V_{QPC}, V_{sd}^{dc}) = \alpha \frac{dg_{tot}}{dV_{QPC}} I_{sd}^{dc} + I_{pc}\ , \tag{6.2}$$

where the scaling constant α is determined by a fit in the total V_{QPC} range of Eqs. 6.1 and Eq. 6.2 to $|I_{ph}|$ for a given f_{chop} and V_{sd}^{dc}. The respective fit result was already presented in Fig. 6.9(a). In Eq. 6.2 the form of I_{pc}

$$I_{pc}(V_{QPC}) = \begin{cases} I_{pc}^{leak} & \text{if } V_{QPC} < V_{crit} \\ I_{pc}^{leak} + g_{pc}(V_{QPC} - V_{crit}) & \text{if } V_{QPC} \geq V_{crit} \end{cases} \tag{6.3}$$

was chosen. It is as simple as possible and yet provides all main features of the measured MPL in Fig. 6.10(a). The form of Eq. 6.3 is shown in Fig. 6.9(b) (red, right y-axis). It depends on the leakage current $I_{pc}^{leak} = -16 \pm 1$ pA, the critical QPC voltage

$V_{\mathrm{crit}} = -3.755 \pm 0.001$ V, and the slope $g_{\mathrm{pc}} = 0.21 \pm 0.01$ GΩ^{-1}. The details on how these parameter values were inferred is discussed in the following section.

The resulting calculated $|I_{\mathrm{D}}|$ using Eqs. (6.1-6.3) is presented in Fig. 6.10(b), using the same logarithmic color scale as in Fig. 6.10(a). It also features two superimposed corresponding line cuts of $|I_{\mathrm{D}}|$ (linear scale) for comparison. The positions, magnitudes and trends of the calculated PR maxima agree well with the measurement. Moreover, the shape of the calculated MPL caused by Eq. 6.3 is in good agreement with the shape of the measured MPL.

Equation 6.2 now directly allows to explain the shape of the MPL in terms of g_{tot}, $I_{\mathrm{sd}}^{\mathrm{dc}}$, and I_{pc} which contribute to $|I_{\mathrm{D}}|$. At a given DC bias voltage (e. g. $V_{\mathrm{sd}}^{\mathrm{dc}} = 10\ \mu$V), each time the distorted MPL is crossed (at $V_{\mathrm{QPC}} \simeq V_{\mathrm{QPC}}^{\mathrm{pinch-off}}$, $\simeq -3.9$ V, and $\simeq -3.7$ V, see Fig. 6.10) the overall sign of I_0 changes which is equivalent to a simultaneous phase shift of π of both $\mathrm{Re}\,[I_{\mathrm{ph}}]$ and $\mathrm{Im}\,[I_{\mathrm{ph}}]$. In other words, the shape of the MPL in Fig. 6.10 maps the area where $\alpha\, \mathrm{d}g_{\mathrm{tot}}/\mathrm{d}V_{\mathrm{QPC}}\, I_{\mathrm{sd}}^{\mathrm{dc}} = -I_{\mathrm{pc}}$. As a consequence, the phase-*in*dependent PR magnitude becomes a sensitive measure of I_{pc} in the regime of finite $V_{\mathrm{sd}}^{\mathrm{dc}}$.

Finally it should be pointed out that the frequency dependence $I_{\mathrm{D}}(f_{\mathrm{chop}})$ of the PR (see Fig. 6.8 in Sec. 6.2.2) was calculated by assuming $I_{\mathrm{pc}} = 0$. This is in fact justified a posteriori because $|I_{\mathrm{pc}}| < 30$ pA $\ll I_{\mathrm{ph}}$ in the considered V_{QPC} range (compare Fig. 6.9(b)).

In the context of Eqs. 6.1, the findings of Eq. 6.2 and Eq. 6.3 will be evaluated in detail in Sec. 6.2.6. First of all, however, several relevant features of the resulting parameters τ and I_0 obtained from the model fits in Sec. 6.2.2 are discussed in Sec. 6.2.4 and Sec. 6.2.5. In addition, the details on how the parameter values of I_{pc} (Eq. 6.3) were inferred is discussed in the following section.

Extraction of the static current component

In this section the details are presented on how the parameters $I_{\mathrm{pc}}^{\mathrm{leak}}$, V_{crit}, and g_{pc} of I_{pc} (Eq. 6.3) were obtained from the application of the relaxation model I_{D} (Eqs. 6.1, Sec. 6.2.2) and the static PR limit I_0 (Eq. 6.2) to the measured PR. The measured PR $|I_{\mathrm{ph}}|$ is shown again in Fig. 6.11(d) (logarithmic color scale, scale bar in pA on the right, the graph is identical with Fig. 6.10(a)). The V_{QPC}-axis of each individual PR at a given $V_{\mathrm{sd}}^{\mathrm{dc}}$ in Fig. 6.11(d) was adjusted so that the PR maxima I align. This compensated for slight temporal fluctuations of the local electrostatic QPC environment and thus of the QPC pinch-off voltage $V_{\mathrm{QPC}}^{\mathrm{pinch-off}}$. This alignment of the PR accordingly aligned all in-situ measured transport quantities such as the conductance g_{tot} and the static QPC current $I_{\mathrm{sd}}^{\mathrm{dc}}$ which are input parameters of the static PR limit I_0 (Eq. 6.2) of the relaxation model I_{D}. The input parameter $\mathrm{d}g_{\mathrm{tot}}/\mathrm{d}V_{\mathrm{QPC}}$ was already discussed above (see Fig. 6.9(a)), the corresponding $I_{\mathrm{sd}}^{\mathrm{dc}}$ is shown in Fig. 6.11(a) (color-coded, left scale bar in nA, linear scale). $I_{\mathrm{sd}}^{\mathrm{dc}}$ shows no deviation from the expected behavior. It vanishes if the QPC is pinched-off ($V_{\mathrm{QPC}} < V_{\mathrm{QPC}}^{\mathrm{pinch-off}} \simeq -4.2$ V) or if $V_{\mathrm{sd}}^{\mathrm{dc}} = 0$ (violet areas in Fig. 6.11(a)), and it increases (decreases) linearly for positive (negative) applied $V_{\mathrm{sd}}^{\mathrm{dc}}$ for $V_{\mathrm{QPC}} > V_{\mathrm{QPC}}^{\mathrm{pinch-off}}$, as shown orange to white (blue to black) in Fig. 6.11(a). Note that the $V_{\mathrm{sd}}^{\mathrm{dc}}$-axis of Figs. 6.11(a) and 6.11(d) was corrected for a non-zero constant voltage offset caused by

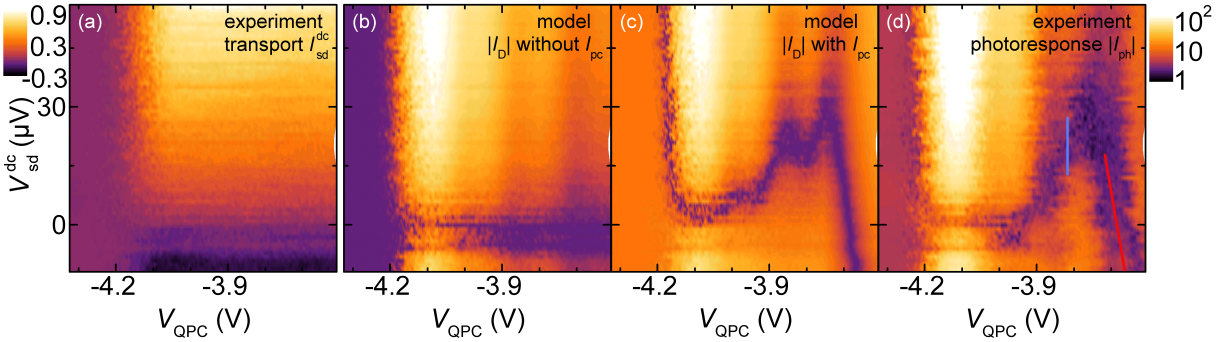

Figure 6.11: (a) and (d): The (a) QPC current I_{sd}^{dc} and (d) PR $|I_{ph}|$, simultaneously measured as a function of the QPC gate voltage V_{QPC} for different source-drain DC voltages V_{sd}^{dc} (step size: $\Delta V_{sd}^{dc} = 1\ \mu V$, $f_{chop} = 112$ Hz, $P_{exc} = 160$ nW, $x_{exc} = 2\ \mu m$, $y_{exc} = 0$) (b) and (c): Calculated $|I_D|$ using (b) $I_{pc} = 0$ and (c) I_{pc} as defined by Eq. 6.3. The color scales are (a) linear as shown by the left scale bar in nA and (b-d) logarithmic as shown by the right scale bar in pA. The graphs (d) and (c) are the same as in Fig. 6.10. Along the straight lines in (d) $|I_D|$ was fitted to $|I_{ph}|$ in order to obtain the parameter values that determine I_{pc} (see text for details).

the input of the transimpedance amplifier (compare Sec. 6.1.2). In addition, a shift in the voltage offset of the transimpedance amplifier is very likely the cause for I_{sd}^{dc} vanishing again at a non-zero source-drain voltage (at about $V_{sd}^{dc} = -6\ \mu V$) in Fig. 6.11(a), as confirmed by the simultaneously vanishing PR in Fig. 6.11(d).

Fig. 6.11(b) shows $|I_D|$ (logarithmic scale, right scale bar) calculated by means of dg_{tot}/dV_{QPC} and I_{sd}^{dc} for $I_{pc} = 0$. The positions and heights of the maxima I, II, and III at $V_{QPC} \simeq -4.1$ V (white), -3.95 V (yellow), and -3.8 V (orange), respectively, of $|I_D|$ well reproduce the measured result Fig. 6.11(d). However, the calculated MPL is fixed around $V_{sd}^{dc} = 0$ (it appears broadened due to I_{sd}^{dc} vanishing at about $V_{sd}^{dc} = -6\ \mu V$ too) and can *not* be deformed by any parameter of the model. Adding a static component $I_{pc} \neq 0$ yields a deformation of the MPL. This is shown in Fig. 6.11(c) (logarithmic scale, right scale bar, the graph is identical with Fig. 6.10(b)) showing $|I_D|$ calculated by means of dg_{tot}/dV_{QPC} and I_{sd}^{dc} including I_{pc} (Eq. 6.3). The form of I_{pc} was chosen to be as simple as possible yet providing the characteristic features of the measured MPL in Fig. 6.11(d). I_{pc} was determined by least mean square fits of $|I_D|$ to $|I_{ph}|$ along specific lines in the V_{QPC} - V_{sd}^{dc} plane where the parameters I_{pc}^{leak}, V_{crit}, and g_{pc} of I_{pc} were used as free fit parameters. Owing to the form of $I_{pc}(V_{QPC})$ (Eq. 6.3), the shape of the resulting MPL is determined at $V_{QPC} < V_{crit}$ by the independent parameter I_{pc}^{leak} and at $V_{QPC} \geq V_{crit}$ by the interdependent parameters V_{crit} and g_{pc}. I_{pc}^{leak} was determined by a fit along the blue straight line in Fig. 6.11(d) ($V_{QPC} = -3.82$ V). Then V_{crit} and g_{pc} were determined by a fit along the red line in Fig. 6.11(d) which coincides with the MPL. The resulting parameters of I_{pc} including fit error margins are $I_{pc}^{leak} = -16 \pm 1$ pA, $V_{crit} = -3.755 \pm 0.001$ V, and $g_{pc} = 0.21 \pm 0.01\ G\Omega^{-1}$ and are discussed in Sec. 6.2.6 below.

6.2.4 Relaxation times and static photoresponse limits

In this section the static PR limits I_0 and the relaxation times τ are discussed that were obtained from the measured dynamic PR (compare Fig. 6.8 in Sec. 6.2.2) by means of the application of the relaxation model (Eqs. 6.1). The model fits as a function of the modulation frequency f_{chop} at the various excitation spot positions x_{exc} were carried out individually for all maxima I - IV of the measured PR. Consequently, the parameters I_0 and τ are evaluated individually too. Moreover, in all measurements with optical excitation close to the QPC constriction it turned out that the response described by the relaxation model I_{D} simultaneously occurred twice. As discussed below, one response was attributed to the excitation on the QPC source side and the other response was attributed to the excitation on the QPC drain side, referred to as I_{D} and I_{dr}, respectively. I_{dr} is discussed in this section too. It can be approximated as frequency-independent in the considered excitation spot range $x_{\mathrm{exc}} > 0$, as discussed below.

In Fig. 6.12 the parameters τ (panel (a)) as well as I_0 (from I_{D}) and I_{dr} (panel (b)) obtained from the fits are summarized (dots) for PR maximum I (yellow) to IV (dark red). I_0 and I_{dr} in Fig. 6.12(b) were normalized by $\mathrm{d}g_{\mathrm{tot}}/\mathrm{d}V_{\mathrm{QPC}}$ using the result Eq. 6.2 (Sec. 6.2.3) for the static PR limit. The data Figs. 6.12(a) and 6.12(b) additionally feature the experimentally estimated uncertainty in x_{exc} (horizontal lines) and the inaccuracies determined from the best fit results (vertical lines). The fit errors in Fig. 6.12(b) further include the numerically determined uncertainty in $\mathrm{d}g_{\mathrm{tot}}/\mathrm{d}V_{\mathrm{QPC}}$. The remaining lines in Fig. 6.12 are guides to the eye.

First I_{dr} is considered. The assumption that it is the PR stemming from excitation on the QPC drain side $x_{\mathrm{exc}} < 0$ is justified first by the observed feature that I_{dr} vanishes for all PR maxima at $x_{\mathrm{exc}} \gtrsim 0.8\ \mu$m (Fig. 6.12(b)) that is very similar to the actual half width at half maximum (HWHM) of 0.75 μm of the confocal excitation spot. Moreover, the raw I_{dr} at a given x_{exc} on average vary by one order of magnitude (data not shown). However, after normalization by the inferred characteristic strength of the QPC PR $\mathrm{d}g_{\mathrm{tot}}/\mathrm{d}V_{\mathrm{QPC}}$ all curves as a function of x_{exc} collapse to a single trend in Fig. 6.12(b). This confirms the conclusion that I_{dr} actually is a PR of the QPC. Additionally, the resulting ratio $I_0/I_{\mathrm{dr}} \simeq 10$ was calculated from Fig. 6.12(b) by averaging in the range of $x_{\mathrm{exc}} \leq 0.8\ \mu$m (this range corresponds to non-vanishing I_{dr}). This ratio is in accord with the corresponding ratio obtained from the *independent* measurements of the PR arising from excitation on the QPC source side and on the QPC drain side (see Sec. 6.2.5 below). Thus all three independent observations confirm that I_{dr} can also be attributed to the QPC PR which is caused by excitation on the QPC drain side. I_{dr} was used to distinguish two regimes in Fig. 6.12: region *on* where $I_{\mathrm{dr}} > 0$ and excitation also occurs on the QPC drain side (light blue) and region *off* where excitation is off the QPC drain side only (remaining x_{exc} range). Both regimes are illustrated in the insets of Fig. 6.12 where the I_{dr}-inducing fraction (hatched) of the excitation spot (red) is marked.

For increased x_{exc} the position of the corresponding effective excitation spot fraction on the QPC drain side remains nearly unchanged close to the QPC, in contrast to the

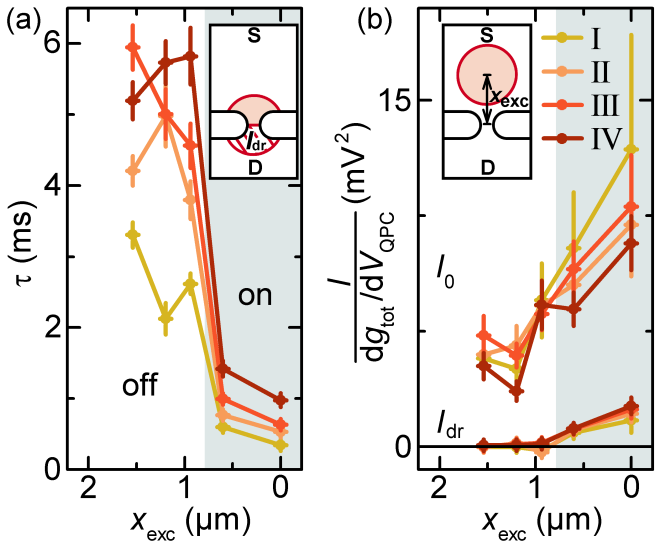

Figure 6.12: The results from the fits of Eqs. 6.1 (see Sec. 6.2.2) to the PR at the maximum I (yellow) to maximum IV (dark red) for different excitation spot positions x_{exc} ($y_{\mathrm{exc}} = 0$). In both panels, the uncertainties from each fit and the experimentally estimated uncertainty in x_{exc} are indicated by the vertical and horizontal lines, respectively. (a) The obtained relaxation times τ. (b) The static limit I_0 of the PR and the drain-side-excitation-related PR I_{dr}, both plotted using Eq. 6.2 (Sec. 6.2.3) by the scaling with $\mathrm{d}g_{\mathrm{tot}}/\mathrm{d}V_{\mathrm{QPC}}$. The x_{exc} range can be divided into the regime *on* (light blue), where the excitation on the QPC drain side takes place too, and *off* (remaining x_{exc} range) as indicated. Remaining lines in (a) and (b) are guides to the eye. Insets: Sketches of the excitation spot (red) at (a) $x_{\mathrm{exc}} = 0$ and (b) $x_{\mathrm{exc}} > 0$ along the source (S) - drain (D) direction close to the QPC. They illustrate the regimes *on* and *off*.

QPC source-side excitation spot fraction. Therefore, as opposed to I_0, the drop of I_{dr} for increasing x_{exc} is expected to stem from the decrease in effective excitation power exclusively. Furthermore, the persistent drain-side spot fraction close to the QPC gives rise to a correspondingly large resonance frequency $1/(2\pi\tau)$ (compare Fig. 6.12(a)). Consequently, in combination with the less than 10 % contribution to the overall PR magnitude, it was sufficient to include the drain-side-related PR in terms of the real-valued constant I_{dr} (that basically corresponds to the respective static limit $I_{0,\mathrm{dr}}$). All fits of the relaxation model included both PR contributions simultaneously whereas the evaluated results, including Fig. 6.8(b) (Sec. 6.2.2), only refer to the actual source-side-excitation-related PR contribution I_{D}, omitting the *artefactual* drain-side-excitation-related PR I_{dr}.

Fig. 6.12(a) summarizes the relaxation times τ as a function of the excitation spot position x_{exc}. They spread in the range of $0.3\ \mathrm{ms} \leq \tau \leq 1.0\ \mathrm{ms}$ at $x_{\mathrm{exc}} = 0$ and $3\ \mathrm{ms} \leq \tau \leq 6\ \mathrm{ms}$ at $x_{\mathrm{exc}} = 1.5\ \mu\mathrm{m}$. The overall monotonic increase of $\tau(x_{\mathrm{exc}})$ is accompanied by an abrupt jump at $x_{\mathrm{exc}} \simeq 0.8\ \mu\mathrm{m}$ of comparable relative height for each individual PR maximum. This position coincides well with the *on*-*off* regions boundary derived from the characteristics of I_{dr}. Hence it indicates a mutual relation despite τ refers to the QPC source-side excitation exclusively (see discussion in Sec. 6.2.6).

Figure 6.12(b) also shows the extracted static limits I_0 using the basic feature $\mathrm{d}g_{\mathrm{tot}}/\mathrm{d}V_{\mathrm{QPC}}$ of the QPC PR. Despite the raw values vary by a factor of 30 (compare Fig. 6.8(a) in Sec. 6.2.2), after the normalization they coincide within the error bars at each x_{exc}. The scaling result of I_0 in Fig. 6.12(b) at a given x_{exc} furthermore confirms Eq. 6.2 as a key characteristic of the PR of a QPC. Slight deviations of I_0 not matching within the error bars are observed at the maximum IV for $x_{\mathrm{exc}} \geq 1.2\ \mu$m. In that regime the decrease of $\tau(x_{\mathrm{exc}})$ for increased x_{exc} in Fig. 6.12(a) is also contrary to the otherwise consistently observed monotonous increase. The source of the deviations in the regime of a more opened QPC and at larger excitation spot distances is not known. I_0 shows deviations from the overall decrease indicated by a kink which induces a smoother variation beyond $x_{\mathrm{exc}} \simeq 1.2\ \mu$m. The kink in the static amplitude, however, can neither be linked unambiguously to the observed jump in τ in Fig. 6.12(a) nor to the ceasing excitation of the QPC drain side.

6.2.5 Photoresponse due to drain-side excitation

In this section the PR caused by excitation on the QPC drain side is investigated independently. Figure 6.13 shows the result of two separate measurements of the PR of the QPC, one with the excitation spot located at $x_{\mathrm{exc}} = 2\ \mu$m (filled dots) and the other with $x_{\mathrm{exc}} = -2\ \mu$m (open dots) under otherwise identical conditions. For each x_{exc}, I_{ph} as a function of V_{QPC} was recorded several times, each time with a different constant voltage $-6\ \mathrm{mV} \leq V_{\mathrm{sd}}^{\mathrm{dc}} \leq 6\ \mathrm{mV}$ applied to the 2DES. The extracted lock-in-phase independent magnitudes $|I_{\mathrm{ph}}|$ at PR maximum $j = \mathrm{I}$ (yellow) to $j = \mathrm{IV}$ (dark red) are plotted using $\mathrm{d}g_{\mathrm{tot}}/\mathrm{d}V_{\mathrm{QPC}}$ of Eq. 6.2 (Sec. 6.2.3) for normalization. The data are successively offset for clarity.

The excitation spot distance exceeds the radius of the confocal excitation spot, $|x_{\mathrm{exc}}| > 0.75\ \mu\mathrm{m} \simeq \mathrm{HWHM}$. Figure 6.13 thus allows the comparison between the PR due to QPC source-side excitation and the PR due to QPC drain-side excitation without mutual influence. The first general conclusion is that sole QPC drain-side excitation induces an identical PR (the V_{QPC}-dependent data is not shown). Moreover, the characteristics of the static limit (Eq. 6.2) prove to be a general feature of the QPC PR independent of the sign of x_{exc}: for each x_{exc} at a given $V_{\mathrm{sd}}^{\mathrm{dc}}$, $|I_{\mathrm{ph}}|$ in Fig. 6.13 coincide after the normalization by $\mathrm{d}g_{\mathrm{tot}}/\mathrm{d}V_{\mathrm{QPC}}$. Additionally, the relation $|I_0| \propto |I_{\mathrm{sd}}^{\mathrm{dc}}|$ is fulfilled too, as evident from Fig. 6.13 due to $|I_{\mathrm{sd}}^{\mathrm{dc}}| \propto |V_{\mathrm{sd}}^{\mathrm{dc}}|$. The latter relation is valid because the different $I_{\mathrm{ph}}/(\mathrm{d}g_{\mathrm{tot}}/\mathrm{d}V_{\mathrm{QPC}})$ in each of both data sets $x_{\mathrm{exc}} = \pm 2\ \mu$m were evaluated at a given PR maximum j where the QPC conductance g_{QPC} and thus g_{tot} is constant. Slight deviations from the proportionality are only observed toward highest $|V_{\mathrm{sd}}^{\mathrm{dc}}|$ where the transition to the non-linear transport regime already sets in (the non-linear data is not shown).

The magnitudes of the PRs at a given $V_{\mathrm{sd}}^{\mathrm{dc}}$ for the different x_{exc} clearly differ with respect to each other. The mean ratio of $|I_{\mathrm{ph}}|$ at $2\ \mu$m to $|I_{\mathrm{ph}}|$ at $-2\ \mu$m averaged over the data in Fig. 6.13 was calculated as 15 ± 3. Though inferred only for the constant excitation spot distances $x_{\mathrm{exc}} = \pm 2\ \mu$m the result is consistent with the correspondingly

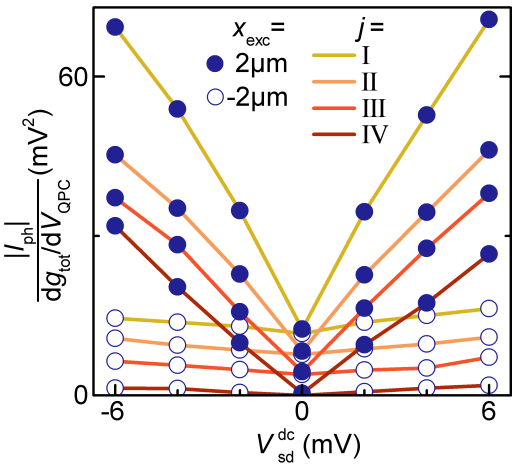

Figure 6.13: PR measured with several DC voltages $V_{\mathrm{sd}}^{\mathrm{dc}}$ applied to the 2DES. For two different measurements, one with a excitation spot position $x_{\mathrm{exc}} = 2\,\mu$m (filled dots) and one with $x_{\mathrm{exc}} = -2\,\mu$m (open dots), the extracted values $|I_{\mathrm{ph}}|$ at maximum $j = \mathrm{I}$ (yellow) to $j = \mathrm{IV}$ (dark red) are shown, each normalized by the corresponding $\mathrm{d}g_{\mathrm{tot}}/\mathrm{d}V_{\mathrm{QPC}}$ of Eq. 6.2 (Sec. 6.2.3). The PR at III, II, and I are successively offset by 4 mV^2 for clarity. The laser modulation frequency is $f_{\mathrm{chop}} = 112$ Hz, the excitation power is $P_{\mathrm{exc}} = 42$ nW, and $y_{\mathrm{exc}} = 0$. The lines are guides to the eye.

obtained ratios in Sec. 6.2.4. Therefore it is concluded that the PR due to QPC drain-side excitation is one order of magnitude smaller than the PR due to QPC source-side excitation at otherwise identical conditions. Since f_{chop} was constant in Fig. 6.13 the same holds for the static limits, $I_{0,\mathrm{source}} \sim 10 I_{0,\mathrm{drain}}$. In addition, Fig. 6.13 further confirms that the asymmetry in the PR strengths is independent of $V_{\mathrm{sd}}^{\mathrm{dc}}$ in the investigated linear transport range. We attribute the PR asymmetry to the present asymmetric geometry of the sample layout (compare Sec. 6.1.1).

6.2.6 Origin of the dynamic and the static photoresponse

Based on the detailed results of the previous sections, in this section the relaxation model (Eqs. 6.1 and Eq. 6.2, Sec. 6.2.2 and Sec. 6.2.3) describing the dominant QPC PR and the additional static PR contribution I_{pc} (Eq. 6.3, Sec. 6.2.3) are interpreted.

In the experiments electrons and holes were optically generated in the 2DES within the QW in close QPC vicinity. This is illustrated in Fig. 6.14 showing the schematic band diagram at the QPC channel along three lines in the 2DES plane using the coordinate system in panel (i). The valence band edge (VB) and the conduction band edge (CB) are sketched with respect to the 2DES Fermi energy E_{F} (dashed line) in y direction at $x = 0$ (panel (ii)) as well as in x direction at $y = 0$ ((iii)) and at $y = 0.3\,\mu$m ((iv)). The laser excites electron-hole (e^--h^+) pairs resonantly at the lowest interband transition ((iii)). Decreasing V_{QPC} raises the band energies at the constriction center ((ii) and (iii)) and below the QPC gates where the 2DES becomes fully depleted if the CB sufficiently

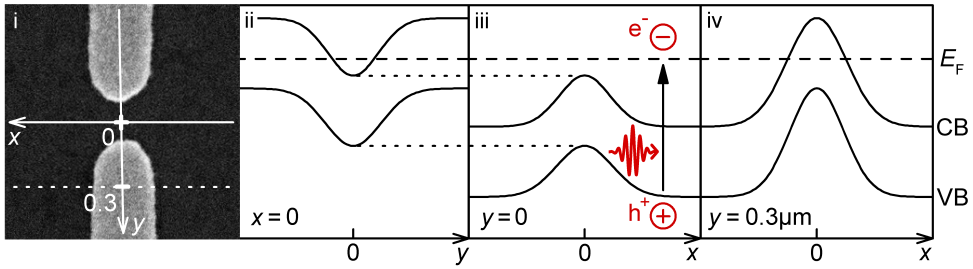

Figure 6.14: (i) SEM picture of the QPC which illustrates the coordinate system used to specify the excitation spot position x_{exc}. (ii-iv) Conduction band edge (CB) and valence band edge (VB) in QPC vicinity, sketched with respect to the 2DES Fermi energy E_{F} along lines in the 2DES plane using the coordinate system in (i). The dotted lines in (ii) and (iii) connect the concurring energies at the QPC constriction center.

exceeds E_{F} ((iv)) confining the resulting QPC channel ((ii)). Further lowering V_{QPC} eventually pinches off the channel such that the lowest QPC subband gets fully depleted.

While the negatively charged QPC gates repel electrons they attract positive holes and consequently generate a hole-trapping potential below the gates (Fig. 6.14(iv)) and in the QPC channel ((iii)). The result Fig. 6.12(a) (Sec. 6.2.4) yields PR relaxation times in the order of ms which by far exceed typical electron-hole recombination times of 10 - 100 ps in a QW potential [109, 110] with electron and hole wavefunctions having sizable overlap. However, such prolonged recombination times have been reported in samples with spatially separated electrons and holes that had strongly reduced wave function overlap [111]. It is in accord with Eq. 6.2 which shows that the dominant PR is determined by $\mathrm{d}g_{\mathrm{tot}}/\mathrm{d}V_{\mathrm{QPC}}$ indicating the modulation of g_{QPC} in response to the photo excitation. The main PR of a QPC can thus be explained in terms of holes trapped below the negatively charged QPC gates. The holes modulate g_{QPC} and, according to Eq. 6.2, the PR is generated by the correspondingly modulated QPC current $I_{\mathrm{sd}}^{\mathrm{dc}}$. Hence the dominant PR can be related to photoconductance due to a hole-induced photogating I_{pg} of $I_{\mathrm{sd}}^{\mathrm{dc}}$: $I_{\mathrm{pg}} = I_{\mathrm{ph}}(I_{\mathrm{pc}} = 0)$. This conclusions implies that I_{pg} must vanish in the case of $V_{\mathrm{sd}}^{\mathrm{dc}} = 0$ even if the laser excitation and thus the gating of the QPC conductance occurs. The vanishing photogating response is observed in the experiments (compare Fig. 6.11).

The parameters τ and I_0 that characterize the dominant I_{pg} are now discussed in terms of the photogating. When x_{exc} is varied a change in τ is expected which is given by the dipolar matrix element μ_{eh}, $\tau^{-1} \sim \mu_{\mathrm{eh}}^2 = |\langle\psi_{\mathrm{e}}|xe|\psi_{\mathrm{h}}\rangle|^2 \sim V_{\mathrm{h}}^{\mathrm{trap}} \sim n_{\mathrm{h}}^{\mathrm{trap}}$: the recombination rate which is sensitive to the actual overlap of the wavefunctions of the electrons and the holes changes with the mean trapped holes density $n_{\mathrm{h}}^{\mathrm{trap}}$ underneath the QPC gates that self-consistently modifies the trapping potential of the holes $V_{\mathrm{h}}^{\mathrm{trap}}$ and thus their overlap with 2DES electrons. This is qualitatively in compliance with the observed general gain of τ for larger x_{exc} (Fig. 6.12(a), Sec. 6.2.4). It is furthermore closely related with the fact that τ is increasing at a given x_{exc} while the QPC is opened up, as well as with the observed abrupt increase in τ at the x_{exc} where the drain-side-related hole supply to

the traps ceases rather abruptly (Fig. 6.12(a)). Eventually, the observed decline in I_0 for increasing x_{exc} (see Fig. 6.12(b)) provides further indications of the trapped-holes scenario because the strength of the QPC potential modulation is expected to scale with the mean trapped hole density. The latter drops for larger x_{exc} as a result of the on average higher radiative recombination possibility for holes before reaching the traps. A more detailed analysis would include the particular 2D hole distribution as well as detailed information regarding the 2D trapping potential below the QPC gates and was not pursued in the scope of this thesis.

Next the additional static contribution I_{pc} is evaluated. The conductivity of a high-mobility 2DES at low temperatures is determined by scattering processes of the electrons with impurities. Corresponding relaxation rates are typically around 100 GHz [112]. In the considered kHz frequency range the 2DES electrons are consequently expected to produce a *static* PR contribution which does apply to I_{pc}. I_{pc} in Eq. 6.3 is furthermore independent of $V_{\mathrm{sd}}^{\mathrm{dc}}$, in contrast to the directly $V_{\mathrm{sd}}^{\mathrm{dc}}$-generated I_{pg} via $I_{\mathrm{sd}}^{\mathrm{dc}}$ in Eq. 6.2 at a given PR maximum. This provides further indications that I_{pc} and I_{pg} have different origins. The inferred I_{pc} also shows a dependence on the actual QPC transmission via V_{QPC} that is related to the 2DES Fermi energy, but at the same time I_{pc} shows no dependence on the feature $\mathrm{d}g_{\mathrm{tot}}/\mathrm{d}V_{\mathrm{QPC}}$, characteristic of I_{pg}, which is strongest around $V_{\mathrm{QPC}}^{\mathrm{pinch-off}}$ where I_{pc} is actually constant (compare Figs. 6.9(a) and 6.9(b), Sec. 6.2.3). This excludes a significant link of I_{pc} to the dynamics of the trapped holes in the QPC vicinity.

It is important to note that the currents arising from (or flowing onto) all involved metal gates, including the QPC gates, on top of the sample were monitored simultaneously during the measurements of I_{ph}. No evidence for a gate-induced origin of the change in I_{pc} was found which in particular would have become apparent at the distinct onset at V_{crit}. Because I_{pc} is detected at the photomodulation frequency f_{chop} we therefore attribute a photo-induced electron-related origin.

However, the onset of the variation in I_{pc} at $V_{\mathrm{crit}} = -3.755$ V in Fig. 6.9(b) clearly differs from $V_{\mathrm{QPC}}^{\mathrm{pinch-off}} \simeq -4.25$ V where the QPC current $I_{\mathrm{sd}}^{\mathrm{dc}}$ sets in. With the aid of independent non-linear transport conductance measurements, this energy difference was calibrated to $\Delta E = 25 \pm 3$ meV. The error is caused by the uncertainty in the determination of the QPC subband energies. ΔE coincides well with the expected QW binding energy of negatively charged excitons X^- (trions) $E_{\mathrm{bind,X^-}} = 23 \pm 3$ meV which is increased due to the strong QW confinement and the high 2DES density [104]. $E_{\mathrm{bind,X^-}}$ was determined from the neutral exciton X binding energy in the QW $E_{\mathrm{bind,X}} = 10 \pm 1.5$ meV [113] and from QW 2DES photoluminescence measurements (compare Sec. 5.2) that yielded $E_{\mathrm{bind,X^-}} - E_{\mathrm{bind,X}} = 13 \pm 1.5$ meV. Preferred X^- formation under optical QW excitation is expected due to the high 2DES density [102, 104] and was observed in the characterization measurements (see Sec. 5.2).

The experimental findings in combination with the established relaxation model therefore consistently suggest that I_{pc} is a photo-induced 2DES electron current closely related to abundant X^- formation [114] and may include V_{QPC}-induced disintegration of the X^- in QPC vicinity. Accordingly, the cause of $I_{\mathrm{pc}}^{\mathrm{leak}}$ in I_{pc} (Eq. 6.3) can be attributed to

the radiative recombination of gate-trapped holes with 2DES electrons originating from the QPC drain side where the readout is performed. The radiative recombination is expected to generate a persistent net-electron current from the drain reservoir toward the QPC independently of g_{QPC} and thus independently of g_{tot}. It is in compliance with the observed opposite sign of $I_{\mathrm{pc}}^{\mathrm{leak}}$ compared to the g_{QPC}-related I_{pc} that onsets at V_{crit} (compare Fig. 6.9(b)). In this respect, $I_{\mathrm{pc}}^{\mathrm{leak}}$ can also be considered a photocurrent contribution since it is generated by electrons independently of the actual hole-induced dynamics of the dominant photogating.

6.3 Conclusions

The QPC transport conductance at various 2DES densities showed an emerging 0.7-anomaly in the investigated QPC. Consequently a main goal has been achieved: in the specifically designed 2DES a QPC could be integrated which is accessible in terms of transport spectroscopy and which can be tuned into the 0.7-anomaly regime. However, after the illumination of the sample no indication of the distinct 0.7-shoulder could be found anymore. On the other hand, the QPC transport conductance including the pinched-off QPC channel were accessible even *during* confocal laser illumination of the QPC channel center.

The PR of a QPC was investigated in detail for the case of resonant excitation of the 2DES in QPC vicinity. It was shown that for any given constant QPC transmission, the dominant PR contribution as a function of the varying excitation frequency is well captured by a basic relaxation model. The corresponding relaxation times of the order of ms were strongly increased. The large relaxation times were attributed to the recombination of 2DES electrons with holes that were trapped below the QPC gates, resulting in considerably decreased wave function overlap. Thus the cause of the dominant PR was attributed to photogating of optically induced holes which become trapped in the 2DES-depleted regions below the QPC gates.

By additionally including the *in-situ measured* transport conductance and static QPC current, the relaxation model reproduced the characteristics of the full experimentally observed dominant photoresponse of a QPC. This capability yielded additional PR contributions two orders of magnitude smaller than the dominating photogating at finite voltages applied to the 2DES. The additional contributions were distinguished based on their static character in the investigated kHz-frequency range. Two static PR components were extracted, a QPC-transmission-independent current which was attributed to electron transport caused by the continuous recombination of trapped holes with 2DES electrons from the QPC drain side, and a QPC-transmission-dependent component which was attributed to an photo-induced electron current crossing the QPC constriction. The latter showed the feature of setting in not before the QPC channel had already opened. The corresponding energy difference at the Fermi edge of the 2DES indicated a relation to negatively-charged exciton states. The preferred generation of the latter in the 2DES was confirmed by independent measurements of the photoluminescence of the 2DES.

Hence it was demonstrated that the relaxation model enables to distinguish the dominant photogating response from two orders of magnitude smaller static PR contributions. However, the indicated complex origin of the static PR constitutes a major challenge for the application of optical excitation schemes in QPC vicinity that aim at generating spin-resolved electron populations for controlled spin transport through the QPC channel.

Summary and outlook

The electron transport response and the response to local optical excitation of depletion-gate defined QPCs in a 2DES were investigated. The transport spectroscopy emphasized the detailed combined experimental and theoretical analysis of the 0.7-anomaly. On the other hand, the optical studies served the fundamental understanding of the transport response of a QPC to local optical excitation of charge carriers in QPC proximity.

The combined experimental and theoretical transport spectroscopy in Chapter 2 demonstrated that both the emergence and the characteristic features of the 0.7-anomaly can be inferred from a smeared Hove singularity occurring in the local density of states of the lowest QPC subband. The "slowly moving" electrons in the QPC constriction exhibit amplified interaction effects which are strongest when the 2DES Fermi energy crosses the Hove singularity. This crossing occurs at about $0.7G_{\mathrm{Q}}$ for a parabolic top of the QPC barrier potential but can vary between $0.5G_{\mathrm{Q}}$ and $1G_{\mathrm{Q}}$ for different barrier top curvatures, accounting for the experimentally varying appearance of the 0.7-anomaly. At large enough interactions, model calculations demonstrated the emergence of the 0.7-anomaly even at zero magnetic field. In combination with the calculated spin-dependent asymmetry of the spin-resolved QPC conductance in the 0.7-regime at finite magnetic fields it explains the magnetoconductance of the 0.7-anomaly. Furthermore, increased interactions at finite 2DES bias voltage due to inelastic backscattering and stronger electron-Coulomb repulsion produced a zero-bias peak in the calculated QPC conductance. Increased temperatures additionally cause inelastic backscattering which decreased the zero-bias peak, accounting for a more pronounced 0.7-shoulder in accordance with the experiments.

In Chapter 2 and Chapter 3, the calculated and measured QPC conductance agreed in the regime of low-energy excitations of the magnetic field, the temperature, and the 2DES bias voltage in that each excitation was similarly governed by a single energy scale. Likewise observed in a quantum dot in the Kondo effect regime (Kondo quantum dot, KQD) [45], it provided striking evidence that the QPC in the 0.7-anomaly regime and a KQD are closely related. It led to the key theoretical prediction which can be considered as the microscopic origin of the 0.7-anomaly: the amplified interactions of a QPC in the 0.7-anomaly regime emerge due to local electrons-spin fluctuations, similarly to those observed in the KQD. These fluctuations become apparent by a strong enhancement of the spin susceptibility in the 0.7-regime of the QPC which are intimately linked to the strong negative magnetoconductance, a relation also fulfilled for the KQD [78]. The calculated interaction-enhanced spin susceptibility in Chapter 3 further showed a characteristic spa-

tial pattern in QPC proximity arising from the *geometry* of the confining potential. The constraint of absent spontaneous spin polarization in the QPC self-imposed on our model calculations precluded built-in magnetization effects such as a "quasi-bound" spin state [39–42] a priori. Thus, the governing low-energy scales emerge as a result of the interactions of 2DES electrons with a single localized spin in the KQD, yet in the QPC they arise from interactions along the elongated, yet confined, Hove singularity and include multiple spin states. Accordingly, in the limit of high magnetic fields the theoretical analysis of the local magnetization showed a constant spatial distribution and a saturating magnitude in the KQD, in contrast to a changing spatial distribution and a continuous rise in magnitude in the QPC 0.7-anomaly regime. It showed that the 0.7-anomaly and the Kondo effect are in general distinct phenomena and that in particular in the 0.7-anomaly regime *no actual* Kondo effect is present. The strength of the presented theory lies in the comprehensive integration of the elastic and inelastic regimes. An important consequence of our model calculations is the requirement of non-zero many-particle interactions for an emerging 0.7-anomaly, in contrast to recent proposals [115]. Furthermore, systematic experimental studies of the crossover from parabolic to wide, flat QPC barrier tops would be beneficial in order to test the obtained quantitative theoretical prediction of the actual occurrence of the 0.7-anomaly as a function of the actual QPC barrier curvature.

As an initial step toward a possible experimental test of the predicted close connection between the 0.7-anomaly and the local spin susceptibility by optical means, in Chapter 4 a confocal microscope based on Faraday rotation (FR) readout was presented which is sensitive to local magnetization. The microscope was tested on a polarized single electron spin state confined in a self-assembled quantum dot. The sensitivity of the microscope was 500 $\mu\text{rad}/\sqrt{\text{Hz}}$ for the single spin state with an optical resonance linewidth of $\Gamma = 10$ μeV. Hence the simple microscope setup proved to be a sensitive single-spin detector.

In Chapter 5, semiconductor heterostructure simulations and subsequent experimental characterizations were presented in order to adapt a 2DES in a heterostructure for optical excitation. Adequate densities and mobility were experimentally confirmed for a 2DES which provides the required well-defined interband optical selection rules in optically transparent surroundings. Additionally, the analysis of the photoluminescence of the adapted heterostructure identified both the lowest 2DES optical interband transitions and negatively-charged exciton (trion) formation dominating the optical 2DES response.

Based on the adapted 2DES, in Chapter 6 the QPC transport response to resonant confocal optical excitation of the 2DES in the QPC proximity (termed photoresponse, PR) was analyzed. The differential PR was read out using a modulation of the excitation intensity in the kHz range. As an important finding, the sample design allowed full control of the QPC potential under illumination of the actual QPC constriction. It was shown that a basic relaxation model well describes the dominant PR of a QPC. The inferred relaxation times of the order of 1 ms were identified as the lifetimes of charges in the valence band (holes) which become trapped in the 2DES-depleted areas below the QPC gates and recombine with the spatially separated 2DES electrons. It was further demonstrated that the dominant PR of a QPC equals the static QPC current which is periodically gated by photo-generated holes that are trapped below the QPC gates. Moreover, an additional

PR contribution two orders of magnitude weaker than the dominant PR was identified based on its static behavior in the modulation-frequency range of the optical excitation. The QPC-transmission-dependent static PR was shown to be consistent with the laser-induced photocurrent in the 2DES. However, the onset of the photocurrent did not occur before the QPC already contained several transmitting channels. The corresponding energy difference at 2DES Fermi energy was comparable to the trion binding energy in the 2DES, in accordance with the photoluminescence results. This may indicate that the photocurrent is closely related to the disintegration of the trion states in close QPC vicinity.

As a result, it could be demonstrated that the relaxation model can be used to distinguish and extract the dynamic and static contributions to the PR of a QPC. Our result that the PR of a QPC is dominated by the optically gated static QPC current is consistent with similar previous experiments where the access of photocurrent was not possible [116, 117]. The dominant photogating furthermore implies that photoexcitation-induced shifts in electrostatically defined potential landscapes have to be taken into account in prospective experimental schemes which aim at charge or spin control due to optical excitation in a depletion-induced 2DES potential landscape [118].

In general, the presented FR-based microscope could establish a new technique for an all-optical local spin detection with minimal interaction with the system whose potential in the field of spintronics would go far beyond the evaluation of the striking predictions regarding the fundamental origin of the 0.7-anomaly. For the latter, the transformation of the optical-fiber-based microscope setup into a He3 cryostat with a bath temperature of about 300 mK is straightforward. It would allow to test the predicted enhancement of the local spin polarization of a QPC in the regime of the 0.7-anomaly as a function of relevant parameters such as the magnetic field, the temperature, the 2DES bias voltage, and the geometry of the confinement potential. Moreover, the detector unit of the microscope that enables the FR readout can be exploited for differential transmission experiments on a sample containing the specifically adapted 2DES in order to experimentally determine the spin-resolved optical interband transition rules using a finite magnetic field. If operated in a He3 cryostat, the correspondingly decreased optical resonance linewidths further facilitate spin-resolved optical access to the 2DES. The latter would allow to optically generate a spin imbalance in QPC vicinity by using the FR-based microscope for optical charge excitation aiming at spin-resolved current spectroscopy of a QPC in the 0.7anomaly regime. However, the indicated trion-related origin of the photocurrent detected by means of the relaxation model would constitute a major challenge for QPC spectroscopy experiments based on nearby optical excitation of charge carriers. The experimental analysis of the photocurrent by means of the relaxation model in dependence on basic parameters such as the excitation power, the laser detuning, or the excitation site would further clarify the nature of the photocurrent.

References

[1] L. M. K. Vandersypen, J. M. Elzerman, R. N. Schouten, L. H. Willems van Beveren, R. Hanson, and L. P. Kouwenhoven. Real-time detection of single-electron tunneling using a quantum point contact. *Appl. Phys. Lett.*, 85(19):4394–4396, 2004.

[2] Y. K. Kato, R. C. Myers, A. C. Gossard, and D. D. Awschalom. Observation of the spin Hall effect in semiconductors. *Science*, 306(5703):1910–1913, 2004.

[3] N. P. Stern, D. W. Steuerman, S. Mack, A. C. Gossard, and D. D. Awschalom. Time-resolved dynamics of the spin Hall effect. *Nature Physics*, 4(11):843–846, 2008.

[4] Sara M. Cronenwett, Tjerk H. Oosterkamp, and Leo P. Kouwenhoven. A Tunable Kondo Effect in Quantum Dots. *Science*, 281(5376):540–544, 1998.

[5] P. Debray, S. M. S. Rahman, J. Wan, R. S. Newrock, M. Cahay, A. T. Ngo, S. E. Ulloa, S. T. Herbert, M. Muhammad, and M. Johnson. All-electric quantum point contact spin-polarizer. *Nat Nanotechnol*, 4:759–764, 2009.

[6] S. M. Frolov, A. Venkatesan, W. Yu, J. A. Folk, and W. Wegscheider. Electrical generation of pure spin currents in a two-dimensional electron gas. *Phys. Rev. Lett.*, 102(11):116802, 2009.

[7] T.-M. Chen, M. Pepper, I. Farrer, G. A. C. Jones, and D. A. Ritchie. All-electrical injection and detection of a spin-polarized current using 1D conductors. *Phys. Rev. Lett.*, 109(17):177202, 2012.

[8] Yang Ji, Yunchul Chung, D. Sprinzak, M. Heiblum, D. Mahalu, and H. Shtrikman. An electronic Mach-Zehnder interferometer. *Nature*, 422:415–418, 2003.

[9] G. Yusa, Koji Muraki, K. Takashina, K. Hashimoto, and Y. Hirayama. Controlled multiple quantum coherences of nuclear spins in a nanometre-scale device. *Nature*, 434:1001–1005, 2005.

[10] M. Field, C. G. Smith, M. Pepper, D. A. Ritchie, J. E. F. Frost, G. A. C. Jones, and D. G. Hasko. Measurements of Coulomb blockade with a noninvasive voltage probe. *Phys. Rev. Lett.*, 70(9):1311–1314, 1993.

[11] M. C. Cassidy, A. S. Dzurak, R. G. Clark, K. D. Petersson, I. Farrer, D. A. Ritchie, and C. G. Smith. Single shot charge detection using a radio-frequency quantum point contact. *Appl. Phys. Lett.*, 91(22):222104, 2007.

[12] D. Schröer, A. D. Greentree, L. Gaudreau, K. Eberl, L. C. L. Hollenberg, J. P. Kotthaus, and S. Ludwig. Electrostatically defined serial triple quantum dot charged with few electrons. *Phys. Rev. B*, 76(7):075306, 2007.

[13] A. J. Shields, M. P. O Sullivan, I. Farrer, D. A. Ritchie, R. A. Hogg, M. L. Leadbeater, C. E. Norman, and M. Pepper. Detection of single photons using a field-effect transistor gated by a layer of quantum dots. *Appl. Phys. Lett.*, 76(25):3673–3675, 2000.

[14] Photoconductance quantization in a single-photo detector. H. kosaka and d. s. rao and h. d. robinson and p. bandaru and t. sakamoto and e. yablonovitch. *Phys. Rev. B*, 65(20):201307, 2002.

[15] B. J. van Wees, H. v. Houten, C. W. J. Beenakker, J. G. Williamson, L. P. Kouwenhoven, D. v. d. Marel, and C. T. Foxon. Quantized conductance of point contacts in a two-dimensional electron gas. *Phys. Rev. Lett.*, 60(9):848–850, 1988.

[16] D. A. Wharam, T. J. Thornton, R. Newbury, M. Pepper, H. Ahmed, J. E. F. Frost, D. G. Hasko, D. C. Peacock, D. A. Ritchie, and G. A. C. Jones. One-dimensional transport and the quantisation of the ballistic resistance. *J. Phys. C*, 21(8):L209, 1988.

[17] M. Büttiker. Quantized transmission of a saddle-point constriction. *Phys. Rev. B*, 41(11):7906(R), 1990.

[18] J. I. Pascual, J. Mendez, J. Gomez-Herrero, A. M. Baro, N. Garcia, Uzi Landman, W. D. Luedtke, E. N. Bogachek, and H. P. Cheng. Properties of metallic nanowires: From conductance quantization to localization. *Science*, 267(5205):1793–1795, 1995.

[19] C. J. Muller, J. M. Krans, T. N. Todorov, and M. A. Reed. Quantization effects in the conductance of metallic contacts at room temperature. *Phys. Rev. B*, 1022(3): 53, 1996.

[20] S. Frank, P. Poncharal, Z. L. Wang, and W. A. de Heer. Carbon nanotube quantum resistors. *Science*, 280(5370):1744–1746, 1998.

[21] N. Tombros, A. Veligura, J. Junesch, M. H. D. Guimaraes, I. J. Vera-Marun, H. T. Jonkman, and B. J. van Wees. Quantized conductance of a suspended graphene nanoconstriction. *Nature Physics*, 7(9):697–700, 2011.

[22] L. Olesen, E. Laegsgaard, I. Stensgaard, F. Besenbacher, J. Schiotz, P. Stoltze, K. W. Jacobsen, and J. K. Norskov. Quantized conductance in an atom-sized point contact. *Phys. Rev. Lett.*, 72(14):2251, 1994.

[23] S. Krinner, D. Stadler, D. Husmann, J.-P. Brantut, and T. Esslinger. Observation of quantized conductance in neutral matter. *Nature*, 517(7532):64–67, 2015.

[24] K. J. Thomas, J. T. Nicholls, M. Y. Simmons, M. Pepper, D. R. Mace, and D. A. Ritchie. Possible spin polarization in a one-dimensional electron gas. *Phys. Rev. Lett.*, 77(1):135–138, 1996.

[25] K. J. Thomas, J. T. Nicholls, N. J. Appleyard, M. Y. Simmons, M. Pepper, D. R. Mace, W. R. Tribe, and D. A. Ritchie. Interaction effects in a one-dimensional constriction. *Phys. Rev. B*, 58:4846–4852, 1998.

[26] N. J. Appleyard, J. T. Nicholls, M. Pepper, W. R. Tribe, M. Y. Simmons, and D. A. Ritchie. Direction-resolved transport and possible many-body effects in one-dimensional thermopower. *Phys. Rev. B*, 62(24):R16275–R16278, 2000.

[27] S. M. Cronenwett, H. J. Lynch, D. Goldhaber-Gordon, L. P. Kouwenhoven, C. M. Marcus, K. Hirose, N. S. Wingreen, and V. Umansky. Low-temperature fate of the 0.7 structure in a point contact: A Kondo-like correlated state in an open system. *Phys. Rev. Lett.*, 88:226805, 2002.

[28] L. DiCarlo, Y. Zhang, D. T. McClure, D. J. Reilly, C. M. Marcus, L. N. Pfeiffer, and K. W. West. Shot-noise signatures of 0.7 structure and spin in a quantum point contact. *Phys. Rev. Lett.*, 97(3):036810, 2006.

[29] E. J. Koop, A. I. Lerescu, J. Liu, B. J. van Wees, D. Reuter, A. D. Wieck, and C. H. van der Wal. The influence of device geometry on many-body effects in quantum point contacts: signatures of the 0.7-anomaly, exchange and Kondo. *J. Supercond. Nov. Magn.*, 20:433–441, 2007.

[30] Shuji Nakamura, Masayuki Hashisaka, Yoshiaki Yamauchi, Shinya Kasai, Teruo Ono, and Kensuke Kobayashi. Conductance anomaly and Fano factor reduction in quantum point contacts. *Phys. Rev. B*, 79:201308, 2009.

[31] Y. Komijani, M. Csontos, I. Shorubalko, T. Ihn, K. Ensslin, Y. Meir, D. Reuter, and A. D. Wieck. Evidence for localization and 0.7-anomaly in hole quantum point contacts. *Eur. Phys. Lett.*, 91:67010, 2010.

[32] Y. Ren, W. W. Yu, S. M. Frolov, J. A. Folk, and W. Wegscheider. Zero-bias anomaly of quantum point contacts in the low-conductance limit. *Phys. Rev. B*, 82(4):045313, 2010.

[33] L. W. Smith, A. R. Hamilton, K. J. Thomas, M. Pepper, I. Farrer, J. P. Griffiths, G. A. C. Jones, and D. A. Ritchie. Compressibility measurements of quasi-one-dimensional quantum wires. *Phys. Rev. Lett.*, 107:126801, 2011.

[34] A. M. Burke, O. Klochan, I. Farrer, D. A. Ritchie, A. R. Hamilton, and A. P. Micolich. Extreme sensitivity of the spin-splitting and 0.7-anomaly to confining potential in one-dimensional nanoelectronic devices. *Nano Letters*, 12(9):4495, 2012.

[35] S. Sarkozy, F. Sfigakis, K. Das Gupta, I. Farrer, D. A. Ritchie, G. A. C. Jones, and M. Pepper. Zero-bias anomaly in quantum wires. *Phys. Rev. B*, 79(16):161307(R), 2009.

[36] K. A. Matveev. Conductance of a quantum wire at low electron density. *Phys. Rev. B*, 70(24):245319, 2004.

[37] A. D. Güclü, C. J. Umrigar, Hong J., and H. U. Baranger. Localization in an inhomogeneous quantum wire. *Phys. Rev. B*, 80(20):201302(R), 2009.

[38] K. Aryanpour and J. E. Han. Ferromagnetic spin coupling as the origin of 0.7-anomaly in quantum point contacts. *Phys. Rev. Lett.*, 102(5):056805, 2009.

[39] Y. Meir, K. Hirose, and N. S. Wingreen. Kondo model for the 0.7-anomaly in transport through a quantum point contact. *Phys. Rev. Lett.*, 89(19):196802, 2002.

[40] A. Golub, T. Aono, and Yigal Meir. Suppression of shot noise in quantum point contacts in the 0.7 regime. *Phys. Rev. Lett.*, 97(18):186801, 2006.

[41] T. Rejec and Y. Meir. Magnetic impurity formation in quantum point contacts. *Nature*, 442(7105):900–903, 2006.

[42] M. J. Iqbal, R. Levy, E. J. Koop, J. B. Dekker, J. P. de Jong, J. H. M. van der Velde, D. Reuter, A. D. Wieck, R. Aguado, Y. Meir, and C. H. van der Wal. Odd and even Kondo effects from emergent localization in quantum point contacts. *Nature*, 501:79–83, 2013.

[43] L. P. Rokhinson, L. N. Pfeiffer, and K. W. West. Spontaneous spin polarization in quantum point contacts. *Phys. Rev. Lett.*, 96(15):156602, 2006.

[44] M. Kawamura, K. Ono, P. Stano, K. Kono, and T. Aono. Electronic magnetization of a quantum point contact measured by nuclear magnetic resonance. *Phys. Rev. Lett.*, 115(3):036601, 2015.

[45] D. Goldhaber-Gordon, H. Shtrikman, D. Mahalu, D. Abusch-Magder, U. Meirav, and M. A. Kastner. Kondo effect in a single-electron transistor. *Nature*, 391:156–159, 1998.

[46] W. G. van der Wiel, S. De Franceschi, T. Fujisawa, J. M. Elzerman, S. Tarucha, and L. P. Kouwenhoven. The Kondo effect in the unitary limit. *Science*, 289(5487): 2105–2108, 2000.

[47] A. V. Kretinin, H. Shtrikman, D. Goldhaber-Gordon, M. Hanl, A. Weichselbaum, J. von Delft, T. A. Costi, and D. Mahalu. Spin-1/2 Kondo effect in an InAs nanowire quantum dot: Unitary limit, conductance scaling, and Zeeman splitting. *Phys. Rev. B*, 84:245316, 2011.

[48] B. J. van Wees, L. P. Kouwenhoven, E. M. M. Willems, C. J. P. M. Harmans, J. E. Mooij, H. van Houten, C. W. J. Beenakker, J. G. Williamson, and C. T. Foxon. Quantum ballistic and adiabatic electron transport studied with quantum point contacts. *Phys. Rev. B*, 43(15):12431–12453, 1991.

[49] E. N. Economou and C. M. Soukoulis. Static conductance and scaling theory of localization in one dimension. *Phys. Rev. Lett.*, 46(9):618–621, 1981.

[50] R. Landauer. Spatial variation of currents and fields due to localized scatterers in metallic conduction. *IBM J. Res. Dev.*, 1(3):223–231, 1957.

[51] J. Spector, H.L. Stormer, K.W. Baldwin, L.N. Pfeiffer, and K.W. West. Ballistic electron transport beyond 100 micrometer in 2D electron systems. *Surf. Sci.*, 228 (1–3):283–285, 1990.

[52] Y. Hirayama, T. Saku, S. Tarucha, and Y. Horikoshi. Ballistic electron transport in macroscopic four-terminal square structures with high mobility. *Appl. Phys. Lett.*, 58(23):2672, 1991.

[53] V. Umansky, M. Heiblum, Y. Levinson, J. Smet, J. Nübler, and M. Dolev. Mbe growth of ultra-low disorder 2DEG with mobility exceeding 35000000 cm^2/Vs. *J.Cryst.Growth*, 311(7):1658–1661, 2009.

[54] Glazman L. I., Lesovik G. B., Khmel'nitskii D. E., and Shekhter R. I. Reflectionless quantum transport and fundamental ballistic-resistance steps in microscopic constrictions. *JETP Lett.*, 48(4):238–241, 1988.

[55] Ya. M. Blanter and M. Büttiker. Shot noise in mesoscopic conductors. *Phys. Rep.*, 336:1–166, 2000.

[56] G. B. Lesovik. Excess quantum noise in 2D ballistic point contacts. *JETP Lett.*, 49 (9):592, 1989.

[57] M. Büttiker. Scattering theory of thermal and excess noise in open conductors. *Phys. Rev. Lett.*, 65(23):2901, 1990.

[58] J. Kondo. Resistance minimum in dilute magnetic alloys. *Prog. Theor. Phys.*, 32 (1):37–49, 1964.

[59] P. W. Anderson. Localized magnetic states in metals. *Phys. Rev.*, 124(1):41–53, 1961.

[60] K. G. Wilson. The renormalization group: Critical phenomena and the Kondo problem. *Rev. Mod. Phys.*, 47(4):773, 1975.

[61] L. Kouwenhoven and L. Glazman. Revival of the Kondo effect. *Physics World*, 14 (1):33–38, 2001.

[62] N. E. Bickers. Review of techniques in the large-N expansion for dilute magnetic alloys. *Rev. Mod. Phys.*, 59(4):845, 1987.

[63] S. Hershfield, J. H. Davies, and J. W. Wilkins. Probing the Kondo resonance by resonant tunneling through an Anderson impurity. *Phys. Rev. Lett*, 67(26):3720–3723, 1991.

[64] N. S. Wingreen and Y. Meir. Anderson model out of equilibrium: Noncrossing-approximation approach to transport through a quantum dot. *Phys. Rev. B*, 49 (16):11040–11052, 1994.

[65] David Borowsky. Transportmessungen zur Untersuchung der 0.7-Struktur in Quantenpunktkontakten. Diplomarbeit, Ludwig-Maximilians-Universität München, Munich, Germany, 2011.

[66] A. Oguri. Transmission probability for interacting electrons connected to reservoirs. *J. Phys. Soc. Jap.*, 70:2666, 2001.

[67] S. Andergassen, T. Enss, V. Meden, W. Metzner, U. Schollwöck, and K. Schönhammer. Renormalization-group analysis of the one-dimensional extended Hubbard model with a single impurity. *Phys. Rev. B*, 73(4):045125, 2006.

[68] C. Karrasch, T. Enss, and V. Meden. Functional renormalization group approach to transport through correlated quantum dots. *Phys. Rev. B*, 73(23):235337, 2006.

[69] W. Metzner, M. Salmhofer, C. Honerkamp, V. Meden, and K. Schönhammer. Functional renormalization group approach to correlated fermion systems. *Rev. Mod. Phys.*, 84(1):299, 2012.

[70] C. Sloggett, A. I. Milstein, and O. P. Sushkov. Correlated electron current and temperature dependence of the conductance of a quantum point contact. *Eur. Phys. J. B*, 61:427–432, 2008.

[71] D. J. Reilly, G. R. Facer, A. S. Dzurak, B. E. Kane, R. G. Clark, P. J. Stiles, R. G. Clark, A. R. Hamilton, J. L. O Brien, N. E. Lumpkin, L. N. Pfeiffer, and K. W. West. Many-body spin-related phenomena in ultra low-disorder quantum wires. *Phys. Rev. B*, 63(12):121311(R), 2001.

[72] A. M. Lunde, A. De Martino, A. Schulz, R. Egger, and K. Flensberg. Electron-electron interaction effects in quantum point contacts. *New J. Phys.*, 11:023031, 2009.

[73] D. J. Reilly. Phenomenological model for the 0.7 conductance feature in quantum wires. *Phys. Rev. B*, 72(3):033309, 2005.

[74] L. W. Smith, H. Al-Taie, F. Sfigakis, P. See, A. A. J. Lesage, B. Xu, J. P. Griffiths, H. E. Beere, G. A. C. Jones, D. A. Ritchie, M. J. Kelly, and C. G. Smith. Statistical study of conductance properties in one-dimensional quantum wires focusing on the 0.7-anomaly. *Phys. Rev. B*, 90:045426, 2014.

[75] B. Brun, F. Martins, S. Faniel, B. Hackens, G. Bachelier, A. Cavanna, C. Ulysse, A. Ouerghi, U. Gennser, D. Mailly, S. Huant, V. Bayot, M. Sanquer, and H. Sellier. Wigner and Kondo physics in quantum point contacts revealed by scanning gate microscopy. *Nature Comm.*, 5:4290, 2014.

[76] F. Bauer, J. Heyder, and J. von Delft. Functional renormalization group approach for inhomogeneous interacting Fermi systems. *Phys. Rev. B*, 89:045128, 2014.

[77] T. A. Costi. Magnetotransport through a strongly interacting quantum dot. *Phys. Rev. B*, 64:241310, 2001.

[78] P. Nozières. A "Fermi-Liquid" description of the Kondo problem at low temperatures. *J. Low Temp. Phys.*, 17:31–42, 1974.

[79] L.I. Glazman and M. Pustilnik. Low-temperature transport through a quantum dot, 2005. Nanophysics: Coherence and Transport, eds. H. Bouchiat et al. (Elsevier, 2005).

[80] D. M. Schröer, A. K. Hüttel, K. Eberl, S. Ludwig, M. N. Kiselev, and B. L. Altshuler. Kondo effect in a one-electron double quantum dot: Oscillations of the Kondo current in a weak magnetic field. *Phys. Rev. B*, 74:233301, 2006.

[81] F. D. M. Haldane. Scaling theory of the asymmetric Anderson model. *Phys. Rev. Lett.*, 40:416–419, 1978.

[82] V. Sih, R. C. Myers, Y. K. Kato, W. H. Lau, A. C. Gossard, and D. D. Awschalom. Spatial imaging of the spin Hall effect and current-induced polarization in two-dimensional electron gases. *Nature Physics*, 1:31–35, 2005.

[83] J. Berezovsky, M. H. Mikkelsen, O. Gywat, N. G. Stoltz, L. A. Coldren, and D. D. Awschalom. Nondestructive optical measurements of a single electron spin in a quantum dot. *Science*, 314(5807):1916–1920, 2006.

[84] B. B. Buckley, G. D. Fuchs, L. C. Bassett, and D. D. Awschalom. Spin-light coherence for single-spin measurement and control in diamond. *Science*, 330(6008): 1212–1215, 2010.

[85] I. Gerhardt, G. Wrigge, M. Agio, P. Bushev, G. Zumofen, and V. Sandoghdar. Scanning near-field optical coherent spectroscopy of single molecules at 1.4 k. *Opt. Lett.*, 32(11):1420–1422, 2007.

[86] B. Alen, A. Högele, M. Kroner, S. Seidl, K. Karrai, R. J. Warburton, A. Badolato, G. Medeiros-Ribeiro, and P. M. Petroff. Absorptive and dispersive optical responses of excitons in a single quantum dot. *Appl. Phys. Lett.*, 89(12):123124, 2006.

[87] P. C. Maurer, J. R. Maze, P. L. Stanwix, L. Jiang, A. V. Gorshkov, A. A. Zibrov, B. Harke, J. S. Hodges, A. S. Zibrov, A. Yacoby, D. Twitchen, S. W. Hell, R. L. Walsworth, and M. D. Lukin. Far-field optical imaging and manipulation of individual spins with nanoscale resolution. *Nature Physics*, 6(11):912–918, 2010.

[88] S. Seidl, M. Kroner, P. A. Dalgarno, A. Högele, J. M. Smith, M. Ediger, B. D. Gerardot, J. M. Garcia, P. M. Petroff, K. Karrai, and R. J. Warburton. Absorption and photoluminescence spectroscopy on a single self-assembled charge-tunable quantum dot. *Phys. Rev. B*, 72(19):195339, 2005.

[89] R. J. Warburton, C. Schaflein, D. Haft, F. Bickel, A. Lorke, K. Karrai, J. M. Garcia, W. Schoenfeld, and P. M. Petroff. Optical emission from a charge-tunable quantum ring. *Nature*, 405:926–929, 2000.

[90] A. Högele, S. Seidl, M. Kroner, K. Karrai, R. J. Warburton, B. D. Gerardot, and P. M. Petroff. Voltage-controlled optics of a quantum dot. *Phys. Rev. Lett.*, 93(21): 217401, 2004.

[91] B. Alen, F. Bickel, K. Karrai, R. J. Warburton, and P. M. Petroff. Stark-shift modulation absorption spectroscopy of single quantum dots. *Appl. Phys. Lett.*, 83 (11):2235, 2003.

[92] A. Högele, S. Seidl, M. Kroner, K. Karrai, C. Schulhauser, O. Sqalli, J. Scrimgeour, and R. J. Warburton. Fiber-based confocal microscope for cryogenic spectroscopy. *Rev. Sci. Instrum.*, 79(2):023709, 2008.

[93] J. M. Elzerman, R. Hanson, L. H. Willems van Beveren, B. Witkamp, L. M. K. Vandersypen, and L. P. Kouwenhoven. Single-shot read-out of an individual electron spin in a quantum dot. *Nature*, 430(6998):431–435, 2004.

[94] M. Kroutvar, Y. Ducommun, D. Heiss, M. Bichler, D. Schuh, G. Abstreiter, and J. J. Finley. Optically programmable electron spin memory using semiconductor quantum dots. *Nature*, 432(7013):81–84, 2004.

[95] M. Atatüre, J. Dreiser, A. Badolato, A. Högele, K. Karrai, and A. Imamoglu. Quantum-dot spin-state preparation with near-unity fidelity. *Science*, 312(5773): 551–553, 2006.

[96] M. Kroner, A. O. Govorov, S. Remi, B. Biedermann, S. Seidl, A. Badolato, P. M. Petroff, W. Zhang, R. Barbour, B. D. Gerardot, R. J. Warburton, and K. Karrai. The nonlinear Fano effect. *Nature*, 451:311–314, 2008.

[97] *http://www.nextnano.de/nextnano3*.

[98] G. B. Stringfellow, W. Koschel, F. Briones, J. Gladstone, and G. Patterson. Photoluminescence of carbon implanted GaAs. *Appl. Phys. Lett.*, 39:581, 1981.

[99] G. D. Mahan. Excitons in degenerate semiconductors. *Phys. Rev.*, 153:882, 1967.

[100] P. Hawrylak. Optical properties of a two-dimensional electron gas: Evolution of spectra from excitons to Fermi-edge singularities. *Phys. Rev. B*, 44:3821, 1991.

[101] C. L. Kane, K. A. Matveev, and L. I. Glazman. Fermi-edge singularities and backscattering in a weakly interacting one-dimensional electron gas. *Phys. Rev. B*, 49:2253, 1994.

[102] K. Kheng, R. T. Cox, Y. Merle d'Aubigne, F. Bassani, K. Saminadayar, and S. Tatarenko. Observation of negatively charged excitons X- in semiconductor quantum wells. *Phys. Rev. Lett.*, 71(11):1752–1755, 1993.

[103] G. Finkelstein, H. Shtrikman, and I. Bar-Joseph. Negatively and positively charged excitons in GaAs/Al(x)Ga(1-x)As quantum wells. *Phys. Rev. B*, 53(4):R1709(R), 1996.

[104] G. Finkelstein, H. Shtrikman, and I. Bar-Joseph. Optical spectroscopy of a two-dimensional electron gas near the metal-insulator transition. *Phys. Rev. Lett.*, 74 (6):976–979, 1995.

[105] I. Bar-Joseph. Trions in GaAs quantum wells. *Semicond. Sci. Technol.*, 20:R29–R39, 2005.

[106] Matthias Benecke. Untersuchungen an Quantenpunktkontakten im Hinblick auf 0.7-Anomalie. Diplomarbeit, Ludwig-Maximilians-Universität München, Munich, Germany, 2010.

[107] A. Reinhard. Probing a single quantum dot-cavity system with photoluminescence and resonant excitation. diploma thesis, Quantum Photonics group, ETH Zürich, 2008.

[108] P. Drude. Zur Elektronentheorie der Metalle. *Annalen der Physik*, 306:566–613, 1900.

[109] D. Sanvitto, R. A. Hogg, A. J. Shields, D. M. Whittaker, M. Y. Simmons, D. A. Ritchie, and M. Pepper. Rapid radiative decay of charged excitons. *Phys. Rev. B*, 62(20):R13294(R), 2000.

[110] M. T. Portella-Oberli, J. Berney, L. Kappei, F. Morier-Genoud, J. Szczytko, and B. Deveaud-Pledran. Dynamics of trion formation in In(x)/Ga(1-x)As quantum wells. *Phys. Rev. Lett*, 102(9):096402, 2009.

[111] S. Zimmermann, A. Wixforth, J. P. Kotthaus, W. Wegscheider, and M. Bichler. A semiconductor-based photonic memory cell. *Science*, 283(5406):1292–1295, 1999.

[112] M. van Exter and D. Grischkowsky. Carrier dynamics of electrons and holes in moderately doped silicon. *Phys. Rev. B*, 41(17):12140–12149, 1990.

[113] M. Volk, S. Lutgen, T. Marschner, W. Stolz, E. O. Göbel, P. C. M. Christianen, and J. C. Maan. Carrier effective masses in symmetrically strained (GaIn)As/Ga(PAs) multiple-quantum-well structures. *Phys. Rev. B*, 52(15):11096, 1995.

[114] D. Sanvitto, F. Pulizzi, A. Shields, P. C. M. Christianen, S. N. Holmes, M. Y. Simmons, D. A. Ritchie, J. C. Maan, and M. Pepper. Observation of charge transport by negatively charged excitons. *Science*, 294(5543):837–839, 2001.

[115] T. Figielski. The 0.7-anomaly in quantum point contact: Many-body or single-electron effect? *WJCMP*, 6(3):217–223, 2016.

[116] K.-D. Hof, C. Rossler, S. Manus, J. P. Kotthaus, A. W. Holleitner, D. Schuh, and W. Wegscheider. Dynamic photoconductive gain effect in shallow-etched AlGaAs/GaAs quantum wires. *Phys. Rev. B*, 78(11):115325, 2008.

[117] C. Rössler, K.-D. Hof, S. Manus, S. Ludwig, J. P. Kotthaus, J. Simon, A. W. Holleitner, D. Schuh, and W. Wegscheider. Optically induced transport properties of freely suspended semiconductor submicron channels. *Appl. Phys. Lett.*, 93(7): 071107, 2008.

[118] D. Kim, A. A. Kiselev, R. S. Ross, M. T. Rakher, C. Jones, and T. D. Ladd. Optically loaded semiconductor quantum memory register. *Phys. Rev. Applied*, 5 (2):024014, 2016.

List of publications

P1 G. J. Schinner, E. Schubert, M. P. Stallhofer, J. P. Kotthaus, D. Schuh, A. K. Rai, D. Reuter, A. D. Wieck, and A. O. Govorov, *Electrostatically trapping indirect excitons in coupled $In(x)Ga(1-x)As$ quantum wells*, Phys. Rev. B 83, 165308 (2011)

P2 G. J. Schinner, J. Repp, K. Kowalik-Seidl, E. Schubert, M. P. Stallhofer, A. K. Rai, D. Reuter, A. D. Wieck, A. O. Govorov, A. W. Holleitner, and J. P. Kotthaus, *Quantum Hall signatures of dipolar Mahan excitons*, Phys. Rev. B 87, 041303(R) (2013)

P3 G. J. Schinner, J. Repp, E. Schubert, A. K. Rai, D. Reuter, A. D. Wieck, A. O. Govorov, A. W. Holleitner, and J. P. Kotthaus, *Confinement and Interaction of Single Indirect Excitons in a Voltage-Controlled Trap Formed Inside Double InGaAs Quantum Wells*, Phys. Rev. Lett. 110, 127403 (2013)

P4 G. J. Schinner, J. Repp, E. Schubert, A. K. Rai, D. Reuter, A. D. Wieck, A. O. Govorov, A. W. Holleitner, and J. P. Kotthaus, *Many-body correlations of electrostatically trapped dipolar excitons*, Phys. Rev. B 87, 205302 (2013)

P5 F. Bauer, J. Heyder, E. Schubert, D. Borowsky, D. Taubert, B. Bruognolo, D. Schuh, W. Wegscheider, J. von Delft, and S. Ludwig, *Microscopic origin of the '0.7-anomaly' in quantum point contacts*, Nature 501, 73 (2013)

P6 F. Seilmeier, M. Hauck, E. Schubert, G. J. Schinner, S. E. Beavan, and A. Högele, *Optical Thermometry of an Electron Reservoir Coupled to a Single Quantum Dot in the Millikelvin Range*, Phys. Rev. Applied 2, 024002 (2014)

P7 J. Repp, G. J. Schinner, E. Schubert, A. K. Rai, D. Reuter, A. D. Wieck, U. Wurstbauer, J. P. Kotthaus, and A. W. Holleitner, *Confocal shift interferometry of coherent emission from trapped dipolar excitons*, Appl. Phys. Lett. 105, 241101 (2014)

P8 E. Schubert, J. Heyder, F. Bauer, B. Waschneck, W. Stumpf, W. Wegscheider, J. von Delft, S. Ludwig, and A. Högele, *Toward combined transport and optical studies of the 0.7-anomaly in a quantum point contact*, Phys. Status Solidi B 251, 1931 (2014)

P9 J. Heyder, F. Bauer, E. Schubert, D. Borowsky, D. Schuh, W. Wegscheider, J. von Delft, and S. Ludwig, *Relation between the 0.7 anomaly and the Kondo effect: Geometric crossover between a quantum point contact and a Kondo quantum dot*, Phys. Rev. B 92, 195401 (2015)

P10 E. Schubert, B. Waschneck, W. Wegscheider, S. Ludwig, and A. Högele, *Determination of the dynamic and static contributions to the photoresponse of a quantum point contact*, (in preparation)

Danksagung

Auch wenn es oft lange Phasen in der Arbeit an dieser Dissertation gab, in denen mir das Konzept Mitmensch etwas fremd geworden ist, wäre diese Arbeit ohne die tatkräftige Mithilfe und Unterstützung sehr vieler ...Mitmenschen nicht möglich gewesen.
Ich danke:

Alex Högele für die sehr angenehme, sehr faire und sehr geförderte produktive Zusammenarbeit, für die Hilfe in allen Lagen und Fragen des Projekts, für die entscheidenden Ideen zum Experiment in den letzten Wochen des schlussendlich 16-monatigen Messmarathons, für das hilfreiche kritische Nach- und Hinterfragen der Ergebnisse in den unzähligen meist stundenlangen Besprechungen und für das Zeitnehmen für jegliche Fragen des Doktoranden, auch wenn (bzw. trotz das praktisch immer) eigentlich gar keine Professorenzeit dafür zur Verfügung stand.

Stefan Ludwig für die enorme Unterstützung während seiner Mitbetreuung meines Projekts über die gesamte Projektphase hinweg, vor allem auch in der Zeit seiner bereits offiziellen Tätigkeit in der Landeshauptstadt.

Jan von Delft, Jan Heyder und Florian Bauer für die wertvolle Sicht auf die gemessenen Ergebnisse in unzähligen gemeinsamen Besprechungen, und vor allem für die maßgebliche exzellente Unterstützung seitens der Theorie, welche praktisch ausschließlich in Form von direkten Vorhersagen des direkt experimentell zugänglichen Leitwerts unseren Fokus in den Experimenten optimal gelenkt hat.

Bernd Waschneck für die tatkräftige Unterstützung beim Aufbau des kombinierten Optik-Transport-Setups, für wertvolle Ideen zu Details im Aufbau und im Dschungel der Auswertungen der Probenantworten in Abhängigkeit von dutzenden zugänglichen Parametern, und für die Mithilfe bei der schließlich notwendig gewesenen 24/7-Experimentbetreuung.

Simon Lehnert, der im Detail wie auch in allgemeinen Fragen immer mit Rat, Tat und bestem Wissen zur Seite stand. Und das vor allem auch ganz am Anfang - ich erinnere mich sehr gut an seine Antwort an einen etwas zögerlichen, frisch gebackenen KFZ-Mechaniker, in der Zivi-Mittagspause im Krankenhausinnenhof im strahlenden Sonnenschein auf einer Bank: “He man, wenn du Physik studieren willst, dann studier’ Physik!”.

Diana Schubert für die allzeit direkte und indirekte Unterstützung, guten Rat und immer ein offenes Ohr, sowohl in meinem Studium als auch in der Zeit meiner Doktorarbeit.

Philipp Altpeter für die hervoragende Betreuung im Reinraum, für sein jederzeit bereitwilliges Zeitnehmen, wenn man sich mit einer egal wie stark oder weniger stark auf die eigentliche Reinraumtätigkeit bezogene Frage an ihn wendet, und für seine exzellenten Ideen, die in der Regel sofort funktionieren, insbesondere im Zusammenhang mit den Spezialanforderungen an die Fabrikation meiner Probe und den aus dem Nichts aufgetretenen Problemen inhomogener Schichtdicken der PMMA-Schichten.

Bert Lorenz für die jederzeit zuvorkommend angebotene Zeit und Hilfe bei jeglichen Fragen, auch oder vor allem zum Thema Physik, sowie für die Organisation der wohl grundlegenden Basis des Lehrstuhls, was wohl hin und wieder auch ein persönliches Eintreten für den Lehrstuhl darstellt und was auch manchmal eine Argument zugunsten eines horrend hohen Heliumverbrauchs bedarf, welches nicht sofort auf der Hand liegen muss.

Friedrich, "unser" Photograph mit (glücklicherweise) LKW-Führerschein, der zuverlässig, sympathisch und zuvorkommend immer zur Seite stand bei den Fahrten für die Heliumversorgung, vor allem bei der zuletzt benötigten 16-monatigen ununterbrochenen Dauerversorgung für die QPC-Probe.

Anton "Toni" Heindl für den schnellen, professionellen Bau der beiden Voigt-Adapter für den Probenhalter, und natürlich für alle Arbeiten im Hintergrund sowie im Vordergrund rund um die Stickstoffverflüssigung und die Heliumversorgung.

Reinhold Rath für die zuverlässigen Wartungen und Reparaturen im Reinraum.

Stephan Manus für guten Rat und vor allem Tat bei Leistungsstabilisierungen sowie Laborgeräten aller Art.

Johannes Rieger für jederzeit wertvollen Rat in Sachen Mathematica, in Sachen Software- und Rechnerdetails, bzgl. Sachen schräger Typen aus der Zukunft, sowie für die spontane Mitarbeit bei spontanen Musikproduktionen im Unibüro, wie zum Beispiel: save as untitled (P. R. Wesley feat. Lars Vegas remix).

Thomas Faust für die Beantwortung von Fragen aller Art, und für die kompetente Unterstützung bzgl. allgemein Computer und speziell diverser Software.

Manuel Nutz für kompetente Rechneradministration und kompetente Antworten zu Rechnerfragen aller Art, und für die Hilfe in Sachen Mathematica.

Quirin Unterreithmeier für den Labmaster und Unterstützung in Sachen Mathematica.

Martina Jüttner für jederzeit zuvorkommend angebotene Hilfe und Rat in allen Details rund um Verwaltung, Urlaub und co. .

Meinen Eltern, denen ich nun auch endlich die Frage beantworten kann, wann ich denn fertig werde.

Außerdem danke im dem gesamten Lehrstuhl für die klasse Atmosphäre und für die sehr angenehme Zusammenarbeit, miteinander und nebeneinander.